UNIVERSITY OF CALIFORNIA

Los Angeles

Hybrid Combustion Analysis Via Laser Absorption Spectroscopy for Rocket Propulsion and Fire Environments

A dissertation submitted in partial satisfaction
of the requirements for the degree
Doctor of Philosophy in Aerospace Engineering

by

Isabelle Constance Sanders

2023

ABSTRACT OF THE DISSERTATION

Hybrid Combustion Analysis
Via Laser Absorption Spectroscopy for
Rocket Propulsion and Fire Environments

by

Isabelle Constance Sanders
Doctor of Philosophy in Aerospace Engineering
University of California, Los Angeles, 2023
Professor Raymond M. Spearrin, Chair

This dissertation details novel experimental methods and analytical techniques developed to characterize hybrid combustion of solid fuels with gaseous oxidizers. The primary focus of this work is on hybrid rocket motors, which are less developed than liquid and solid fuel chemical propulsion systems. Historically poor performance of hybrid propulsion systems is attributed, in part, to combustion efficiencies below theoretical limits, hindering hybrid rocket development and motivating experimental and modeling studies to explain shortcomings. Combustion in such systems is typified by a turbulent reacting boundary layer above the fuel surface that involves a convolution of fluid dynamics, heat transfer, and chemical kinetics. Although modeling efforts have advanced significantly in recent years, there remains a lack of quantitative data, particularly in-situ in the reacting flow regions, that are necessary to validate combustion models and make definitive assessments of the reacting boundary layer flow-field. Optical diagnostics have become invaluable tools for obtaining such data due to their non-intrusive nature and their capability in harsh combustion envi-

ronments. For much of the research detailed herein, an axisymmetric solid fuel burner was used to examine the near-surface reaction layer via spatially-resolved measurements using laser absorption tomographic methods. The data obtained from these experiments were compared to relevant multi-physics combustion models.

The hybrid rocket motor experiments discussed in this dissertation primarily involve polymethyl methacrylate (PMMA) as the fuel with gaseous oxygen. The solid fuel burner and laser diagnostic sensors were used to assess hybrid PMMA/GOx combustion as influenced by differing oxidizer injector geometries, those including both axial and swirl varieties. Two-dimension quantitative measurements of species and temperature provided crucial comparisons to theorized and modelled thermochemical structure evolution. Additionally, the injector specific findings highlight the sensitivity of the combustion performance to motor geometry and quantify the utility of introducing incipient swirling flow into the combustion chamber. Significant discrepancies were observed between reactive flow modeling and the 2D experimental results for hybrid combustion of polymethyl methacrylate (PMMA) in gaseous oxidizer cross-flow, prompting a fundamental shock-tube chemical kinetic studies of the monomer, methyl methacrylate (MMA), that involved measuring time evolution of intermediate and product species. This additional data was used to improve the existing chemical kinetic mechanisms by modifying Arrhenius rate parameters of sensitive reactions via genetic algorithm optimization anchored to the speciation measurements. The aforementioned spectroscopic, experimental, and analysis techniques designed for hybrid rocket propulsion were also extended to study hybrid combustion of the fire-resistant polymer polytetrafluorethylene (PTFE) in oxidizer-cross flow to help inform toxicant predictions in structural fires and develop useful sensors for fire safety.

It is envisioned that the data in this dissertation will be used to anchor and improve reacting flow models relevant to both hybrid rocket propulsion and fire safety. The sensors, experimental facilities, and analysis procedures can also be further employed in the future to study a wide range of solid fuels across combustion applications.

The dissertation of Isabelle Constance Sanders is approved.

Artur R. Davoyan

Kunihiko Taira

Ann R. Karagozian

Raymond M. Spearrin, Committee Chair

University of California, Los Angeles

2023

TABLE OF CONTENTS

1 Introduction **1**

1.1 Solid Fuel Combustion in Oxidizer Cross-Flow 1

1.2 Governing principles 1

1.3 Hybrid rocket propulsion 8

1.3.1 Hybrid rocket combustion dynamics 10

1.3.2 Hybrid rocket oxidizer injectors 14

1.4 Fire toxicity 15

1.5 Solid Fuel Combustion Analysis Methods 18

1.5.1 Experimental Methods 18

1.5.2 Diagnostic Techniques 23

1.6 Scope and Organization 27

2 Mid-infrared Laser Absorption Spectroscopy **29**

2.1 Fundamentals 30

2.2 Direct absorption spectroscopy 33

2.3 Laser absorption tomography 35

2.3.1 Deconvolution Methods 37

3 Axial injector effects on hybrid polymethylmethacrylate combustion assessed by thermochemical imaging **40**

3.1 Introduction 40

3.2 Methods 41

3.2.1 Injector geometries . . . 41
3.2.2 Sensing strategy . . . 42
3.2.3 Testing procedure . . . 45
3.2.4 Spectroscopic data processing . . . 46
3.2.5 Fuel regression analysis . . . 49
3.3 Results and discussion . . . 50
3.3.1 Planar thermochemical measurements . . . 51
3.3.2 Two-dimensional thermochemical images . . . 55
3.3.3 Fuel regression measurements . . . 57
3.3.4 Injector cold-flow CFD . . . 60
3.4 Conclusion . . . 64

4 Swirl injection in hybrid PMMA combustion assessed by thermochemical imaging . . . 66

4.1 Introduction . . . 66
4.2 Theory . . . 68
4.2.1 Spectroscopy and Tomography . . . 68
4.3 Experimental Setup . . . 71
4.3.1 Hybrid Test Article . . . 71
4.3.2 Injector Geometries . . . 73
4.4 Results . . . 75
4.4.1 Space-time Averaged Fuel Regression Rates . . . 75
4.4.2 Thermochemical Flow-field Measurements . . . 76
4.5 Summary and Future Work . . . 81

5 Spatially-resolved characteristic velocity (c*) measurements for hybrid rocket combustion analysis 82

5.1 Introduction 82

5.1.1 Rocket performance characterization 84

5.2 Theoretical approach 86

5.3 Methods 89

5.3.1 Laser absorption spectroscopy 89

5.3.2 Localized flow-field properties 92

5.4 Demonstration results 95

5.4.1 Liquid-propellant rocket combustion 95

5.4.2 Hybrid rocket combustion 97

5.5 Uncertainty analysis 101

5.6 Conclusions 106

6 Methyl methacrylate thermal decomposition: Modeling and laser spectroscopy of species time-histories behind reflected shock waves 107

6.1 Introduction 108

6.2 Experimental Methods 111

6.2.1 Experimental setup 111

6.2.2 Laser Absorption Spectroscopy 114

6.3 Results 116

6.4 Kinetic modeling 120

6.4.1 Decomposition Pathway Analysis 121

6.4.2 Mechanism Modification 126

6.5 Conclusion 130

7 Polytetrafluorethylene (PTFE) burn characteristics in a convective oxidizer cross-flow 131

7.1 Introduction 131

7.2 Methods 134

7.2.1 Solid Fuel Burner 134

7.2.2 Laser Absorption Spectroscopy 138

7.2.3 Tomographic Imaging 140

7.3 Results 141

7.3.1 PMMA pre-burner boundary condition 142

7.3.2 PTFE reaction layer measurements 143

7.4 Discussion/Analysis 147

7.4.1 Chemical equilibrium analysis 147

7.4.2 Reaction kinetics analysis 149

7.5 Conclusion 151

8 Conclusions and Future Research 154

8.1 Current and future research directions 156

8.1.1 Hybrid rocket motor designs 156

8.1.2 High-pressure hybrid combustion measurements 157

8.1.3 Laser absorption imaging for hybrid combustion analysis 157

8.1.4 Fire-resistant fuel characterization 158

8.1.5 Lithium-Ion Battery Fires 159

8.1.6 TFE Chemical Kinetics 159

A Uncertainty analysis **162**

A.1 O/F uncertainty 162

A.2 Regression rate uncertainty 165

A.3 Oxidizer mass flux uncertainty 166

B JPP supplementary material **168**

C CFD mesh convergence study **177**

D Fuel: Supplementary Material **180**

D.1 Sample spectral data 180

D.2 Comparison of modified and existing MMA models 181

E MMA Mechanism **184**

F High pressure hybrid combustion rig **274**

References **277**

LIST OF FIGURES

1.1 A) Idealized diffusion flame structure distribution of fuel, oxidizer, and product species with flame sheet assumptions. B) Diffusion flame structure species distributions reaction zone. 3

1.2 Schematic of classical diffusion-limited hybrid combustion 6

1.3 Simple schematic of a hybrid-propellant rocket [1] 9

1.4 SpaceShipOne and SpaceShipTwo-class VSS Unity 10

1.5 Diagram of the characteristic flow-field regions resulting from axial oxidizer injection in a hybrid motor geometry (adopted from [2]) 12

1.6 Post-firing image of axial injection into a hybrid rocket motor [3] 14

1.7 House fires with traditional construction and fire-resistant materials 16

1.8 Stanford flow facility for imaging of hybrid combustion turbulent boundary layers. Diagram from [4]. 19

1.9 Concurrent air-flow over solid fuel slab burner configuration used for experiments in [5]. 21

1.10 Vertical test stand utilized for temperature and species measurements in hybrid rocket combustion. Optical setup is shown for both CO and CO_2/H_2O configurations used in [6]. 22

1.11 Piping and instrumentation diagram illustrating both GOx and N_2 gas delivery systems. Flow rates for all experiments are regulated using a sonic orifice 23

2.1 Spectral survey of absorption linestengths for select combustion relevant species. Spectral parameters used for simulation obtained from the HITRAN database [7]. 30

2.2 Axisymmetric flow-field deconvolution coordinate system and geometry from line-of-sight measurements. The radially-resolved absorption coefficient $K(r)$ can be reconstructed from the projected area $A_{proj}(y)$ through an Abel transform. . . . 37

3.1 Dimensioned drawings for the single-port and axial showerhead injectors alongside a cross-sectional view of the hybrid rocket motor geometry used in all experiments. Units: mm [in.] 41

3.2 Absorbance simulations at representative combustion conditions for CO, CO_2, and H_2O thermochemistry measurements. Individual transitions comprising each feature are shown in black. 42

3.3 Linestrength, $S(T)$, and temperature sensitivity, $(\mathrm{d}R/R)/(\mathrm{d}T/T)$, as a function of temperature for the CO and H_2O line pairs used in this study. 44

3.4 Representative direct-absorption scans for targeted CO, CO_2, and H_2O transitions, I_t. The dashed lines indicate the background signals, I_0, taken with the flame off and a N_2 purge through the fuel-grain core. 46

3.5 Measured absorbance averaged over 100 scans versus wavenumber. The corresponding Voigt fits illustrate a 95% confidence interval of the measured data. Reasonable residuals for each fit confirm appropriateness of a Voigt line shape model. 47

3.6 *From left to right*: Measured CO absorbance with a Voigt line-shape fit, A_{proj} versus distance y from the center of the fuel grain, Abel-inverted radially-resolved K, and the resulting planar thermochemistry distributions 48

3.7 Measured temperature versus radial distance from the fuel-grain center ($r = 0$) for the single-port (*left*) and axial showerhead (*middle*) injectors. Chemical equilibrium temperature for PMMA/GOx combustion versus equivalence ratio, ϕ (*right*) 52

3.8 Species mole fraction measurements for CO (*left*), CO_2 (*middle*), and H_2O (*right*) versus radial distance, r, from the fuel grain center ($r = 0$ mm) at three axial positions 53

3.9 Comparison of mole fraction measurements for the single-port (*left*) and axial showerhead (*middle*) injectors. Chemical equilibrium mole fraction composition versus equivalence ratio, ϕ, for PMMA/GOx combustion (*right*) 53

3.10 Two-dimensional thermochemistry measurements demonstrating PMMA/GOx combustion progression along the axial direction for the single-port (*left*) and axial showerhead injectors (*right*). 56

3.11 Measured space-time averaged regression rates, $\bar{\dot{r}}$, for both the single-port and axial showerhead injector geometries over the range of fuel-grain heights considered 59

3.12 Non-reacting (cold-flow) CFD simulation results showing velocity contours, pathlines, and wall shear stress for the single-port injector (*left*) and the axial showerhead injector (*right*) 63

4.1 Hybrid combustion facility utilized for exit-plane temperature and species measurements 71

4.2 Isometric views of the tangential swirl, canted swirl, and axial showerhead injector designs 73

4.3 Simulated pathlines representative of axial and swirl injection into the test article geometry obtained from ANSYS Fluent cold flow simulations of gaseous oxygen 74

4.4 *Left*: ANSYS Fluent cold flow results for wall shear versus downstream axial distance from the precombustion chamber and fuel grain interface shown for axial showerhead, canted swirl, and tangential swirl injector designs. *Right*: Experimentally measured space-time averaged regression rates versus fuel grain length 77

4.5 Temperature and mole fraction results of CO and H_2O versus radial distance from the fuel grain center ($r = 0$ mm) shown at two axial positions for the axial showerhead (*left*), tangential swirl (*center*), and canted swirl injector (*right*) . . 78

4.6 Two-dimensional thermochemistry measurements demonstrating PMMA/GOx combustion progression along the axial direction for the canted swirl, tangential swirl, and axial showerhead injectors 79

5.1 Theoretical c^* with corresponding temperature, molecular weight, and specific heat ratio, over a range of equivalence ratios (ϕ). Results are shown for two propellant combinations, MMA/O_2(g) and CH_4/O_2(g), at $P = 1$ atm 87

5.2 *Left to right*: Transmitted (I_t) and incident (I_0) light intensities for two CO transitions near 2008.5 cm^{-1}, the corresponding measured absorbance profile with a Voigt line-shape fit, projected absorbance areas (A_{proj}) and integrated spectral absorption coefficients (K) versus distance r from the center of an axisymmetric flow-field, and the resulting thermochemistry (T, X_i) distributions 88

5.3 *Top*: Species mole fractions (X_i) at chemical equilibrium for MMA/O_2(g) combustion at $P = 1$ atm and varying equivalence ratios (ϕ). Species inaccessible via LAS (O_2, H_2) are shown in gray. *Bottom*: Equivalence ratio sensitivity of multiple species pairs, $Z = X_i/X_j$, used for determining local flow-field properties 93

5.4 Characteristic velocity (c^*), temperature, and CO and CO_2 mole fraction measurements over a range of pressures (P = 28–83 bar) and mixture ratios (MR = 2.5–5) in an RP-2/O_2(g) rocket combustor. Shaded regions demonstrate the expected values from chemical equilibrium. 96

5.5 *Left to right:* Spatially-resolved temperature, species mole fractions (CO, CO_2, H_2O), and characteristic velocity (c^*) measurements in a PMMA/O_2(g) hybrid rocket combustion experiment with single-port injection. Results are shown for various fuel-grain heights to illustrate axial combustion progress. The center of the fuel grain is located at $r = 0$ mm and the fuel-gain wall is located at $r \approx 6.8$ mm. 97

5.6 Spatially-resolved c^* measurements for two injector geometries (single-port, axial showerhead) in a PMMA/O_2(g) hybrid rocket combustion experiment. A classical depiction of diffusion-limited hybrid rocket combustion is shown for comparison. 100

5.7 The corresponding uncertainty in characteristic velocity ($\Delta c^*/c^*$) for a given uncertainty in temperature ($\Delta T/T$), molecular weight ($\Delta M/M$), and specific heat ratio ($\Delta\gamma/\gamma$) over a representative range of possible values. The different lines represent $a = T$, M, and γ 105

6.1 Predicted combustion species evolutions at 1350 K from a 1% initial concentration of MMA diluted in argon at 1 atm using the chemical models published by Yang et al. (dot-dashed line) and Dakshnamurthy et al. (dashed). 110

6.2 (top left) Cross sectional view of HEST facility showing optical access and laser/detector setup. (bottom) Side view of HEST facility marking location of cross section at the end of the driven section on the left. (top right) Representative time histories of pressure (black), formaldehyde (green), CO (red) and CO_2 (blue) from shock heated mixture of MMA. 112

6.3 *Bottom:* Absorption linestrengths for CH_4, CH_2O, CO_2, H_2O, and CO at 1200 K, simulated using the HITRAN [7] and HITEMP [8] databases. *Top:* Absorption simulations for CH_2O (left), CO_2 (middle), and CO (right), highlighting targeted wavelength regions and spectral features. CH_2O absorption simulated using the AYTY line list [9]. 113

6.4 Time evolution of absorbance of CO, CO_2, and CH_2O shown for a test at mid-range condition (T_5 = 1390 K, P_5 = 0.98 atm) 115

6.5 Comparison of measured CO, CO_2, CH_2O mole fractions with simulations using the short MMA mechanism from Dakshnamurthy et al. (dashed line), the full mechanism from Yang et al. (dot-dashed line), and the modified mechanism from the current work (solid line). 117

6.6 Comparison of measured CO and CO_2 mole fractions with simulations (solid lines) using the short MMA mechanism from Dakshnamurthy et al. (top) and the modified mechanism from the current work (bottom). 118

6.7 Mole fraction yield for CO, CO_2, and CH_2O at 0.5 ms for 1% MMA/Ar pyrolysis. Markers represent measurements and lines represent the Yang et al. [10], Dakshnamurthy et al. [11], and final modified models. 119

6.8 Sensitivity coefficients for 1% MMA in argon at P_5 = 1 atm using the Dakshnamurthy et al. mechanism are shown at 0.1 ms for temperatures of 1200 K (left) and 1500 K (right). Reactions showing positive sensitivity factors increase species production. 122

6.9 MMA decomposition pathways considered in this work. 123

6.10 Comparison of rates between the Dakshnamurthy mechanism and the modified mechanism for the unimolecular decomposition reactions of MMA (left) and hydrogen abstraction reactions (right). 128

7.1 Fire growth/decay stages of compartment fire experiments with firefighter operations. 132

7.2 Composite solid fuel combustion experiment with forced oxidizer convection and two-dimensional laser absorption tomography setup. 135

7.3 *Top.* Absorption line strengths of HF, CO, and other relevant combustion species simulated at 2500 K [7]. *Bottom.* Simulated target transitions of CO and HF ($X = 15\%$) with exaggerated water interference. 137

7.4 *Left.* Projected integrated absorbance area verses distance y from the center of the reacting flow. *Right.* Tomographically-inverted radially-resolved integrated absorption coefficient. 139

7.5 PTFE mass burn rate versus PTFE fuel grain length. The mass burn rates are space- and temporally-averaged parameters over the total burn duration. 143

7.6 CO mole fraction and temperature radial distribution measured from the 25.4 mm long PMMA pilot burner in GOx cross-flow. 144

7.7 Planar species and temperature measurements for PTFE combustion along the radial dimension at different axial planes. 145

7.8 Two-dimensional thermochemical structure in the near-surface reaction layer of PTFE in an oxidizer cross-flow 146

7.9 Species mole fractions (X_i) and max temperature at chemical equilibrium, T_{eq}, for PTFE combustion over a range of mass flow rates of PTFE, with oxidizer vitiated with MMA/GOx products at equivalence ratios of 0.5 and 1.5. 152

7.10 Reaction pathway diagram tracking the fluorine atom through PTFE pyrolysis and oxidation with water along pathways that result in hydrogen fluoride (and carbon monoxide) production (T = 2500K) 153

8.1 *Left:* Diagram of test facility setup for hybrid combustion measurements at elevated chamber pressures with optical access. *Right:* Assembled view of hybrid rocket motor test facility 158

8.2 Tesla Model S e-vehicle in the midst of an uncrolled lithium-ion battery fire [12]. 160

A.1 Representative experimental uncertainties contributing to the overall uncertainty in the reported O/F values in Table 7.1 163

A.2 Representative experimental uncertainties contributing to the overall uncertainty in the reported $\bar{\dot{r}}$ values in Table 7.1 164

A.3 Representative experimental uncertainties contributing to the overall uncertainty in the reported $\bar{G}_{ox}$ values in Table 7.1 166

B.1 Planar thermochemistry measurements for PMMA/GOx combustion at 25.4 and 38.1 mm using a single-port injector geometry 169

B.2 Planar thermochemistry measurements for PMMA/GOx combustion at 50.8 and 63.5 mm using a single-port injector geometry 170

B.3 Planar thermochemistry measurements for PMMA/GOx combustion at 76.2 and 88.9 mm using a single-port injector geometry 171

B.4 Planar thermochemistry measurements for PMMA/GOx combustion at 101.6 and 114.3 mm using a single-port injector geometry 172

B.5 Planar thermochemistry measurements for PMMA/GOx combustion at 127.0 and 139.7 mm using a single-port injector geometry 173

B.6 Planar thermochemistry measurements for PMMA/GOx combustion at 25.4, 38.1, 50.8, and 63.5 mm using an axial showerhead injector geometry 174

B.7 Planar thermochemistry measurements for PMMA/GOx combustion at 76.2, 88.9, 101.6, and 114.3 mm using an axial showerhead injector geometry 175

B.8 Planar thermochemistry measurements for PMMA/GOx combustion at 127.0 and 139.7 mm using an axial showerhead injector geometry 176

C.1 Plot of maximum axial velocity in the injector outlet plane (*left*) and inlet pressure (*middle*) over a range of mesh coarseness for the single-port and axial showerhead injector simulations. Error in results from each mesh compared to the most fine grid results are shown (*right*) 179

D.1 Spectrally-resolved CO, CO_2, and CH_2O measurements during a representative MMA thermal decomposition experiment. 180

D.2 Comparison of simulated species profiles in a pre-mixed laminar flame at atmospheric pressure for the existing and modified mechanisms. Symbols represent the experimental speciation data from [23]. 182

D.3 Laminar flame speeds for MMA/Ar mixture at P = 1 atm. Simulations using existing mechanism and modified mechanism are shown as dashed and solid lines, respectively. 183

F.1 Hybrid rocket motor post-combustion chamber. 275

F.2 High pressure hybrid rocket test rig during a hot fire test with $P_c = 10bar$. . . . 276

LIST OF TABLES

1.1 Overview of oxidizer injector designs used in modern hybrid rocket research works 13

3.1 Spectroscopic parameters for targeted CO, CO_2, and H_2O transitions 43

3.2 Summary of the experimental results from fuel regression analysis for PMMA/-GOx combustion studies 58

4.1 Injector design specifications and swirling flow parameters 73

6.1 Rate constants of the Dakshnamurthy et al. and the modified MMA pyrolysis models 126

7.1 Global fuel regression parameters for PTFE with PMMA/GOx pre-burner and $\dot{m}_{ox} = 1.5$ g/s 142

A.1 Details of mesh convergence study for CFD cold-flow analysis 167

ACKNOWLEDGMENTS

I must, of course, first thank my supervisor Professor Spearrin. Thank you for always being engaged with our research progress and for always making the time in your schedule to meet when we are in dire need of guidance. Your awareness of and compassion for some of the challenges faced by me and other international students (regarding jobs, visas, travelling home, etc.) do not go unnoticed and are greatly appreciated. Most of all, thank you for answering the first email I sent years ago and for giving me the opportunity to join your lab; it has really been an incredible learning experience.

I would also like to greatly thank the members of my committee, Professor Karagozian, Professor Taira, and Professor Davoyan for their helpful feedback and guidance. Additionally, I must thank the MAE department staff, in particular Miguel Lozano and Anthony Singleton for all of their facilities and manufacturing help. Throughout my doctoral studies, I had the privilege of working on projects funded by NASA Jet Propulsion Laboratory and the Federal Emergency Management Agency, and I am particularly grateful for the funding from my doctoral research fellowship awarded by the Natural Sciences and Engineering Research Council of Canada.

It is hard to believe over four years have passed since I arrived in Los Angeles and joined the lab. I was incredibly nervous and intimidated, it was my first time moving outside of Canada and I knew no one in the area, but from the get-go, the guys in the lab went out of their way to make me feel welcomed and included. In particular, Fabio Bendana, Daniel Pineda, David Morrow, Kevin Schwarm, Anil Nair, Chuyu Wei, and Travis Fujimoto, thank you for your kindness and immediate acts of friendship. The late night experiments, the disheartening and seemingly never-ending troubleshooting, and the frantic last-minute meeting slide preparations were made bearable (and frankly, sometimes fun) by the wonderful graduate students I have had the pleasure of working alongside. I'd also like to thank the great undergraduate students I had the opportunity to work with: Kate Oberlander, Nora

Stacy, and Miles Richmond, among others.

Fabio Bendana, I feel so lucky to have had the privilege of learning from you and working with you on the hybrid rocket project. You are truly gifted at both engineering and teaching. I look forward to seeing all that you accomplish professionally and personally. And to your lovely wife Kaelly, thank you for teaching Fabio the crucially important information that acetone ruins a gel manicure. Chuyu Wei, I both blame you and am grateful to you for getting my coffee habit started and for encouraging my frivalous sneaker purchases. I'm so happy we had so much time together in the lab during your PhD and postdoc – I have such fond memories of our coffee walks to Anderson, our Pho and DineLA dinners, and your quiet companionship on late bus rides home. Anil Nair, thank you for being such a helpful labmate and great TA partner. Although our late night writing (and chatting) session fueled by cocacola coffee before that conference paper submission was stressful at the time, it is such a positive memory I look back on now. I would be remiss to not properly thank Christopher Jelloian for jumping into action during the, now infamous, 'Arson Incident' of 2020. And, of course, David Morrow, thank you for the laughs, loyalty, and, most importantly, the pumpkin.

Alex Keller, I have learned so much from our great, productive conversations – I hope the feeling is mutual. Thank you for the many times you made the extra effort to check in on me, celebrate my milestones, and drive me home from campus after dark. Nicolas Minesi, thank you for the energy and enthusiasm you brought to the lab (despite how jarring your exclamations of excitement or frustration could be at times). I will never forget your incredible charm when meeting my friends or the time you pulled me up to "rock and roll" dance when I was upset. Barathan Jeevaratenem, thanks for being such a good listener, perhaps too good at times – how else could you keep on top of all the lab news and, dare I say, gossip? Thank you for being a loyal friend and for always looking out for me. I am appreciative of every time you went out of your way to remind me when it was time to renew my bus pass or to check that my international travel paperwork wasn't expired.

Griffin Houston, thank you for keeping us on our toes. From your famous hot takes to powerful operatic performances, you always keep things interesting. I have no doubts our paths with cross again in the future, be it on the ski slopes or in the Mars yard at JPL. Yi Yan, it has been great working with you in the lab this year. Your positive attitude and openness to learning have been such an asset to the lab research and culture. Ariya Olaee, I think we were friends from the moment we met. Your kindness and empathy are unwavering and your smile is infectious. I look forward to many more laughs and Mammoth ski days together in the future.

Kevin Schwarm, your resourcefulness and your willingness to drop everything to help others never ceased to impress me during our four years in the lab together, as did the level of warmth and respect you never failed to extend to everyone you worked with. I am so grateful for your patience, for your support, for the countless drives home, and for helping to ground me back in reality when my stress levels precluded logical reasoning – thank you for being such a great coworker. I look forward to seeing all that you accomplish and continuing to pester you with my questions at JPL. Last, I must thank my dear friend and partner in crime and hydrocarbon cross-sections, Nick Kuenning. You are an incredibly brilliant, multi-talented engineer and somehow an even better person. As you know, if you ever run for office, I will quit my job to work on your campaign. You have been my guide to American culture and cuisine (thank you for giving me my first hot pocket). I am so grateful for how you never failed to make me smile and laugh while in the trenches of teaching, running experiments, or passivation procedure woes. Working with you has been one of the greatest joys of my time in grad school, thank you for everything.

Beyond the lab, I have been extremely fortunate to have such an amazing support system. Alana and Sydney, the amazing women who help to balance out the gender ratio of my days. I am incredibly lucky to call you my roommates and friends. It is a huge privilege to have one's home be such a loving and safe space. Thank you for your encouragement and for your interest in my work (Syd, famously a huge proponent of Benzene LAS diagnostics). Thank

you for quickly embracing my friends from the lab as your own (Alana's attendance at lab events may rival my own). I am so grateful that I get to start my next chapter with you two still by my side. You make LA feel like home.

Back in Canada, I am grateful to my friends, family, and Riverdale neighbors that have made me feel supported throughout my PhD. In particular, I'm so thankful to Christina Loh and Tom Johnston, who I consider to fall into all of those categories.

Finally, importantly, I must profoundly thank my immediate family. Charlotte, my big sister. You showed me how amazing it can be to pursue your goals, even though they may take you far from home – I am so proud of you and look up to you so much. Thank you for making huge efforts to always keep us in contact and feeling connected, despite our inconvenient 8-9 hour time differences. You and me, forever. The only person I would run through an airport for is you. To my parents, Peter and Carole: I am eternally thankful. I could fill a second dissertation volume trying to list all of the things I am grateful to you both for. Thank you for encouraging and enabling Charlotte and I to follow our interests and dreams, despite those leading us to places far from home. Peter, thank you for always talking to me on the phone when I walked home from the bus stop late at night, even though it was 3 hours later for you. Thank you for your patience and for being such a good listener. Thank you for instilling in me a desire to constantly keep learning and for sending me carefully selected novels so my brain doesn't turn to mush from only reading scientific journals. Maman, thank you for taking me with you to work at the UN when I was 13 days old and, from then on, always exemplifying that being an involved mother and being hugely successful in your work do not have to be mutually exclusive. Thank you for dedicating your career to trying to make the world more habitable for your daughters' futures and for everyone around the world. Thank you for always making sure I knew I could home at the drop of a hat if I ever needed to and, when I asked you to visit, for dropping everything to fly to LA within hours. Mum and dad, for the constant love and support you have shown me over the last 26 years and for trying to learn the word "spectroscopy": thank you.

VITA

2019 **B.A.Sc. in Engineering Physics**
and Mechanical Engineering
Queen's University, Kingston, Ontario, Canada.

2021 **M.S. in Aerospace Engineering**
University of California, Los Angeles (UCLA), Los Angeles, CA

2023 **Ph.D. (Expected) in Aerospace Engineering**
University of California, Los Angeles (UCLA), Los Angeles, CA

PUBLICATIONS

[1] **Sanders, I.C.**, Oberlander, K.A., Spearrin, R.M. (2023). Polytetrafluorethylene (PTFE) burn characteristics and toxicant formation in an oxidizer cross-flow via laser absorption tomography. Submitted to Proceedings of The Combustion Institute

[2] Kuenning, N.M., **Sanders, I.C.**, Minesi, N.Q., Pineda, D.I., Spearrin, R.M. (2023). High-temperature absorption cross-sections and interference-immune sensing method for formaldehyde near 3.6 μ m. Journal of Quantitative Spectroscopy and Radiative Heat Transfer, 108690

[3] **Sanders, I.C.**, Kuenning, N.M., Minesi, N.Q., Pineda, D.I., Spearrin, R.M. (2022). Methyl methacrylate thermal decomposition: Modeling and laser spectroscopy of species time-histories behind reflected shock waves. Fuel 335, 126846

[4] **Sanders, I.C.**, Bendana, F.A., Kuenning, N.M., Spearrin, R.M. (2022). Spatially-resolved characteristic velocity (c*) measurements for hybrid rocket combustion analysis using laser spectroscopy. AIAA SciTech 2022 Forum, 2233

[5] Kuenning, N.M., **Sanders, I.C.**, Minesi, N.Q., Pineda, D.I., Spearrin, R.M., Kinetics of MMA combustion assessed by time-resolved speciation behind shock waves (2022). AIAA SciTech 2022 Forum, 2231

[6] **Sanders, I.C.**, Bendana, F.A., Stacy, N.G., Spearrin, R.M. (2021) Injector effects on hybrid polymethylmethacrylate combustion assessed by thermochemical tomography. Journal of Propulsion and Power 37 (6), 928-943

[7] Bendana, F.A., **Sanders, I.C.**, Stacy, N.G., Spearrin, R.M. (2021). Localized characteristic velocity (c*) for rocket combustion analysis based on gas temperature and composition via laser absorption spectroscopy. Measurement Science and Technology 31 (12), 125203

[8] **Sanders, I.C.**, Bendana, F.A., Stacy, N.G., Schwarm, K.K., Spearrin, R.M. (2021). Swirl injection in hybrid polymethylmethacrylate combustion assessed by thermochemical imaging. AIAA Propulsion and Energy, 3513

[9] Bendana, F.A., **Sanders, I.C.**, Castillo, J.J., Hagstrom, C.G., Pineda, D.I., Spearrin, R.M. (2020). In-situ thermochemical analysis of hybrid rocket fuel oxidation via laser absorption tomography of CO, CO_2, and H_2O. Experiments in Fluids, 61(9), 190

[10] **Sanders, I.C.**, Bendana, F.A., Hagstrom, C.G., Spearrin, R.M. (2020). Assessing oxidizer injector design via thermochemical imaging of PMMA combustion in a hybrid rocket motor geometry. AIAA Propulsion and Energy, 3747

CHAPTER 1

Introduction

1.1 Solid Fuel Combustion in Oxidizer Cross-Flow

Solid fuel combustion is a complex, multi-phase process that humans have been trying to understand, control, and benefit from throughout history. It has been crucial for civilization growth, industrialization, technological advancement and, in the most basic forms, to human survival. The fuel types - from wood and coal to complex modern synthetic polymers - and associated combustion systems are widely varied and tailored to the goals of specific applications. There are, of course, also the instances of undesirable solid fuel combustion, namely building fires and wildfires, that are crucial to understand to mitigate damage and hazards. This dissertation focuses on combustion of solid fuels in the context of hybrid combustion, wherein a solid fuel is exposed to a gaseous oxidizer cross flow, or forced convection, as is typical of hybrid rockets, but also relevant to wind-blown fires. The following sections provide an overview of the governing physics in hybrid solid fuel combustion and also connect the field of study to the applications that motivate the research described in subsequent chapters.

1.2 Governing principles

The basic governing principles and physics involved in solid fuel combustion are reviewed here to provide context for the experiments and analysis that follows. To burn, the solid fuel must first pyrolyze and undergo gasificiation, via heating, such that the volatile gaseous molecules

created from the fuel surface can react and burn with the gaseous oxidizer. This fuel surface heating may result from an ignition source, exposure to existing fire, or even ambient environment temperatures. Once ignited, the ongoing fuel pyrolysis is maintained from heat radiated from the flame and convected to the fuel surface. The regression rate and resulting gaseous fuel species production are coupled to the evolving flow-field and flame structure through heat feedback from exothermic chemistry. Correlations developed in the 1960s by *Marxman et al.* to describe this multi-phase system are still widely used today. In recent years, researchers have revisited the Marxman correlations and highlighted their validity or lack thereof for different motor configurations and under different conditions, particularly with respect to adequately accounting for thermal radiative effects [13, 14]. The Marxman equations include one-way coupling of radiation effects on convective blowing by way of including a perturbation term to the baseline non-radiating case. Discrepancies observed between Marxman-derived heat fluxes and experimental results have motivated studies to find empirically derived corrections to the Marman correlations as well as new model formulations based on experimental slab burner data [13, 15]. However, within the context of this work, with a primary focus on the gaseous flow-field, the Marxman correlations serve as a useful model for analyzing fuel regression behavior. These include the following coupled, first order partial differential equations to govern gas generation in hybrid combustion related to the fuel surface regression rate (Eq. 1.1) and the port mass flow growth rate (Eq. 1.2):

$$\frac{\delta r(x,t)}{\delta t} = \frac{a}{x^m}\left(\frac{\dot{m}_{port}}{\pi r^2}\right)^n \tag{1.1}$$

The dependence on the axial position, x, arises due to heat transfer from a turbulent boundary layer.

$$\frac{\dot{m}_{port}(x,t)}{\delta x} = \rho_f(2\pi r)\frac{a}{x^m}\left(\frac{\dot{m}_{port}}{\pi r^2}\right)^n \tag{1.2}$$

However, for many hybrid rocket regression rate analysis, a simplified equation is used

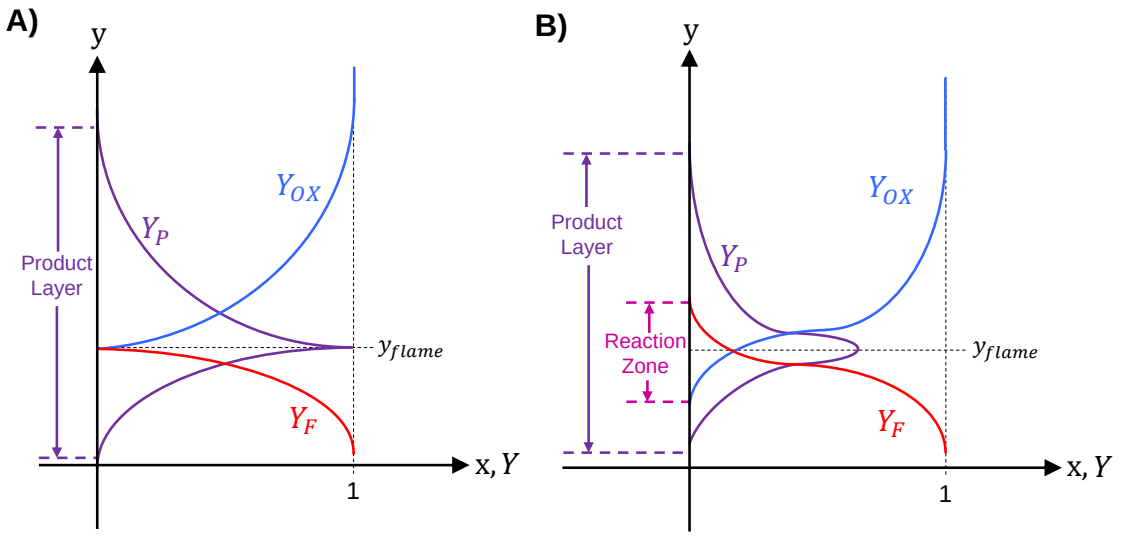

Figure 1.1 A) Idealized diffusion flame structure distribution of fuel, oxidizer, and product species with flame sheet assumptions. B) Diffusion flame structure species distributions reaction zone.

that is often sufficient for characterizing the fuel regression rate provided that the O/F ratio is not very low. In this case, the fuel surface regression rate, $\dot{r}$, is simply determined as a function the oxidizer mass flux, G_{ox}, as shown in Eq. 1.3 [16, 17]:

$$\dot{r} = \frac{a}{x^m} G_{ox}^n \tag{1.3}$$

where x is the length of the fuel grain and a, n, and m are empirical constants for a given propellant combination. Previous works have found weak dependence on axial position, supporting an assumption of $m = 0$ in most cases [18, 19, 20].

The resulting gaseous flow-field in hybrid combustion is characterized by the diffusion flame structure that forms within the boundary layer along the fuel grain wall. The vaporized fuel is advected and diffused away from the fuel grain surface towards the diffusion flame where it reacts with oxidizer transported from the core flow by turbulent diffusion [21]. Diffusion flames, also known as non-premixed flames, occur when initially separate fuel and

oxidizers are brought together and form a thermochemically-varied reaction zone governed by chemical reaction and molecular diffusion speeds [22]. These are typically diffusion limited with high Damköhler numbers, defined simplistically as:

$$D_A = \frac{\tau_{transport}}{\tau_{reaction}} \tag{1.4}$$

in which $\tau_{transport}$ is the timescale of the mixing and transport processes and $\tau_{reaction}$ is timescale of the chemical kinetics. Thus, a high Damköhler number in a diffusion flame implies that the fuel and oxidizer react to form products much faster than the diffusion can transport the species to the flame. At the limit as $D_A \to \infty$, the reaction chemistry is infinitely fast; this widely used assumption for studying diffusion flames was first introduced by Burke and Schumann in 1928 [22]. An idealized diffusion flame structure is shown in Fig. 1.1 A); this scenario corresponds to the limit of infinitely fast chemistry, stoichiometric fuel and oxidizer proportions across the flame, and effectively single-step irreversible combustion from reactants to products:

$$Fuel(F) + Oxidizer(OX) \to Products(P) \tag{1.5}$$

The bounds of this schematic dictate that at $y = 0$, the mass fraction of the fuel, Y_f, is 1 while as $y \to \infty$, the oxidizer mass fraction, $Y_{OX} = 1$. In an idealized flame structure, no oxidizer exists on the the fuel-rich side of the flame, and vice versa. The flame lies between these extremities at a location, y_F, on the fuel and oxidizer consumption rates with respect to stoichiometry. In essence, the flow-field in this model is chemically frozen everywhere other than at the infinitely thin flame sheet. Given the one-step irreverible reaction converting fuel and oxidizer to product species, there is a single global stoichiometric ratio [23]. The fuel and oxidizer species are consumed at the flame sheet according to this ratio:

$$f^* = \frac{\dot{w_F}}{\dot{w_{OX}}} \tag{1.6}$$

wherein f^* is the stoichiometic ratio and $\dot{w_F}$ and $\dot{w_{OX}}$ are the fuel and oxidizer mass consumption rates, respectively. This assumption of an infinitely thin flame location, or flame sheet,

has been widespread and of great utility across combustion literature and research, despite real world practical limitations. Shortcomings in this model are often due to the multi-step reaction kinetics that involve the formation and consumption of intermediate species and include multiple reaction pathways contributing to product formation [24]. Figure 1.1 B) shows diffusion flame species distributions with relaxing of the flame sheet assumptions on reaction chemistry. In reality, the flame sheet is replaced by a reaction zone with some domain of overlap in fuel and oxidizer species. The thickness of this reaction zone is affected by the chemical reaction speeds (again, relative to the diffusion timescales) and is typically very thin compared to other flow-field length scales, such as the product layer; thus for characterizing the external structure of the diffusion flame, the assumption of infinitely fast chemistry is often still sufficient. As such, generalized equations to determine the fuel and oxidizer distribution on either side of the flame sheet or reaction zone can be formulated from conservation of mass as:

$$\rho\left[\frac{\partial Y_F}{\partial t} + v\frac{\partial Y_F}{\partial y}\right] = \frac{\partial}{\partial y}\left[\rho D_F, P\frac{\partial Y_F}{\partial y} + \dot{w_F}\right] \tag{1.7}$$

$$\rho\left[\frac{\partial Y_{OX}}{\partial t} + v\frac{\partial Y_{OX}}{\partial y}\right] = \frac{\partial}{\partial y}\left[\rho D_{OX,P}\frac{\partial Y_{OX}}{\partial y} + \dot{wOX}\right] \tag{1.8}$$

where ρ is the density, v is the flow velocity, $D_{i,P}$ are the diffusivities of species i into the products (P), and $\dot{w_i}$ are again the mass consumption rates [23, 25]. Assuming the mixture is calorically perfect, conservation of energy yields:

$$\rho c_p\left[\frac{\partial T}{\partial t} + v\frac{\partial T}{\partial y}\right] = \frac{\partial}{\partial y}(k\frac{\partial T}{\partial y}) + \dot{Q} \tag{1.9}$$

The terms on the right hand side represent the heat diffusion, where k is the conductivity, followed by $\dot{Q}$, the heat released from the combustion reactions which is the product of $\dot{w_F}$ and q_H, the heat of combustion or heating value:

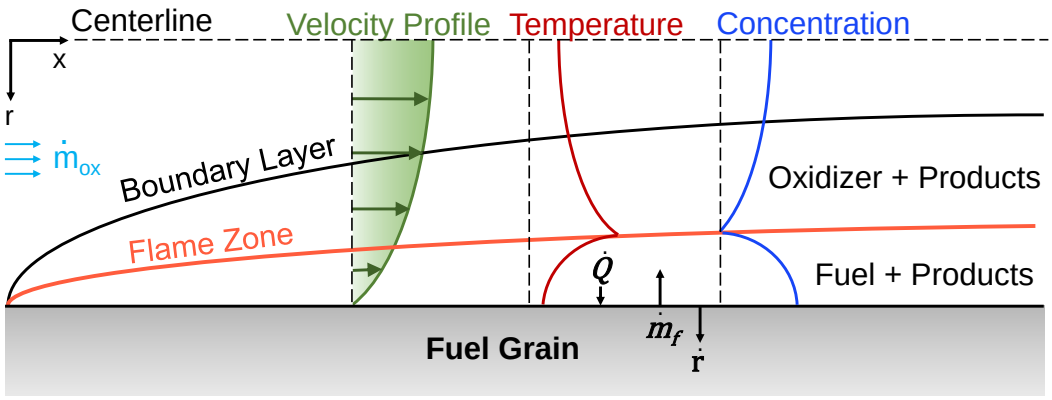

Figure 1.2 Schematic of classical diffusion-limited hybrid combustion

$$Q = \dot{w}_F q_H \tag{1.10}$$

The energy balance in Eq. 1.9 effectively indicates that heat leaving the flame via conduction is equal to the heat released by the species reacting at the flame.

A coupled system of the fuel regression and gas production sustained by heat feedback from a diffusion flame structure effectively describes the classical hybrid combustion flow-field structure depicted in Figure 1.2. The flame lies within a boundary layer that is expected to be turbulent over most of its length, attributed to the decreased transition Reynolds number caused by the multi-phase structure. The presence of evaporation when a gas stream flows over a liquid can lead to greater than an order of magnitude reduction in transition Reynolds number. This effect is exacerbated in hybrid combustion due to the extensive fuel sublimation along the surface. As such, the derivations and empirical correlations used to describe hybrid combustion systems, such as those by *Marxman et al.*, are grounded in turbulent boundary layer theory [16]. The turbulence of the flowfield effects the efficiency of the species and heat transfer between the flame and the fuel grain wall. Since, in the model, the diffusion flame is located within this turbulent boundary layer, available oxidizer cannot be depleted until the boundary layer thickness fills the available domain (reaches the centerline where $r = 0$), thus the turbulent flow is effectively fully developed. Within the boundary layer, flame

separates an oxidizer-rich region from a fuel-rich region containing pyrolyzed fuel molecules and product species. Since the combustion is again diffusion-limited, the rate at which these reactants burn is dictated by the rate at which they are brought together at the flame location by diffusive mixing caused by concentration gradients. The temperature increases moving radially inward towards a peak at the exothermic reaction zone or flame location.

The combustion reaction processes, in reality, often involve many competing pathways towards product formation including multiple reaction steps and reversible reactions. Many solid fuels, including both those relevant to chemical rocket propulsion and unwanted fires, have complex compositions with large hydrocarbons that produce a multitude of smaller CxHy molecules through thermal decomposition. These fuel fragment molecules interact, oxidize, or further decompose to produce the final combustion products. The evolving heterogeneity and coupled nature of the species' existence to each other through reactions make the local stoichiometric ratios of fuel to oxidizer and heating values difficult to predict. Theoretical models of reaction pathways and rates have enabled generation of countless useful mechanisms for modeling combustion; although, experimental data has been essential for making these mechanisms more robust and accurate.

In summary, adequate understanding of a hybrid combustion system's behavior requires analysis of the pyrolysis process (thermal decomposition temperature, phase change, resulting pyrolyzed products) and the reacting gaseous flow dynamics and heat production that sustain the combustion, encompassing effects of chemical kinetics, fluid dynamics, and heat and mass transfer. As such, hybrid combustion can be extremely difficult to sufficiently predict; however, diagnostic tools and experiments can provide useful data to constrain models and illuminate key phenomena affecting the overall combustion performance. In the forthcoming chapters, we detail some such diagnostic, experimental, and analysis methods developed to characterize hybrid combustion with particular application to hybrid rocket propulsion and structure fires.

1.3 Hybrid rocket propulsion

Hybrid rocket motors, by their most general definition, are chemical propulsion systems that store the fuel and oxidizer in different phases; they have been of interest to the propulsion community for many decades owing to the numerous theoretical benefits. Of particular note, storing the fuel and oxidizer in different phases allows for relatively simplistic propellant feed systems and reduced safety infrastructure compared to typical liquid propellant rocket engines. This also makes hybrid rockets far more cost effective and accessible for implementation on smaller scales. While solid rocket motors are in some ways even more simplistic (than hybrids), their performance capability, as assessed by the specific impulse, I_{sp}, is far less than can be achieved by liquid rockets. I_{sp} effectively characterizes the engine thrust produced per unit propellant weight:

$$I_{sp} = \frac{F}{\dot{m}_p g} \tag{1.11}$$

where F is the thrust, $\dot{m}_p$ is the propellant mass flow rate which is multiplied by g, the gravitational constant, such that the denominator is in units of weight. This gives an I_{sp} in units of seconds. Specific impulse, among other rocket performance parameters, is further discussed in Sec. 5.1.1. Conversely, hybrid rocket motors have theoretical I_{sp} magnitudes that are comparable to liquid rocket engines. Hybrid rockets can also be easily throttled by controlling the flow rate of the gaseous oxidizer into the combustion chamber, enabling a wide range of thrust profiles. Despite these advantages over the other two chemical propulsion systems, hybrid rocket motor implementation has been limited in real world applications due, in part, to low regression rate of suitable polymer-based fuels, inherent variation in the oxidizer-to-fuel ratio as the solid fuel grain regresses, and relatively immature understanding of the combustion dynamics and instabilities.

Among the most successful launches of a hybrid rocket is that of SpaceShipOne, an air-launched vehicle designed by Scaled Composites that won the Ansari X-Prize in 2004. The motor included four ports with hydroxyl-terminated polybutadiene (HTPB) and liquid

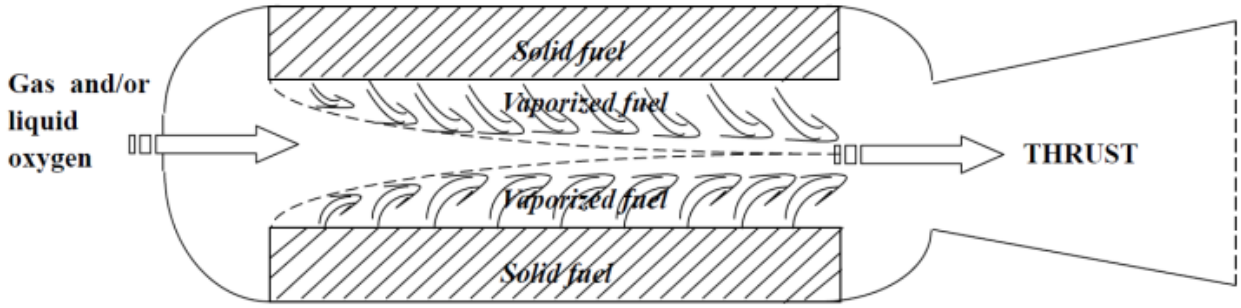

Figure 1.3 Simple schematic of a hybrid-propellant rocket [1]

nitrous oxide as propellants capable of generating 16,500 lbf of thrust, enabling the rocket to reach a sub-orbital altitude of 112 km. The successor to the SpaceShipOne, aptly dubbed SpaceShipTwo, was developed by Scaled Composites with Virgin Galactic in the late 2000s and has completed many flights with its first true space flight (based on the United States of America's altitude definition but below the FAI-defined Karman Line) occurring in 2018. As with its predecessor, SpaceShipTwo initially used HTPB as its fuel however, once Virgin Galactic took sole ownership of the technology and vechicle design in 2014, they redesigned the motor and switched to a polyamide plastic fuel. Upon unsuccessful flight tests with the new propellant, they eventually switched back to HTPB which they continue to use for flights to date. Virgin Galactic currently operates one SpaceShipTwo-class vehicle, named the Virgin Space Ship (VSS) Unity, which completed another successful and highly publicized hybrid rocket launch; that being the first space flight (again, by USA definition) in December 2018 during which it hit Mach 2.9 and reached 82.7 km at its apogee. In November 2023, Virgin Galactic announced their plans to retire their SpaceShipTwo vehicles by mid-2024 and to ramp up work on their next generation "*Delta*" commercial rockets.

Aside from these notable hybrid rocket launches in the United States, research and development on hybrid rocket motors has significantly ramped up worldwide over the last two decades. This re-ignited interest in hybrid rockets can be attributed, in part, to the development and availability of higher-regression rate synthetic solid fuels and the rapid expansion

Figure 1.4 SpaceShipOne and SpaceShipTwo-class VSS Unity

of the commercial aerospace sector. A useful overview of commercial and governmental hybrid rocket development projects in 15 countries over the last 17 years is provided in the review paper by Okninski et al. [26]. Of recent note, South Korean company Innospace successfully launched a hybrid motor suborbital rocket in March 2023 and is working on development of a next-generation orbital launch vehicle. India, Norway, Canada, Germany, and the United States are among other countries where non-governmental hybrid rocket vehicles exist with near-term launch goals. Additionally, laboratory-scale research and development on hybrid rockets has also become increasingly prevalent over this time period, advancing the technological maturity and enabling improved motor designs.

1.3.1 Hybrid rocket combustion dynamics

As previously discussed, in hybrid rocket motors, the fuel and oxidizer are stored in different phases. They most commonly consist of a gaseous oxidizer (as discussed in this work) that is injected into a combustion chamber lined with a solid fuel, usually of cylindrical geometry. Upon injection of the oxidizer, a turbulent boundary layer forms that sweeps over the fuel grain wall, as was shown in Fig. 1.2. To initialize the combustion reaction, an ignition source heats the solid fuel wall, vaporizing a thin layer of fuel, which then enters the boundary layer region of the flow-field. The subsequent combustion progression is governed by the heat and

mass transfer that occurs between the gas-phase oxidizer and the evaporated fuel near the grain surface as discussed in Sec. 1.1. As this fuel moves incrementally inward, the local ratio of oxidizer to fuel (O/F) becomes sufficiently conducive to combustion and a thin flame appears. For simple axial injection, this location is estimated to be around 10-20% of the boundary layer thickness, δ, from the wall and approximately 0.1δ in thickness [17, 16]. Depending on the geometry of the injector, the local regression rate can vary significantly near the injection/fuel grain interface and assumes the classical boundary layer structure at a location downstream.

For a hybrid rocket motor geometry with axial oxidizer injection, there are three distinctive flow-field regions as shown in Fig. 1.5: a recirculation zone, an impingement point, and a boundary layer development region [2]. Oxidizer from the main jet is directed into the recirculation zone across a turbulent shear layer wherein the fuel from the adjacent wall reacts with and is recirculated with this oxidizer [2, 27]. This region is very fuel-rich along the wall whereas the core flow composition at this point is still nearly pure oxygen [28]. Here, the combustion process largely takes place in the shear layer of the core oxidizer jet and the recirculation zone. The impingement point occurs when the core oxidizer jet spreads and interacts directly with the grain wall at some distance downstream of the injector. Several studies, with varied results, have focused on the flow-field region between the oxidizer injector and the impingement point to try and determine the axial position of maximum fuel regression. Specifically, Carmicino et al. [2] determined maximum regression rate to occur when the oxidizer jet impinges the fuel grain; however, high-speed images by Mechentel et al. [3] suggest that maximum regression occurs within the recirculation zone. In the flow region downstream of this impingement point, the turbulent boundary layer develops and, within, the characteristic diffusion flame forms. Beyond the recirculation zone, oxygen concentration in the core flow decreases and a greater portion of combustion products diffuse inwards towards the core as the reaction progresses along the axial direction. This theoretical framework for the hybrid combustion flow-field serves as a reference for discussion of the

results in subsequent chapters.

While undoubtedly useful, the aforementioned findings rely largely on measuring global parameters, such as pressure or aggregate fuel mass burned, to make conclusions about the flow through the injectors. A limitation of such measurements is the inability to quantify how the reaction is progressing within the fuel grain and along the grain length. More recent work by Mechentel et al. [3, 29] has involved using high-speed cameras to obtain spatially-resolved measurements, see Fig.1.6, of the fuel regression rate along the grain length in a hybrid motor. Results using this methodology have supported axial injection theory for hybrid geometries and can be useful for assessing effects of differing motor components on the regression rate and its axial uniformity [3, 29]. Fuel regression, and the aggregate burn rate, is a key combustion parameter as it relates directly to achievable combustion chamber pressure and thrust for a given motor size. To better grasp the causes of variable burn rates and spatial regression non-uniformity, an improved understanding of the reacting flow physics in the gas-phase core flow is required.

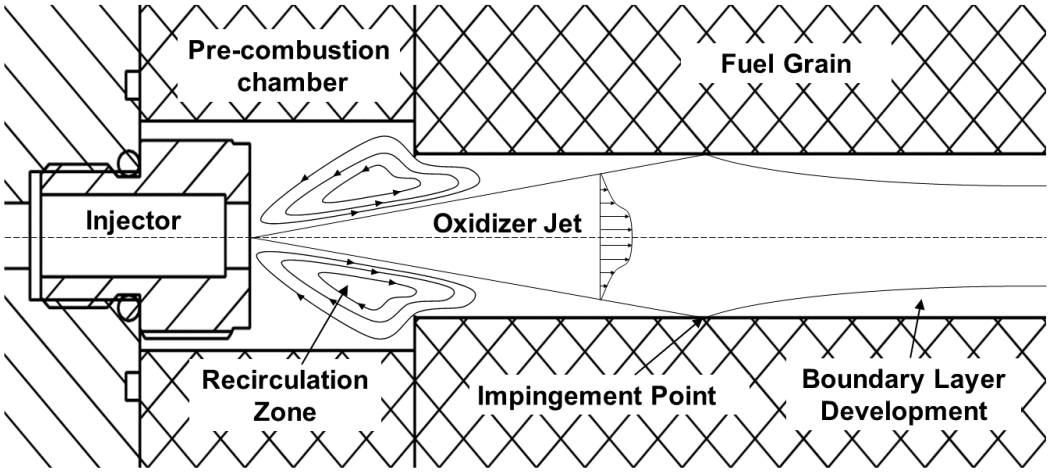

Figure 1.5 Diagram of the characteristic flow-field regions resulting from axial oxidizer injection in a hybrid motor geometry (adopted from [2])

Author et al.	Institution	Injector Type	Propellant	Assessment Metrics
Carmicino	Universitadì Napoli "Federico II"	Axial (straight port and impinging)	Polyethylene/ GOx	Ultrasound pulse-echo
Mechentel	NASA JPL	Axial	PMMA/ GOx	Imaging
Waxman	Stanford University	Axial	Paraffin wax/N_2O	Global pressure measurement
Kumar	Indian Institute of Technology Madras	Swirl	HTPB/ GOx	Numerical results
Gomes	Instituto Tecnológico de Aeronáutica - Brasil	Axial and swirl	HDPE/ GOx	Post-fire diameter measurements
Karabeyoglu	KOC UNiversity	Axial and swirl	Paraffin wax/LOx and HDPE/N_2O	Global pressure measurement
Invigorito	Italian Aerospace Research Centre	Axial	Paraffin wax/N_2O	Numerical results

Table 1.1 Overview of oxidizer injector designs used in modern hybrid rocket research works

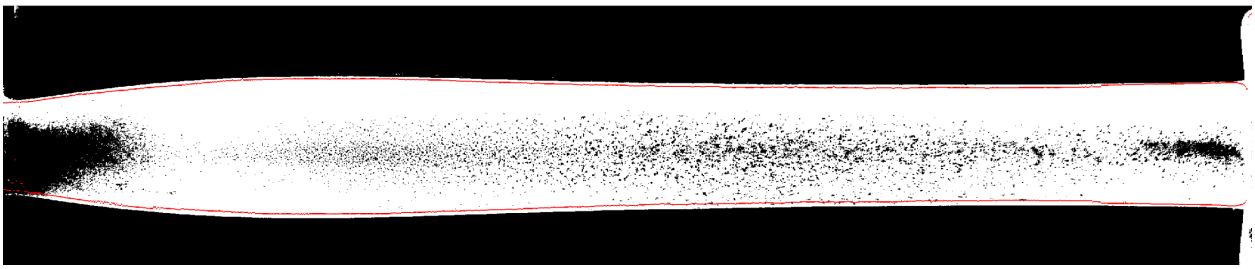

Figure 1.6 Post-firing image of axial injection into a hybrid rocket motor [3]

1.3.2 Hybrid rocket oxidizer injectors

The oxidizer injector influences hybrid rocket combustion performance by initializing the flow-field characteristics entering the combustion chamber. The oxidizer mass flux and associated convective heat transfer to the wall controls the fuel vaporization and, thus, the local O/F ratio, which, on aggregate for a given cross-section, decreases with axial distance. As such, an increase in oxidizer mass flux must be accompanied by an increase in fuel regression or the mixture will become too fuel-lean to support combustion. Similarly, if the oxidizer flow rate is insufficient and the O/F ratio is too low, extinction of the flame can also occur. In this light, the oxidizer injector largely controls combustion for a given fuel and grain geometry.

While the theoretical models have largely focused on axial injection of oxidizer into hybrid motors, there is significant interest in employing injectors with more complex geometries to promote increased turbulent mixing and fuel regression. In particular, several projects where swirl injectors have been used have reported significantly improved fuel regression rates over axial injection methods [30, 31, 32, 33]. Several recent works assessing hybrid combustion with both axial and swirl injector types and varied propellants are compiled in Table. 1.1. Gomes et al. found a 50% improvement in regression rates for polyethylene fuel when swirl injection was introduced. For their experiments, a four-port radial swirl injector was compared to a simple single-port axial injector with constant mass flux rates through the injectors [31]. There is strong evidence across many of these works that indicate

that the effects of the swirl injection are more prominent for shorter fuel grain lengths [30, 31, 33]. Specifically, Kumar et al. found that introducing swirl injection improved the average regression rate with short grains (defined there as total length over inner diameter, L/D, being less than 5) but caused minimal improvement for longer grains. While these encouraging results of increased regression rate with swirl injection exist, there are some potential drawbacks that have also arisen through these works. Most significantly, unstable combustion and loss of vortex strength along the length of the fuel grain.

Overall, within these broad categories of injectors, there are any number of variations in port sizes, positions, angles, and shapes that determines the flow structure in the rocket combustion chamber. In order to gain a comprehensive understanding of the mixing intricacies as influenced by any particular injector geometry, spatially-resolved measurements taken within the reaction layer are needed.

1.4 Fire toxicity

Analogous to hybrid rockets, wind-blown fires involve a forced convective oxidizer cross-flow with a reacting boundary layer. The conditions and composition of this reacting boundary layer determine the ultimate emissions of fires, which can be highly toxic. This is due, in part, to normal emissions associated with diffusion flames where high-temperature regions are closely coupled to fuel rich regions leading to higher carbon monoxide and unburned hydrocarbons, including aromatics and soot, that present a public health concern. The health and safety risk of unwanted fires have led to a prevalence of synthetic fire-resistant polymers used in construction of residential and industrial buildings. However, when exposed to a hot oxidative cross-flow, some of these fire-resistant materials, which are often halogenated polymers, can form hydrogen halides and higher proportions of other toxicants due to incomplete combustion which amplifies the risk of death and injury.

The fire resistance of polymers is primarily evaluated through ignitability, flame spread,

Figure 1.7 House fires with traditional construction and fire-resistant materials

and heat release [34]. The ignitability of a polymer depends on the rate by which a surface of a polymer reaches its ignition temperature, which correlates to the energy stored by the polymer during exposure to a heat source. This is affected by its heat capacity, enthalpy of fusion and degree of crystallinity. The resistance to ignition of a polymeric material is often quantified by a "level of oxygen" (LOI) value, defined by the minimum concentration of oxygen in nitrogen required to support the combustion of the material for at least 3 minutes or consumption of 5 cm of the evaluated sample [34, 35]. Thus, the higher the LOI value, the more fire resistant the polymer is determined to be. Given that the oxygen concentration of air is around 21%, materials with an LOI value below 21 are considered combustable whereas those with values above 21 are classified as self-extinguishing or fire-retardant since they cannot sustain combustion at ambient conditions without an external energy source.

Self-extinguishing materials interfere with the combustion cycle through various physical or chemical mechanisms depending on their composition. The prevalent underlying mechanisms include the following:

- *Inert gas generation* leading to dilution of the oxygen supply near the polymeric surface.

This results in flame snuffing beacuse of the lack of available oxidizer.

- *Inhibition of oxidation* reactions by way of polymer degradation trapping free radicals. In particular, the hydrogen radicals, responsible for important chain-branching reactions to propagate the fuel combustion, and hydroxyl radicals, which are involved in highly exothermic reactions in polymer decomposition needed to sustain combustion (eg. $\mathrm{OH}\cdot + \mathrm{CO} \rightarrow \mathrm{H}\cdot + \mathrm{CO}_2$).

- *Carbon layer formation* on the polymeric surface through low-energy solid state reactions that proceed at the expense of gaseous volatile production. The formed layer also acts as a physical semi-permeable barrier between the solid and gas phase regions

- *Highly endothermic reactions* in the polymer decomposition that act as a heat sink, cooling the temperature to that below what can maintain combustion

Thorough discussion and a more complete list of the combustion cycle interence factors in regard to polymer combustion can be found in *Kiliaris et al.* [34]. In general, the above listed mechanisms are somewhat coupled and act in combination. The flame retardancy of halogen based polymers is largely driven by the trapping of free radical species through the decomposition process, inhibiting the promotion of oxidation reactions, and thus leading to extinguishing and inhibition of flame propagation [36, 34]. This inhibition is often the consequence of the generation of hydrogen halides, such as hydrogen fluoride (HF), hydrogen bromide (HBr), and hydrogen chloride (HCl), or of halogen atoms for polymer molecules not containing hydrogen. Thermophysical factors have also been shown to contribute to their flame retardancy. In particular, the heat capacity of halogen atoms causes them to act as heat sinks, reducing the available heat from polymer combustion gases and precluding further thermal decomposition. Halogens can have a "blanketing" effect wherein oxygen is excluded from existing near the surface of the decomposiing polymer. They are believed to catalyze oxidation of solid phase decomposition species, yielding products that can cyclize and form a solid barrier layer over the surface of the burning polymer [37].

Despite their characterization as flame-resistant materials, halogenated polymers can achieved sustained combustion at elevated temperatures when exposed to an external energy or heat source, such as a surrounding fire. In these instances, the ongoing decomposition processes with oxidation inhibition, as discussed above, can result in high concentrations of hydrogen halides and carbon monoxide in the fire emissions that can be hazardous or even lethal. Although theoretically-derived models of polymer decomposition exist that incorporate some of the important underlying phenomena, their implementation for multi-phase reacting flow simulations is complex and reaction pathway relative contributions are largely lacking in experimental validation. Improvements to these halogenated flame resistant models anchored to thermochemical data are crucial for improving predictions of toxicant formation and emission hazard levels.

1.5 Solid Fuel Combustion Analysis Methods

It is of interest to create fundamental combustion experiments that enable a rigorous examination of the combustion zone for a solid fuel in oxidizer cross-flow. Measurements of the evolution of critical gas properties in this zone (temperature, composition, other) can enable thorough characterization of the competing physics of heat transfer, fluid dynamics, and chemical kinetics.

1.5.1 Experimental Methods

Burners, of varied geometric configurations, are widely used to study hybrid combustion of a solid fuel with a gaseous oxidizer. Many burners can produce and maintain stable flames enabling steady diagnostic measurements for analysis and propellant flow rates are typically well characterized and can be tuned to suit specific testing goals.

Stanford utilizes a flow facility with optical access to study hybrid combustion turbulent reacting boundary layers for varied fuels reacting with a steady gaseous oxygen stream

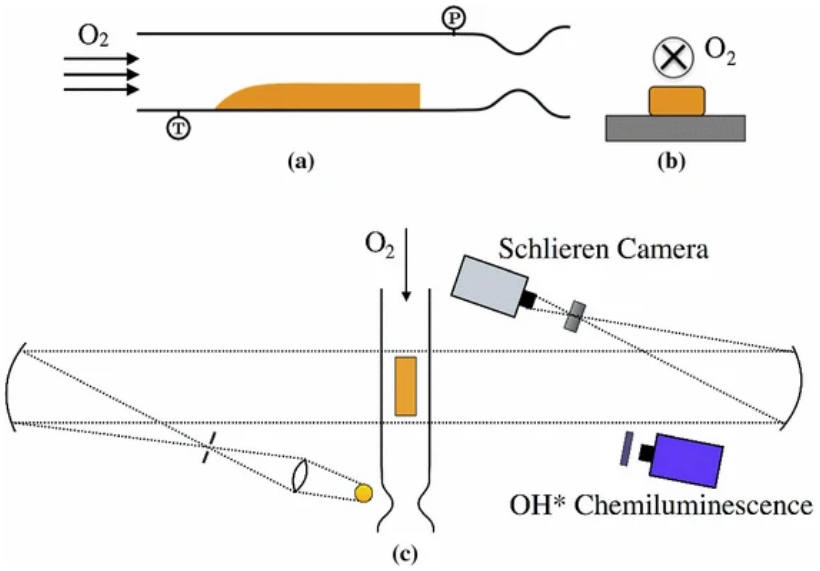

Figure 1.8 Stanford flow facility for imaging of hybrid combustion turbulent boundary layers. Diagram from [4].

[38, 39, 19, 4]. They employ both Schlieren imaging and chemiluminescence diagnostic methods as shown in Fig. 1.8. The flame location is estimated from imaging OH*, although they note the challenges in obtaining quantitative OH* results due to indistinguishable signal intensity offsets from broadband CO_2* emission and conflicting studies on the relationship of heat-release rates to chemiluminescent signals. The Schlieran images are used to discern evolution of boundary layer height along the fuel grain from density. They infer the edge of the thermal boundary layer by relating the observed density to temperature with the ideal gas law. This facility and diagnostics have been used to study several classical and high-regression hybrid rocket fuels including PMMA, HTPB, and paraffin wax. These studies provided novel visualization results of paraffin-wax droplet entrainment and liquid layer instability. Similar facilities including 2D slab burners coupled with optical diagnostics for hybrid combustion visualization for propulsion research have been used at Université Libre de Bruxelles, Politecnico di Milano, Chiba Institute of Technology with JAXA, and NASA Jet Propulsion Laboratory (as previously discussed in Sec 1.3.1) , among others [40, 41, 29, 3].

Counter-flow burners can also be used for combustion experiments analogous to a 1D hybrid rocket system, in which the counter flow serves as a proxy for cross flow component in hybrids After ignition, pyrolyzed fuel and product species emerge from a melted fuel layer. A diffusion flame forms below the stagnation plane between the fuel-rich and fuel-lean regions and the gases flow away from the injection systems along streamlines bounded by the stagnation plane. As in hybrid rocket combustion, the heat feedback from the flame sustains the ongoing pyrolysis post-ignition and the heat directly affects the fuel regression rates. One such counter-flow burner at the Naval Surface Warefare Center has been used to assess effects of varied oxidizers and fuels on regression behavior using high speed cinematography coupled to linear variable displacement transducer (LVDT) traces for temporally resolving regression rate[42, 43]. Modifications of this facility by removing the oxidizer nozzle and replacing it with a hot air gun have provided data of particular interest for solid fuel ramjets [43]. Recently, they have used data obtained using this facility with PMMA as the solid fuel to develop and validate multi-phase numerical models [44].

Beyond propulsion applications, burner studies or hybrid combustion have also been readily utilized by the fire science communities. Wind tunnels have been used to provide concurrent airflow over thin fuel slabs, such as in *Huang et al.* [5]. This study, among numerous others, have aimed to characterize the flame spread and the underlying complexities of the turbulent boundary layer and interactions between flame and fuel [45, 46]. Their experimental setup is shown in Fig. 1.9. The flame spread process was assessed using CCD cameras that target the pyrolysis region front and rear positions, and enabled visual determination of preheating length, flame tip position, and standoff distance.

In this dissertation, we utilize an axisymmetric solid fuel burner to analyze the combustion behavior of hybrid rocket fuels with optical diagnostics. The first iteration of the facility, related diagnostic methods, and early hybrid combustion experiments conducted can be found in *Bendana et al* [6]. It should be noted that that caution must be exercised when burning polymers and other materials in pure oxygen as they commonly produce toxic

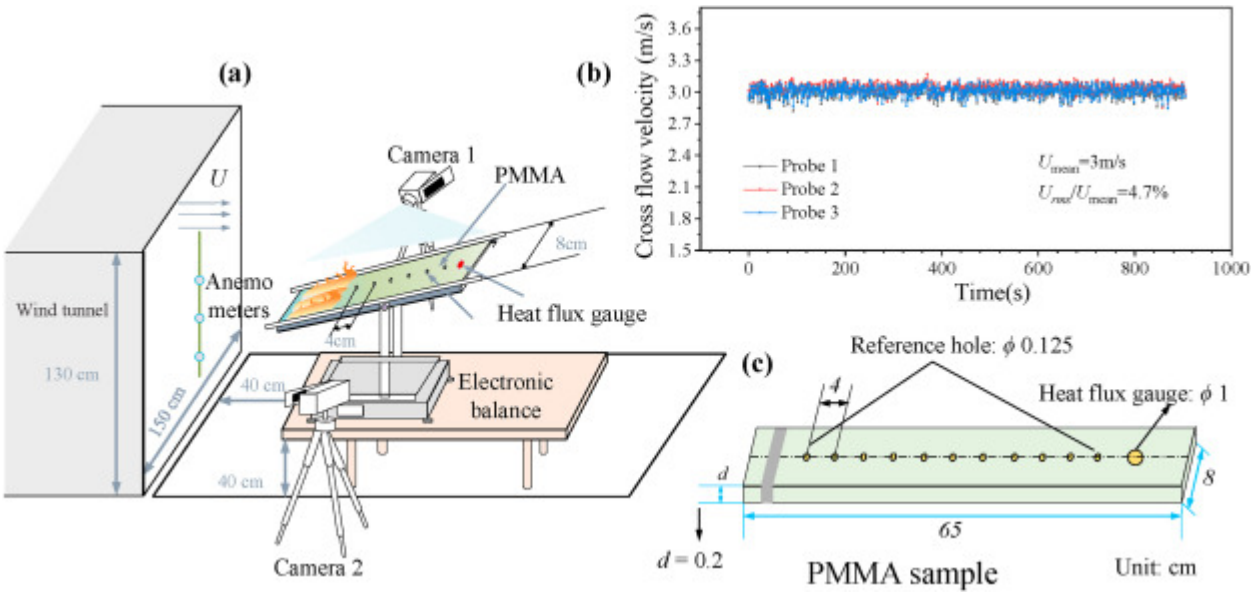

Figure 1.9 Concurrent air-flow over solid fuel slab burner configuration used for experiments in [5].

gases in substantial quantities. All experiments shown in this study were located in a high-efficiency low-volume laboratory fume hood (Kewaunee Scientific: Supreme Air LV) that rapidly exhausts the combustion products at a rate of ∼1150 cfm.

The vertical test stand was designed to accommodate solid cylindrical fuel grains with an outer diameter up to 50.8 mm and lengths varying from 25.4 mm to 203.2 mm. The fuel grains can be manufactured to incorporate different fuel port geometries; however, an axially symmetric profile is required for the tomographic reconstruction techniques discussed herein. The setup enables in-situ measurements of the combustion zone by providing an unobstructed optical line-of-sight at the exit-plane of the fuel grain (referred to as measurement plane). In order to minimize the effects of entrainment/thermal boundaries on the measurement, the measurement plane is located within ∼0.5 mm of the fuel-grain exit, and assumed to be primarily determined by upstream flow conditions. Spatially-resolved measurements are obtained by mounting the vertical test stand on a motorized translation stage (Thorlabs NRT100) that moves horizontally at up to 5 mm/s during experiments. To

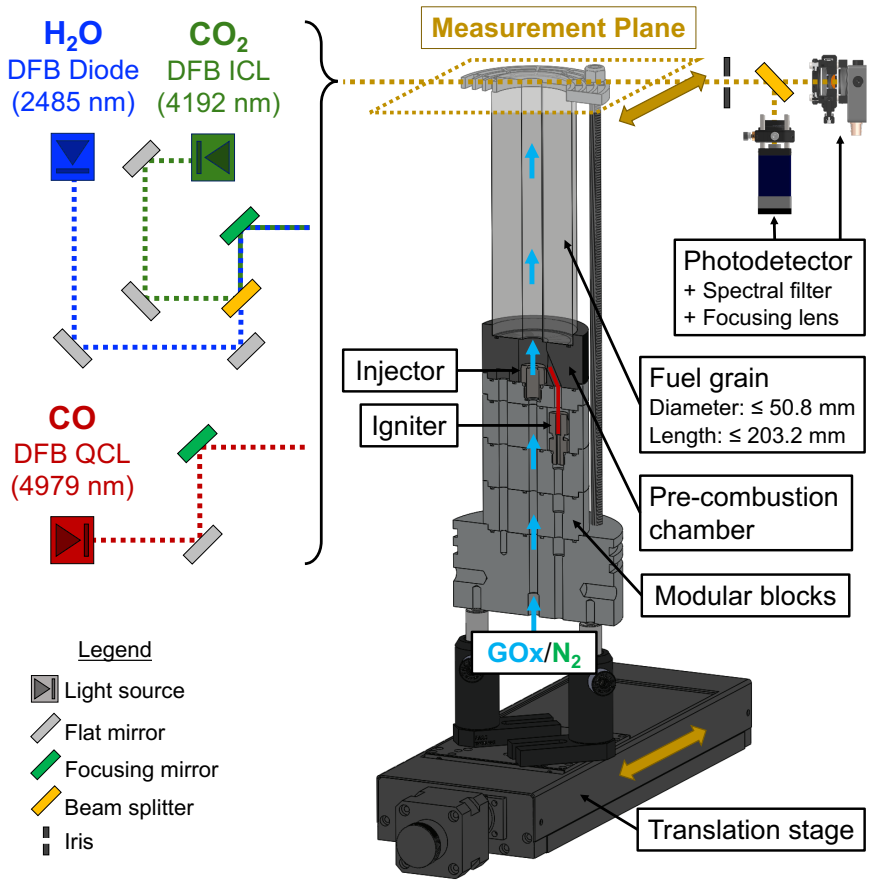

Figure 1.10 Vertical test stand utilized for temperature and species measurements in hybrid rocket combustion. Optical setup is shown for both CO and CO_2/H_2O configurations used in [6].

conduct measurements at multiple axial locations for a spatially-resolved image, modular blocks can be added/removed to allow different fuel grain lengths to be burned. This also minimizes the amount of optical adjustments between experiments. Typically, the mass of each fuel grain and diameter of the exit is measured before and after each test to estimate overall equivalence ratio and regression rate.

During the experiment, gaseous oxygen is introduced into the center of a graphite pre-combustion chamber with an internal diameter of 17.8 mm. The injector exit is located 15.2 mm from the front end of the fuel grain and is designed to be easily interchangeable

to facilitate experiments with different injection geometries. Remote ignition is achieved via an electrical igniter located in the precombustion chamber. After each hot-fire, a gaseous nitrogen (N_2) purge system clears the lines of any excess oxygen and extinguishes the flame. Oxygen and nitrogen flow rates are measured using a sonic orifice ($D = 1.27$ mm) with a discharge coefficient of $C_d = 0.85$ and an upstream pressure transducer (Setra 225G), both of which can be interchanged to target different flow rates. Further information on plumbing and instrumentation can be found on the schematic in Fig. 1.11.

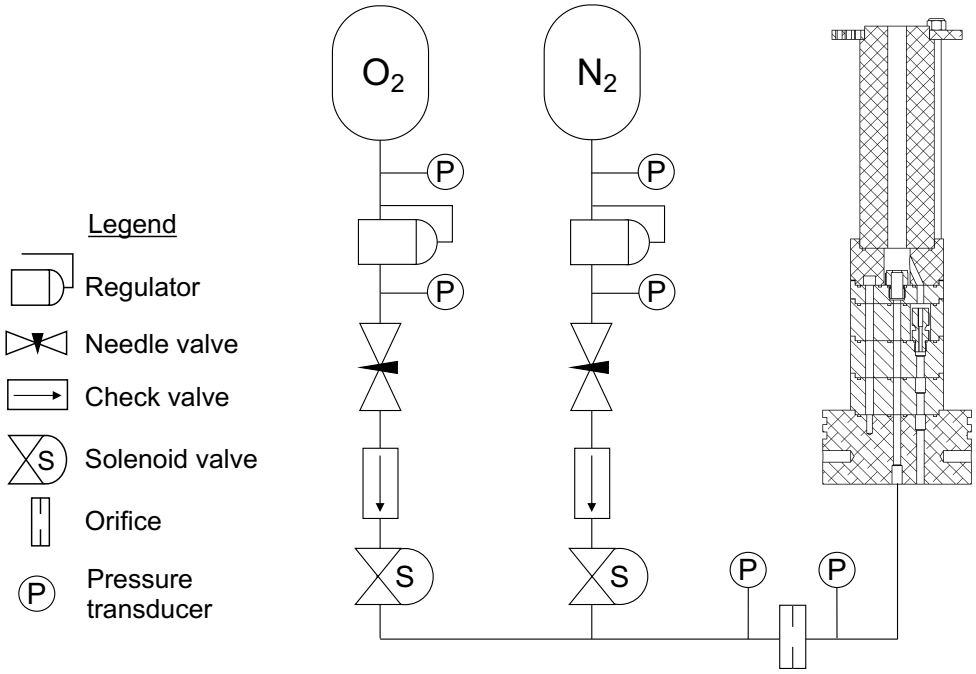

Figure 1.11 Piping and instrumentation diagram illustrating both GOx and N_2 gas delivery systems. Flow rates for all experiments are regulated using a sonic orifice

1.5.2 Diagnostic Techniques

To experimentally assess the coupled physics of fluid dynamics, chemical kinetics, and heat and mass transfer involved in hybrid combustion, researchers have used a number of different diagnostic methods. Many traditional instruments for measuring species and temperatures,

such as thermocouples or mass spectrometry (via sampling probes), disturb the targeted flowfield and are unsuitable for the extreme temperature and pressure conditions present in rocket engines and other combustion systems. Instead, varied non-intrusive optical diagnostic methods have been developed and employed to characterize harsh combustion environments by exploiting light-matter interactions such as emission, absorption, scattering, and refraction. In this section, relevant optical diagnostic methods for propulsion and combustion will be briefly reviewed, with discussion on their respective strengths and limitations:

- *Laser-induced fluorescence (LIF)* is a technique that uses intense laser radiation to excite a molecule to an electronic state after which electronic relaxation occurs and spontaneous emission of the previously absorbed photon is measured. Calibration is required to interpret measurement data, but if done correctly, species concentrations can be determined and, if multiple electronic transitions are measured for a single species, temperature can be obtained as well. When extended into two-dimensions, the method is commonly referred to as Planar laser-induced fluorescence (PLIF). PLIF measurements of combustion environments have been made extensively across varied applications and have provided insight into combustion processes. However, in conditions relevant to propulsion systems, dynamic flowfields and harsh thermodynamics make PLIF imaging unsuitable for most quantitative analysis.

- *Raman Spectroscopy* is based on targeting the spectra resulting from the scattering of photons by molecules. In Anti-Stokes Raman scattering, interaction between a molecule and a photon involves energy transfer from the molecule to the photon, resulting in a decreased wavelength of the photon. Often, multiple light sources are used to produce a single coherent beam at the anti-Stokes frequency called Coherent anti-Stokes Raman spectroscopy (CARS). The resulting measurements can be done with high spatial and temporal resolution making it a very useful tool for combustion diagnostics; however, CARS calibration and alignments can be highly complex and costly.

- *Chemiluminescence* is electromagnetic radiation that is emitted by molecules when they relax from an excited energy state to a lower energy state through chemical reactions. Diagnostic instruments targeting chemiluminescent radiation often target $OH\cdot$, $CH\cdot$, $C_2\cdot$, and $CO_2\cdot$ in the visible and ultraviolet spectral ranges. These tools are attractive for combustion diagnostics due to their simplicity and non-instrusivity. Chemiluminescence data can provide information about relative conditions in flow-fields and have be used to determine equivalence ratios, flame locations, and heat release rates; however, quantitative interpretation of the data is challenging and is often based on empirical correlations and modeling for specific conditions. Calibration must also be performed and is specific to each experiment setup, limiting the feasibility of implementing chemiluminescent diagnostics outside of carefully controlled laboratory experiments.

- *Schlieren imaging* uses deflection of light as a proxy for determining index of refraction changes in the air which enables inference of density variation. A point-like light source, such as a laser, is pitched across the gas sample of interest to a spherical mirror with a long focal length that focuses the light onto a thin light block in front of a camera. Changes in refractive index in the gas will lead to deflection of the focused light beyond the light block, which will be captured on the camera. Schlieren imaging can be useful for determining position and length scales in combustion environments, such as boundary layer height or flame location, and for flow field visulization. However, these measurements are limited in their quantitative nature and lack capability of determining most thermochemical properties.

- *Fourier-transform infrared (FTIR) spectroscopy* similarly targets infrared molecular absorption. FTIRs utilize broadband light sources that can capture spectrally-resolved absorbance over a large spectral domain. The radiated light passes a gas sample through an interferometer before reaching a detector. The resulting interferogram signal is amplified and a Fourier transform is performed to convert the recorded waves into

the frequency domain, providing absorbance as a function of wavelength (or wavenumber). FTIRs can be useful for detecting multiple species given the broadband light source radiation; however, the granularity of their spectral resolution is limited and their data acquisition speeds (on the order of seconds to minutes) makes them insufficient for many combustion sensing applications. Additionally, the gas sample typically has to travel from a flowfield probe through plumbing infrastructure to the FTIR during which time the gas temperature and composition may be affected, compromising the validity of the results.

- *Laser absorption spectroscopy (LAS)* is a optical diagnostic technique that exploits absorption of light at wavelengths resonant to molecular energy level transitions to determine thermophysical properties of a gas. Molecular species have unique absorbance spectra, enabling quantitative species-specific measurements. LAS measurements have been used in numerous combustion environments to successfully target fuel, intermediate, and product species. Unlike for LIF and Raman spectroscopy, laser absorption spectroscopy is calibration-free. Successful quantitative measurements using LAS can be obtained using low-power, relatively inexpensive lasers and simplistic optical alignment configurations. Advancements in laser technology in the last few decades have enabled LAS measurements of previously inaccessible strong absorption features in the mid-infrared wavelength range, extending the diagnostic's capability to additional species and increasingly sensitive detection limits. Many other diagnostics lack the species specific sensitivity, time resolution, and possibility for spatial resolution (by way of tomography and imaging, see Sec. 2.3), that can be achieved with laser absorption spectroscopy and provide uniquely granular assessment of hybrid combustion performance.

1.6 Scope and Organization

This dissertation details the development and implementation of laser absorption spectroscopy and tomography methods for resolving reacting flow thermochemistry relevant to hybrid combustion of solid fuels. The overarching goal is to improve understanding of the combustion physics in the reacting boundary layer near the fuel surface. The utility of such measurements are demonstrated through application to fuels relevant to hybrid rocket propulsion and fire toxicity.

The work is organized into chapters for narrative clarity. Chapter 2 provides a brief review of laser absorption spectroscopy, the key diagnostic uniting the research across different experimental methods and applications. Chapter 3-5 focus on investigations of hybrid rocket motor combustion with PMMA/GOx propellants. Specifically, Chapter 3 details a method for obtaining two-dimensional measurements of the thermochemical structure. Results are presented for two different axial oxidizer injectors to illustrate the scale of the effect such geometry can have on the flowfield evolution. Chapter 4 extends the previous study to include injectors with varied axial and swirl inlet port configurations of increased relevance to larger scale hybrid rocket applications. The data presented in Chapters 3-4 are analyzed further in Chapter 5 in which a method for determining local characteristic velocity (c*) from temperature and speciation measurements is detailed. Two-dimensional spatially-resolved characteristic velocity images are presented for the studied oxidizer injectors and used to draw conclusions about their combustion efficiency and comparative utility. In Chapter 6, the focus is shifted from PMMA to the monomer: methylmethacrylate (MMA) with the goal of improving modelling efforts of PMMA combustion. This chapter details a shock tube study of thermal decomposition of MMA via time-resolved LAS measurements of intermediate and product species. Existing relevant chemical kinetic mechanisms are discussed and compared with the experimental data. Updated reaction rates for identified sensitive reactions are included based on findings using computational optimization techniques. Chapter 7 revisits

the laser absorption tomography strategy utilized previously for hybrid rockets and extends the capability to study other fuels with PMMA as a pilot burner. In particular, this chapter focuses on the combustion of polytetrafluoroethylene (PTFE), a fire-resistant polymer often referred to by the brand name Teflon, studied via measurements of carbon monoxide and the highly hazardous toxicant, hydrogen fluoride. The goal of this study of PTFE was to provide data to inform models of incipient formation of toxicants in structural fires. Finally, Chapter 8 summarizes the efforts and findings of this dissertation and discusses future research efforts to advance hybrid combustion understanding for both rocket propulsion and fire toxicity applications.

CHAPTER 2

Mid-infrared Laser Absorption Spectroscopy

Laser absorption spectroscopy (LAS) is an optical diagnostic technique that exploits the resonance of coherent light with the transitions between quantum energy states for a given species. Its usage has been increasingly widespread over the last two decades as capability has continually advanced for characterizing flow-fields with species specific, high bandwidth, calibration-free, and in situ measurements. Developments in optical equipment, have enabled sensitive measurements of combustion relevant species previously inaccessible with LAS. In particular, quantum cascade lasers (QCLs) and interband cascade lasers (ICLs) have made the mid-infrared range, where spectral transitions are significantly stronger in magnitude than those in the near-infrared, more readily accessible. The increased availability of strong absorbance features in the mid-IR has enabled diagnostics with high sensitivity for several fuel, intermediate, and product species relevant to hybrid combustion. Spectral absorption strength of several such species are shown in Figure 2.1, simulated at a condition of 1000K and 1 atm using spectral paramters from the HITRAN database [7]. This chapter discusses the fundamental governing principles of laser absorption spectroscopy and the measurement techniques leveraged to obtain in-situ measurements of physical gas properties including temperature and species composition within harsh high-temperature hybrid combustion environments.

2.1 Fundamentals

An overview of the fundamentals of laser absorption spectroscopy is provided here for reader familiarity with common nomenclature and definitions; a comprehensive review can be found in [47]. Species have unique spectral "fingerprints", determined by the energy spacing between the quantum states (transitions) specific to a given molecule. By exposing a molecule to coherent light radiation of equivalent energy to the targeted species' quantum energy spacing, the molecule can absorb photon energy and transition from a lower state to an upper state quantum energy level. Energy contained by photons of a particular wavelength is specified in Eq. 2.1:

$$E = \frac{hc}{\lambda} \tag{2.1}$$

where h is Planck's constant [m^2kg/s], c is the speed of light [m/s], and λ is the wavelength of light [m].

The absorption of light that allows for the transition between energy levels results in an

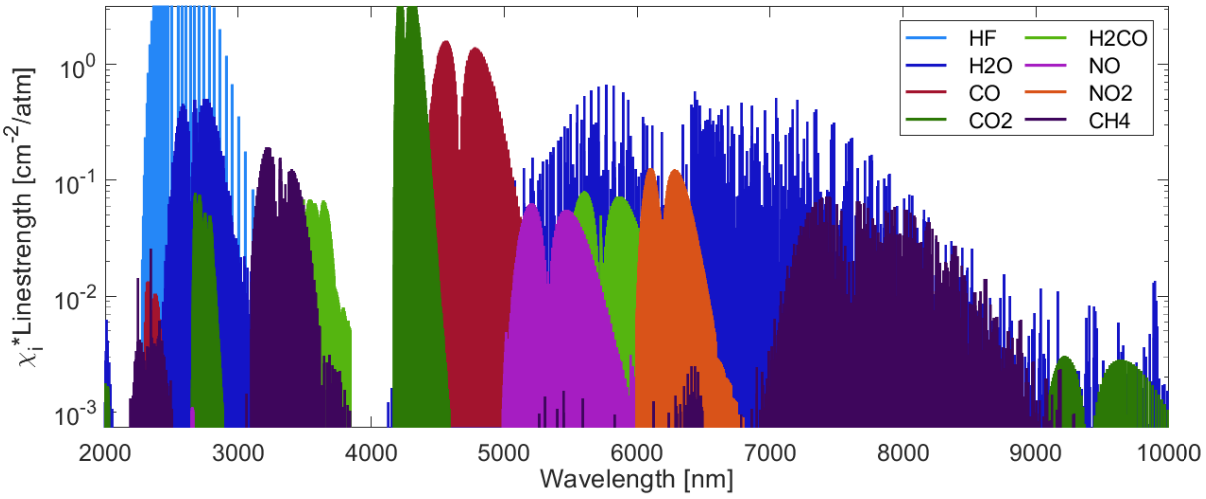

Figure 2.1 Spectral survey of absorption linestengths for select combustion relevant species. Spectral parameters used for simulation obtained from the HITRAN database [7].

attenuated light intensity of the source (i.e. laser beam). The Beer-Lambert law relates the change in light intensity (via spectral absorbance) to thermochemical properties of the flow environment. Eq. 2.2 describes this relationship for the spectral absorbance, $\alpha(\nu)$, of a non-uniform gas medium along a line-of-sight, l [cm]:

$$\begin{aligned}\alpha(\nu) &= -\ln\left(\frac{I_\mathrm{t}}{I_0}\right)_\nu \\ &= \int_0^L \sum_j PS_j(T(l))X_i(l)\phi_j(\nu)\mathrm{d}l\end{aligned} \tag{2.2}$$

Here I_0 and I_t are the incident and transmitted light intensities, respectively, at a specific frequency, ν [cm^{-1}], L [cm] is the aggregate absorbing path length, P [atm] is the total pressure, $S_j(T(l))$ [cm^{-2}/atm] is the linestrength of rovibrational transition, j, at temperature, $T(l)$ [K], $X_i(l)$ is the mole fraction of the absorbing species, i, and $\phi_j(\nu)$ [cm] is the line-shape function. It should be noted that this expression is a line-of-sight integral over an optical path length with non-uniformity in temperature and species.

For a gas in thermal equilibrium, the temperature-dependent linestrength for each transition j at temperature T can be determined by Eq. 2.3:

$$\begin{aligned}S_j(T) =& S_j(T_0)\frac{Q(T_0)}{Q(T)}\left(\frac{T_0}{T}\right)exp\left[-\frac{hcE_j^{"}}{k}\left(\frac{1}{T}-\frac{1}{T_0}\right)\right] \\ &\cdot\left[1-exp\left(\frac{-hc\nu_{0,j}}{kT}\right)\right]\left[1-exp\left(\frac{-hc\nu_{0,j}}{kT_0}\right)\right]^{-1}\end{aligned} \tag{2.3}$$

where T_0 is the reference temperature, Q is the species partition function, $E_j^{"}$ is the lower state energy of the transition, $\nu_{0,j}$ is the center frequency of the transition, and k is the Botlzmann constant ($1.38 \cdot 10^{-23}$ J/K). The normalized lineshape function ϕ for a given transition over the unbounded spectal domain, by definition, integrates to 1:

$$\int_{-\infty}^{+\infty} \phi \, d\nu = 1 \tag{2.4}$$

This lineshape function is typically approximated by a Voigt function, which is a convolution of Gaussian and Lorentzian distribution functions reflecting Doppler and collisional

broadening effects, respectively. Doppler broadening occurs when the velocity component of a molecule in the same direct of photon propagation causes absorbance to occur at a Doppler-shifted frequency. For molecules following a Maxwellian-velocity distribution, the absorption line shape affected by Doppler broadening can be described by a Gaussian profile as:

$$\phi_{D,j}(\nu,T) = \frac{2}{\Delta\nu_{D,j}}(\frac{ln2}{\pi})^{(1/2)} \exp\left[-4\ ln2\left(\frac{\nu-\nu_{0,j}}{\Delta\nu_{D,j}}\right)^2\right] \tag{2.5}$$

where $\Delta_{D,j}[cm^{-1}]$ is the Doppler halfwidth given by:

$$\Delta_{D,j} = \nu_{0,j}(7.1623x10^{-7})\sqrt{\frac{T}{M}} \tag{2.6}$$

wherein $T[K]$ is the temperature and $M[g/mol]$ is the molecular weight. Doppler width increases proportionally with temperature, as in Eq. 2.6, and, to a lesser effect, with increased frequency and decreased molecular weights.

Collisional broadening occurs when inelastic collisions decrease molecular lifetime in an absorbing state, elastic collisions dephase and perturb molecular rotation and/or vibration, or angular-momentum altering elastic collisions cause a re-orientation of the dipole's angular momentum vector. When collisional broadening effects are prevalent, such as for high density gases, the absorption lineshape takes the form of a Lorentzian profile such as:

$$\phi_{L,j}(\nu,T,P,X_i) = \frac{1}{2\pi}\left[\frac{\Delta\nu_{C,j}}{(\nu-\nu_{0,j})^2 + (\frac{\Delta\nu_{C,j}}{2})^2}\right] \tag{2.7}$$

where $\Delta\nu_{C,j}[cm^{-1}]$ is the collisional halfwidth given by:

$$\Delta\nu_{C.j}(T,P,X_i) = P\sum X_k 2\gamma_{(i-k)j} \tag{2.8}$$

where $P[atm]$ is the pressure, $\gamma_{(i-k)j}[cm^{-1}/atm]$ is the broadening coefficient between the molecule absorbing, i, and the molecule perturbing, k, for some rovibrational transition j, and X_k is the perturbing species mole fraction. The effects of self-broadening (where $i = k$) must be included in determination of collisional broadening. The collisional width, as

indicated by Eq. 2.8, scales linearly with pressure. The effects of temperature are contained within the $\gamma_{(i-k)j}(T)$ term.

The resulting Voigt lineshape function, encompassing the effects of both Doppler broadening (Gaussian distribution) and collisional broadening (Lorentzian distribution), can be written as:

$$\phi_V(\nu) = \phi_D(\nu_0)\frac{a}{\pi}\int_{-\infty}^{+\infty}\frac{exp(-y^2dy)}{a^2+(w-y)^2} = \phi_D(\nu_0)V(a,w) \tag{2.9}$$

where $\phi_D(\nu_0)$ is the Doppler linecenter magnitude, a is the Voigt "a" parameter, w is the nondimensional line position, and y is the integral variable:

$$\phi_D(\nu_0) = \frac{2}{\Delta\nu_D}\sqrt{\frac{ln2}{\pi}} \tag{2.10}$$

$$a = \frac{\sqrt{ln2}\Delta\nu_C}{\Delta\nu_D} \tag{2.11}$$

$$w = \frac{2\sqrt{ln2}(\nu-\nu_0)}{\Delta\nu_D} \tag{2.12}$$

$$y = \frac{2u\sqrt{ln2}}{\Delta\nu_D} \tag{2.13}$$

These equations are the theoretical basis from which laser absorption spectrocopy techniques are derived. The spectroscopic parameters needed to apply this theory to real measurement systems are obtained from theoretical derivations as well as experimental spectroscopic studies.

2.2 Direct absorption spectroscopy

Scanned-wavelength direct absorption spectroscopy (DAS) is among the most widely utilized methods grounded in laser absorption spectroscopic principles. Its appeal is related to its relative implementation simplicity, wide applicability, and signal processing requirements. In this technique, a light source, often a tunable semiconductor distributed feedback laser, is sent a modulating injection current that results in a simultaneous output light wavelength

and intensity modulation. The modulation (often in a waveform shape that is sinusoidal, sawtooth, triangular, or square) is selected such that the output light scans over wavelengths that are resonant with molecular absorbance transitions. The light is directed such that it passes through a target gas flow or gas sample and the transmitted light is recorded by a photodetector. Absorbance is obtained from the ratio of the transmitted light to the incident output light through Eq. 2.2. The absorbance signal is fit (typically) with a Voigt lineshape function as discussed previously and gas properties can be obtained from the absorbance areas. From the Beer-Lambert Law relationship, the gas temperature can be determined from simultaneous measurement of two absorption transitions of the same molecule through two-line (or two-color) thermometry:

$$R = \frac{A_1}{A_2} = \frac{S_1(T)}{S_2(T)} = f(T) \tag{2.14}$$

This absorbance area ratio is a function of temperature alone, eliminating the dependence on pressure, pathlength, and concentration. With temperature know, mole fraction can be subsequently determined from the area of a single transition through:

$$X_i = \frac{A}{PS(T)L} \tag{2.15}$$

A given gas species contains many candidate absorption transitions that can be optically targeted, so careful line selection is required for optimal sensor performance. The most suitable transitions for this methodology are spectrally distinct lines that avoid cross-species interference due to other species present in the gas medium with similar transition energies. Additionally, a high-temperature sensitivity of the line pair ratio is desired. To achieve the desired sensitivity, we examine the linestrength ratio, $R(r)$, dependence on temperature, T:

$$\left|\frac{dR/R}{dT/T}\right| \approx \left(\frac{hc}{k}\right)\frac{|E_1'' - E_2''|}{T} \tag{2.16}$$

It is worth noting that line pairs with a large difference in lower state energy, $\Delta E''$, are desirable for sensitive thermometry, correlating to absorption transitions with very different temperature dependence over the dynamic range of interest.

2.3 Laser absorption tomography

Tomography is a technique by which an unknown spatial distribution of interest (inverse problem) can be reconstructed from a set of projection measurements (forward problem). In laser absorption tomography (LAT), this involves recovering a distribution of gas properties from multiple line-of-sight measurements. For the applications discussed in this dissertation, one-dimensional (1D) tomography was employed, enabled by the axisymmetric nature of the experiments, which enables reconstructionof the flow-field from a single projection angle [48]. The forward problem projected absorbance is still governed by the Beer-Lambert Law, as in Eq. 2.2, where absorbance depends on the total pressure, transition line-strength, mole fraction, lineshape function, and aggregate path length. The projected absorbance measurements can be integrated over the spectral domain to eliminate dependence on the line-shape function, $\phi_j(\nu)$. This integrated term is the projected absorbance area, $A_{\text{proj}}(y)$ [cm^{-1}], which, for an azimuthal symmetric flow-field, can be obtained at discrete locations, y [cm], from the axis of symmetry and, using Abel's integral equation [49, 50], can be related to the inverse problem through estimating the radial distribution of the integrated spectral absorption coefficient, $K(r)$ [cm^{-2}]. This relationship is described by Eq. 2.17:

$$\begin{aligned} A_{\text{proj}}(y) &= \int_{-\infty}^{\infty} \alpha(\nu)\mathrm{d}\nu \\ &= \int_0^{L(y)} K(l)\mathrm{d}l = 2\int_y^R \frac{K(r)r}{\sqrt{r^2-y^2}}\mathrm{d}r \\ &= \int_0^{L(y)} \sum_j PS_j(T(l))X_i(l)\mathrm{d}l \end{aligned} \tag{2.17}$$

In Eq. 2.17, $L(y)$ [cm] is the absorbing path length at position, y, from the axis of symmetry and the radially-resolved thermochemical flow-field properties, $T(r)$ and $X_i(r)$, are embedded in $K(r)$, which can be determined from $A_{\text{proj}}(y)$ using the tomographic reconstruction methods discussed in [6]. As previously noted, this approach assumes an axisymmetric flow-field, which is expected in the gas-phase core flow of a cylindrical fuel grain for a hybrid rocket geometry. The relationship between the projected and reconstructed coordinate systems are shown in Fig. 2.2.

Temperature and species are recovered from measurements of the projected absorbance areas, which are inverted via tomography to yield the integrated spectral absorption coefficients for various spectral lines. $A_{\text{proj}}(y)$ is obtained by fitting a Voigt line-shape function to the absorbance profile of each absorption feature. These features may encompass one or more transitions ($j \geq 1$) that are closely spaced. For the latter case, $A_{\text{proj}}(y)$ and $K(r)$ simply represent a summation of individual contributions, which can be reasonably well extracted from a Voigt fit. In practice, $T(r)$ is obtained by measuring two spectral absorption features of the same species and taking the ratio between the two integrated spectral absorption coefficients, $K_1(r)$ and $K_2(r)$. This eliminates the pressure and mole fraction dependence and $T(r)$ can be inferred from the linestrength ratio, as shown in Eq. 2.18:

$$R(r) = \frac{K_1(r)}{K_2(r)} = \frac{\sum_i S_i(T(r))}{\sum_j S_j(T(r))} = f(T(r)) \tag{2.18}$$

Linestrength values, $S_j(T(r))$, for each species and their associated uncertainties are taken from the HITRAN [51] and HITEMP [8] spectroscopic databases. Eq. 2.19 indicates that, with pressure and the radial distribution of temperature known, $X_i(r)$ of the absorbing species, i, can be evaluated from the integrated spectral absorption coefficient, $K(r)$:

$$X_i(r) = \frac{K(r)}{\sum_j P S_j(T(r))} \tag{2.19}$$

Implementing this strategy for multiple transverse planes at varying axial distances in

the solid-fuel reaction layer enables quantitative two-dimensional imaging of temperature and gas composition [52, 53, 6].

2.3.1 Deconvolution Methods

This section discusses the deconvolution methods used to convert line-of-sight absorption data to radially-resolved profiles of the integrated spectral absorption coefficient, $K(r)$, which are in turn utilized for determining temperature and species profiles. With the assumption of axisymmetry, the spatial distribution of a line-of-sight measurement is well-described by Abel's integral equation [49, 50]:

$$P(y) = 2\int_{y}^{R} \frac{f(r)r}{\sqrt{r^2 - y^2}}\mathrm{d}r \tag{2.20}$$

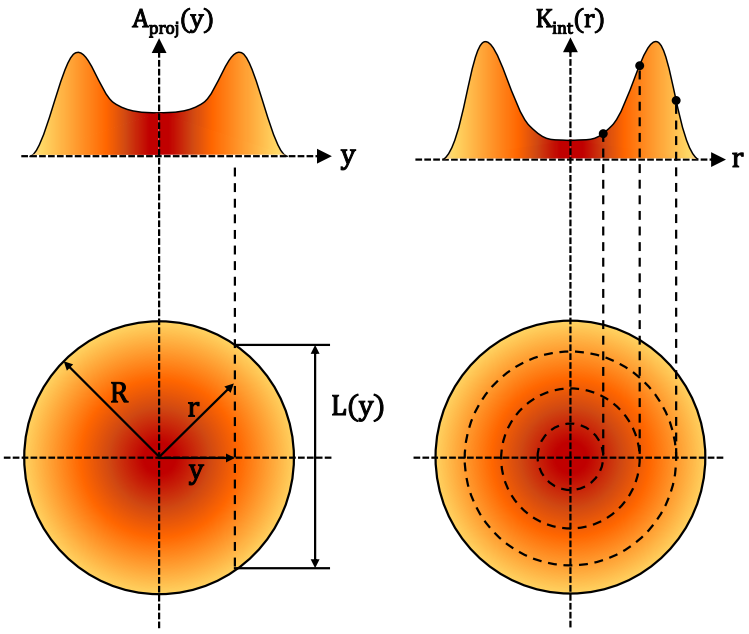

Figure 2.2 Axisymmetric flow-field deconvolution coordinate system and geometry from line-of-sight measurements. The radially-resolved absorption coefficient $K(r)$ can be reconstructed from the projected area $A_{proj}(y)$ through an Abel transform.

where R is the field radius and y is a given distance from the axis of symmetry. In this work, $P(y)$ is the measured projected absorbance area, $A_{\text{proj}}(y)$, and $f(r)$ is the radial distribution of the integrated spectral absorption coefficient, $K(r)$, as seen in Eq. 2.17.

In practice, the Abel inversion is implemented numerically [54], and the field distribution, $f(r)$, is approximated by implementing the three-point Abel (TPA) transform [55]. This enables Eq. 2.17 to be written at every radial location, r, giving rise to a system of linear equations:

$$\mathbf{A_{TPA}f} = \mathbf{P} \tag{2.21}$$

where $\mathbf{f} = [f_0,\ f_1,...f_{N-1}]^T$ and $\mathbf{P} = [P_0,\ P_1,...{}_{N-1}]^T$ contain values of $K(r)$ and $A_{\text{proj}}(y)$, respectively, at every radial location and $\mathbf{A_{TPA}}$ is the projection matrix. To solve Eq. 2.21 and address the inherent ill-conditioned nature of $\mathbf{A_{TPA}}$, a Tikhonov-regularization [54] is adopted.

The Tikhonov method imposes a regularization parameter, λ, that controls the relative importance of accuracy and smoothness in the solution to the inversion. This regularization can be represented as an additional set of equations that constrain the solution:

$$\lambda \mathbf{L_0 f} = 0 \tag{2.22}$$

where $\mathbf{L_0}$ $(N \times N)$ is a discrete gradient operator that characterizes the smoothness of the solution:

$$\mathbf{L_0} = \begin{bmatrix} 1 & -1 & 0 & \dots & 0 \\ 0 & 1 & -1 & \ddots & 0 \\ \vdots & \ddots & \ddots & \ddots & \vdots \\ 0 & 0 & 0 & \dots & -1 \\ 0 & 0 & 0 & \dots & 1 \end{bmatrix} \tag{2.23}$$

An appropriate value for λ is determined for each reconstruction based on the L-curve method [56, 57]. A least-squares solution of the field distribution, $f(r)$, can now be deter-

mined by combining Eq. 2.21 and Eq. 2.22:

$$\mathbf{f}_\lambda = \arg\min \left\| \begin{bmatrix} \mathbf{A_{TPA}} \\ \lambda \mathbf{L_0} \end{bmatrix} \mathbf{f} - \begin{bmatrix} \mathbf{P} \\ 0 \end{bmatrix} \right\| \tag{2.24}$$

The described technique enables reconstruction of the integrated spectral absorption coefficient, $K(r)$, from the measured projected absorbance areas, $A_{\text{proj}}(y)$. $K(r)$ can then be utilized as above to obtain radially resolved profiles of temperature and mole fraction, as detailed above, by Eq. 2.18 and Eq. 2.19, respectively, at a single measurement plane.

CHAPTER 3

Axial injector effects on hybrid polymethylmethacrylate combustion assessed by thermochemical imaging

3.1 Introduction

This work compares two canonical hybrid rocket oxidizer injector designs via spatially-resolved measurements of temperature and mole fractions of CO, CO_2, and H_2O within the near-surface reaction layer of a solid-fuel combustion experiment involving polymethyl methacrylate (PMMA) and gaseous oxygen (GOx). In the following sections, the underlying theory and experimental methods are first described, followed by measurement results at several axial positions (fuel grain lengths) with a single-port axial injector design and a multi-port axial showerhead injector design. Two-dimensional thermochemical results are compiled to illustrate the reaction layer spatial evolution. Cold-flow computational fluid dynamics simulations are also performed to compare the initial flow characteristics of the respective injectors, the results of which are used along with hybrid rocket injector theory to interpret the granular measurements.

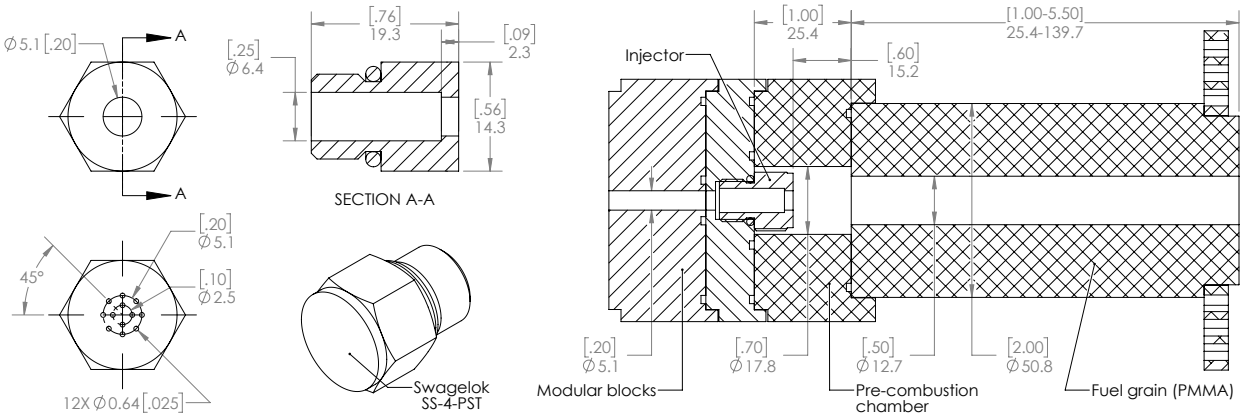

Figure 3.1 Dimensioned drawings for the single-port and axial showerhead injectors alongside a cross-sectional view of the hybrid rocket motor geometry used in all experiments. Units: mm [in.]

3.2 Methods

3.2.1 Injector geometries

Dimensioned drawings of the injectors are provided in Fig. 3.1. These injectors represent a canonical single axial port design and a multi-port axial showerhead design. The single-port injector design is perhaps most common and simple for hybrid rockets and provides a baseline for comparative analysis. The single port design examined here has an inner diameter of 5.1 mm (0.2 in.) expelling a concentric oxidizer jet into the core of the combustion chamber. The showerhead injector design consists of 12 axial ports (d = 0.64 mm (0.025 in.)), evenly distributed about two concentric rings, the outermost ring being at the same diameter as the single-port injector. As mentioned, flow rate through the injectors is controlled by a choked orifice with prescribed back-pressure upstream.

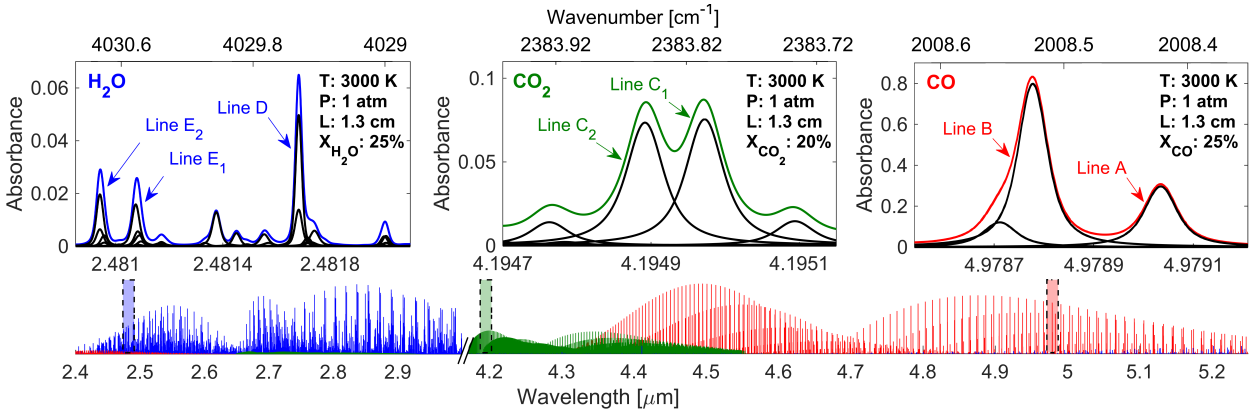

Figure 3.2 Absorbance simulations at representative combustion conditions for CO, CO_2, and H_2O thermochemistry measurements. Individual transitions comprising each feature are shown in black.

3.2.2 Sensing strategy

Wavelength selection for LAS is influenced by the absorption strength, spectral isolation, and temperature sensitivity of the transitions (called *lines*) at the expected flow-field conditions. In order to develop a rigorous sensing approach suitable for a variety of hybrid rocket systems, a range of operating conditions was estimated through thermochemical equilibrium calculations [58, 59] for multiple hybrid rocket fuels (PMMA, HDPE, paraffin, etc.). These results provided upper bounds on the theoretical maximum temperature and species concentrations in the flow-field, which helps in simulating and surveying the rovibrational spectra of the target molecules.

Fig. 3.2 shows simulated spectra of the specific rovibrational lines chosen for CO, CO_2, and H_2O sensing at expected hybrid rocket combustion temperatures and concentrations. For CO and CO_2, the strongest rovibrational transitions with minimal H_2O interference occur in the fundamental bands centered near 4.7 μm and 4.3 μm, respectively. However, in this region, the R-branch of CO and the P-branch of CO_2 interfere significantly with one another near 4.4 μm, making it difficult to target spectrally-isolated transitions. Consequently,

absorption features in the more isolated P-branch of CO near 4.98 μm and R-branch of CO_2 near 4.19 μm were chosen for thermochemistry measurements [60, 61]. The absorption spectra of H_2O, which is present throughout most of the infrared, is strongest at the fundamental vibrational frequencies (important for probing short pathlengths). The fundamental band of H_2O near 2.48 μm offers spectral windows of relatively strong well-isolated transitions suitable for LAS sensing. Line pairs A and B from CO and line pairs D and E_1 plus E_2 from H_2O are utilized to obtain gas temperature in addition to mole fraction distributions of the flow-field. With the temperature field known, CO_2 mole fraction is then obtained through lines C_1 and C_2. The relevant spectroscopic parameters for the selected transitions, as well as associated uncertainties and source databases, are detailed in Table 3.1.

Line	Species	Wavenumber [cm^{-1}]	E'' [cm^{-1}]	S(296 K) [$cm^{-1}/(molec \cdot cm^{-2})$]
A	CO[a]	2008.42	5051.74	$1.149 \times 10^{-28(2)}$
B	CO[a]	2008.53	1901.13	$2.669 \times 10^{-22(1)}$
C_1	CO_2[a]	2382.81	4677.40	$4.659 \times 10^{-27(1)}$
C_2	CO_2[a]	2383.85	4762.90	$3.105 \times 10^{-27(1)}$
D	H_2O[a]	4029.52	2660.94	$4.570 \times 10^{-24(1)}$
E_1	H_2O[b]	4030.48	7193.51	$3.285 \times 10^{-34(3)}$
E_1	H_2O[b]	4030.49	5949.22	$2.019 \times 10^{-31(3)}$
E_1	H_2O[a]	4030.50	4902.61	$9.679 \times 10^{-29(3)}$
E_2	H_2O[b]	4030.70	8916.25	$4.788 \times 10^{-37(4)}$
E_2	H_2O[a]	4030.73	4889.49	$1.154 \times 10^{-28(3)}$

[a] Values taken from HITRAN 2016 [**?**]

[b] Values taken from HITEMP 2010 [8]

Uncertainty codes: $^{(1)}$1–2%, $^{(2)}$2–5%, $^{(3)}$10–20%, $^{(4)}$>20%

Table 3.1 Spectroscopic parameters for targeted CO, CO_2, and H_2O transitions

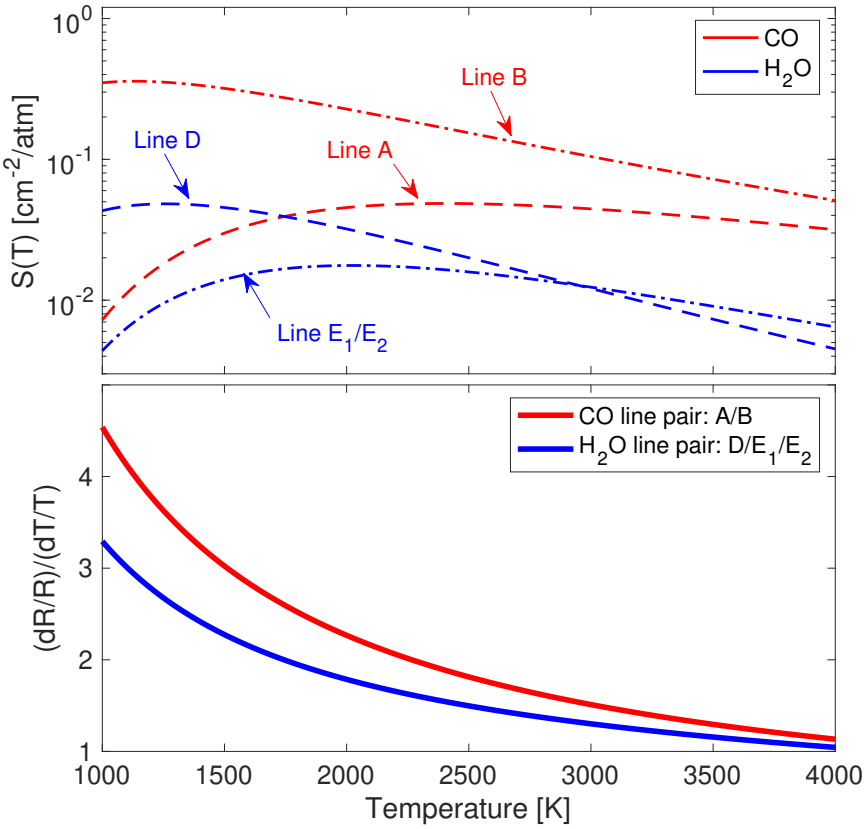

Figure 3.3 Linestrength, $S(T)$, and temperature sensitivity, $(\mathrm{d}R/R)/(\mathrm{d}T/T)$, as a function of temperature for the CO and H_2O line pairs used in this study.

As discussed previously, the temperature distribution of the flow-field is obtained through CO and H_2O absorption. In order to assess the temperature sensitivity of the line pairs, the linestrengths, $S(T)$, of each transition are plotted in Fig. 3.3.

It should be noted that the linestrengths of line E_1 and line E_2 exhibit a very similar temperature dependence; therefore, to simplify the analysis and increase the robustness of the thermometry measurement, the two values were summed and treated as a single transition (i.e. line group E). The same procedure was done for line C_1 and line C_2 (line group C). The temperature sensitivity, $(\mathrm{d}R/R)/(\mathrm{d}T/T)$, of each line pair was evaluated numerically through Eq. 4.3 over the temperature range of interest. The large difference in lower state energies, $\Delta E''$, between the paired transitions (shown in Table 3.1) results in high

temperature sensitivity at the expected combustion temperatures, reducing the uncertainty of the resulting profiles obtained from tomographic reconstruction [62].

3.2.3 Testing procedure

All of the light sources in this study were scanned in wavelength by modulating the injection current at a frequency of 2 kHz using a sawtooth waveform, as seen in Fig. 3.4. In order to correct for thermal emission during the experiment, each laser was also scanned below its lasing threshold to provide a baseline for the detector. A germanium etalon with a free spectral range of 0.0231 cm^{-1} was used to find the relative frequency in the time domain. Data were collected on a data acquisition card (NI PXI-6115) at a sample rate of 2.5 MHz with every 100 scans binned for averaging and statistical analysis. For a translational motion of 5 mm/s, this yields an effective sample resolution of 0.25 mm in the radial direction (half the beam diameter). Thus, the radial spatial resolution can be approximated by the beam diameter.

Fig. 3.4 illustrates representative transmitted, I_t, and incident intensities, I_0, recorded on each detector. In order to measure I_0 appropriately, background measurements were taken while horizontally translating the test stand—as is done during a hot-fire test—and purging N_2 gas through the fuel grain. These background measurements effectively correct for ambient water vapor and/or CO_2 present in the targeted flow field that would otherwise interfere with the transmitted intensity. It should be noted that the selected absorption lines are weakly active at room temperature, thus having little ambiguity when measured in the high-temperature combustion exhaust. Data collection and horizontal translation during a hot-fire test commenced once a repeatable quasi-steady-state was reached (typically < 1 s after ignition). The system was translated 30 mm to ensure measurements over the full combustion zone and aid tomographic reconstruction efforts. Transient effects inherent to hybrid combustion systems were found to be negligible during the measurement time. This, along with test repeatability, is discussed further in [6].

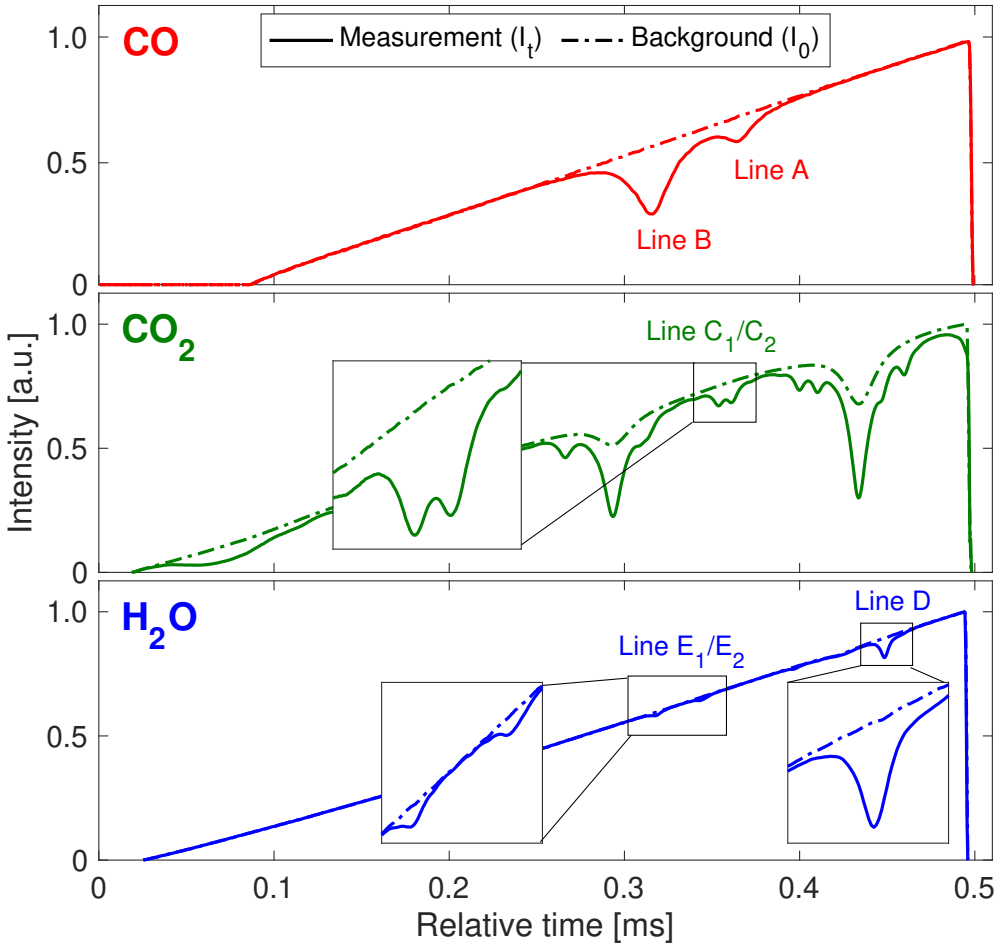

Figure 3.4 Representative direct-absorption scans for targeted CO, CO_2, and H_2O transitions, I_t. The dashed lines indicate the background signals, I_0, taken with the flame off and a N_2 purge through the fuel-grain core.

3.2.4 Spectroscopic data processing

This subsection outlines the process used to convert the line-of-sight absorption data into radially-resolved profiles of the integrated spectral absorption coefficient, $K(r)$, from which the temperature and species profiles can then be extracted [52, 53, 63, 64]. The flame is assumed to be axially-symmetric to enable reconstruction of the flow-field from a single projection angle [48] using a regularized Abel transform [52, 6]. This one-dimensional strategy is

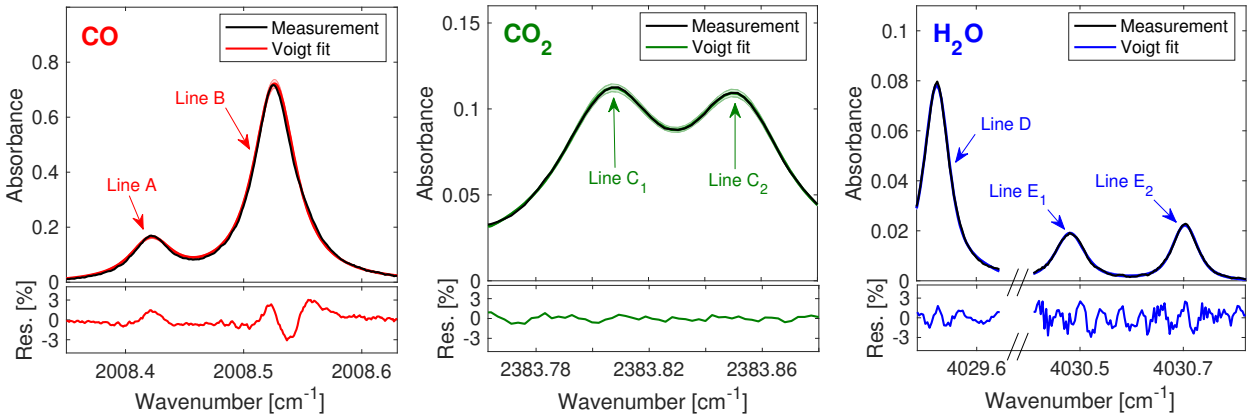

Figure 3.5 Measured absorbance averaged over 100 scans versus wavenumber. The corresponding Voigt fits illustrate a 95% confidence interval of the measured data. Reasonable residuals for each fit confirm appropriateness of a Voigt line shape model.

implemented at multiple axial positions downstream of the injector (by way of using differing fuel grain lengths) to obtain two-dimensional images [52, 53, 64, 6].

The key data processing steps from line-of-sight absorption measurement to temperature and species inference are shown in Fig. 3.6 at a representative axial position. The measured absorbance, $\alpha(\nu)$, was obtained through Eq. 2.2 using the incident and transmitted light intensities. A Voigt line-shape function was least-squares fit to the targeted lines over the absorbance spectra. The absorbance results were averaged (over 100 laser scan periods) prior to calculating the projected absorbance areas, $A_{\text{proj}}(y)$, through Eq. 2.17. The aforementioned mechanical translation of the vertical test stand enabled spatial resolution, plotted here as a function of distance, y, from the center of the fuel grain or gaseous core ($y = 0$ mm). $A_{\text{proj}}(y)$ measurements across the full reaction zone were mirrored and averaged about the fuel grain center to confirm axisymmetry. Afterwards, a Tikhonov-regularized Abel inversion scheme was implemented to transform the $A_{\text{proj}}(y)$ distributions into radially-resolved profiles of the integrated absorption coefficient, $K(r)$. Temperature for H_2O and CO (when sufficiently abundant) was extracted from each radial $K(r)$ value through Eq. 2.18 and, thereafter, mole fraction for each species was found from Eq. 2.19 to get the complete radially-resolved

thermochemical flow-field.

A few additional details and assumptions are notable in the laser absorption tomography data processing. To implement the spectral fitting, the Doppler width, $\Delta\nu_D$, was fixed corresponding to a temperature estimate from chemical equilibrium. $A_{\text{proj}}(y)$ and the collisional width, $\Delta\nu_C$, were set as free parameters and were solved for using the temperature estimate. This determined $A_{\text{proj}}(y)$ was then used to calculate a path-integrated temperature using the two-line thermometry technique shown in Eq. 2.18 and the Doppler width was recalculated using this new temperature. This process was iterated upon until the resulting temperature converged. It should be noted that the transition line-shapes are not expected to perfectly correspond to a Voigt profile due to overlapping transitions and thermochemical gradients along the line of sight; however, Voigt line fitting proved to be a sufficient method for recovering the projected line areas with a relatively low residual error [64, 52]. A Voigt fit over the measured absorbance for the pair of targeted CO lines is shown in Fig. 3.6. The fractional residuals were typically less than 3% for CO, less than 2% for CO_2, and less than 3% for H_2O. From the fitted absorbance spectra, the projected absorbance areas, $A_{\text{proj}}(y)$, were determined for each height of PMMA fuel grain to attain two dimensional images,

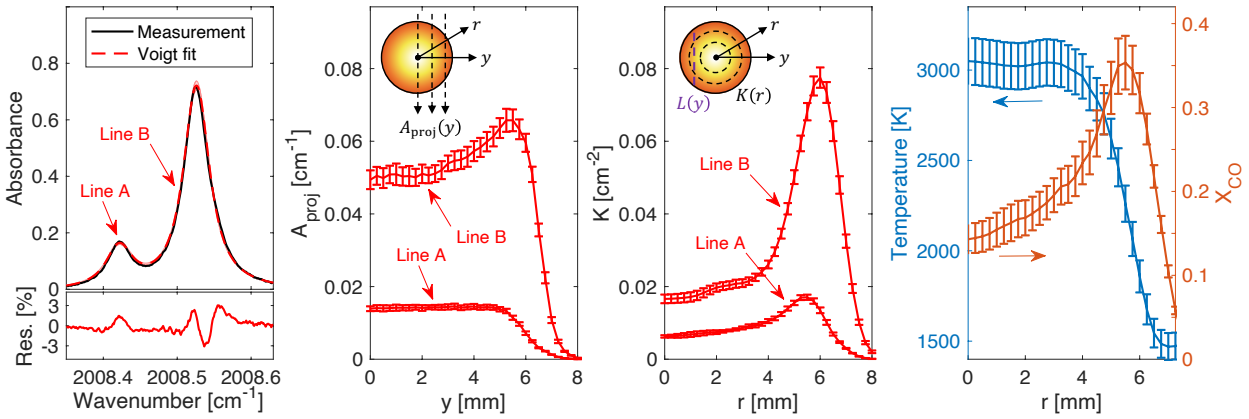

Figure 3.6 *From left to right*: Measured CO absorbance with a Voigt line-shape fit, A_{proj} versus distance y from the center of the fuel grain, Abel-inverted radially-resolved K, and the resulting planar thermochemistry distributions

representing a snapshot of the spatially-evolving reaction zone.

3.2.5 Fuel regression analysis

In addition to the optical measurements, the total burn time and post-test fuel grain mass were used to calculate fuel regression rate, effective mass fluxes, and oxidizer-to-fuel ratio. For a fuel-grain with a circular port geometry, as used in this study, the space-time averaged regression rate, $\bar{\dot{r}}$ [mm/s], during a hot-fire can be determined as follows:

$$\bar{\dot{r}} = \frac{\bar{\dot{m}}_f}{\pi \rho_f L_f \bar{D}} = \frac{\bar{D}_f - D_i}{2t_b} \tag{3.1}$$

where ρ_f [g/mm^3] is the density of the fuel (11.85 g/mm^3 for the PMMA used), L_f [mm] is the length of the fuel grain, and $\bar{\dot{m}}_f$ [g/s] is the space-time averaged fuel mass flow rate, which can be determined by dividing the total consumed fuel mass, ΔM_f [g], by the total burn time, t_b [s]. $\bar{D}$ [mm] is the space-time averaged port diameter given by the initial and average final port diameters, D_i [mm] and $\bar{D}_f$ [mm], respectively [32]:

$$\bar{D} = \frac{D_i + \bar{D}_f}{2} \tag{3.2}$$

Previous works [65] have found that $\bar{D}_f$ can be most accurately estimated based on the total consumed fuel mass, ΔM_f, measurements:

$$\bar{D}_f = \sqrt{D_i^2 + \frac{4\Delta M_f}{\pi \rho_f L_f}} \tag{3.3}$$

In addition to the average final port diameter, $\bar{D}_f$, it is often of interest to also compare dimensional measurements of the fuel-grain port diameter at the aft end of the oxidizer injector. This was conducted for each fuel-grain length and the reported diameter is referred to as D_{L_f}. It is important to note that Eqs. 3.1–3.2 assume a constant regression rate around the circumference of the fuel-grain port at any given axial location. This is a well-accepted approximation for fuel-grains with circular ports, but loses validity when considering other geometries.

With knowledge of the space-time averaged port diameter, the space-time averaged oxidizer mass flux, $\bar{G}_{ox}$ [g/mm^{2}s], and the space-time averaged total mass flux, $\bar{G}$ [g/mm^{2}s], can also be determined:

$$\bar{G}_{\text{ox}} = \frac{4\dot{m}_{ox}}{\pi \bar{D}^2} \tag{3.4}$$

$$\bar{G} = \frac{4(\dot{m}_{ox} + \bar{\dot{m}}_f)}{\pi \bar{D}^2} \tag{3.5}$$

where $\dot{m}_{ox}$ [g/s] is known through the use of a calibrated choked orifice as discussed in Sec. 1.5.1. Although the focus of this work was not to characterize regression rate behavior, Eq. 3.1 and Eq. 3.4 can be used to determine the empirical constants found in Eq. 3.1 that govern hybrid rocket performance for a given propellant combination and motor design.

Another key parameter in assessing combustion performance is the propellant O/F ratio. The space-time averaged O/F ratio can be calculated through the oxidizer and fuel mass flow rate measurements:

$$\text{O/F} = \frac{\dot{m}_{ox}}{\bar{\dot{m}}_f} \tag{3.6}$$

Determination of the O/F ratio provides a parameter to estimate combustion product composition through chemical equilibrium calculations. Since Eq. 3.6 involves space-time averaged parameters ($\bar{\dot{m}}_f$), different O/F values are reported depending on the total integration time being considered. In this study, two integration times were considered, the total burn time, t_b, which accounts for the full hot-fire burn, and the total measurement time, t_m, which provides a more appropriate reference condition for the spectroscopic measurements. A summary of all the experimental conditions including the aforementioned parameters are reported in Table 3.2, with detailed discussion in the following section.

3.3 Results and discussion

To quantitatively evaluate the influence of oxidizer injector design on PMMA/GOx combustion, planar thermochemistry measurements (T, CO, CO_2, H_2O) were conducted over

a range of fuel-grain lengths for two injector geometries. Planar measurements were then compiled into two-dimensional images to better highlight the spatial evolution of the solid-fuel reaction layer. This section details the results obtained from the spectroscopic sensing and discusses the observed trends in combustion behavior that arise from varying injector design. In addition, the experimental measurements are complimented with cold-flow computational fluid dynamics (CFD) simulations to help visualize the initial flow structure and identify mechanisms that result in variable combustion performance.

3.3.1 Planar thermochemical measurements

Planar temperature and species measurements were conducted for fuel-grain lengths varying from 25.4–139.7 mm (1–5.5 in.) in 12.7 mm (0.5 in.) increments. The individual test details for both injector designs are summarized in Table 7.1. As discussed in Sec. 3.2.4, radially-resolved temperature fields were reconstructed for each fuel-grain length using multiple spectral transitions from H_2O and CO (illustrated in Fig. 3.2). With a known temperature distribution for each fuel-grain length, radially-resolved species profiles for CO, CO_2, and H_2O were also obtained.

Fig. 3.7 shows the radial spatial evolution of the temperature field for both injector designs at multiple downstream distances. We note again that $r = 0$ mm corresponds to the core of the cylindrical axisymmetric flow. The radial distance associated with the boundary of the gaseous core and fuel grain surface involves some ambiguity due to phase-change and the lack of combustion products in the initial fuel pyrolysis, but is estimated to be within 0.5–1 mm of the termination of the data array, supported by post-test measurements of grain diameter. The right side of Fig. 3.7 plots equilibrium temperature versus equivalence ratio, ϕ, for PMMA/GOx combustion at atmospheric conditions for reference. While equivalence ratio is determined globally by the fixed oxidizer mass flux and corresponding burn rate, it is expected that the developing reaction layer is characterized by a range of local equivalence ratios as discussed in Sec. 1.3.1 Of most immediate note, we observe that the maximum

expected equilibrium temperature over the range of ϕ ($T_{eq} \approx 3060$ K), matches very well with the local maxima of each radial profile, with the exception of the lowest axial distances for the single-port injector, wherein the combustion zone appears to be developing and is likely diluted. For both injector designs, there is a progressive shift of the local maximum temperature towards the core with increasing axial distance, representative of radial diffusion and mixing. However, the two injectors exhibit distinct radial profiles, with higher core temperatures (at $r = 0$ mm) observed at much shorter axial distances for the showerhead injector relative to the single-port injector, suggesting that the core flow remains lean for the single-port at longer axial distances.

A similar planar comparison is shown in Fig. 3.8, which depicts respective radially-resolved CO, CO_2, and H_2O species measurements for both injector geometries over a range of fuel-grain lengths. Similar to the temperature fields, all product species appear to diffuse radially inward with increasing axial length. When comparing the two injector designs, the showerhead injector shows an increased presence of combustion species in the core of the flow-field at any given axial distance, while the species distributions for the single-port injector

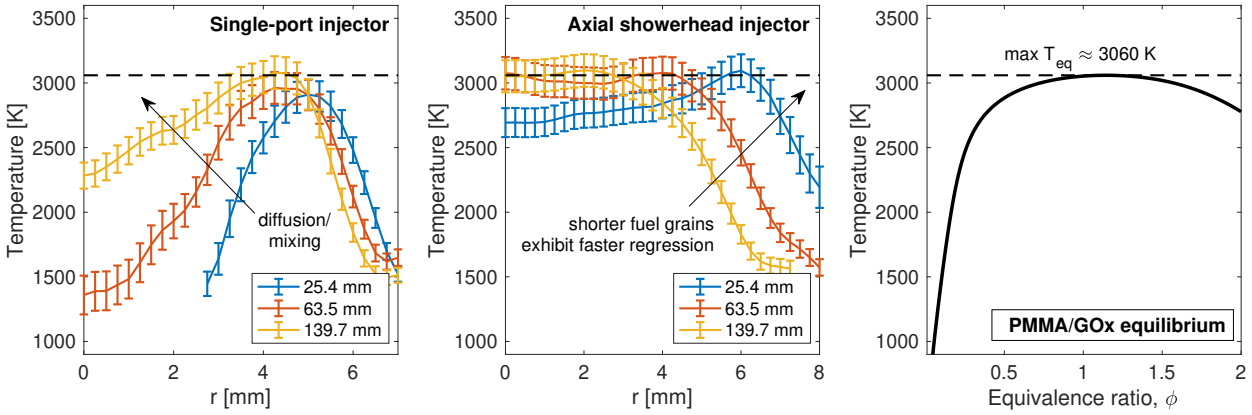

Figure 3.7 Measured temperature versus radial distance from the fuel-grain center ($r = 0$) for the single-port (*left*) and axial showerhead (*middle*) injectors. Chemical equilibrium temperature for PMMA/GOx combustion versus equivalence ratio, ϕ (*right*)

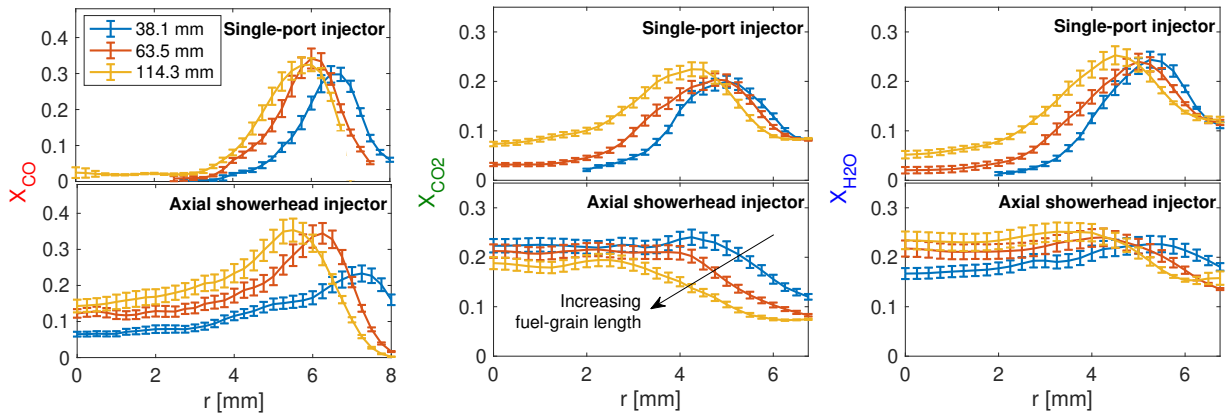

Figure 3.8 Species mole fraction measurements for CO (*left*), CO_2 (*middle*), and H_2O (*right*) versus radial distance, r, from the fuel grain center ($r = 0$ mm) at three axial positions

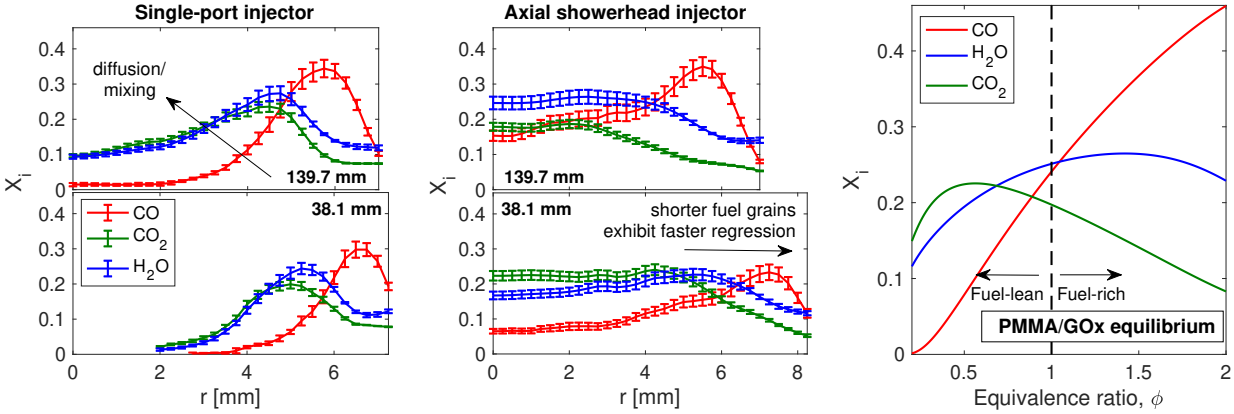

Figure 3.9 Comparison of mole fraction measurements for the single-port (*left*) and axial showerhead (*middle*) injectors. Chemical equilibrium mole fraction composition versus equivalence ratio, ϕ, for PMMA/GOx combustion (*right*)

peak closer to the fuel surface. The relative magnitudes of the species mole fractions are also notable. For CO and H_2O, the peak mole fraction and width of the distribution tends to increase with increasing fuel-grain length. This trend is similar for CO_2 with single-port injection, but differs with the showerhead design. Though the radial distribution of CO_2 for the showerhead injector suggests a high relative abundance, peak CO_2 mole fraction is

observed to decrease as fuel-grain length increases.

Quantitative mole fractions can be compared with the equilibrium values at varying equivalence ratios, shown in Fig. 3.9. We first note that the mole fraction magnitudes for all measurements are within the range expected from chemical equilibrium. The species measurements for the single-port injector well-represent a radial distribution of varying local equivalence ratios, with a fuel-lean region in the core due to high oxidizer dilution and a fuel-rich region closer to the fuel-grain surface. Approaching the fuel-grain surface, CO peaks and higher concentrations of H_2O are present when compared to CO_2, as anticipated from fuel-rich chemical equilibrium. Towards the oxidizer core, CO_2 and H_2O peak and CO decreases as it is oxidized to CO_2. Within the core of the flow, combustion is sufficiently fuel-lean such that CO fully oxidizes and CO_2 mole fraction surpasses H_2O. This cross-over (CO_2 mole fraction exceeding H_2O mole fraction) is observed in the chemical equilibrium simulation at an equivalence ratio of approximately $\phi = 0.65$. All product species are further diluted by oxygen in the core flow. When comparing the two fuel-grain lengths (38.1 mm and 139.7 mm) using the single-port injector, the species-distribution is observed to behave very similarly, albeit with slightly higher peak magnitudes and a distribution shift towards the core at the longer axial position. The cross-over of the CO and H_2O mole fractions, which corresponds to near stoichiometric fuel to oxidizer balance ($\phi = 1$), shifts from $r = 6$ mm at $x = 38.1$ mm to $r = 5$ mm at $x = 139.7$ mm.

For the axial showerhead injector, the radial variation of species (at the same axial distances) is considerably diminished relative to the single-port injector distributions. This is most evident in the core of the flow ($r = 0 - 4$ mm), where the species concentrations are relatively constant. Some radial variation remains near the fuel-grain boundary. The showerhead injector flow-field reveals a more distinct axial change in mole fractions. Specifically, the CO and H_2O mole fraction distributions increase in magnitude, while CO_2 mole fraction decreases with increasing fuel-grain length. This is consistent with a reduction in the global O/F as the fuel-grain length increases due to additional fuel regression and constant oxidizer

mass flow rate, as similarly noted in the measured space-time averaged O/F values in Table 3.2. Lastly, we note that the radial scales for the plots in Fig. 3.9 are different, reflecting greater aggregate fuel regression with the showerhead injector and a larger axial variation in regression rate.

The uncertainties in the temperature and mole fraction profiles have been determined by propagating systematic uncertainties in spectral properties (i.e. linestrength) and using a 95% confidence interval on the measured absorbance. Further details on the calculation of uncertainties for thermometry and species sensing are discussed in the Appendix of Wei et al. [52]. Typical temperature uncertainties were approximately ±75 K near the fuel-grain wall and up to ±125 K near the core, while typical mole fraction uncertainties were approximately 5% near the fuel grain wall and up to 10% near the core.

3.3.2 Two-dimensional thermochemical images

To better visualize the thermochemical structure of the reaction layer, planar measurements were assembled to form two-dimensional images, illustrated in Fig. 3.10. Spatially-resolved temperature and species (CO, CO_2, H_2O) are shown for both the single-port injector and the axial showerhead injector. As previously mentioned, the two test cases were conducted at the same oxidizer mass flow rates to isolate the influence of injector design. Additionally, all temperature and species images are shown on the same scale for purposes of comparison.

Dramatic differences between the thermochemical flow-fields of the two injectors can be readily observed. Consistent with the planar measurements shown in Fig. 3.7 and Fig. 3.8, the two-dimensional images for the single-port injector indicate that the temperature in the core of the flow stays relatively low (compared to the peak temperature) and nearly all the species are contained in the thin boundary layer region near the fuel surface. Over the range of lengths considered here, most of the chemical reaction occurs in this region, which grows in width and shifts slightly towards the core as axial distance increases, consistent with Fig. 1.2 and Fig. 1.5. The relatively cool core and lack of combustion product species near

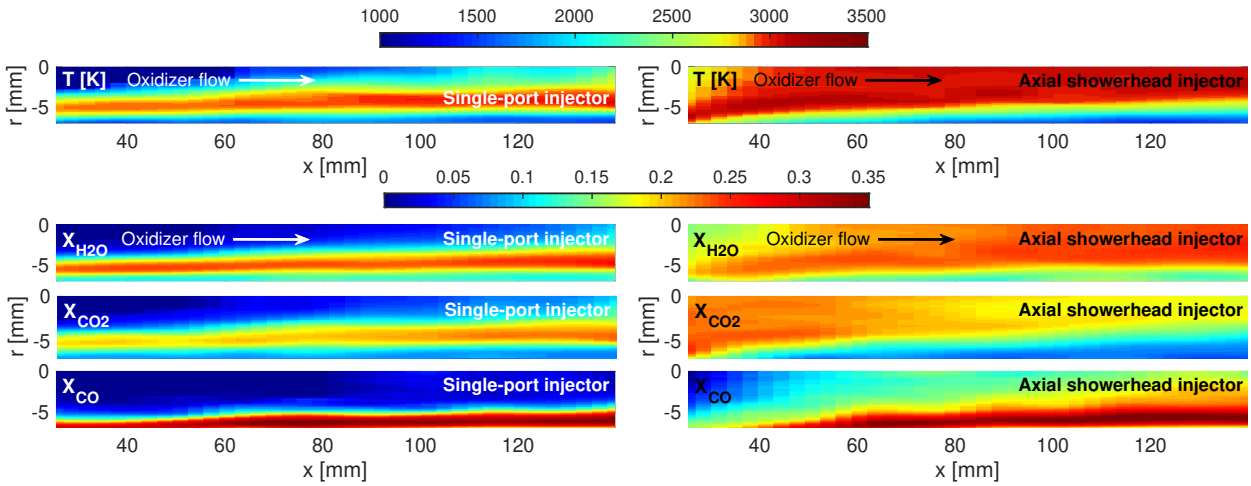

Figure 3.10 Two-dimensional thermochemistry measurements demonstrating PM-MA/GOx combustion progression along the axial direction for the single-port (*left*) and axial showerhead injectors (*right*).

$r = 0$ mm indicates that much of the oxidizer propellant is not participating in the reaction even at the furthest axial distance. Conversely, the axial showerhead injector achieves a core temperature near the maximum equilibrium temperature at a relatively short fuel-grain length ($x < 50$ mm) and it is sustained throughout the rest of the axial distance. An axial progression of O/F from fuel-lean to fuel-rich is noticeably evident. At lower fuel-grain lengths where the O/F is high (fuel-lean), CO_2 mole fraction dominates, followed by H_2O and trace amounts of CO. As combustion progresses and fuel is added axially, the O/F reduces and the concentration of CO_2 decreases while concentrations of both H_2O and CO continue to increase. The incremental addition of CO appears primarily from radial diffusion. It should also be noted that as the highly fuel rich near-surface boundary layer grows, the lowest temperatures are seen near the wall.

In aggregate, these results provide a comprehensive spatial perspective on combustion progress and efficiency, and reveal stark variations associated with oxidizer injector design. As combustion proceeds in the hybrid rocket geometry, a greater portion of the temperature distribution in the gaseous core flow more uniformly approaches the expected equilibrium

temperature, reflective of the chemical to thermal energy conversion. The initial radial gradients in species and temperature associated with equivalence ratio variation in the boundary layer transition to predominantly axial gradients that depend on fuel regression, with this transition likely a function of the intensity of turbulence-induced radial diffusion. Accordingly, the downstream distance at which complete combustion of PMMA/GOx occurs with respect to the axial O/F ratio is characteristic to a specific oxidizer injection design. For the geometric designs and propellants evaluated in this study, the results suggest that an axial showerhead injector is clearly advantageous to a single-port injector regarding combustion efficiency per unit axial distance.

3.3.3 Fuel regression measurements

In addition to the preceding spectroscopic results, fuel regression rate and O/F ratio were also measured to assess and compare combustion performance between the two injector geometries. As mentioned previously, these results are reported in Table 3.2 and their associated uncertainties are detailed in Appendix A. The total consumed fuel mass, ΔM_f, was calculated by measuring the mass of each fuel-grain before and after each hot-fire. Comparing these values indicate that, on average, the single-port injector resulted in $\sim 54\%$ less fuel consumption than the axial showerhead injector for similar burn times, t_b, and equivalent oxidizer mass flow rates. Since space-time averaged regression rates are directly measured using the total consumed fuel mass and burn time, these values exhibit a similar trend. This is illustrated in Fig. 3.11, which compares the measured space-time averaged regression rates, $\bar{\dot{r}}$, for different axial distances, x, between the two injector designs. As shown, the fuel-grain regresses approximately twice as much, at every axial location, when using the showerhead injector design. Additionally, $\bar{\dot{r}}$ is observed to generally decrease with increasing axial distance, which can be attributed to a decrease in available oxygen from the ongoing reaction. Similar regression rate behavior for different axial distances has been observed in other works [3, 29].

Test no.	L_f [mm]	D_i [mm]	D_{L_f} [mm]	$\bar{D}$ [mm]	t_b [s]	ΔM_f [g]	$\bar{\dot{r}}$ [mm/s]	$\bar{G}_{ox}$ [kg/m^{2}s]	$\bar{G}$ [kg/m^{2}s]	O/F$\|_{t_b}$	O/F$\|_{t_m}$
Single-port injector											
1	139.7	12.7	13.7	13.4	8.31	4.7	0.082	8.53	12.55	2.12	2.14
2	127.0	12.7	13.8	13.5	8.94	4.8	0.084	8.44	12.22	2.24	2.30
3	114.3	12.7	13.8	13.5	8.02	4.7	0.102	8.36	12.44	2.05	2.10
4	101.6	12.7	13.8	13.5	8.50	3.9	0.090	8.42	11.65	2.62	2.68
5	88.9	12.7	13.8	13.5	8.34	3.6	0.097	8.37	11.38	2.78	2.85
6	76.2	12.7	14.0	13.5	8.51	3.2	0.098	8.34	10.95	3.19	3.27
7	63.5	12.7	14.0	13.5	8.36	2.7	0.101	8.33	10.57	3.72	3.81
8	50.8	12.7	14.3	13.7	9.45	2.5	0.103	8.17	9.97	4.54	4.68
9	38.1	12.7	14.3	13.6	8.50	1.8	0.110	8.22	9.67	5.67	5.82
10	25.4	12.7	14.7	13.9	9.56	1.5	0.120	7.97	9.01	7.65	7.96
Axial showerhead injector											
11	139.7	12.7	13.8	14.0	8.75	9.8	0.154	7.75	14.98	1.07	1.09
12	127.0	12.7	13.9	14.1	8.49	9.1	0.161	7.72	14.61	1.12	1.16
13	114.3	12.7	14.2	14.2	8.74	9.0	0.170	7.59	14.11	1.17	1.21
14	101.6	12.7	14.1	14.1	7.45	7.5	0.189	7.68	14.12	1.19	1.20
15	88.9	12.7	14.4	14.3	8.28	7.8	0.198	7.43	13.26	1.27	1.32
16	76.2	12.7	14.9	14.5	8.47	7.2	0.208	7.31	12.48	1.41	1.46
17	63.5	12.7	15.3	14.6	8.64	6.6	0.221	7.15	11.71	1.57	1.61
18	50.8	12.7	16.5	15.0	9.76	6.4	0.234	6.81	10.53	1.83	2.04
19	38.1	12.7	17.0	14.9	9.09	4.6	0.241	6.89	9.80	2.37	2.53
20	25.4	12.7	17.8	14.8	9.23	3.0	0.232	6.93	8.81	3.69	3.97

Table 3.2 Summary of the experimental results from fuel regression analysis for PMMA/GOx combustion studies

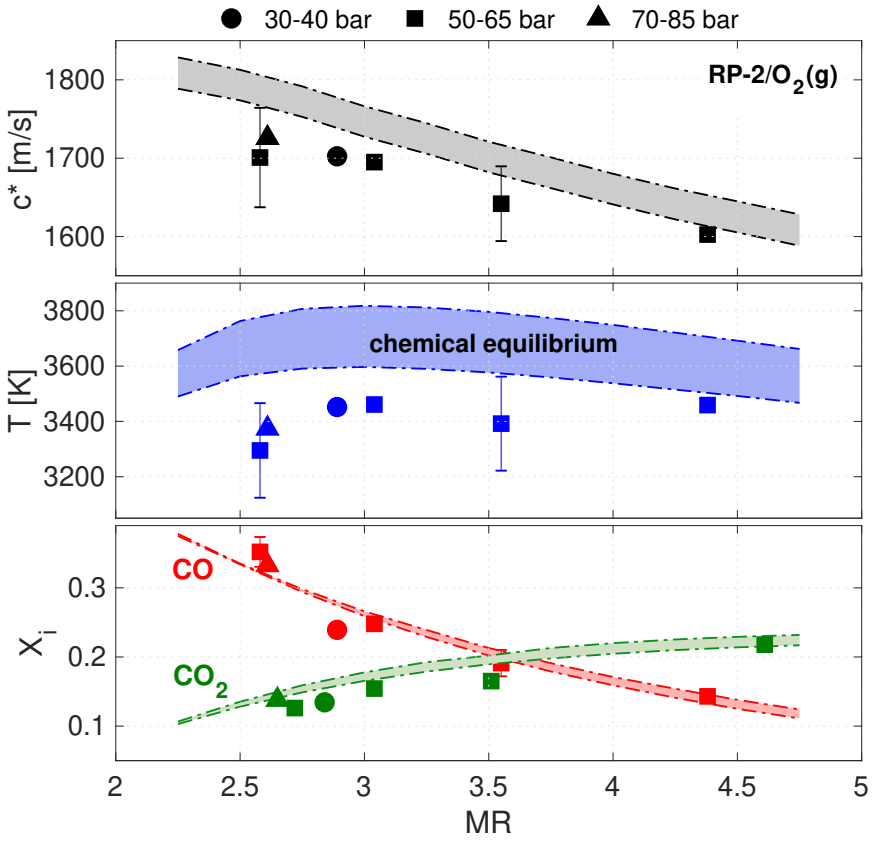

Figure 3.11 Measured space-time averaged regression rates, $\bar{\dot{r}}$, for both the single-port and axial showerhead injector geometries over the range of fuel-grain heights considered

In addition to fuel burn rates, another key parameter for evaluating combustion performance is the propellant O/F ratio, which was inferred from complimentary measurements of oxidizer mass flow rate. The experimental O/F values can be compared to stoichiometric conditions, which for PMMA/GOx is $\mathrm{O/F}|_{\mathrm{stoic}} = 1.92$, to determine fuel-rich or fuel-lean combustion. Space-time averaged O/F was calculated using oxidizer and fuel mass flow rate measurements over two integration times, the total burn time, t_b, and the total spectroscopic measurement time, t_m, with the latter being a more relevant reference to the optical measurements. As previously discussed, the axial showerhead injector resulted in more total fuel consumption over a given time frame. Accordingly, the reported space-time averaged

O/F values for the single-port injector are consistently higher for the axial distances considered. Specifically, for the single-port injector, the global O/F values during the measurement time range from O/F = 7.65 at the shortest axial distance to O/F = 2.12 at the longest. As a result, the global reaction over all axial distances can be considered fuel-lean when compared to stoichiometric conditions. Conversely, the axial showerhead injector exhibited higher fuel-grain regression, which lowered the measured O/F values from O/F = 3.69 at the shortest axial distance to O/F = 1.07 at the longest. Since $\mathrm{O/F}|_{\mathrm{stoic}} = 1.92$, the global reaction transitions from fuel-lean to fuel-rich with increasing distance and the stoichiometric condition being attained between $x = 38.1$–50.8 mm (1.5–2 in.).

These reported combustion parameters provide an additional means of evaluating the aggregate performance and efficiency of the oxidizer injector designs considered in this work. The axial showerhead injector showed higher regression rates and O/F ratios closer to stoichiometric conditions, indicative of higher combustion performance. These observations are consistent with the thermochemical imaging results presented in Sec. 3.3.1 and Sec. 3.3.2. Specifically, the transition from fuel-rich to fuel-lean in the axial showerhead injector is evident in the measured mole fraction results shown in Fig. 3.10.

3.3.4 Injector cold-flow CFD

To assist in the interpretation of the experimental results, a numerical study using computational fluid dynamics methods was conducted in ANSYS Fluent 2020 for the two injector geometries considered in this work. ANSYS Fluent is a commercial CFD software that uses a finite volume solver with cell-centered variable agreement. Non-reacting (cold-flow), single-phase gas simulations were performed to better understand the oxidizer fluid dynamics in the pre-combustion zone. This complimentary analysis proved useful for investigating differences in the initial flow structure (via pathlines and velocity contours) exiting the injector and resulting shear stress on the fuel grain walls due to the different oxidizer injector designs.

The CFD setup consisted of the fluid domain confined by the oxidizer delivery line, in-

jector, pre-combustion chamber, and initial portion of the fuel grain, as illustrated in Fig. 3.1. A mesh convergence study (See Appendix D) was conducted to determine a suitable grid coarseness for accurate simulations for both injectors. The inlet boundary condition was defined by the known oxidizer mass flow rate (1.2 g/s) and the outlet boundary condition was set to atmospheric pressure (101,325 Pa). Oxygen gas at room temperature was used for the fluid medium with constant property values including viscosity (2.05×10^{-5} kg m^{-1} s^{-1}), density (1.29 kg/m^3), and thermal conductivity (0.0246 W/m-K). Inlet turbulence intensity was prescribed as 5 percent. For this study, we employed a pressure-based coupled solver, which uses pressure as a mapping parameter for satisfying the incompressibility requirement which then updates the velocity, pressure, and mass flux for the following iteration until solutions converge. This solver type is suitable for simulations over a large range of incompressible to high-speed compressible flows [66]. Hybrid initialization is used to find an initial solution to the velocity and pressure fields by using Laplace's equation with the inlet boundary condition.

ANSYS Fluent employs the Reynolds-averaged Navier-Stokes (RANS) equations. Assuming incompressible flow, as shown in Eq. 3.7, the RANS mean flow equations reduce to Eq. 3.8 [67], in which repeated indices imply summation.

$$\frac{\partial u_i}{\partial x_i} = 0 \tag{3.7}$$

$$u_i \frac{\partial u_i}{\partial x_j} - \frac{\partial \tau_{ij}}{\partial x_j} + \frac{\partial P}{\partial x_i} = 0 \tag{3.8}$$

where u_i are the velocity components, P is the pressure, and the viscous stress tensor τ is defined by:

$$\tau_{ij} = (\nu + \nu_t) \left(\frac{\partial u_i}{\partial x_j} + \frac{\partial u_j}{\partial x_i} \right) \tag{3.9}$$

where ν is the kinematic viscosity and ν_t is the turbulent viscosity.

For each injector geometry, steady-state simulations were conducted with the k-ω Shear Stress Transport (SST) turbulence model. The model is based on a blending function that activates the k-omega model near the walls and the k-epsilon model away from the walls to exploit the benefits and accuracy of each solver. The two turbulence model partial differential equations complete the system of state equations. Such equations for the general form of the two-equation model are shown below in Eqs. 3.10 and 3.11 [68].

$$u_j \frac{\partial k}{\partial x_j} - \frac{\partial}{\partial x_j}\left([\nu + \sigma_k \nu_t]\frac{\partial k}{\partial x_j}\right) - A + \beta^* \omega k = 0 \tag{3.10}$$

$$u_j \frac{\partial \omega}{\partial x_j} - \frac{\partial}{\partial x_j}\left([\nu + \sigma_\omega \nu_t]\frac{\partial \omega}{\partial x_j}\right) - \gamma \frac{\partial u_i}{\partial x_j}\left(\frac{\partial u_i}{\partial x_j} + \frac{\partial u_j}{\partial x_i}\right) + \beta\omega^2 - 2(1 - F_1)\frac{\sigma_{\omega_2}}{\omega}\frac{\partial k}{\partial x_j}\frac{\omega}{\partial x_j} = 0 \tag{3.11}$$

where ρ is the density, ν is the kinematic viscosity, μ_t is the turbulent viscosity coefficient, F_1 is the blending functions specific to the model, A is a function of k and β, β^*, σ_ω, σ_k, and γ are constants. Full details on this turbulence model can be found in [69] and [67].

Fig. 3.12 shows the results for both injectors using the setup described above. The top contours show the flow-field velocity magnitude, defined by the contributions of the axial, radial, and tangential components. For the single-port injector, the flow velocity adjacent to the pre-combustion chamber and the fuel-grain walls is negligible in comparison to the magnitude in the core oxidizer flow. Whereas, with the showerhead injector, higher velocities are present throughout the pre-combustion chamber and into the fuel grain, implying greater levels of shear-induced mixing and more velocity components in the off-axial directions. This can be directly related to the higher cross-sectional perimeter-to-area ratio associated with a large number of small axial ports/jets (i.e. showerhead) compared to a single axial port/jet geometry. As observed in the pathline structures, there is a recirculation zone present in both injector designs that is predominantly contained within the pre-combustion chamber. This flow-field feature is consistent with what is expected based on previous experimental results and theory (discussed in Section 1.3.1). Based on these simulation results, it is expected that the recirculation zones for both injectors only minimally extend past the axial

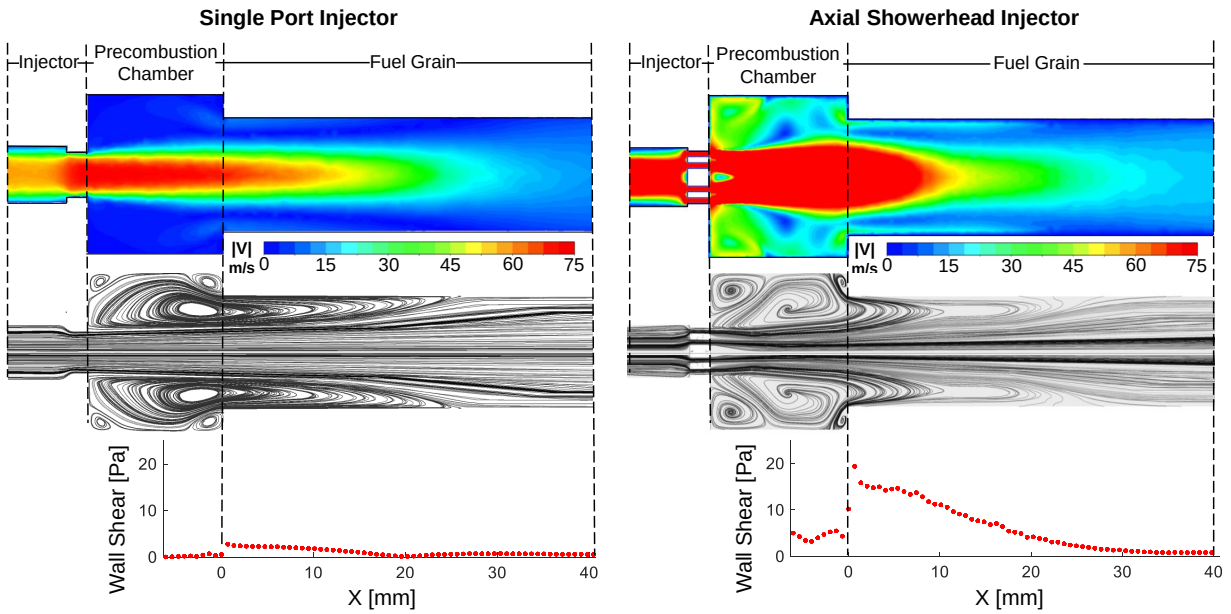

Figure 3.12 Non-reacting (cold-flow) CFD simulation results showing velocity contours, pathlines, and wall shear stress for the single-port injector (*left*) and the axial showerhead injector (*right*)

location where the first spectroscopic measurements are taken ($x \sim 25.4$ mm). In other words, the thermochemistry measurements presented in this work should be largely within the downstream boundary layer development region, previously shown in Fig. 1.2.

To connect the CFD results to the burn characteristics, wall shear stress can be viewed as an indicative metric of initial fuel-grain regression. Fig. 3.12 shows that for both injector designs, the shear stress peaks near the interface of the pre-combustion chamber with the fuel grain ($x = 0$ mm). The wall shear stress for the single-port design shows a local maxima of 3 Pa, while the axial showerhead injector achieves a local maxima of 18 Pa. Thereafter, the wall shear stress decreases to a local minima near the end of the recirculation zone, which corresponds to $x \approx 25$ mm for the single-port injector and $x \approx 35$ mm for the axial showerhead injector, and exhibits another slight increase in the boundary layer development region. It is evident through Fig. 3.12 that the wall shear stress associated with the axial

showerhead injector is significantly higher than the single-port injector just downstream of the pre-combustion chamber. This is consistent with the higher regression rates reported in Table 7.1 and the increased combustion efficiency observed in Fig. 3.10.

The results from cold-flow CFD cannot predict flow properties beyond which chemical reaction and heat transfer mechanisms become significant, but they still provide useful insight into the incipient physics that lead to observed injector-specific differences in the downstream thermochemical structure and fuel regression measurements presented above. The significant variation seen in the distribution and magnitude of velocity, particularly the non-axial velocity and in the wall shear stress on the fuel grain just downstream of the pre-combustion chamber are consistent with increased mixing and higher regression rates measured experimentally for the showerhead injector compared to the single-port injector.

3.4 Conclusion

In this work, we report quantitative spatially-resolved temperature and species (CO, CO_2, and H_2O mole fraction) profiles for combustion of polymethylmethacrylate (PMMA) with oxygen in a hybrid rocket motor geometry, and compare two oxidizer injector designs: a single-port and an axial showerhead. The thermochemistry data was obtained by employing a novel in-situ laser absorption tomography (LAT) sensing technique coupled with a modular axisymmetric solid-fuel combustion experiment, to resolve the reaction layer at varying axial distances downstream of the injectors. Two-dimensional images of temperature and mole fractions were reconstructed by compiling the planar profiles at each measured axial position. By maintaining an equivalent oxidizer mass flow rate across the tests, the effects of the geometric differences of the injectors on the boundary layer thermochemical structure were examined. The thermochemical flow-field for the conventional single-port injector followed a classical reacting boundary layer profile largely governed by a slightly broadening radial distribution of fuel-lean to fuel-rich conditions from the core radially outward to the fuel

grain wall. By contrast, the radial variation of gas properties downstream of the showerhead injector was substantially muted over a short axial distance, and the thermochemical results appeared more acutely governed by axial progression of O/F ratio. In addition, the fuel regression rates for the showerhead injector were found to be approximately double the magnitude of those seen with the single-port injector, consistent with greater combustion progress.

Interpretation of these results was assisted by a complementary cold-flow CFD study that assessed the incipient flow-field structure exiting the respective injectors. The numerical results showed that the showerhead injector design resulted in relatively high non-axial velocities in the pre-combustion zone and higher shear stress on the walls, consistent with greater mixing / property homogeneity in the radial axis and higher fuel regression. Additionally, higher localized fuel regression observed experimentally for the showerhead design could be partly attributed to a steeper oxidizer impingement angle for the showerhead design, which in CFD results is shown to intersect with the fuel grain at a shorter axial distance compared to the single-port injector.

The results presented in this work clearly indicate a strong dependence of hybrid motor combustion performance on oxidizer injector design and the intensity of viscous forces in the incipient flow-fields that induce downstream mixing and radial diffusion.

CHAPTER 4

Swirl injection in hybrid PMMA combustion assessed by thermochemical imaging

ybrid rocket oxidizer injectors with variable initial swirl to axial velocity ratios (tangential, canted, axial) representing variable incipient swirl number were designed and manufactured to evaluate their comparative influence on combustion zone development with polymethylmethacrylate (PMMA) fuel in a cylindrical port geometry. The effective flow area of the three injectors and correlated pressure drop was kept nearly-constant to confine the effects of swirl on propellant mixing and fuel regression rate. For each injector, a laser absorption spectroscopy (LAS) technique was employed to take transverse spatially-resolved measurements of temperature and species (CO, H_2O) at the exit plane of PMMA fuel grains at varying distance from the injector during repeated hot fire tests with constant gaseous oxidizer flow rate. Two-dimensional images were obtained by compiling radially-resolved tomographic planar measurements at several axial distances from 1.0 in. to 5.0 in (x/d = 2–10), assuming axisymmetric flow. Results indicate that swirl injection has a strong initial effect on fuel regression that diminishes with axial distance.

4.1 Introduction

Hybrid rocket engines have potential performance, safety, and cost advantages over purely liquid- or solid-propellant rockets and are, thus, attractive for new space propulsion applications, but the implementation of large-scale hybrid rocket systems has been historically

hindered by sub-optimal combustion performance from low regression rate fuels. The combustion process involves complex physics including turbulent mixing, heat transfer, and chemical reaction in a convoluted spatial domain. Hybrid rocket motors store the fuel and oxidizer in different phases, most commonly consisting of a liquid or gaseous oxidizer that is injected into a combustion chamber lined with a solid fuel, usually of cylindrical geometry. Upon injection of the oxidizer, a turbulent boundary layer forms that sweeps over the fuel-grain wall. To initialize the combustion reaction, an ignition source heats the solid fuel wall, vaporizing a thin layer of fuel, which then enters the boundary layer region of the flow-field. The subsequent combustion progression is governed by the heat and mass transfer that occurs between the gas-phase oxidizer and the evaporated fuel near the grain surface. As this fuel moves incrementally inward, the local ratio of oxidizer to fuel (O/F) becomes sufficiently conducive to combustion and a thin flame appears. Previous studies have shown that geometric variations in hybrid motor designs can significantly affect combustion progress [2]. Depending on the geometry of the oxidizer injector, which is the focus of the current work, the local regression rate can vary significantly near the injection/fuel grain interface. The injector design influences the initial transport dynamics that govern turbulent mixing, viscous wall shear, and diffusion, and ultimately can impact overall combustion performance.

In particular, swirl injector geometries have gained interest for hybrid rockets as they have been shown to improve propellant mixing and fuel regression rate over purely axial injection methods [30, 31, 32, 33]. These varieties typically involve angled ports that induce the formation of a helical flow structure. The exit angle of the ports is referred to as the swirl angle. Swirl injectors may also have a second "canted" angle directed toward the axial direction to promote flow progression and reduce the risk of back-flow. The swirl number parameter, 'SW', is often used to quantify the strength of the swirling flow and is defined as the ratio of tangential momentum flux to axial momentum flux. This study examines a range of swirl to axial injection velocities. It can be noted that some prior works indicate that the effects of the swirl injection are more prominent for shorter fuel grain

lengths [30, 31, 33]. Unique to this work is the employment of a laser absorption tomography method to evaluate variable injector design on the development of the combustion zone. The method involves in-situ measurements of species and temperature which directly reflects the chemical-to-thermal energy conversion. The laser absorption method has been described in previous works [6, 70, 71], and aims to characterize oxidation progress via spatially-resolved measurements of temperature, CO, and H_2O.

4.2 Theory

4.2.1 Spectroscopy and Tomography

Laser absorption spectroscopy (LAS) is an optical diagnostic technique that exploits the resonance of coherent light with the transitions between quantum energy states for a given species. This work utilizes the unique capabilities of laser absorption to attain in-situ measurements of physical gas properties including temperature and species composition within harsh high-temperature environments. An overview of the fundamentals of laser absorption spectroscopy is provided here for reader familiarity with common nomenclature and definitions; a comprehensive review can be found in [47]. Species have unique spectral "fingerprints", determined by the energy spacing between the quantum states (transitions) specific to a given molecule. By exposing a molecule to coherent light radiation of equivalent energy to the targeted species' quantum energy spacing, the molecule can absorb photon energy and transition from a lower state to an upper state quantum energy level.

The absorption of light that allows for the transition between energy levels results in an attenuated light intensity of the source (i.e. laser beam). The Beer-Lambert law relates the change in light intensity (via spectral absorbance) to thermochemical properties of the flow environment. Eq. 4.1 describes this relationship for the spectral absorbance, $\alpha(\nu)$, of a

non-uniform gas medium along a line-of-sight, l [cm]:

$$\begin{aligned}\alpha(\nu) &= -\ln\left(\frac{I_t}{I_0}\right)_\nu \\ &= \int_0^L \sum_j PS_j(T(l))X_i(l)\phi_j(\nu)\mathrm{d}l\end{aligned} \tag{4.1}$$

Here I_0 and I_t are the incident and transmitted light intensities, respectively, at a specific frequency, ν [cm^{-1}], L [cm] is the aggregate absorbing path length, P [atm] is the total pressure, $S_j(T(l))$ [cm^{-2}/atm] is the linestrength of rovibrational transition, j, at temperature, $T(l)$ [K], $X_i(l)$ is the mole fraction of the absorbing species, i, and $\phi_j(\nu)$ [cm] is the line-shape function. It should be noted that this expression is a line-of-sight integral over an optical path length with non-uniformity in temperature and species.

The projected absorbance measurements described in Eq. 4.1 can be integrated over the spectral domain to eliminate dependence on the line-shape function, $\phi_j(\nu)$. This integrated term is the projected absorbance area, $A_{\mathrm{proj}}(y)$ [cm^{-1}], which, for an azimuthal symmetric flow-field, can be obtained at discrete locations, y [cm], from the axis of symmetry and, using Abel's integral equation [49, 50], can be related to the radial distribution of the integrated spectral absorption coefficient, $K(r)$ [cm^{-2}]. This relationship is described by Eq. 4.2:

$$\begin{aligned}A_{\mathrm{proj}}(y) &= \int_{-\infty}^{\infty} \alpha(\nu)\mathrm{d}\nu \\ &= \int_0^{L(y)} K(l)\mathrm{d}l = 2\int_y^R \frac{K(r)r}{\sqrt{r^2-y^2}}\mathrm{d}r \\ &= \int_0^{L(y)} \sum_j PS_j(T(l))X_i(l)\mathrm{d}l\end{aligned} \tag{4.2}$$

In Eq. 4.2, $L(y)$ [cm] is the absorbing path length at position y from the axis of symmetry, and the radially-resolved thermochemical flow-field properties $T(r)$ and $X_i(r)$ are embedded in $K(r)$, which can be determined from $A_{\mathrm{proj}}(y)$ using the tomographic reconstruction methods discussed in [6]. As previously noted, this approach assumes an axisymmetric flow-field, which is expected in the gas-phase core flow of a cylindrical fuel grain for a hybrid rocket geometry.

Temperature and species are recovered from measurements of the projected absorbance areas, which are inverted via 1D laser absorption tomography (LAT) to yield the integrated spectral absorption coefficients for various spectral lines. This strategy has been previously used by our group for investigating the thermochemical structure of hybrid combustion at atmospheric pressures [63, 64] and two-dimensional turbulent jet flames [53, 52]. Projected absorbance area, $A_{\text{proj}}(y)$, can be obtained by fitting a Voigt line-shape function to the absorbance profile of each absorption feature which may encompass one or more closely spaced transitions ($j \geq 1$). $A_{\text{proj}}(y)$ and $K(r)$ simply represent a summation of individual contributions at those local positions, which can be reasonably well extracted from a Voigt fit. In practice, $T(r)$ is obtained by measuring two spectral absorption features, also referred to as 'line pairs', of the same species and taking the ratio between the two radially integrated spectral absorption coefficients, $K_1(r)$ and $K_2(r)$. $T(r)$ can thereafter be inferred from the linestrength ratio, effectively eliminating the pressure and mole fraction dependence, as shown in Eq. 4.3:

$$R(r) = \frac{K_1(r)}{K_2(r)} = \frac{\sum_i S_i(T(r))}{\sum_j S_j(T(r))} = f(T(r)) \tag{4.3}$$

Linestrength values, $S_j(T(r))$, for each species and their associated uncertainties are taken from the HITRAN [51] and HITEMP [8] spectroscopic databases. Eq. 4.4 indicates that, with pressure and the radial distribution of temperature known, $X_i(r)$ of the absorbing species, i, can be evaluated from the integrated spectral absorption coefficient, $K(r)$:

$$X_i(r) = \frac{K(r)}{\sum_j P S_j(T(r))} \tag{4.4}$$

Implementing this strategy for multiple transverse planes at varying axial distances in the solid-fuel reaction layer enables quantitative two-dimensional imaging of temperature and gas composition [52, 53, 6].

The current work is an extension of this technique and is adapted to obtain spatially-resolved temperature and mole fraction in the reaction zone of a hybrid rocket, applicable to study a range of injector designs and operating conditions. The theory of laser absorption

tomography is well-detailed in literature and prior work [72, 73]. The specific measurement technique and line selection for spatially-resolved laser absorption tomography measurements of CO and H_2O in a hybrid rocket motor geometry are detailed in [6].

4.3 Experimental Setup

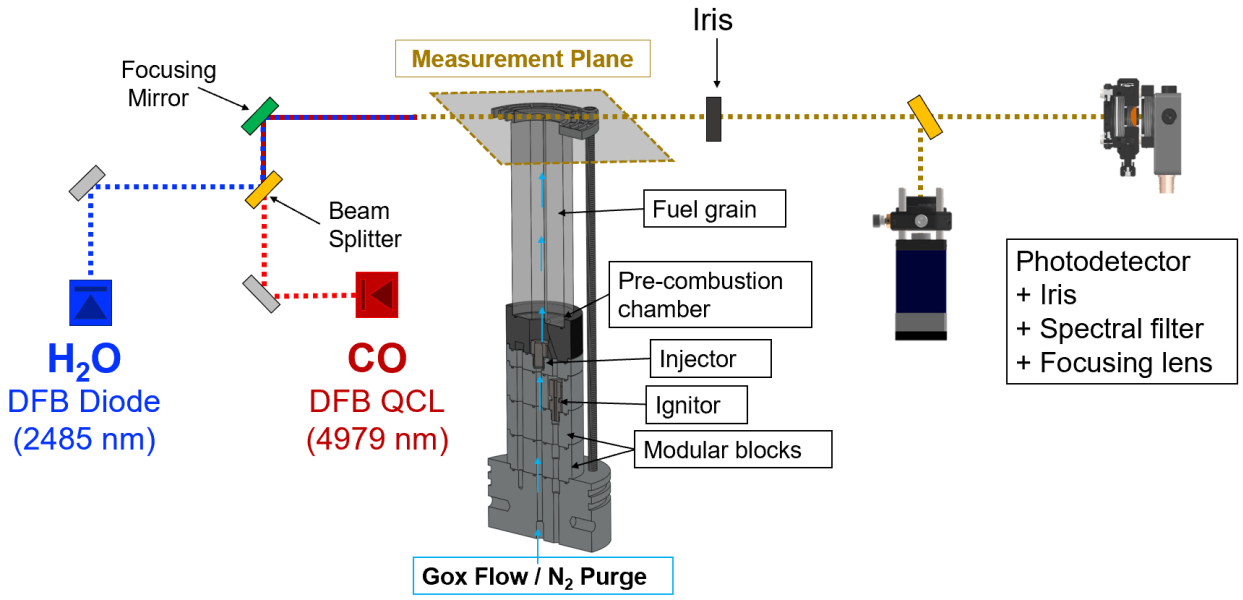

Figure 4.1 Hybrid combustion facility utilized for exit-plane temperature and species measurements

4.3.1 Hybrid Test Article

Figure 4.1 illustrates the combustion facility and optical configuration used for the tomography measurements. For CO, we utilize a quantum cascade laser (QCL) with ~50 mW output power to target rovibrational transitions near 4.9 μm. To measure H_2O, a diode laser with ~5 mW output power is used to target features near 2.5 μm. In order to obtain high spatial resolution in the radial direction, the two light sources are made co-linear using a CaF_2 50/50 beam-splitter and focused over the measurement plane utilizing a 200 mm focusing mirror.

This results in a beam diameter of ∼0.5 mm located within ∼0.5 mm of the fuel grain exit. The transmitted light intensity then passes through an iris before being split once more and refocused onto two photodetectors. Half of the transmitted light is directed through a CaF_2 plano-convex lens onto a thermo-electrically cooled photovoltaic (PV) detector (VIGO PVI-4TE-5) with a narrow bandpass filter that isolates the CO laser radiation near 4.9 μm; the other split beam is focused onto a photodetector (Thorlabs PDA10D) that is only sensitive to wavelengths < 2.6 μm, thereby isolating the H_2O light source.

The combustion facility assembly incorporates remote ignition (via electrical igniter), valve operation, and accommodates variable-length fuel grains. GOx mass flow rate is measured using a sonic orifice with a corresponding upstream pressure transducer (Setra 225G). The experimental setup is located in a high-flow fume hood with an exhaust rate of ∼1150 cfm. The test stand accommodates fuel grains of outer diameter 50.8 mm (2 in.) and of heights in the range of 25.4–203.2 mm (1–8 in.). This modularity is achieved by stackable aluminum blocks that attach to the test stand base and offset the variable fuel grain length to keep the measurement plane effectively constant. This eliminates the need to move optical equipment on either side of the test stand between experiments while examining combustion progress at multiple axial locations.

In order to obtain radially-resolved measurements for tomographic reconstruction, the assembly is mounted on a motorized translation stage that allows for horizontal translation perpendicular to the optical axis. This allows the transmitted light to scan across the full measurement plane at a rate of 5 mm/s, which effectively traverses the laser beam across the combustion zone in 2.5 seconds. It should be noted that evaluating different axial positions requires repeating tests. For discussion on validation of test and optical measurement repeatability, see [6].

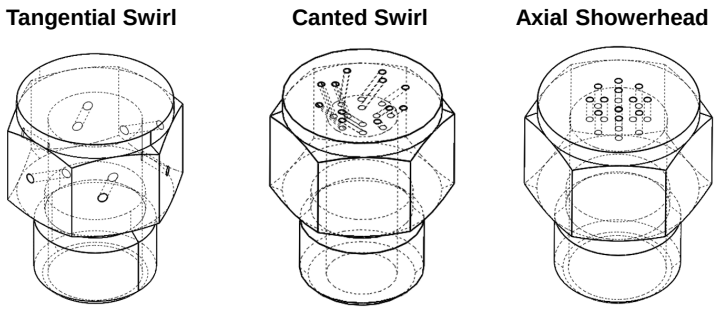

Figure 4.2 Isometric views of the tangential swirl, canted swirl, and axial showerhead injector designs

	Tangential Swirl	**Canted Swirl**	**Axial Showerhead**
No. of ports	6	12	12
Port diameter [in.]	0.035	0.025	0.025
Swirl Angle []	60	60	0
Canted Angle []	0	45	90
Swirl Number	∼1.4	∼0.5	∼0

Table 4.1 Injector design specifications and swirling flow parameters

4.3.2 Injector Geometries

For this work, the two swirl injector designs were influenced by Computation Fluid Dynamics (CFD) cold flow analysis performed using ANSYS Fluent, which examined wall shear per axial length of fuel grain as a proxy for fuel grain regression rate. Simulated pathlines of flow through representative swirl and axial injector designs are shown in Fig. 4.3 to highlight the significant difference in flow structure inherent to swirl injection. The injectors were also designed to have the same effective flow area, have the same L/D (port length to port diameter ratio), and operate at the same oxidizer mass flow rate as the axial showerhead injector used in previous studies to facilitate meaningful comparison. In iterative design

and CFD analysis, the main parameters that were varied were the number of ports and the swirl/canted angles, with the objective to maximize wall shear at different cant angles of 0, 45, and 90 degrees (along the axial direction). Isometric views of the finalized designs are shown in Fig. 4.2. The tangential swirl injector has six ports of diameter 0.035 in. and a swirl angle of 60 degrees, while the canted swirl injector has twelve 0.025 in. diameter ports and canted and swirl angles of 45 degrees and 60 degrees, respectively. For the canted swirl injector, the ports are patterned around two concentric circles similar to the axial showerhead injector. The similarities across the three designs attempt to isolate effects of swirl and cant angle for practical assessment in hot-fire tests. The computational wall shear results for the selected injector designs are later shown in Fig. 4.4.

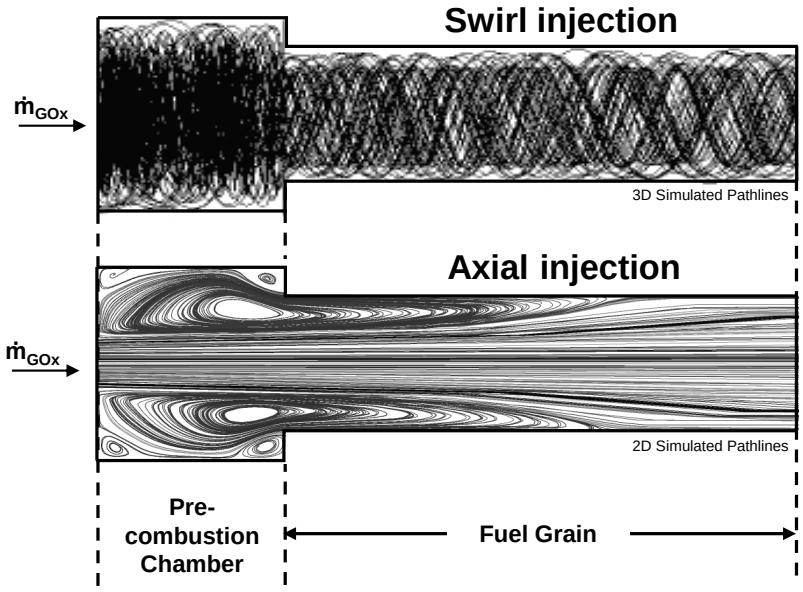

Figure 4.3 Simulated pathlines representative of axial and swirl injection into the test article geometry obtained from ANSYS Fluent cold flow simulations of gaseous oxygen

The swirl number, SW, associated with each injector was determined using average flow properties at the fuel grain inlet based on the ANSYS Fluent cold flow simulations. Swirl numbers effectively represent the ratio of axial flux of tangential or swirl momentum to the

axial flux of axial momentum. Swirl numbers of 1.4 and 0.5 for the tangential and canted swirl injectors, respectively, were calculated as in Eq. 4.5 [74].

$$SW = \frac{\int_S r v_\theta (\vec{v} \cdot \hat{n}) dS}{\bar{r} \int_S v_z (\vec{v} \cdot \hat{n}) dS} \tag{4.5}$$

where r is radial distance from axis of rotation, v_θ is the tangential velocity, $\vec{v}$ is the velocity vector, $\hat{n}$ is the normal unit vector, and $\bar{r}$ is outer radius. We note that the time-averaged swirl number for the axial showerhead design is approximately zero at the same location.

4.4 Results

4.4.1 Space-time Averaged Fuel Regression Rates

As a complementary study to the thermochemical measurements, space-time averaged fuel regression rates for each test were calculated using the total burn time and post-test fuel grain mass. For a fuel grain with a circular port geometry, as used in this study, the space-time averaged regression rate, $\bar{\dot{r}}$ [mm/s], during a hot-fire can be determined as follows:

$$\bar{\dot{r}} = \frac{\bar{\dot{m}}_f}{\pi \rho_f L_f \bar{D}} = \frac{\bar{D}_f - D_i}{2t_b} \tag{4.6}$$

where ρ_f [g/mm^3] is the density of the fuel (11.85 g/mm^3 for the PMMA used), L_f [mm] is the length of the fuel grain, and $\bar{\dot{m}}_f$ [g/s] is the space-time averaged fuel mass flow rate, which can be determined by dividing the total consumed fuel mass, ΔM_f [g], by the total burn time, t_b [s]. $\bar{D}$ [mm] is the space-time averaged port diameter given by the initial and average final port diameters, D_i [mm] and $\bar{D}_f$ [mm], respectively [32]:

$$\bar{D} = \frac{D_i + \bar{D}_f}{2} \tag{4.7}$$

Previous works [65] have found that $\bar{D}_f$ can be most accurately estimated based on the total consumed fuel mass, ΔM_f, measurements:

$$\bar{D}_f = \sqrt{D_i^2 + \frac{4\Delta M_f}{\pi \rho_f L_f}} \tag{4.8}$$

It is important to note that Eqs. 4.6–4.8 assume a constant regression rate around the circumference of the fuel grain port at any given axial location. This is a well-accepted approximation for fuel grains with circular ports, but loses validity when considering other geometries.

Figure 4.4 (right) shows the resulting regression rates measured for the canted swirl, tangential swirl, and axial showerhead injector tests over a range of fuel grain lengths. Results for a single-port axial injector from a previous study are also included for comparison [71]. Additionally, results from ANSYS cold flow simulations are included showing average wall shear on the fuel grain surface along the axial direction. Notably, the measurements start approximately 20 mm axially downstream of the start of the fuel grain due to practical issues burning shorter grains. By contrast, the CFD results are most insightful in the preceding region of the fuel grain. Still, there is a consistent correlation in trends across simulations and experimental results for the respective injector geometries. While the cold flow simulations undoubtedly lose validity progressing downstream of the fuel grain and precombustion chamber interface, these results are strongly indicative that simulated wall shear associated with initial viscous interactions between the oxidizer and fuel grain provide a reasonable proxy for relative fuel regression for different injector or hybrid motor designs. The simulated and experimental results both show high values of wall shear and regression rate, respectively, for the two swirl injector geometries shortly downstream of injection with trends later falling off steeply. This indicates that swirl effects and associated increased regression seen with swirl injectors tend to be contained to lower length to diameter ratio (L/D) fuel grain geometries.

4.4.2 Thermochemical Flow-field Measurements

The spectroscopic technique was implemented to quantitatively analyse the comparative influence of swirl and axial injection effects on the reaction zone of a PMMA/GOx hybrid rocket combustor. Planar measurements of temperature, CO, and H_2O were conducted at atmospheric pressure over a range of fuel grain lengths (25.4–127 mm) with both tangen-

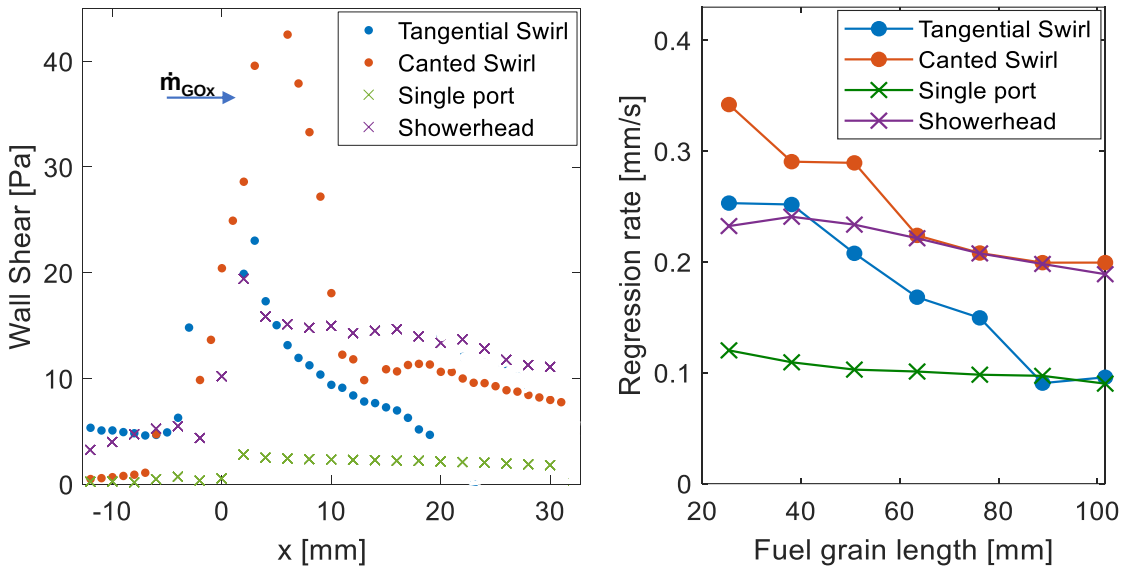

Figure 4.4 *Left*: ANSYS Fluent cold flow results for wall shear versus downstream axial distance from the precombustion chamber and fuel grain interface shown for axial showerhead, canted swirl, and tangential swirl injector designs. *Right*: Experimentally measured space-time averaged regression rates versus fuel grain length

tial swirl and canted swirl injector designs. Planar measurements were then compiled into two-dimensional images to better highlight the spatial combustion progression. Additional measurements with the axial showerhead injector over the same test conditions are included to serve as a baseline for comparison. The oxidizer mass flow rate for all experiments was held constant at 1.2 g/s.

Figure 4.5 depicts radially-resolved single plane measurements of temperature and mole fraction (CO, H_2O) at the two extreme axial positions of the fuel grain length range, those being at 25.4 and 127 mm downstream of the fuel grain surface. As discussed in Sec.4.4.1, the averaged fuel regression rate decreases with increased length and thus less widening of the port diameter occurs on average over the burn time—this is represented by the varied radial domains shown in each subplot. It should be noted that $r = 0$ mm corresponds to the

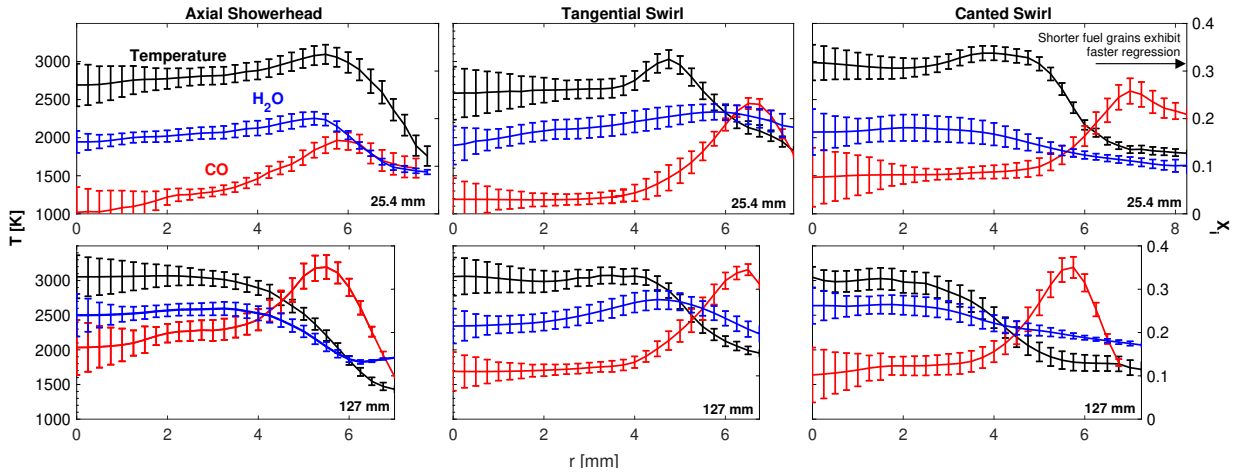

Figure 4.5 Temperature and mole fraction results of CO and H_2O versus radial distance from the fuel grain center ($r = 0$ mm) shown at two axial positions for the axial showerhead (*left*), tangential swirl (*center*), and canted swirl injector (*right*)

core of the cylindrical axisymmetric flow and r is therefore the radial distance from the flow center. The radial distance associated with the boundary of the gaseous core and fuel grain surface involves some ambiguity due to phase-change and the lack of combustion products in the initial fuel pyrolysis, but is estimated to be within 0.5–1 mm of the termination of the data array, supported by post-test measurements of grain diameter. Across injector geometries, the local maximum temperature position trends towards the core with increasing axial distance as radial diffusion and turbulent mixing effects become prevalent. Both of the swirl injector and the axial injector results indicate a peak temperature of ∼3000 K reached by the first measurement plane at 25.4 mm that is consistent over the axial range, however, the three injectors exhibit distinct trends in radial profiles. As with temperature, radial diffusion causes both product species to become more abundant around the core at the further axial position. While we observe the highest CO concentration with the canted swirl injector at the first length position at x = 25.4 mm, all three injectors reach a similar concentration downstream at $x = 127$ mm.

The full length range of planar measurements are compiled into two-dimensional images

in Fig. 4.6 to visualize the reaction layer structure. Both species are shown on the same color scale for purpose of comparison. Over the range of measurement lengths, we expect that most of the chemical reaction occurs in a thin boundary layer region adjacent to the wall, which grows in width and shifts slightly towards the core as axial distance increases. Adjacent to the PMMA grain surface, fuel pyrolysis at fuel-rich conditions leads to high CO concentration. As this fuel contacts the core oxidizer stream, we expect to see, and indeed here observe, the thin reaction zone of the characteristic diffusion forming where the temperature as well as H_2O mole fractions are at their peak. Compared to $x = 25.4$ mm, an increased portion of the radial temperature distribution at further downstream positions approach PMMA/GOx equilibrium temperature ($\sim$ 3050 K), reflective of the chemical to thermal energy conversion.

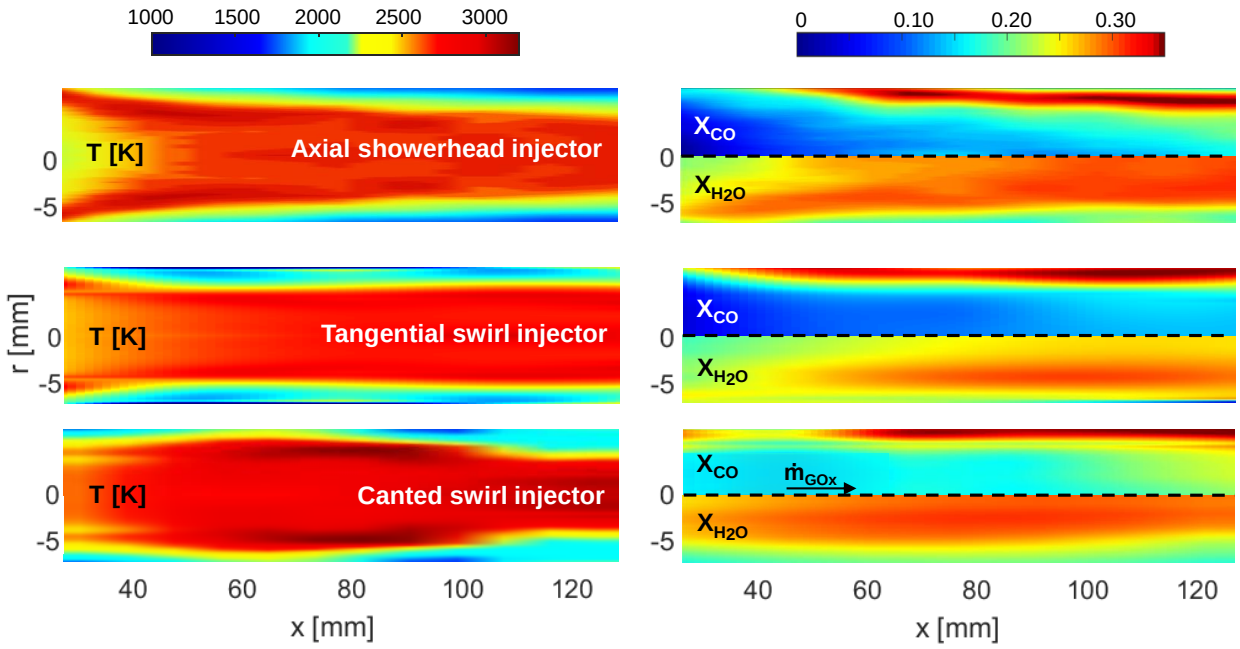

Figure 4.6 Two-dimensional thermochemistry measurements demonstrating PMMA/GOx combustion progression along the axial direction for the canted swirl, tangential swirl, and axial showerhead injectors

There are, however, significant differences in spatial progression of this thermochemical

structure that can be readily observed across the axial injector and both swirl injectors. Over ∼25–60 mm, the swirl injector temperature peak locations are comparatively closer to the core than in the axial showerhead profiles, indicative of the aforementioned higher fuel regression rates seen in this length range for the two swirl injectors. Progressing downstream, we observe similar radial temperature profiles for the tangential swirl as with the axial injector—a further indication that the beneficial swirl injection effects are indeed largely contained to shorter axial lengths or smaller L/D ratio geometries. Conversely, the canted swirl injector exhibits a distortion to the swept boundary layer region characteristic to axial injection in hybrids. In the mid axial range of measurement (∼60–90 mm), the temperature maxima shifts radially outward from the initial position creating a local hot region close to the wall, thereafter downstream following the overall radial diffusive trend with inward temperature peak shift. A similar, though less distinct, distortion to local maxima trends is also seen in the CO and H_2O images. It is likely that this reaction zone structure is due to particularly non-uniform regression axially relative to the axial showerhead and tangential swirl injectors. This is consistent with the post-burn geometry of the fuel grain inner ports that appear to have experienced greater local fuel regression around this region. The canted swirl injector, though it produces the least uniform axial regression, appears to most immediately reach high product species concentrations within the core. The differences are relatively muted further downstream.

Consolidated, these results provide a comprehensive perspective on combustion progress and flow field structure in hybrid PMMA combustion for oxidizer injection with varying incipient swirl. The radial and axial evolution of temperature and speciation highlight the significance of the injector design on the overall combustion performance and reveal effects of varied degrees of inlet swirling flow on mixing and diffusive effects, including non-uniform axial regression and more rapid convergence to maximum thermal energy.

4.5 Summary and Future Work

The primary goal of this effort was to assess the influence of induced swirl in oxidizer injection on the development of the hybrid PMMA combustion reaction layer using laser absorption tomography. Two-dimensional measurements of the thermochemical structure of the PMMA/GOx motor geometry using swirl injectors with varying initial swirl number illustrate effects on flow field structure and combustion progress relevant to hybrid rocket performance. These data correlate incipient injection swirl number with the axial combustion progress, facilitated by comparison to an axial showerhead injector. Spatially-resolved thermochemical results, in conjunction with regression rate measurements, indicate that improved performance from swirling inlet flow is largely contained to a region immediately downstream of injection with low L/D ratios. A canted swirl injector (effectively an intermediate between a tangential swirl and axial showerhead injector) exhibited higher regression rates, core temperatures, and product species concentrations (CO, H_2O) at shorter (or earlier) axial distances than either the tangential swirl injector or axial showerhead injector, but differences were largely diminished downstream. Such data and insights into the effects of the incipient flow-fields that induce downstream mixing, radial diffusion, and non-uniformity in fuel regression can be used to further inform hybrid rocket motor design and anchor reacting flow simulations.

CHAPTER 5

Spatially-resolved characteristic velocity (c*) measurements for hybrid rocket combustion analysis

5.1 Introduction

Chemical rockets have an acute need for high propellant efficiency due to the typically large propellant mass fractions and correspondingly low payload mass fractions. Accordingly, small improvements in propulsion system performance can significantly increase payload capacity or mission duration. The aggregate performance of a propulsion system can be defined by the axial thrust produced per unit mass flow rate of propellant consumed, or specific impulse (I_{sp}). In propulsion system testing and analysis, the thrust and mass flow rate can be measured and compared to ideal performance for a given propellant combination [75, 76, 77, 78, 79]. This overall propulsive performance depends on the components of the system, most notably the combustor, which converts the chemical energy in the propellants to thermal energy, and the nozzle, which accelerates and expands the hot combustion product gas to generate jet thrust, effectively converting the thermal energy into kinetic energy. As such, the efficiency of the combustor limits the eventual thrust generation and is critical to meeting overall performance targets and mission objectives.

Rocket combustion efficiency relates to multiple physical processes that often involve complex physical interactions that progress and vary spatially in a combustion chamber. In liquid and hybrid rockets, propellant injection induces mixing, which is followed by phase-change and exothermic chemical reactions. In solid and hybrid rockets, the regression of a

solid fuel varies spatially in time as it burns. In addition, the high combustion temperatures (∼3000 K) present in all systems often require chamber wall cooling to preserve structural integrity and durability. Each of these physical processes or mechanisms involve spatial variations in thermophysical properties which influence combustion efficiency.

The primary metric for assessing rocket combustion efficiency is the characteristic velocity (c^*), which reflects the thermal energy density of the working fluid. Traditionally, combustion chamber properties are assumed to be homogeneous or uniform and c^* is determined via chamber pressure and total mass flow rate measurements, as these properties vary little in the spatial domain of a steady-state combustor [80, 81, 82]. Inasmuch, the traditional c^* metric reflects a global indicator of numerous combustion processes, which often do vary spatially, and does little to inform the specific loss mechanisms that result in decreased combustion efficiency. Here, we present an alternative approach to attain a more granular spatially-resolved c^* based on in-situ laser absorption spectroscopy (LAS) measurements of temperature and species in rocket combustion environments.

LAS is an optical diagnostic technique known for its quantitative, species-specific measurement capability, which, when combined with tomographic reconstruction methods [54, 55, 48], can be used to characterize reacting flow-fields in the harsh combustion environments [6, 64, 53, 52]. Simultaneous multi-species measurements, in particular, provide key insights into the physiochemical mechanisms governing combustion performance and further elucidate complex combustion physics [83, 84, 85]. In recent years, such sensors have been developed, demonstrated, and deployed across various propulsion applications, including gas turbine combustors [86], rotating detonation engines (RDEs) [87, 88, 89], scramjets [90, 91, 92], liquid-propellant rocket combustors [93], and hybrid rockets [6, 71], among others.

The work presented herein leverages the aforementioned capabilities and provides a new avenue to better assess combustion performance by measuring and tracking changes in gas temperature and composition along the reaction coordinate. The spatial variation of these parameters, internal to a rocket combustion chamber, more directly reflects the chemical-to-

thermal energy conversion and provides better insight into propulsion system performance. After description of the theoretical approach and methodology, demonstrations of the technique in liquid and hybrid rocket combustion experiments are presented along with a discussion of uncertainty and limitations.

5.1.1 Rocket performance characterization

In analysing rocket performance, thrust and specific impulse are often the major parameters referenced. The thrust encapsulates both the momentum and pressure forces acting on the rocket and can be calculated as:

$$F = \dot{m}_p V_e + (P_e - P_a)A_e \tag{5.1}$$

where $\dot{m}_p$ is the propellant mass flow rate, V_e is the exhaust velocity, P_e is the pressure at the exit of the nozzle, P_a is the ambient pressure, and A_e is the nozzle exit areas. Thrust is maximized when the gas is perfectly expanded through the nozzle, effectively when P_e and P_a are the same and thus the pressure term in the thrust equation cancels out. In the likely case that the gas is not perfect expanded, Equation 5.1 is sometimes rewritten to define a metric to evaluate propulsion efficiency. In this case, thrust is calculated as a function of 'c', an effective exhaust velocity:

$$F = \dot{m}_p c \tag{5.2}$$

To evaluate performance and efficiency in terms of propellant needed to generate some amount of thrust, F, it is useful to look at the specific impulse, Isp, which normalizes the force on the rocket by weight of propellant that is consumed:

$$I_{sp} = \frac{F}{\dot{m}_p g} \tag{5.3}$$

where again $\dot{m}_p$ is the propellant mass flow rate which is multiplied by g, the gravitational constant, such that the denominator is in units of weight. This gives an I_{sp} in units of seconds.

Specific impulse provides a useful overarching performance metric that encapsulates the chemical to kinetic energy conversion of the propulsion system as a whole. However, Isp does little to inform on the separate conversion mechanisms that lead to that overall efficiency, those being the chemical to thermal energy conversion in the chamber and the thermal to kinetic energy conversion through nozzle expansion. To determine those relative contributions, it is often useful to define parameters for each of those processes with which Isp can be expressed by:

$$I_{sp} = \frac{c}{g} = \frac{c^* C_f}{g} \tag{5.4}$$

where c^*, the characteristic velocity, is the parameter to assess the chemical to thermal energy conversion through propellant combustion in the chamber and C_f, the thrust coefficient, is the parameter to characterize the efficiency of the gas expansion through the nozzle. c^* is determined as:

$$c^* = \frac{P_o A^*}{\dot{m}} = \sqrt{\left(\frac{\gamma+1}{2}\right)^{\frac{\gamma+1}{\gamma-1}} \frac{R_u T_o}{M\gamma}} \tag{5.5}$$

in which P_c is the combustion chamber pressure, A_t is the nozzle throat area, and $\dot{m}_p$ is the mass flow rate of propellants. In the second definition of c^*, T_c is the chamber temperature, M is the gas molecular weight, and γ is the specific heat ratio. The thrust coefficient, C_f, is expressed as:

$$C_f = \frac{F}{A_t P_c} \tag{5.6}$$

Here, F is again the engine thrust, A_t is the nozzle throat area, and P_C is the chamber pressure. In this work, we are focused on the assessment of the combustion performance and the underlying chemical to thermal energy conversion governing it. As such, the definitions of I_{sp} and c^* will be referred to readily throughout.

5.2 Theoretical approach

The overall performance of a rocket propulsion system can be quantified by the specific impulse (I_{sp}), as per Eq. 5.7, which defines the thrust, T, generated per unit mass flow rate, $\dot{m}$. This specific-impulse parameter describes a propellant efficiency, which directly influences the achievable incremental velocity and payload capacity of a vehicle for a given mission, and is constrained by propellant selection, mixture ratio, and thrust chamber component design and engineering. Specific-impulse can be further characterized by the coupled performance of the combustion chamber and nozzle, the performance of which can be determined by the characteristic velocity, c^*, and thrust coefficient, C_f, respectively, as shown in Eq. 5.7:

$$I_{sp} = \frac{T}{\dot{m}g} = \frac{c^* C_f}{g} \tag{5.7}$$

Here, characteristic velocity, c^*, is the primary parameter used to assess propellant combustion performance (chemical-to-thermal energy conversion) and thrust coefficient, C_f, is used to evaluate how effectively combustion products are expanded through the nozzle (thermal-to-kinetic energy conversion). As such, combustion chamber performance, c^*, limits the overall kinetic energy produced by the nozzle and, as a result, greatly impacts overall vehicle performance and mission capabilities.

Due to the substantial impact combustion performance has on the mission capabilities of flight vehicles and spacecrafts, and the high propellant mass fractions of rockets, there are persistent efforts to identify processes or mechanisms that increase combustion performance. The theoretical characteristic velocity can be calculated based on chemical equilibrium conditions of combustion. In practice, c^* is typically measured via chamber pressure, P_o, total mass flow rate, $\dot{m}$, and nozzle throat area, A^*, through Eq. 5.8, as these are either known or simple to measure in rocket systems. The measured and theoretical c^* values can then be compared and losses quantified.

$$c^* = \frac{P_o A^*}{\dot{m}} = \sqrt{\left(\frac{\gamma+1}{2}\right)^{\frac{\gamma+1}{\gamma-1}} \frac{R_u T_o}{M\gamma}} \tag{5.8}$$

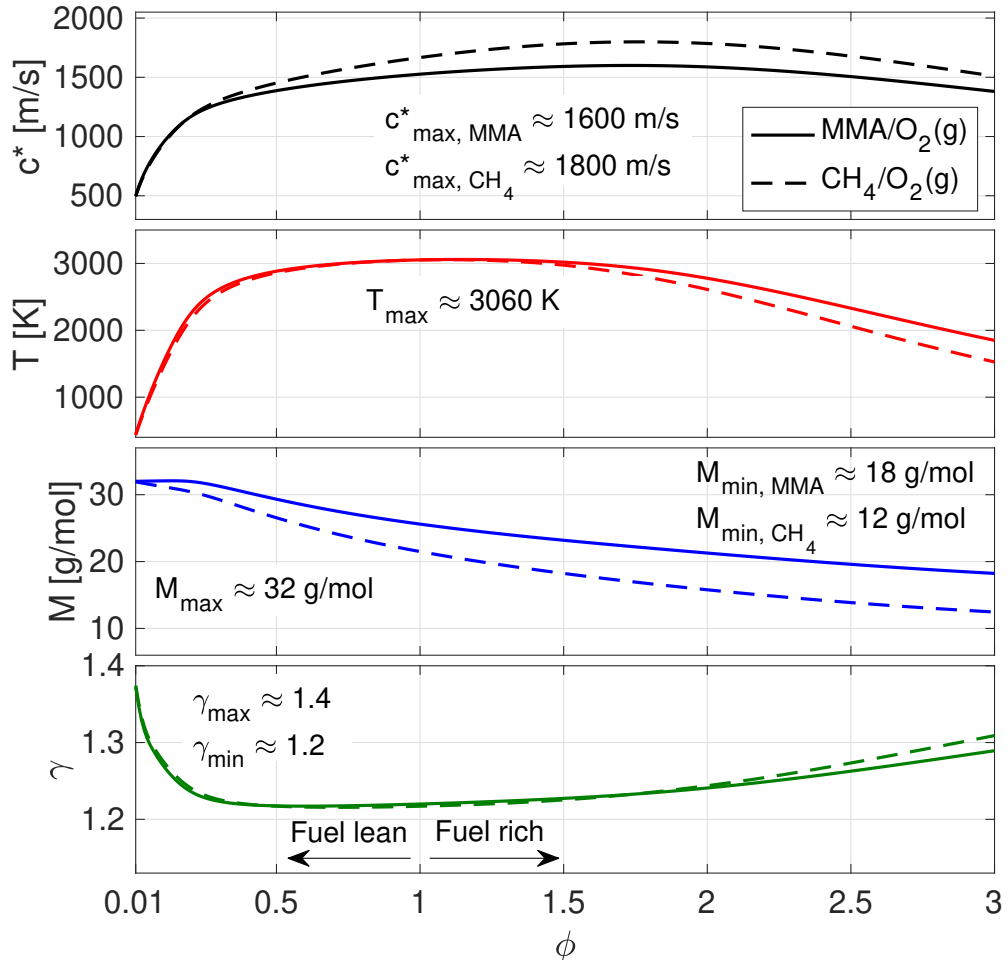

Figure 5.1 Theoretical c^* with corresponding temperature, molecular weight, and specific heat ratio, over a range of equivalence ratios (ϕ). Results are shown for two propellant combinations, $MMA/O_2(g)$ and $CH_4/O_2(g)$, at $P = 1$ atm

Notably, the traditionally measured parameters of pressure and mass flow rate vary minimally in the spatial domain, which is convenient for measurement purposes and in determining a global c^* of the combustion chamber, but provides little detail on the complex, multi-dimensional combustion processes, such as mixing, vaporization, and chemistry. We present a different approach to measuring c^* that employs in-situ optical sensing of thermochemical properties. By employing the laser absorption spectroscopy technique discussed herein, characteristic velocity can alternatively be measured more granularly through quanti-

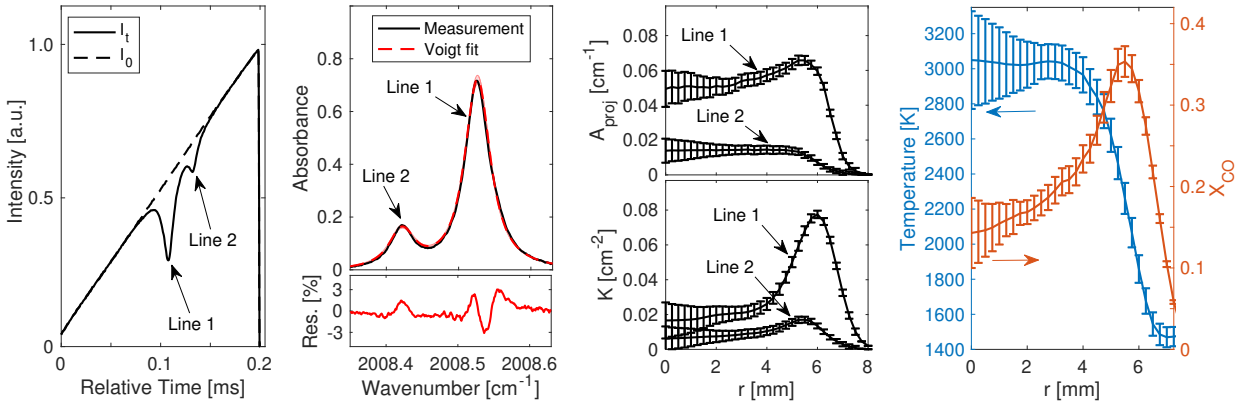

Figure 5.2 *Left to right*: Transmitted (I_t) and incident (I_0) light intensities for two CO transitions near 2008.5 cm^{-1}, the corresponding measured absorbance profile with a Voigt line-shape fit, projected absorbance areas (A_{proj}) and integrated spectral absorption coefficients (K) versus distance r from the center of an axisymmetric flow-field, and the resulting thermochemistry (T, X_i) distributions

tative measurements of temperature and species composition, which vary spatially in rocket combustion chambers as chemical energy is converted to thermal energy. Knowing species composition, informed estimates on the bulk molecular weight, M, and specific heat ratio, γ, of the combustion chamber gases can be made and c^* can be calculated directly via the second equality of Eq. 5.8.

From Eq. 5.8, it is evident that c^* increases as combustion gas temperature increases and molecular weight decreases. Additionally, albeit less apparent, c^* also increases when the specific heat ratio of the combustion gases decreases. In practical combustion systems, however, these parameters do not vary independently and are primarily dependent on oxidizer and fuel mixture ratio, $MR = \text{O/F}$, as well as combustion progress. Fig. 5.1 illustrates the variation of temperature, species composition (M, γ), and the resulting characteristic velocity over a range of equivalence ratios, $\phi = (\text{O/F})_{\text{stoic}}/(\text{O/F})$, for two propellant combinations, methyl methacrylate – oxygen, $(\text{MMA})/\text{O}_2$, and methane – oxygen, CH_4/O_2. For a given equivalence ratio and propellant combination, temperature, molecular weight, and

specific heat ratio, prescribe c^*. Accordingly, the method described herein involves local and spatially-resolved measurements of temperature and species composition, namely CO, CO_2, and H_2O, to determine local and spatially-resolved characteristic velocity, assisted by assumptions of a local equivalence ratio. Local and spatially-resolved c^* measurements provide a better understanding of the underlying chemical and physical processes governing propulsion devices, elucidate rocket combustion physics, and, ultimately, inform specific mechanisms that may enable increased combustion performance.

5.3 Methods

5.3.1 Laser absorption spectroscopy

The selected optical method for measuring species and temperature in rocket combustion environments is laser absorption spectroscopy. LAS is a non-intrusive diagnostic technique that exploits the resonance of coherent light with differences between the quantum energy states of molecules with intrinsic dipole moments. This enables quantitative measurements of species-specific flow-field properties from spectrally-resolved light attenuation. Typically these measurements provide local beam path-integrated data; when employing multiple beam paths in a given plane with tomographic reconstruction techniques, 2D spatially-resolved thermochemistry can be obtained [6, 52, 94]. This work utilizes the unique capabilities of LAS for in-situ measurements of temperature and species composition (CO, CO_2, H_2O) in rocket combustion environments to attain localized characteristic velocity, c^*. While a brief overview of LAS fundamentals is provided here for reader familiarity and nomenclature, a more comprehensive review can be found in [47, 95, 96] and additional details on the experimental setup and procedure used for the measurements discussed herein can be found in a previous work by the authors [6].

The attenuation of light due to spectral absorbance, $\alpha(\nu)$, is related to the thermochemical properties of the absorbing gas medium through the Beer-Lambert law. For a

non-uniform flow-field, this is expressed as:

$$\begin{aligned}\alpha(\nu) &= -\ln\left(\frac{I_t}{I_0}\right)_\nu \\ &= \int_0^L \sum_j PS_j(T(l))X_i(l)\phi_j(\nu)\mathrm{d}l\end{aligned} \tag{5.9}$$

where I_0 and I_t are the incident and transmitted light intensities, respectively, at a specific frequency, ν [cm^{-1}], L [cm] is the aggregate absorbing path length, P [atm] is the total pressure, $S_j(T(l))$ [cm^{-2}/atm] is the linestrength of spectral transition, j, at temperature, $T(l)$ [K], $X_i(l)$ is the mole fraction of the absorbing species, i, and $\phi_j(\nu)$ [cm] is the line-shape function. For a uniform flow-field, the integral simplifies to include a pathlength multiple and constant properties.

Fig. 5.2 illustrates representative incident and transmitted light intensities for a single laser scan targeting CO near 4.98 μm (2008.5 cm^{-1}). The corresponding absorbance of the two spectral transitions, denoted as *Line 1* and *Line 2*, are also shown. The measured spectral absorbance is fit with a Voigt line-shape profile to obtain the absorbance area, A [cm^{-1}]. If the thermochemical flow properties along the line-of-sight vary minimally, obtaining temperature is straightforward and can be done by taking the ratio of two absorbance areas, as shown in Eq. 5.10:

$$R = \frac{A_1}{A_2} = \frac{PS_1(T)X_iL}{PS_2(T)X_iL} = \frac{S_1(T)}{S_2(T)} \tag{5.10}$$

In this ratio all terms cancel but the ratio of linestrengths, implying an exclusive temperature dependence. With temperature known, mole fraction can be solved for directly using either spectral transition:

$$X_i = \frac{A_1}{PS_1(T)L} = \frac{A_2}{PS_2(T)L} \tag{5.11}$$

Notably, such a measurement can be done at varying beam locations for spatially-resolved thermochemistry [91], providing a basis to calculate localized characteristic velocity as described later in Sec. 5.4.

If thermochemical properties vary substantially along the line-of-sight, tomography may be employed [48]. Here we consider a simple but common example where the flow-field is

azimuthally symmetric (or axi-symmetric) and one-dimensional tomographic reconstruction methods can be implemented as performed in [6, 52]. In this case, the absorbance area obtained by the Voigt profile is considered a projected measurement, A_{proj} [cm^{-1}]. It should be noted that the absorbance profiles are not expected to strictly follow a Voigt lineshape as a result of the thermochemical gradients along the line-of-sight. However, the fractional fitting residuals were typically less than 3% for CO, less than 2% for CO_2, and less than 3% for H_2O, supporting the appropriateness of the Voigt line fitting routine as an approximation. Spectral absorbance measurements can then be obtained at discrete locations from the axis of symmetry and, using Abel's integral equation [49, 50], can be related to the radial distribution of the integrated spectral absorption coefficient, $K(r)$ [cm^{-2}]. This relationship is described by Eq. 7.1:

$$\begin{aligned} A_{\text{proj}}(y) &= \int_{-\infty}^{\infty} \alpha(\nu)\mathrm{d}\nu \\ &= \int_{0}^{L(y)} K(l)\mathrm{d}l = 2\int_{y}^{R} \frac{K(r)r}{\sqrt{r^2-y^2}}\mathrm{d}r \\ &= \int_{0}^{L(y)} \sum_{j} PS_j(T(l))X_i(l)\mathrm{d}l \end{aligned} \tag{5.12}$$

In Eq. 7.1, the spatially-resolved thermochemical flow-field properties, $T(r)$ and $X_i(r)$, are embedded in the line integrated absorption coefficient $K(r)$, which can be determined from $A_{\text{proj}}(y)$, as shown in Fig. 5.2, using an Abel inversion scheme with Tikhonov regularization [54]. The Tikhonov method imposes a regularization parameter (determined via the L-curve method [56, 57]) that controls the relative importance of accuracy and smoothness in the solution. Further details on the implementation of this technique are discussed in [6, 52]. With $K(r)$ known for each transition, spatially-resolved temperature is obtained through the ratio of two integrated spectral absorption coefficients, as shown in Eq. 5.13:

$$R(r) = \frac{K_1(r)}{K_2(r)} = \frac{PS_1(T(r))X_i(r)}{PS_2(T(r))X_i(r)} = \frac{S_1(T(r))}{S_2(T(r))} \tag{5.13}$$

Similar to a uniform flow-field, spatially-resolved mole fraction can be solved for directly

using either spectral transition once temperature is known:

$$X_i(r) = \frac{K_1(r)}{PS_1(T(r))} = \frac{K_2(r)}{PS_2(T(r))} \tag{5.14}$$

Implementing this strategy for multiple transverse planes enables quantitative two-dimensional imaging of temperature and gas composition [52, 53, 6].

If the flow-field is non-uniform and non-axisymmetric, obtaining spatially-resolved thermochemical properties requires a more complex approach involving multiple projection angles. Nonetheless, spatially-resolved temperature and mole fraction can still be obtained, as shown in recent works from our group [97, 94].

5.3.2 Localized flow-field properties

Per Eq. 5.8, characteristic velocity can be determined with knowledge of the temperature, molecular weight, and specific heat ratio distribution of the flow-field. Using the LAS techniques discussed in the preceding section, localized temperature measurements can be directly used in Eq. 5.8 for calculating a localized c^*. If the mole fraction measurements well-represent the local bulk combustion gas constituents, then the molecular weight and specific heat ratio distributions are also known directly and can be used in Eq. 5.8. However, this is typically not the case and so further assumptions are needed to estimate molecular weight and specific heat ratio distributions. Here, we invoke chemical equilibrium to assist in determining balance gas composition.

If the flow-field is assumed to be in local chemical equilibrium, the measured species mole fractions obtained through LAS can be used to estimate local equivalence ratios at the measurement locations. Fig. 5.3 illustrates the species distribution for MMA/O_2 combustion based on chemical equilibrium [98] (computed using Cantera [58]). Over a wide range of equivalence ratios, CO, CO_2, and H_2O are major constituents of the overall combustion gas mixture and, additionally, have intrinsic dipole moments, which make them accessible via LAS. As such, measuring all three species provides a reasonable estimate of the composition

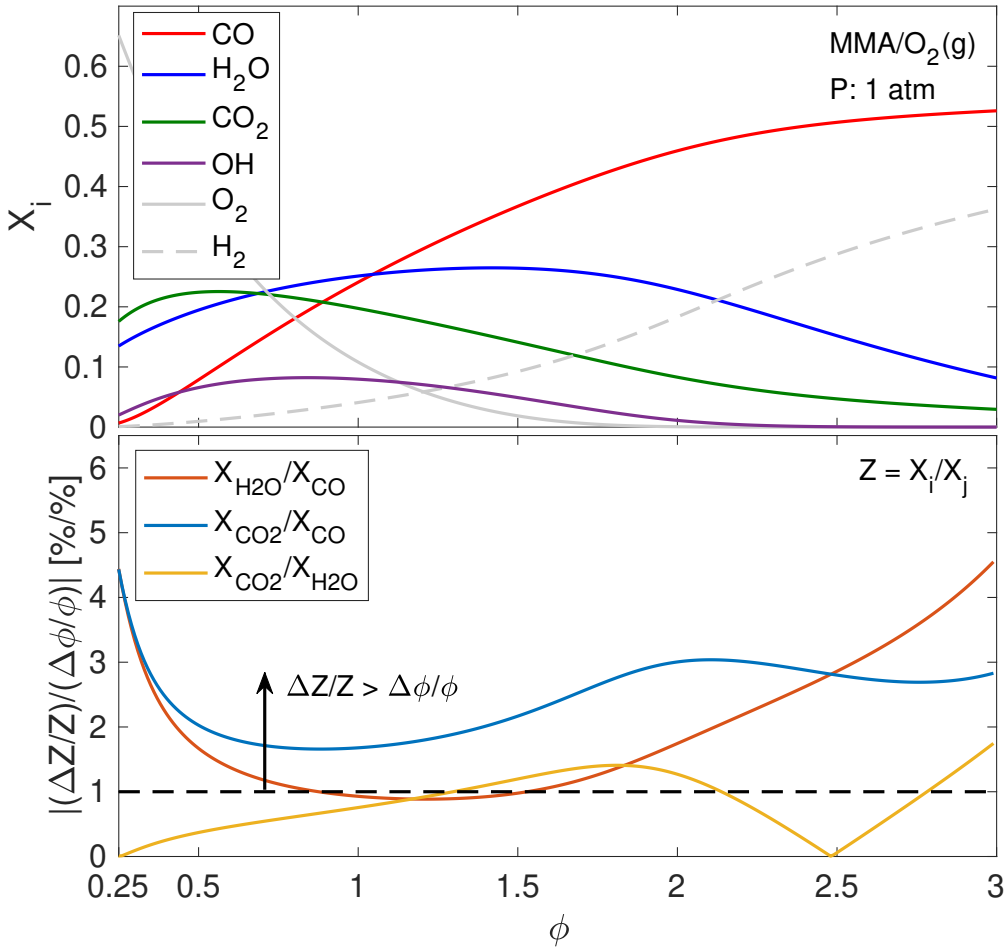

Figure 5.3 *Top*: Species mole fractions (X_i) at chemical equilibrium for MMA/O_2(g) combustion at $P = 1$ atm and varying equivalence ratios (ϕ). Species inaccessible via LAS (O_2, H_2) are shown in gray. *Bottom*: Equivalence ratio sensitivity of multiple species pairs, $Z = X_i/X_j$, used for determining local flow-field properties

of the overall gas mixture (>75% at typical fuel rich conditions). The remainder of the mixture can be estimated by assuming local equivalence ratios (or local chemical equilibrium) at the measurement locations. This is done by taking the mole fraction ratio, Z, between two measured constituents, X_i/X_j, and comparing them to the expected mole fraction ratios from chemical equilibrium. As seen in Fig. 5.3, mole fractions for a given species are not

always unique to an individual equivalence ratio; therefore, using mole fraction ratios is critical to estimating the local equivalence ratio. Notably, CO and CO_2 provide the highest equivalence ratio sensitivity, where uncertainties in the measured mole fractions, $\Delta Z/Z$, are always greater than the corresponding uncertainty in the local equivalence ratio, $\Delta\phi/\phi$. Specifically, for fuel-rich cases ($\phi > 1.0$) the uncertainty in the local equivalence ratio can be up to $2\times$ lower than the uncertainty in the measured species mole fractions. It should be noted that a detailed uncertainty analysis is included in Sec. 5.5.

In the following demonstrations of the method, both the liquid-propellant rocket engine and hybrid rocket combustor experiments target CO and CO_2 as the primary measurement species to achieve high equivalence ratio sensitivity for determining the remaining gas mixture. However, to encompass an even greater amount of the flow-field constituents and further minimize the uncertainty of the remaining gas mixture, additional species accessible via LAS can also be measured. This is demonstrated in the hybrid rocket combustor experiment, where H_2O measurements are also considered. With an estimate of the remaining species in the flow-field, the local molecular weight and specific heat ratio of the bulk gas can be well-estimated. For spatially-resolved measurements, this can be done at every measurement location to obtain the molecular weight and specific heat ratio distributions of the flow-field. The molecular weight and specific heat ratio distributions can then be used with the temperature field to obtained spatially-resolved characteristic velocity.

It should be noted that there are limits to the equilibrium reference frame and additional considerations may be needed for non-equilibrium conditions, including compositional variance in the reaction coordinate. To avoid additional complexity, more species can be measured (as done in the hybrid rocket demonstration); however, this may not always be feasible or practical. If the flow-field is not in chemical equilibrium, a similar approach may be carried out by considering a reaction progress variable using an appropriate chemical kinetic mechanism.

5.4 Demonstration results

5.4.1 Liquid-propellant rocket combustion

As discussed in Sec. 5.3.1, temperature and species composition can be obtained through different implementations of LAS. These measurements can then be used for calculating localized characteristic velocity, c^*, for rocket combustion analysis. Here, this technique is first demonstrated on an RP-2/O_2 liquid-propellant rocket combustor located at the Air Force Research Laboratory on Edwards Air Force Base, CA USA. A detailed description of the test rig and measurement technique can be found in [99, 100]. Temperature and mole fraction measurements of CO and CO_2 were taken over a range of pressures and mixture ratios from 28–83 bar and 2.5–5, respectively. The measurements are shown in Fig. 5.4, along with comparisons to expected values from chemical equilibrium–bounded by the highest and lowest pressures that were measured. Overall, the measured temperature and species follow the expected trends from chemical equilibrium and CO and CO_2 exhibit an inverse relationship consistent with total carbon conservation.

For the LRE measurements, thermochemical properties are assumed to vary minimally along the line-of-sight. This was determined to be a suitable approximation considering LAS measurements were taken at a far downstream (32 cm) location from the injector face and the measured species concentrations closely resembled the expected values from chemical equilibrium. As such, the measured gas temperature was directly used in calculating a local c^*. Since CO and CO_2 only compose $\sim 45\%$ (at most) of the bulk gas, the composition (M, γ) of the remaining mixture is estimated by assuming local chemical equilibrium. As described in Sec. 5.3.2, the measured mole fractions of CO and CO_2 can be used to determine a local equivalence ratio at the measurement location. The local equivalence ratio then dictates the gas composition of the remaining mixture. With an estimate of the bulk gas properties, local c^* can be determined. Fig. 5.4 illustrates localized c^* measurements obtained using the measured thermochemical properties (T, CO, CO_2). Similar to the measured tempera-

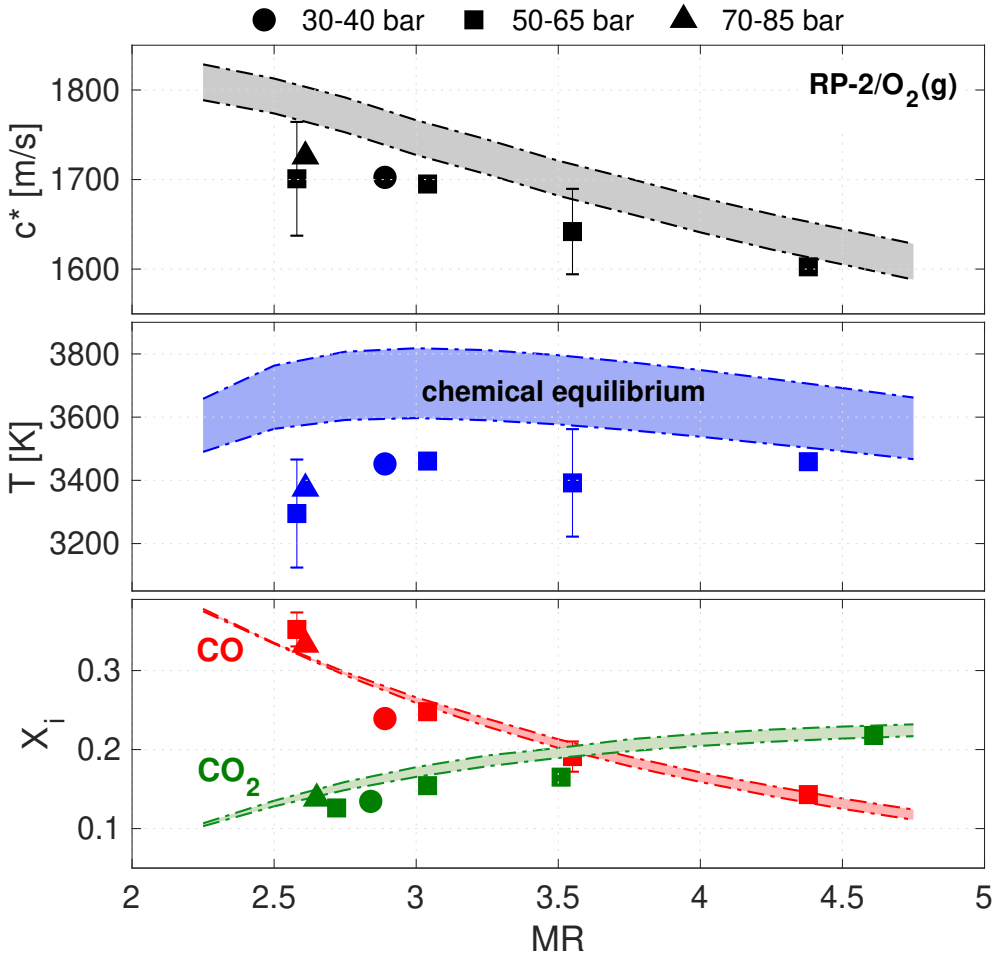

Figure 5.4 Characteristic velocity (c^*), temperature, and CO and CO_2 mole fraction measurements over a range of pressures (P = 28–83 bar) and mixture ratios (MR = 2.5–5) in an RP-2/O_2(g) rocket combustor. Shaded regions demonstrate the expected values from chemical equilibrium.

ture and mole fractions, the localized c^* measurements trend well with the expected values from chemical equilibrium. The measured c^* values are lower by 30–90 m/s, which translates to c^* efficiencies in the range of 94–98%. These results demonstrate the technique's ability to quantify combustion performance at a particular downstream chamber location using measured thermochemical properties over a range of operating conditions. For LRE combustor examined here, all thermochemical measurements were taken at the same axial

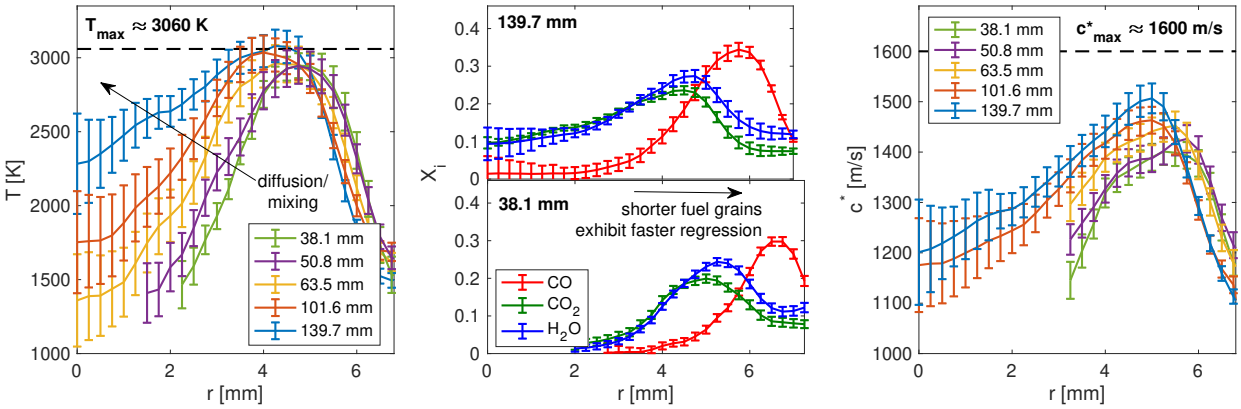

Figure 5.5 *Left to right:* Spatially-resolved temperature, species mole fractions (CO, CO_2, H_2O), and characteristic velocity (c^*) measurements in a PMMA/O_2(g) hybrid rocket combustion experiment with single-port injection. Results are shown for various fuel-grain heights to illustrate axial combustion progress. The center of the fuel grain is located at $r = 0$ mm and the fuel-gain wall is located at $r \approx 6.8$ mm.

position (32 cm downstream of the injector). However, a modular instrumentation spool will enable this procedure to be applied at various axial distances along the combustion chamber to obtain 1D spatially-resolved combustion performance–a current effort from our research group, which will help inform optimal chamber length.

5.4.2 Hybrid rocket combustion

To highlight an example of spatially-resolved characteristic velocity (c^*) measurements, the technique was also demonstrated on a hybrid rocket combustor using poly(methyl methacrylate) (PMMA)/O_2(g) propellants in a canonical hollow fuel cylinder configuration. Combustion progress in hybrid rockets is inherently diffusion-limited due to the different states of the propellants (typically solid fuel and liquid or gaseous oxidizer). As a result, there exist high spatial gradients in the thermochemical flow-field properties at the reacting fuel-oxidizer interface, which not only dictate overall combustion performance, but are remarkably sensi-

tive to changes in engine configuration (oxidizer injector design, pre-/post-combustion chamber, fuel-grain geometry, etc.). Inasmuch, characterizing combustion performance through spatially-resolved characteristic velocity measurements enables a novel granular method for informing engine designs that promote or impede reaction progress.

Description of the hybrid rocket test rig and the LAS measurement procedure is discussed in [6]. Using one-dimensional tomographic reconstruction methods, radially-resolved temperature and species mole fractions for CO, CO_2, and H_2O are obtained at various axial distances along the fuel grain for a single-port injector geometry, as shown in Fig. 5.5. Here, $r = 0$ mm corresponds to the center of the axisymmetric flow-field and the fuel-grain wall is located at $r \approx 6.8$ mm, though some ambiguity exists in the radial distance associated with the fuel-grain surface as a result of the fuel regression throughout the measurement and lack of combustion products in the initial phase change or fuel pyrolysis. Nonetheless, the fuel-grain surface is estimated to be within 0.5 mm of the reported results (supported by post-test measurements of the grain diameter) and these uncertainties are accounted for in the reported error bars. As combustion progresses axially, the local maxima of the flow-field temperature remains fairly constant, but the core temperature increases as a result of the reaction layer growth and turbulent mixing that promotes radial diffusion. Notably, the peak temperature agrees very well with the maximum expected equilibrium temperature, $T_{\max} \approx 3060$ K, shown earlier in Fig. 5.1. Additionally, the peak temperature seemingly corresponds with the oxidation of CO and formation of CO_2, defining a major heat release boundary in the flow-field. Similar to temperature, the measured species mole fractions are observed to increase in the core as distance along the fuel-grain increases. This can also be attributed to increased mixing, a growing reaction layer, and a reduction in oxygen dilution. Overall, the observed trends are consistent with diffusion-limited combustion behavior with a finite reaction zone.

As described in Sec. 5.3.2, the measured temperature and mole fraction distributions are used to estimate a local equivalence ratio to determine the balance gas composition yielding

M and γ of the residual mixture. With this estimate of the overall species composition, in addition to the measured temperature, radially-resolved characteristic velocity can be calculated. Fig. 5.5 illustrates characteristic velocity as a function of radial distance from the center of the flow-field ($r = 0$ mm) at various axial distances along the fuel-grain. The measured c^* values can then be compared to the theoretical maximum, $c^*_{\max} \approx 1600$ m/s, shown previously in Fig. 5.1. Notably, the measured local c^* maxima occur in the high-temperature reaction zone as expected and approach the theoretical maximum, $c^*_{\max}$, as axial distance increases. This increase is also observed in the core of the flow-field, similar to the trends present in the temperature and species measurements. At small axial distances, the center of the flow-field is too dilute with oxygen and precludes further temperature, species, and, accordingly, c^* measurements.

To better visualize the sensitivity of combustion performance to changes in engine design, the c^* results shown in Fig. 5.5 can be compiled into a two-dimensional image by aggregating planar measurements at different axial positions downstream of the injector. The resulting 2D c^* field distribution can be compared for different oxidizer injector geometries. Fig. 5.6 shows spatially-resolved c^* for two injector geometries, single-port and axial showerhead, along with a classical depiction of diffusion-limited hybrid combustion. Aside from the injector change, all other operating parameters (oxidizer mass flow rate, fuel, fuel-grain geometry, etc.) are kept constant to highlight the importance of injector geometry in hybrid rocket combustion.

Comparing the two injectors, the axial showerhead evidently demonstrates higher combustion performance throughout the majority of the combustion chamber. The center of the flow-field, in particular, exhibits significantly higher c^* values at lower axial distances that more closely approach $c^*_{\max}$. Conversely, the single-port injector exhibits much lower c^* values in the core of the flow-field and the highest combustion performance is only attained in a very thin region. These differences are attributed to the reduced level of turbulent mixing present in the single-port injector, which more closely resembles the classical depiction of

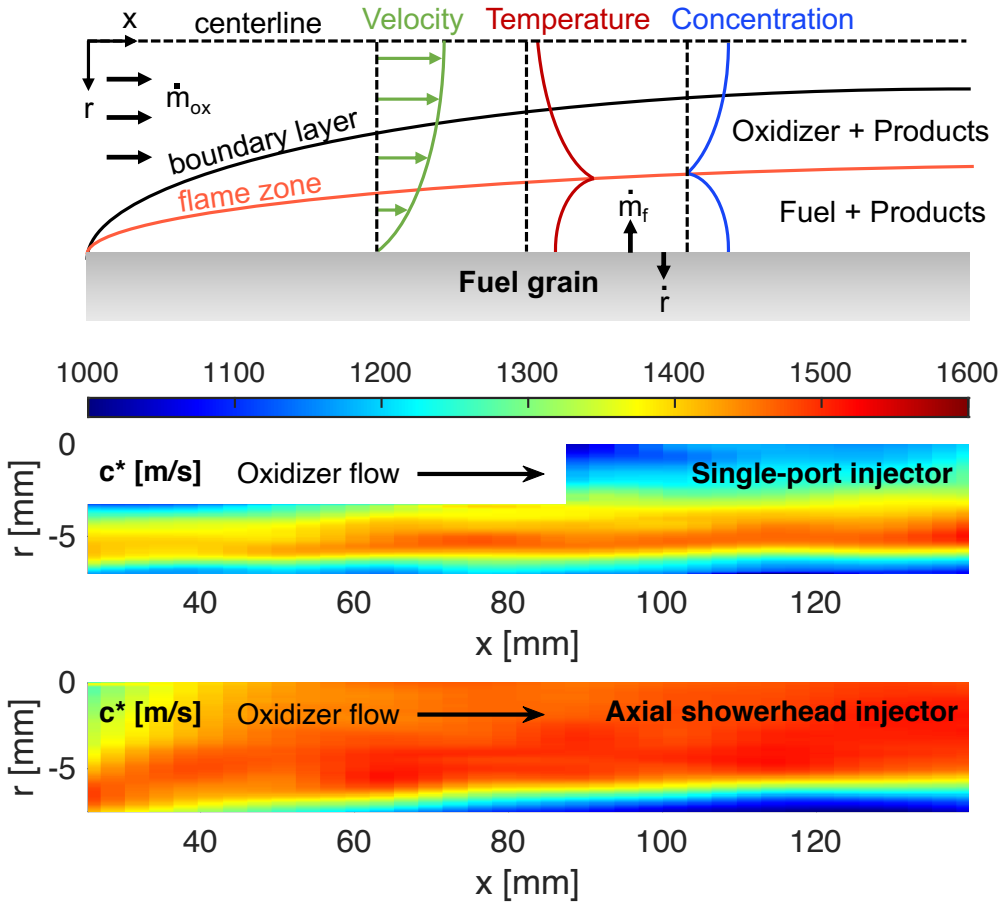

Figure 5.6 Spatially-resolved c^* measurements for two injector geometries (single-port, axial showerhead) in a PMMA/O_2(g) hybrid rocket combustion experiment. A classical depiction of diffusion-limited hybrid rocket combustion is shown for comparison.

diffusion-limited combustion with an infinitely thin flame sheet as shown in Fig. 5.6. In the classical model, the flame zone sits inside a turbulent boundary layer and a fuel-rich region is established near the grain surface, where the fuel vaporizes and reacts with the incoming oxygen. The temperature increases and peaks as it approaches the flame zone, where near stoichiometric conditions are achieved. Afterwards, the oxidizer core dilutes the reaction and the fuel-lean conditions further decrease the combustion temperature. For the

axial showerhead injector, incipient shear-induced turbulence associated with the multitude of high-velocity jets provides for enhanced radial diffusion. At low axial distances ($x < 40$ mm), a low characteristic velocity in the core is observed; however, the turbulent mixing diffuses the downstream reaction layer and increases wall shear, rendering higher concentrations of hot products in the downstream core region relative to the single-port design.

In terms of overall combustion performance, the cool oxidizer core in the single-port injector, which persists over most of the axial length, indicates that much of the oxidizer propellant is not participating in the reaction, resulting in lower combustion efficiencies for practical applications. The axial showerhead injector would provide equivalent performance as a single-port injector while using much shorter fuel-grains. For practical considerations, the implications of this are that, for a desired performance, the propulsion system can see a significant reduction in weight simply from optimizing injector geometry. These results demonstrate the technique's ability to spatially characterize combustion performance and better inform engine designs that promote increased combustion efficiency.

5.5 Uncertainty analysis

This work demonstrates a novel method for calculating localized c^* from temperature and gas composition measurements obtained via LAS. This section details the procedure used to quantify the uncertainties in the resulting c^* values, which encompass both experimental uncertainties in the thermochemical measurements (T, CO, CO_2, H_2O) and systematic uncertainties in estimating the composition (M, γ) of the remaining gas mixture not measured via LAS. Generally, a Taylor series method (TSM) of uncertainty propagation [101] is employed to capture the uncertainty of all dependent variables. For c^*, this takes the form:

$$(\Delta c^*)^2 = \left(\frac{\partial c^*}{\partial \gamma}\Delta\gamma\right)^2 + \left(\frac{\partial c^*}{\partial M}\Delta M\right)^2 + \left(\frac{\partial c^*}{\partial T}\Delta T\right)^2 \tag{5.15}$$

where ΔT is the uncertainty in the measured temperature distribution and $\Delta\gamma$ and ΔM are the uncertainties in the combustion gas composition.

For both the hybrid and liquid-propellant rocket combustor measurements, the reported ΔT incorporates uncertainties associated with the harsh combustion environment (SNR) and systematic uncertainties in spectral properties (i.e. linestrength, collisional broadening) as shown in Eq. 5.16:

$$(\Delta T)^2 = (\Delta T_{\mathrm{SNR}})^2 + (\Delta T_{\mathrm{spec}})^2 \tag{5.16}$$

The uncertainty associated with convoluted environmental and optical noise, ΔT_{SNR}, is determined via a 95% confidence interval on the measured absorbance. The systematic uncertainty in spectral properties, ΔT_{spec}, is determined using the reported HITRAN 2016 [51] and HITEMP 2010 [102] linestrength uncertainties as well as an estimation of the uncertainty in composition-dependent collisional broadening. Additionally, for the hybrid rocket combustor measurements shown in Figs. 5.5–5.6, spatially-resolved thermochemistry is obtained by implementing a one-dimensional tomographic reconstruction technique. As such, an additional uncertainty intrinsic to the tomographic inversion, which reflects the impact of noise in the projection and data point spacing [55], is incorporated to propagate ΔT_{SNR} radially towards the centerline. For the liquid-propellant rocket combustor results shown in Fig. 5.4, thermochemical properties are assumed to vary minimally along the line-of-sight. In this case, spatially-resolved measurements are obtained by simply conducting measurements at various axial locations along the combustor with some added uncertainty associated with line-of-sight non-uniformity. Further details on obtaining the temperature uncertainty in such cases can be found in previous works from our research group [6, 70, 71, 103]; typical values for the measurements presented herein are $\Delta T \approx$ 110–260 K for the hybrid rocket experiments and $\Delta T \approx 170$ K for the liquid-propellant rocket measurements. These uncertainties are also illustrated in Figs. 5.4–5.5.

As mentioned in Sec. 5.3.2, M and γ are partially obtained using the measured mole fractions as shown in Fig. 5.4 and Fig. 5.5. The measured mole fractions, however, do not represent the complete composition of the flow-field and so the remaining gas mixture is estimated by using the measured properties to approximate a local equivalence ratio. As

such, $\Delta\gamma$ and ΔM contain uncertainty contributions from both the measured mole fractions (CO, CO_2, H_2O) and the estimate of the remaining gas mixture composition. This is captured in Eq. 5.17 and Eq. 5.18:

$$\begin{aligned}(\Delta M)^2 = &(M_{\mathrm{CO}}\Delta X_{\mathrm{CO}})^2 + (M_{\mathrm{CO_2}}\Delta X_{\mathrm{CO_2}})^2 \\ &+ (M_{\mathrm{H_2O}}\Delta X_{\mathrm{H_2O}})^2 + \sum_i (M_i \Delta X_i)^2\end{aligned} \tag{5.17}$$

$$\begin{aligned}(\Delta \gamma)^2 = &(\gamma_{\mathrm{CO}}\Delta X_{\mathrm{CO}})^2 + (\gamma_{\mathrm{CO_2}}\Delta X_{\mathrm{CO_2}})^2 \\ &+ (\gamma_{\mathrm{H_2O}}\Delta X_{\mathrm{H_2O}})^2 + \sum_i (\gamma_i \Delta X_i)^2\end{aligned} \tag{5.18}$$

Similar to the uncertainty in the measured temperature, the uncertainty in the measured mole fractions, ΔX_i, also comprise uncertainties associated with the harsh combustion environment and systematic uncertainties in spectral properties. In addition to these, the uncertainty in the measured temperature, ΔT, and how it propagates into ΔX_i is also considered, as shown in Eq. 5.19:

$$(\Delta X_i)^2 = (\Delta X_{i,\mathrm{SNR}})^2 + (\Delta X_{i,\mathrm{spec}})^2 + (\Delta X_{i,\Delta T})^2 \tag{5.19}$$

$\Delta X_{i,\mathrm{SNR}}$ and $\Delta X_{i,\mathrm{spec}}$ are obtained analogously to the aforementioned temperature uncertainties. $\Delta X_{i,\Delta T}$ is calculated based on the added uncertainty in spectral properties (i.e. linestrength, broadening coefficient) that result from an uncertainty in the measured temperature. Further details on obtaining the mole fraction uncertainty can be found in [6, 70, 71]; however, typical values for the measurements presented herein are $\Delta X_i \approx 0.01$–0.02 for the hybrid rocket experiments and $\Delta X_i \approx 0.01$–0.03 for the liquid-propellant rocket measurements. These uncertainties are similarly illustrated in Figs. 5.4–5.5.

In calculating the uncertainties in molecular weight, ΔM, and the specific heat ratio, $\Delta\gamma$, Eq. 5.19 can be implemented for all the measured species. The resulting uncertainty from Eq. 5.19 influences the resulting uncertainty in M and γ via Eqs. 5.17–5.18. For the hybrid rocket measurements, this includes CO, CO_2, and H_2O; however, for the liquid-propellant rocket combustor experiments, H_2O is part of the balance gas. The uncertainty in species

that are not directly measured (i.e. the uncertainty of the remaining gas composition) can be evaluated via Eq. 5.20:

$$(\Delta X_i)^2 = \left(\frac{\partial X_i}{\partial \phi} \Delta \phi \right)^2 \tag{5.20}$$

where $\Delta\phi$ is the uncertainty in the local equivalence ratio determined by the uncertainty in the measured species, as described in Sec. 5.3.2. For the liquid-propellant rocket combustor data shown in Fig. 5.4, mixture ratio, $MR = \text{O/F}$, is related to equivalence ratio via: $\phi = (\text{O/F})_{\text{stoic}}/(\text{O/F})$

The results presented herein consider the uncertainties described in Eqs. 5.16–5.20. These values are then used to calculate the resulting uncertainty in the local characteristic velocity measurements via Eq. 5.15. Typically values for the uncertainty in local characteristic velocity are $\Delta c^* \approx$ 18–62 m/s for the hybrid rocket experiments and $\Delta c^* \approx$ 45–65 m/s for the liquid-propellant rocket combustor experiments. In addition to the reported values, it is often desirable to better understand how the uncertainty in these dependent variables (T, M, γ) ultimately influence the uncertainty in characteristic velocity. This is visually portrayed in Fig. 5.7, which demonstrates how the relative uncertainty in temperature, molecular weight, and specific heat ratio, influences the relative uncertainty in characteristic velocity. In Fig. 5.7, a on the x-axis simply represents a dummy variable, where $\Delta a/a$ corresponds to $\Delta T/T$, $\Delta M/M$, and $\Delta\gamma/\gamma$. The relative uncertainties are plotted over the full range of expected values for MMA/O_2(g) combustion given the chemical equilibrium assumptions considered herein. Notably, the dependent variable that can have the most variability is temperature, which can vary from 300 K, when propellants are introduced, to 3060 K, which is the peak adiabatic flame temperature. Conversely, the specific heat ratio only changes very minimally ($< 10\%$) over a wide range of conditions. As such, when simply considering the range of possible values, temperature has the potential to more largely drive uncertainties in characteristic velocity compared to gas composition. However, since the composition is only partially measured while temperature is measured directly, temperature and molecular weight are found to contribute near equally to the c^* uncertainty. As shown in Fig. 5.7, only

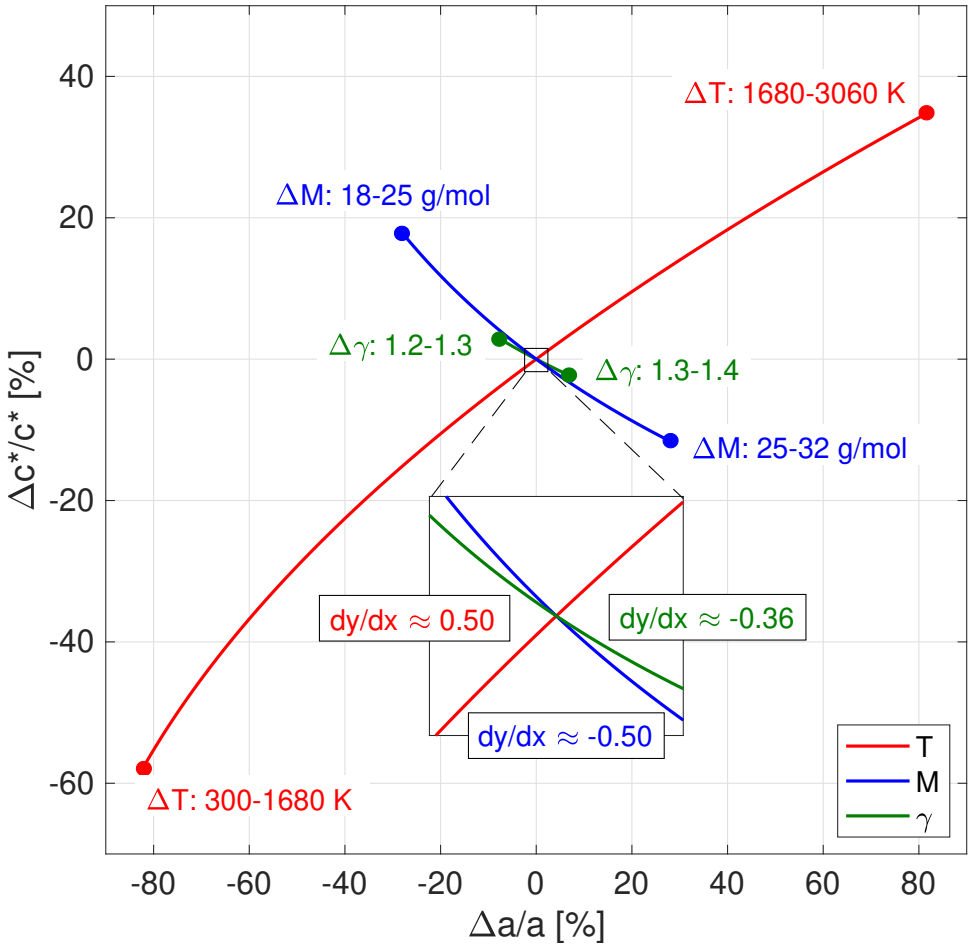

Figure 5.7 The corresponding uncertainty in characteristic velocity ($\Delta c^*/c^*$) for a given uncertainty in temperature ($\Delta T/T$), molecular weight ($\Delta M/M$), and specific heat ratio ($\Delta\gamma/\gamma$) over a representative range of possible values. The different lines represent $a = T$, M, and γ

$\sim 50\%$ of the uncertainty in temperature, $\Delta T/T$, and molecular weight, $\Delta M/M$, propagates into the resulting uncertainty in characteristic velocity, $\Delta c^*/c^*$. For specific heat ratio, even less is observed, where only $\sim 36\%$ of the uncertainty, $\Delta\gamma/\gamma$, propagates into the resulting uncertainty in characteristic velocity, $\Delta c^*/c^*$.

5.6 Conclusions

A novel method for experimentally obtaining localized characteristic velocity from laser absorption spectroscopy measurements of temperature and gas composition has been developed and demonstrated. This method more granularly assesses the spatial variations in chemical-to-thermal energy conversion present in rocket combustion devices and serves as an alternative to the classical c^* measurement that relies on global chamber pressure and mass flow rate. The technique was demonstrated on two distinct chemical rocket test configurations, namely an RP-2/O_2 liquid-propellant rocket engine and a PMMA/O_2 hybrid rocket combustion experiment. For the LRE, in-chamber measurements of temperature, CO, and CO_2 were used to determine local c^* values over varying pressures (P = 28–83 bar) and mixture ratios (MR = 2.5–5). For the hybrid rocket, one-dimensional tomographic reconstruction techniques were incorporated to obtain spatially-resolved measurements of temperature, CO, CO_2, and H_2O, enabling spatially-resolved c^* images of the combustion zone. While this method is evidently not limited to hybrid rockets, this case provides a thorough demonstration of the technique's unique ability to discern spatial-variations in combustion progress relative to chemical equilibrium. Notably, incomplete composition measurements were reconciled by using an estimated local equivalence ratio to approximate the balance gas mixture. An uncertainty analysis was performed to account for such assumptions and other sources of potential error or noise in the two applications.

CHAPTER 6

Methyl methacrylate thermal decomposition: Modeling and laser spectroscopy of species time-histories behind reflected shock waves

he thermal decomposition of methyl methacrylate (MMA) was studied through species time-history measurements of formaldehyde (CH_2O), carbon monoxide (CO), and carbon dioxide (CO_2) behind reflected shock waves over a temperature range of 1200–1600 K near 1 atm. Tunable laser absorption spectroscopy was employed to spectrally and temporally-resolve a cluster of rovibrational lines in the Q-branches of the v_1 fundamental band and the v_2+v_4 combination band of CH_2O near 3.60 µm, three rovibrational transitions in the P-branch of the fundamental band of CO near 4.98 µm, and a transition in the R-branch of the ($01^00 \rightarrow 01^01$) v_3 band of CO_2 near 4.19 µm. Spectral fitting procedures are subsequently used to infer CO, CO_2, and CH_2O mole fraction during the pyrolysis of shock-heated mixtures of MMA in argon. These data provided valuable experimental constraints on MMA pyrolysis chemical kinetic models. Sensitivity analysis of a detailed chemical model for MMA decomposition identified specific reactions likely to account for differences observed between the species measurements and simulations of the test conditions. Modified reaction rate parameters for select MMA decomposition reactions are proposed, determined via a genetic algorithm optimization procedure anchored to the speciation data.

6.1 Introduction

Poly methyl methacrylate (PMMA, also commonly referred to as *acrylic* glass) is a synthetic solid fuel of keen interest to both the fire science and propulsion communities [104, 105, 106, 107, 108, 109, **?**, 71, 110]. In fire science, PMMA has recently been used as a baseline solid fuel to study flame spread in both normal [111] and reduced [112] gravity, with applications to material flammability for in-space missions. In propulsion, the stability of PMMA in long-term storage has motivated its investigation as both a hybrid rocket propellant [113, **?**] and for solid-fuel scramjet applications [114]. In both applications, knowledge of PMMA's regression rate—which is influenced heavily by local radiant heat flux and flow conditions—is critical to device safety, performance, and mission lifetime. Unlike many polymers, the pyrolysis kinetics of PMMA are not complicated by charring or cross-linking behavior and it involves relatively simple depolymerization behavior; its constituent monomer—methyl methacrylate (MMA, $C_5H_8O_2$)—accounts for over 90% of its pyrolysis products [106], providing a relatively tractable model for solid fuel combustion. However, the detailed reaction chemistry of the MMA monomer itself is not well-characterized, hindering the design and modeling of next-generation hybrid combustion devices and advanced fire science experiments.

Existing models describing MMA reaction chemistry have been primarily developed during broader investigations of oxygenated hydrocarbon reaction kinetics. MMA belongs to a class of oxygenated compounds known as *esters*, specific types of which have received increasing attention in recent years owing to their potential to augment or replace conventional fossil-derived hydrocarbon fuels [115]. However, the pyrolysis and oxidation kinetics of many such esters are difficult to characterize in the laboratory owing to their high molecular weights and low vapor pressures [10, 116, 117]. For this reason, relevant experimental and computational research efforts have focused on smaller molecules with similar or analogous functional groups—including short-chain akyl esters like MMA—with the aim of providing kinetic insights on their long-chain counterparts. Examined esters which share reaction chemistry

with MMA include acetates and formates [118, 119], butanoates and propanoates [120, 116], as well as crotonates, propenoates, and acrylates [10, 117], among others.

However, previous chemical kinetic studies specifically involving MMA—which can provide modeling constraints specific to its molecular structure—have been limited to laminar flame investigations [104, 121, 122, 10, 11, 123, 124]. Laminar flames provide useful validation benchmarks, but the convolution of transport mechanisms with pyrolysis and oxidation chemistry complicate the interrogation of specific reaction pathways, specifically the incipient fuel decomposition chemistry. Moreover, the kinetics of fuel pyrolysis and ignition are radically distinct from those of flames [125], wherein the destruction of the fuel molecules is achieved mainly through a convolution of thermal diffusion and H-abstraction reactions readily enabled by an abundance of radicals provided by the flame zone. To illustrate the shortcomings of reaction model optimization on the basis of laminar flames alone, time-resolved well-mixed constant pressure reactor simulations of MMA decomposition at 1350 K and 1 atm using two different chemical kinetic models are shown in Fig. 6.1.

The first chemical model shown, by Dakshnamurthy et al. [11], has been reduced from the second model shown by Yang et al. [10] and optimized for multidimensional reacting flow simulations of MMA combustion. In these chemical models, many Arrhenius reaction rate parameters relevant to MMA decomposition and oxidation have been estimated [120] or based on those of similar reactions of other molecules [11]. Notably, the two models disagree in their time-resolved species predictions by multiple orders of magnitude, despite both reasonably reproducing species profiles and flame speeds of laminar flames fueled by MMA [10, 11].

To address these discrepancies, the predictive capability of fuel decomposition models can be evaluated in the laboratory through comparison with time-resolved species measurements behind reflected shock waves using optically-based measurement methods such as laser absorption spectroscopy (LAS) [126]. Notably, shock tube experiments can provide near homogenous, isothermal conditions absent of transport phenomena, and may be used

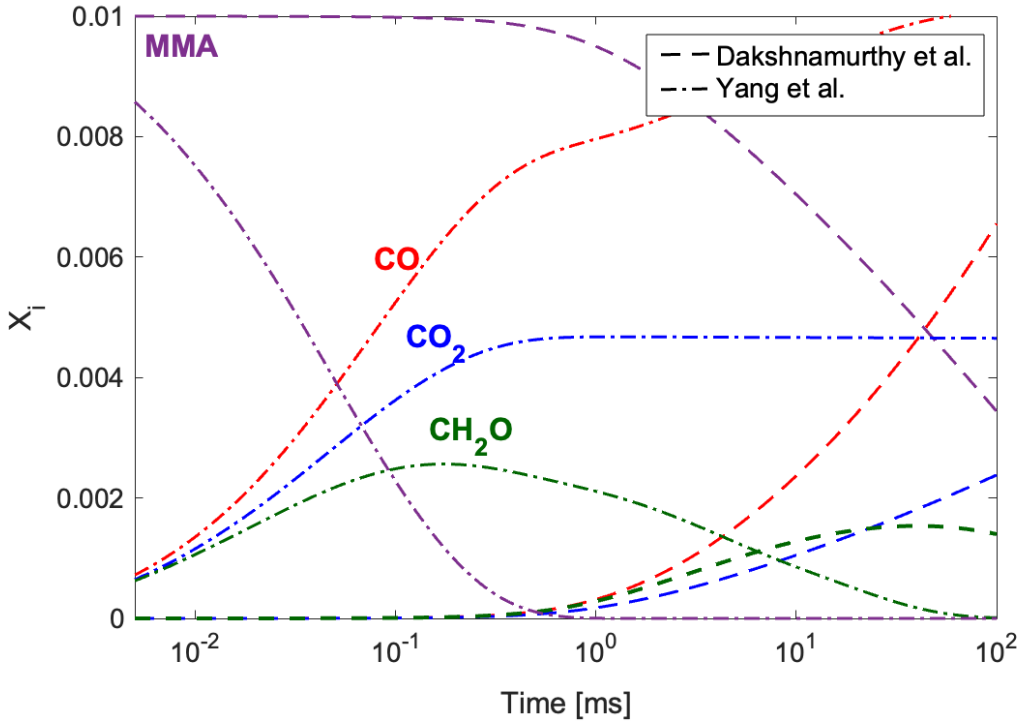

Figure 6.1 Predicted combustion species evolutions at 1350 K from a 1% initial concentration of MMA diluted in argon at 1 atm using the chemical models published by Yang et al. (dot-dashed line) and Dakshnamurthy et al. (dashed).

to study high-temperature chemical kinetics without oxidation chemistry. As such, shock tubes provide an ideal reactor for studies of thermal pyrolysis.

When coupled with automated reaction model optimization [127, 128, 129], multiple Arrhenius rate parameters can be optimized simultaneously across multiple experiments performed at different temperatures, reducing the uncertainties in parameters that were hitherto estimated by functional group analogy or through ab-initio computational chemistry.

In this study, we investigate the reaction kinetics of methyl methacrylate decomposition at elevated temperatures (1200–1600 K) and near-atmospheric pressures behind reflected shock waves via time-resolved laser absorption measurements of CO, CO_2, and CH_2O mole fraction. We first present our experimental methodology, including experimental shock tube

apparatus, optical setup, and laser absorption spectroscopy, with specific attention to wavelength selection and data interpretation. We follow this with a presentation of our novel dataset capturing CO, CO_2, and CH_2O evolution alongside predictions of kinetic models targeting MMA reaction chemistry. A detailed analysis is performed examining the causes of disagreement between model predictions and experimental observations, identifying some key uncertain reactions in the models by performing sensitivity analyses of reactions with respect to predicted mole fractions of CO, CO_2, and CH_2O. We modify multiple rate parameters of these identified reactions using an automated optimization procedure which seeks to minimize the discrepancies between the model predictions and experimental observations across all of the temperatures achieved in the experiments. The modified rate parameters are shown to yield significant improvement in predictive capability for time-resolved CO, CO_2, and CH_2O evolution during MMA decomposition. It is envisioned that the adjusted rate parameters will provide more accurate predictions in applications involving MMA for which chemical timescales are particularly relevant, such as in turbulent [130] and extinction [131] combustion regimes, which pervade propulsion and fire environments, respectively.

6.2 Experimental Methods

6.2.1 Experimental setup

High-temperature chemical kinetics experiments in this study were performed in the High Enthalpy Shock Tube facility (HEST) at UCLA, described in previous work [132, 133] and depicted in Fig. 6.2. The stainless steel shock tube comprises a 1.5-m high-pressure driver section and a 4.9-m low-pressure driven (test gas) section, separated by a polycarbonate diaphragm. The test section of the shock tube has a transverse optical pathlength of $L = 10.32$ cm and is circumscribed by interchangeable ports holding either sensors or optical windows, positioned axially 2 cm from the end wall. For all experiments, reflected shock pressure in the shock tube test section is measured directly with a dynamic pressure trans-

ducer (Kistler 601B1) via a charge amplifier (Kistler 5018A) and post-shock temperature is inferred from the shock wave speed determined via time of arrival sensors (Dynasen, Inc.) along the shock tube. Uncertainty in reflected shock test conditions are typically about 1% when properly accounting for vibrational relaxation of all components of the test gas [134].

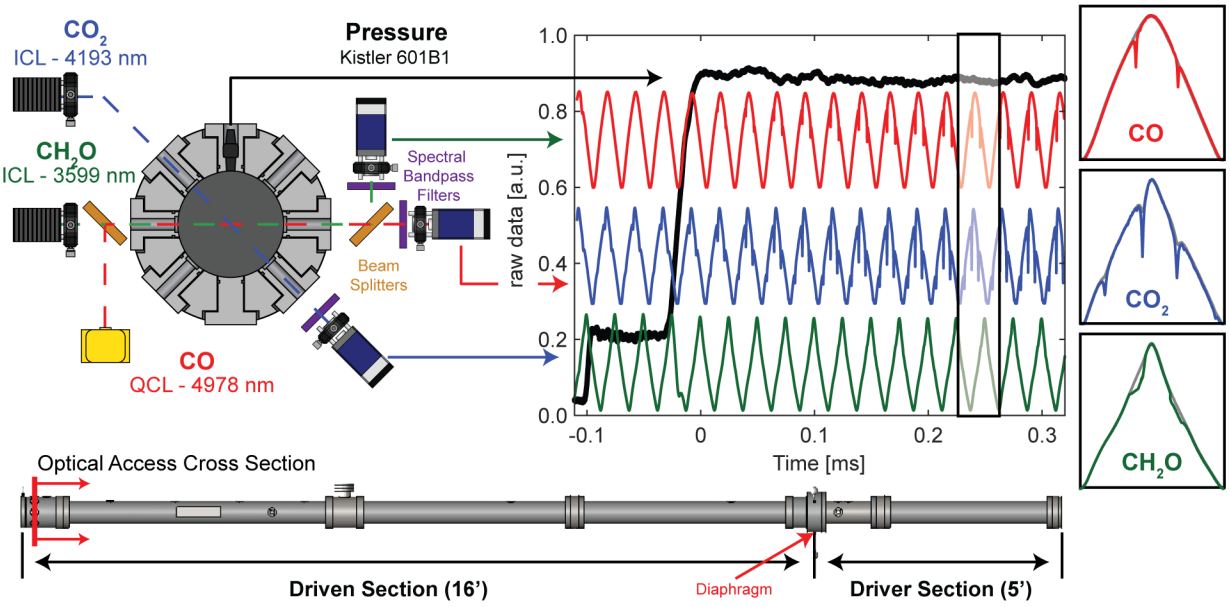

Figure 6.2 (top left) Cross sectional view of HEST facility showing optical access and laser/detector setup. (bottom) Side view of HEST facility marking location of cross section at the end of the driven section on the left. (top right) Representative time histories of pressure (black), formaldehyde (green), CO (red) and CO_2 (blue) from shock heated mixture of MMA.

The shock tube is connected to vacuum pumps, an agitated mixing tank, and a gas delivery manifold used to barometrically prepare gas mixtures for all experiments using dual-capacitance heated manometers (MKS Baratron 627B). Notably, the gas delivery manifold is also connected to an interchangeable glass flask containing either solid or liquid chemicals from which gaseous vapors are evaporated and mixed with inert gases during preparation

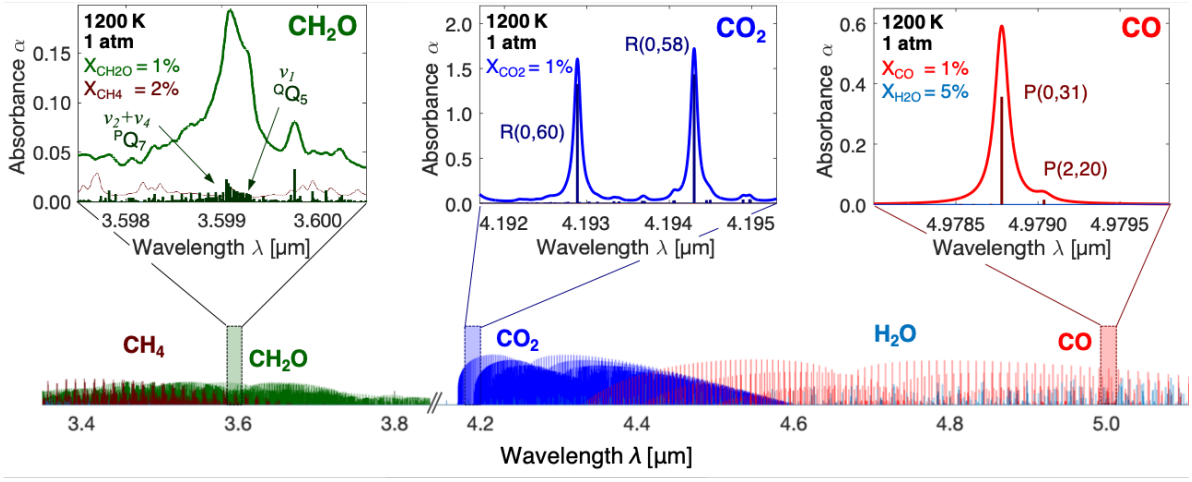

Figure 6.3 *Bottom:* Absorption linestrengths for CH_4, CH_2O, CO_2, H_2O, and CO at 1200 K, simulated using the HITRAN [7] and HITEMP [8] databases. *Top:* Absorption simulations for CH_2O (left), CO_2 (middle), and CO (right), highlighting targeted wavelength regions and spectral features. CH_2O absorption simulated using the AYTY line list [9].

of the test gas mixtures. For studying the decomposition of MMA, mixtures of MMA in argon (Ar) were prepared by evaporating liquid MMA from the interchangeable glass flask into the agitated mixing tank to a desired partial pressure (below MMA's vapor pressure of ∼29 Torr) and subsequently filling the tank with Ar. Prior to the preparation of each mixture and before each shock test, the inner surfaces of the mixing tank and shock tube driven section are passivated with MMA and the prepared MMA/Ar mixture, respectively, after which the mixing tank and shock tube test section are vacuumed and filled to the desired fill pressure. The procedure specifics were developed such to mitigate adsorption of MMA from the test gas mixture into the walls.

6.2.2 Laser Absorption Spectroscopy

Laser absorption spectroscopy (LAS) is a well-established optical diagnostic technique for shock tube kinetics studies, owing to its high time-resolution, species specificity, and quantitative capability in the measurement of species and temperature [126]. Spectral absorbance $\alpha(\nu)$ of species measured in this work is calculated using the ratio of transmitted light (I_t) to incident light (I_0) at wavenumber ν [cm^{-1}] as defined by two different forms of the Beer-Lambert law:

$$\begin{aligned} \alpha(\nu) = -\ln\left(\frac{I_t}{I_0}\right)_\nu &= PX_{\text{abs}}S_i(T)\varphi_i(\nu)L \\ &= \sigma_{\text{abs}}(\nu,P,T)LN_{\text{abs}} \end{aligned} \tag{6.1}$$

In the first form, P [atm] is the total pressure, X_{abs} is the absorbing species mole fraction, $S_i(T)$ [cm^{-2}/atm] is the linestrength for rovibrational transition i at temperature T [K], and L [cm] is the absorption pathlength. In the second form, $\sigma_{\text{abs}}(\nu,P,T)$ [cm^2/molec.] is the absorbing species cross-section (dependent on ν, P, and T), and N_{abs} [molec./cm^3] is the absorbing species number density. The first form, used here to evaluate temperature and concentration of CO and CO_2, is typically employed when a comprehensive line-by-line spectral database of an absorbing species is confidently known and the spectral transitions i are easily separable in the absorbance measurement [71].

The second cross-section formulation of the Beer-Lambert law is appropriate for broadly-absorbing species for which the temperature-dependent line-by-line spectroscopy are less well-known and/or the absorbance spectra are convoluted enough to preclude identification of individual spectral transitions from the absorbance measurement.

In this study, we employ this second form of the Beer-Lambert law to quantitatively evaluate the temperature and concentration of formaldehyde, CH_2O, using a database of spectrally-resolved cross-sections $\sigma_{\text{abs}}(\nu,P,T)$ at multiple pressures and temperatures detailed in a separate work [135].

Spectroscopic measurements of CO and CO_2 are simultaneously performed with line-by-

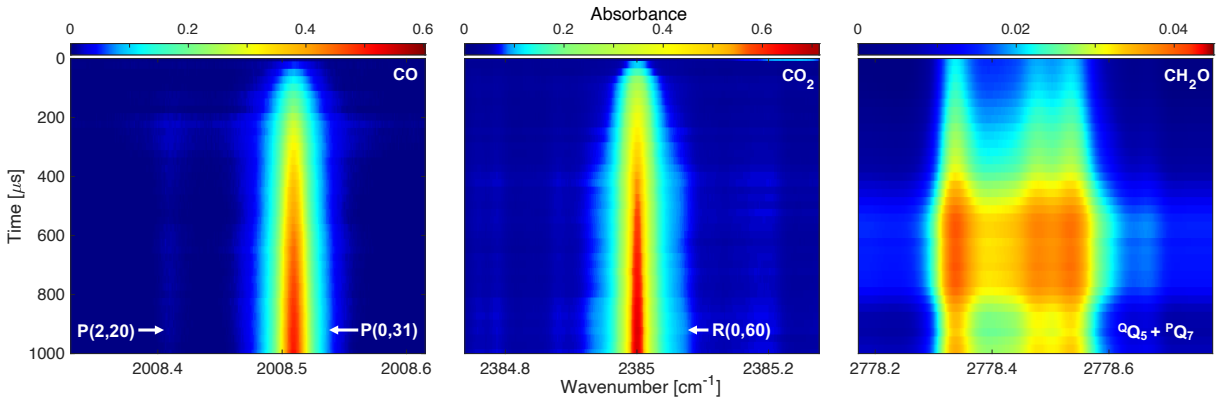

Figure 6.4 Time evolution of absorbance of CO, CO_2, and CH_2O shown for a test at mid-range condition (T_5 = 1390 K, P_5 = 0.98 atm)

line interpretation.

An interband cascade laser (ICL, Nanoplus) with ∼8.3 mW of output power is used to target absorbance features of CH_2O near 3.60 µm, while an ICL (Nanoplus) with ∼6 mW of output power targets CO_2 absorption features near 4.19 µm and a quantum cascade laser (QCL, ALPES Lasers) with ∼50 mW of output power targets CO absorbance features near 4.98 µm. Figure 6.2 shows the optical setup in which the output light from each laser is pitched through the shock tube test section, spectral bandpass filters, irises, and focusing lenses onto photovoltaic (PV) detectors (VIGO Photonics).

The targeted spectral regions for each of the species measurements are shown in Fig. 6.3. The ICL used for CH_2O provides a scan depth of 1.03 cm^{-1} at 40 kHz over a spectral range surrounding a collection of lines near 2778.5 cm^{-1} comprising the $^{Q}Q_5$ branch of the v_1 symmetric C–H stretch band and the $^{P}Q_7$ branch of the v_2+v_4 combination band of CH_2O [136]. Likewise, the ICL targeting CO_2 provides a scan depth of 1.25 cm^{-1} over the R(0,60) line of CO_2's ($01^{0}0 \rightarrow 01^{0}1$) v_3 fundamental band near 2385 cm^{-1}, while the QCL provides a scan depth of 1.45 cm^{-1} over the P(0,31) and P(2,20) lines of CO's fundamental band near 2008.5 cm^{-1}.

All lasers are scanned at 40 kHz using a triangle wave; representative scans for both the incident (I_0) and transmitted (I_t) intensity of each laser are shown in the right of Fig. 6.2 alongside a corresponding dynamic pressure measurement. The measured absorbance over 1 ms of post-shock test time is shown for each of CO, CO_2, and CH_2O in Fig. 6.4. The detection limits for tests over 1200 K to 1600 K for CO, CO_2, and CH_2O ranged from 5–10 ppm, 10–20 ppm, and 50–90 ppm, respectively. Following the procedure described in [71], the CO and CO_2 spectra at each scan or time-step are fit assuming Voigt lineshape profiles [137] using spectral information from the HITEMP database with absorption areas, collisional widths, and linecenters as free parameters [8]. The measured CH_2O spectra are fit against the temperature-dependent cross-section database of Kuenning et al. by fixing temperature (via two-line thermometry of the CO and CO_2 spectra) and pressure (from pressure transducer) and with mole fraction as a free parameter [135].

6.3 Results

Shock tube experiments were conducted with 1% MMA near 1 atm (0.88 atm–1.10 atm) at initial post-shock temperatures in the range 1200–1600 K. Mole fraction time-histories for the three species measured in this work are shown in Fig. 6.5 for two representative experiments at different temperatures, along with corresponding predictions by the chemical models of Yang et al. [10] and Dakshnamurthy et al. [11]. Mole fraction time-history predictions are simulated by assuming the measured reflected shock temperature T_5, pressure P_5, and gas composition as the prescribed initial conditions in a constant pressure well-stirred reactor model. Representative error bars are shown for uncertainty in measured species time histories and were calculated by propagating the uncertainty in measured temperature, reference-temperature transition linestrength (for CO and CO_2), absorption cross-section (for CH_2O), and the reflected shock temperature and pressure, as in previous shock tube studies [133, 132]. The average relative uncertainties in measured mole fractions of CO and CO_2 were 9% and

6%, respectively. For CH_2O, the average relative uncertainty was ~25% due to uncertainty in the cross-sections used to calculate mole fraction and weak relative signals. For this reason we primarily employ the CO and CO_2 measurements to guide the rate parameter modification (discussed later) and use the CH_2O data as a supplementary tool for validation.

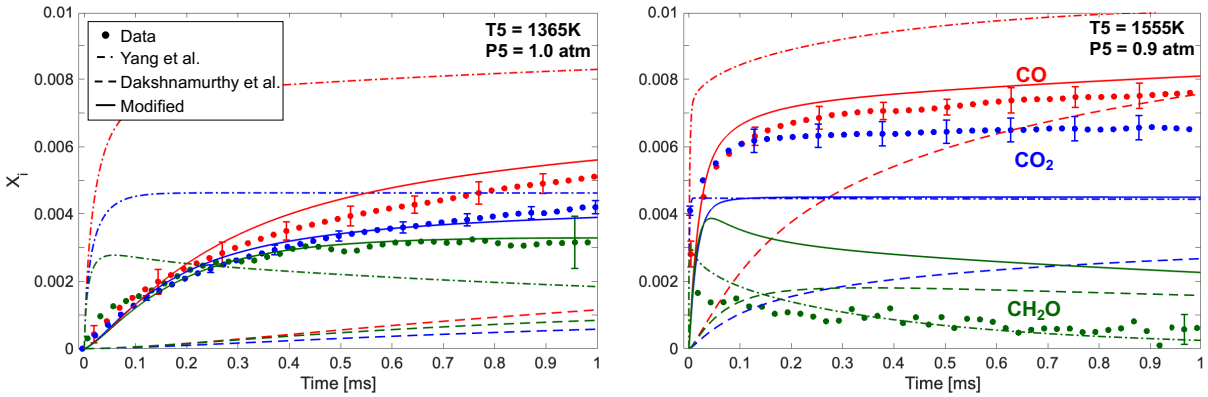

Figure 6.5 Comparison of measured CO, CO_2, CH_2O mole fractions with simulations using the short MMA mechanism from Dakshnamurthy et al. (dashed line), the full mechanism from Yang et al. (dot-dashed line), and the modified mechanism from the current work (solid line).

The measurements deviate significantly from the predictions by both models with respect to CO and CO_2 mole fraction, with the detailed model by Yang et al. [10] over-predicting the production of CO and CO_2, and the reduced model by Dakshnamurthy et al. [11] under-predicting the production of all measured species. Notably, measurements of CH_2O show modest to good agreement with the magnitude of mole fraction predictions by the detailed model of Yang et al. However, the detailed model predicts rapid CH_2O formation followed by slow depletion above $T_5 \approx 1230$ K, whereas this behavior is only observed experimentally at conditions above $T_5 \approx 1390$ K.

The observed temperature dependence of this species production and destruction is better predicted using a modified version of the reduced model presented here (described in Sec. 6.4), despite residual discrepancy in magnitudes at the highest temperatures. We provide detailed

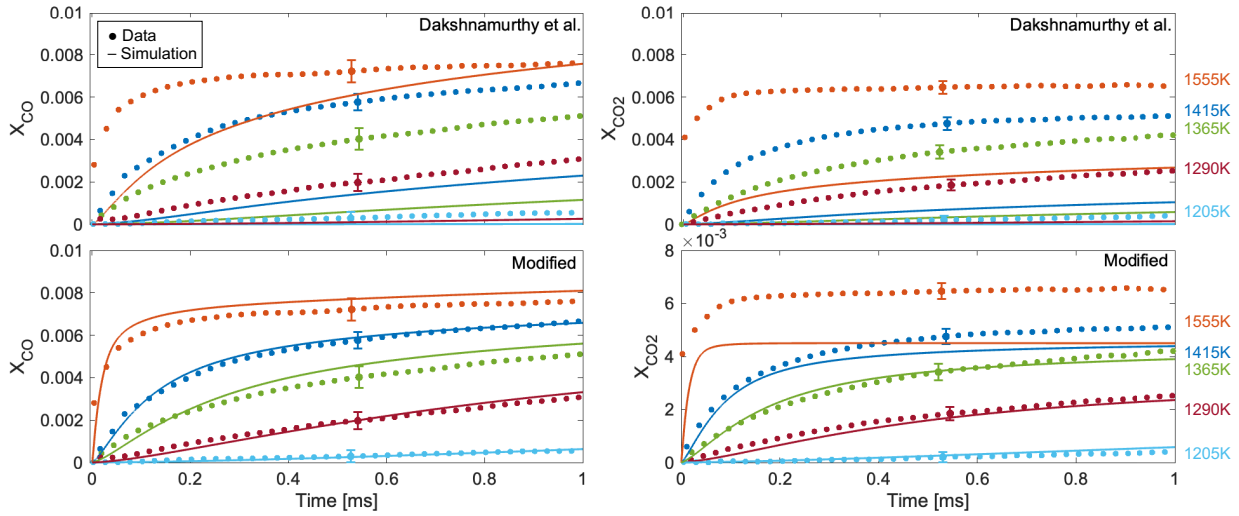

Figure 6.6 Comparison of measured CO and CO_2 mole fractions with simulations (solid lines) using the short MMA mechanism from Dakshnamurthy et al. (top) and the modified mechanism from the current work (bottom).

discussion on the methodology of the rate parameter adjustments in the development of our modified version of the chemical model in Section 6.4; however, we include the modified model predictions in this section for reader convenience and to avoid redundancy in figure content.

Measured species time histories at multiple different initial temperatures are plotted in Fig. 6.6 for CO and CO_2, alongside predictions using both the reduced model by Dakshnamurthy et al. [11] and our modified version of that model. As discussed in Section 6.4, we anchored the rate parameter optimization to the mole fractions time-histories of both CO and CO_2 while the CH_2O data, where available, served as a valuable additional benchmark for independent verification. Across all temperatures examined, CO and CO_2 are produced in measurable quantities immediately post-shock at formation rates that increase with increased initial temperature T_5. At low temperatures ($T_5 < 1400$ K), CO and CO_2 are observed to increase monotonically during the measured test time (~1 ms), while at higher temperatures, a plateau in yield is observed, wherein the mole fractions of CO and

CO_2 both increase rapidly, and subsequently increase more slowly for CO while nearly stagnating for CO_2. The experimentally observed leveling off of CO_2 supports the hypothesized reaction pathways of both the detailed and reduced models, which predict CO_2 formation relatively early in MMA decomposition [10, 11], despite its traditional role as a final product in combustion.

Within the measurement test time, this transition point in kinetic behavior is predicted by the Dakshnamurthy et al. model to occur at higher temperatures than were observed experimentally, whereas the Yang et al. model predicts this trend transition at lower temperatures.

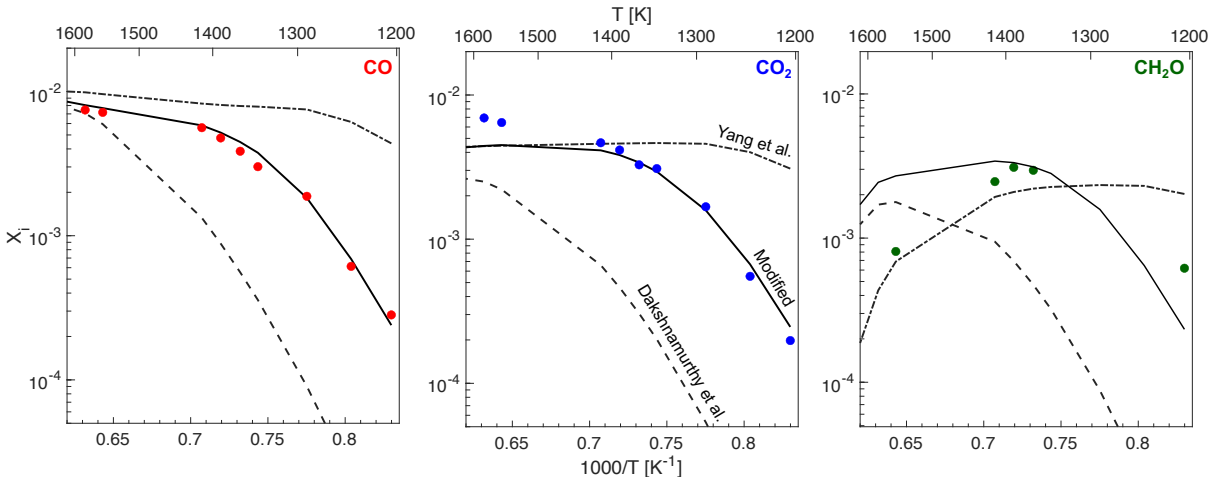

Figure 6.7 Mole fraction yield for CO, CO_2, and CH_2O at 0.5 ms for 1% MMA/Ar pyrolysis. Markers represent measurements and lines represent the Yang et al. [10], Dakshnamurthy et al. [11], and final modified models.

6.7 shows the measured mole fraction of CO, CO_2, and CH_2O at 0.5 ms post-shock as a function of temperature compared to predictions from the three models considered in this work.

Improved agreement is achieved across the measured temperature range for CO and CO_2 mole fractions with our modified model. Starting from 1200 K, CO and CO_2 yields increase rapidly with temperature until a temperature threshold for trend transition is reached near

1400 K, above which the CO and CO_2 yield increase more slowly. As temperatures approach the higher end of the measured range, the three models converge in prediction of CO and CO_2, highlighting the value of data at lower temperatures ($T_5 < 1400$ K) where model predictions more distinctly diverge. For $T_5 = 1500$–1600 K, both the Yang et al. and modified models predict a more dramatic plateau in CO_2 mole fraction than is observed experimentally, while the Dakshnamurthy et al. model under-predicts the mole fraction most significantly.

The measured CH_2O yield initially increases with temperature, peaks around $T_5 \approx 1390$ K, then decreases with further increasing temperature. The models all predict a similar trend, albeit with different temperature ranges governing this trend.

The Yang et al. and Dakshnamurthy et al. models both predict a lower peak CH_2O yield than observed, with the Yang et al. model suggesting peak yield at a lower temperature and the Dakshnamurthy et al. model predicting peak yield at a higher temperature than observed. The modified mechanism more closely matches the peak yield magnitude and temperature. With the exception of the mole fraction yield recorded near $T_5 = 1550$ K, the modified model most effectively reproduces the measured CH_2O yield, despite not being included as a speciation target in the mechanism optimization.

6.4 Kinetic modeling

In this section, we discuss the reaction kinetics of MMA decomposition and analyze chemical models for this kinetic behavior in context of the results presented in the previous section. We first briefly review existing kinetic models describing MMA reaction chemistry by Yang et al. [10] and Dakshnamurthy et al. [11]. We describe our methodology for using sensitivity analyses alongside descriptions of relevant initial MMA decomposition reactions and subsequent reaction pathways, from which a few key reactions were selected for adjustment. Modified rate parameters to these key reactions are proposed, via an optimization process anchored to time-resolved CO and CO_2 speciation data.

6.4.1 Decomposition Pathway Analysis

The detailed model by Yang et al. was developed during the study of three C_5 unsaturated esters—including MMA—anchored to species mass spectrometry measurements in subatmosphere premixed flames [10, 120]. This model includes 411 species and 2926 reactions. In general, the Yang et al. model shows accelerated species formation relative to experimental speciation trends, most notable at the lower end of the temperature range studied. This is clear in the 1365 K condition in Fig. 6.5. Such accelerated species formation at a given temperature suggests that the activation energies for reactions related to MMA decomposition may be underestimated in the detailed model. Such was the observation of Dakshnamurthy et al. in the development of their reduced model [11] optimized against laminar flame experiments; the activation energies for reactions related to MMA decomposition were increased and other reactions were adjusted as part of their model optimization based on recommendations from the literature. Several adjustments to rate parameters were based on those of similar reactions of methyl butanoate [138, 139, 140, 141], methyl tiglate [142], methyl-2-methyl but-3-enoate [143], isobutene [144, 145, 146], 1-butene [**?**], methyl-2-butenoate [147], the isobutenyl radical [148], as well as propyne and allene [149]. The reduced model of Dakshnamurthy et al. also incorporated a base chemistry from Narayanaswamy et al. [150] to achieve accurate predictions for laminar burning velocities of not only MMA, but of smaller hydrocarbons as well. The mechanism, therein referred to as "short MMA mechanism", consists of 1084 reactions and 88 species. We focus here on optimizing the model against our time-resolved speciation measurements and proposing modified rate parameters for select reactions included in their short MMA mechanism.

We identify the reactions to which CO, CO_2, and CH_2O concentrations are most sensitive using a time-resolved sensitivity analysis in an idealized reactor model in Cantera [58]. Although we use the Dakshnamurthy et al. mechanism as our base model for optimization, we also applied our sensitivity analysis to the detailed chemical model by Yang et al. [10], with all 411 species and 2926 reactions to ensure no crucial reactions were missed as many

reaction pathways are often eliminated in a mechanism reduction. For completeness, we performed this analysis over the full range of post-shock initial temperatures in this study.

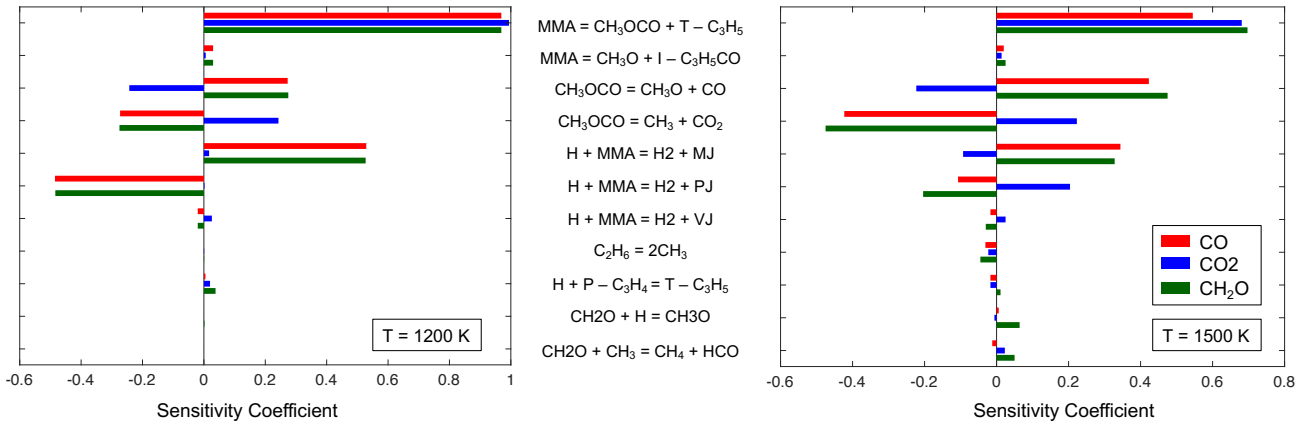

Figure 6.8 Sensitivity coefficients for 1% MMA in argon at $P_5 = 1$ atm using the Dakshnamurthy et al. mechanism are shown at 0.1 ms for temperatures of 1200 K (left) and 1500 K (right). Reactions showing positive sensitivity factors increase species production.

As a first step, a constant UV reactor model is used to screen for sensitive reactions in the existing models, initiated with the experimentally-determined reflected shock conditions T_5 and P_5, as well as the molar composition X. We use the reactions and rates of the short MMA mechanism and rank the reactions by their sensitivity with respect to CO, CO_2, and CH_2O, and consider the top 50 in a subsequent sensitivity analysis utilizing the measured shock tube pressure and post-shock temperature in a split-timestep reactor model described in previous work [151], wherein non-reacting gas temperature changes caused by pressure rise or fall during the experiment are modeled via isentropic compression or expansion, respectively. The resulting sensitivity coefficients for reactions with high sensitivity for some or all of the three targeted species in the Dakshnamurthy et al. model are shown in Fig. 6.8. This analysis indicates that the targeted species sensitivity is heavily dominated by a small number of reactions. Notably, the H-abstraction reactions are more sensitive for CO and CH_2O at 1200 K, while more sensitive for CO_2 at 1500 K. We use these analyses to identify

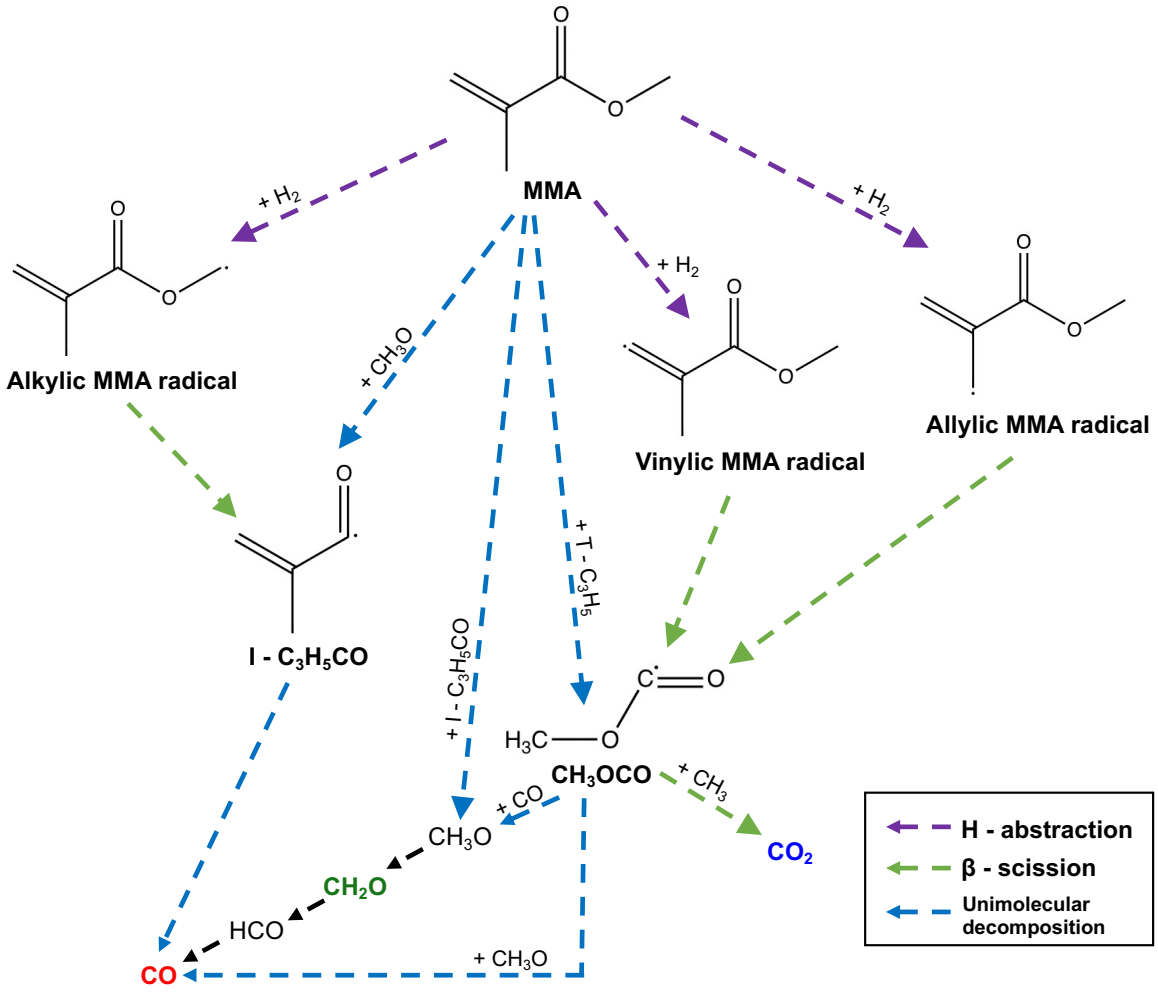

Figure 6.9 MMA decomposition pathways considered in this work.

key reactions for rate parameter modification, informed by the LAS measurements. The first two reactions listed in Fig. 6.8 are the two unimolecular decomposition pathways of MMA:

$$\mathrm{MMA} \longleftrightarrow \mathrm{iC_3H_5CO} + \mathrm{CH_3O} \tag{R1}$$

$$\mathrm{MMA} \longleftrightarrow \mathrm{tC_3H_5} + \mathrm{CH_3OCO} \tag{R2}$$

The reaction leading to CH_3OCO production (R2) is the most sensitive of all reactions included in the mechanism and significantly more sensitive for these species than R1. The sensitivity coefficients are positive for CO, CO_2, and CH_2O for both of these reactions indicating that rate increases will lead to increased production of all three molecules.

The next two reactions listed involve the decomposition of CH_3OCO:

$$CH_3OCO \longrightarrow CH_3O + CO$$

$$CH_3OCO \longrightarrow CH_3 + CO_2$$

The sensitivity coefficients for these reactions notably indicate inverse relationship of species formation for CO and CH_2O versus CO_2. The first reaction directly produces CO as well as CH_3O, which is a precursor to formation of CH_2O and CO; the second reaction produces CO_2. Thus the relative rates between these two pathways will affect the ratio of CO (and CH_2O) to CO_2 formed. Despite the high sensitivity of these reactions, we omit them from our rate parameter modification, as these reactions have been studied more extensively in the literature [11, 116].

The three reactions following (R3 through R5) are the hydrogen abstraction reactions of MMA with atomic hydrogen, resulting in the respective allylic (PJ), alkylic (MJ), and vinylic (VJ) MMA radicals:

$$H + MMA \longleftrightarrow H_2 + CH{=}C(CH_3){-}C(=O)OCH_3 \text{ (PJ)} \quad \text{(R3)}$$

$$H + MMA \longleftrightarrow H_2 + CH_2{=}C(CH_3)C(=O)OCH_2 \text{ (MJ)} \quad \text{(R4)}$$

$$H + MMA \longleftrightarrow H_2 + CH_2{=}C(CH_2)C(=O)OCH_3 \text{ (VJ)} \quad \text{(R5)}$$

CO and CH_2O are also positively sensitive to the reactions R3–R4. Note that abstractions

by O and OH radicals, which are more relevant in oxidation regimes, are included in the mechanism but not optimized in this work.

The remaining reactions listed involve competing pathways for the carbon atoms without presence of oxygenated molecules as well as reactions causing CH_2O production or destruction. We exclude the former from modification as we lack relevant species measurements to which to anchor; and we exclude the latter as these reactions are not specific to MMA kinetics and the rates are comparatively well-studied. Moreover, sensitivity analysis indicates that H-abstraction to the vinylic pathway is much less significant than the allylic and alkylic pathways [11], and so we exclude (R5) from modification. To summarize, rate parameters for 4 reactions are optimized in this work, reflecting both initial decomposition (R1–R2) and H-abstraction reactions (R3–R4).

Figure 6.9 shows the decomposition pathways including the targeted reactions and subsequent reactions leading to the targeted intermediate and product species. These pathways represent the most significant routes for CO, CO_2, and CH_2O production during MMA pyrolysis in the temperature ranges of interest in this chemical model. β-scission of the allylic and vinylic MMA radicals leads to CH_3OCO formation, from which both CO and CO_2 are consequently produced, with CH_2O an intermediate leading to CO. Alternately, H-abstraction of MMA to form the alkylic-position MMA radical has a distinct pathway leading via β-scission to iC_3H_5CO and thereafter, CO. Thus, modifying the respective rates of the hydrogen abstraction reactions significantly impacts the resulting ratio of CO and CO_2 produced. The Yang et al. detailed mechanism uses equal rates for the allylic and alkylic sites; the reduced Dakshnamurthy et al. mechanism differentiates the three H-abstraction reactions as the allylic radical is a relatively more stable molecule and the three abstraction sites have distinct related C-H bond dissociation energies (allylic $<$ alkylic $<$ vinylic) [11, 152].

Though not explicitly detailed here, CH_3O becomes CH_2O via third-body collisions following its formation from CH_3OCO. After complete decomposition of CH_3OCO, reaction pathways to CO_2 are no longer available; however, CO continues to be produced by CH_2O

following the typical route through the formyl radical, HCO. This explains the fast plateau of CO_2 mole fraction seen at the higher temperatures (Figs. 6.5 and 6.6) while the mole fraction of CO continues to increase slightly at the expense of CH_2O.

6.4.2 Mechanism Modification

	Reaction	Original parameters			Modified parameters		
		A	n	E	A	n	E
R1	MMA $\rightarrow$ iC_3H_5CO+CH_3O	$9.55{\cdot}10^{14}$	-0.39	369.0	$4.36{\cdot}10^{15}$	-0.49	350.1
R2	MMA $\rightarrow$ tC_3H_5+CH_3OCO	$6.42{\cdot}10^{15}$	-0.35	350.6	$7.26{\cdot}10^{15}$	-0.37	305.2
R3	MMA+H $\rightarrow$ PJ+H_2	$1.86{\cdot}10^{5}$	2.54	11.66	$2.06{\cdot}10^{6}$	2.69	5.84
R4	MMA+H $\rightarrow$ MJ+H_2	$1.92{\cdot}10^{7}$	2.06	31.08	$1.55{\cdot}10^{8}$	2.21	35.86

A is in $cm^3{\cdot}mol^{-1}{\cdot}s^{-1}$ or $cm^6{\cdot}mol^{-2}{\cdot}s^{-1}$, E is in $kJ{\cdot}mol^{-1}$

Table 6.1 Rate constants of the Dakshnamurthy et al. and the modified MMA pyrolysis models

As a next step beyond sensitivity analysis, an optimization procedure is employed to adjust the Arrhenius rate parameters for the target reactions. Often, shock tube pyrolysis studies aim to examine the decomposition rate of a molecular species at different temperatures, in order to determine elementary reaction rate constants based on pseudo-first-order kinetics [125]. This ideally involves direct time-resolved measurement of the decomposing species; however, with these measured product species time histories, we can compare the model predictions against experimental data and modify the Arrhenius rate parameters of the several targeted reactions to mitigate disagreement in the formation timescales and magnitudes observed. We focused here on selecting reactions from initial to early stages of decomposition and, in particular, reactions for which rate constants had relatively high levels of uncertainty in existing mechanisms. The rate parameters were optimized by employing

a genetic algorithm-based method; the procedure followed is based on and detailed in the work of Sikalo et al. [128]. In each iteration—or *generation*—of the optimization, the sets of reaction rate parameters that minimize error between the measured and predicted species mole fraction (with equal weighting for CO and CO_2) are selected. These best-performing solutions are then *combined* (some parameters from one solution set and merged with some from another set) and *mutated* (randomly selected parameter in a solution is varied) to be tested in the next iteration until a single solution is converged upon. Effectively, different permutations of the 12 Arrhenius rate parameters (for reactions R1 through R4) are evaluated and improved upon until the experimental species time-evolutions can be reproduced by the kinetic model. The optimization was anchored to the first millisecond of test time of CO and CO_2 speciation data. The CH_2O data had higher uncertainty, and so was not weighted in the optimization; however, the improved agreement seen between the CH_2O mole fraction measurements and the modified mechanism serves as a useful independent validation. The final modified rate parameters for the two unimolecular MMA decomposition reactions (R1 and R2) and the key hydrogen abstraction reactions (R3 and R4) are shown in Table 6.1. The resulting rates are shown as a function of temperature in Fig. 6.10.

The overall production of CO, CO_2, and CH_2O are all generally under-predicted by the Dakshnamurthy et al. mechanism compared to this speciation data; our mechanism optimization unsurprisingly resulted in rate increases for all targeted reactions. As the ratio of CO_2 to CO produced and overall production are strongly affected by the rates of R1 and R2, these rates changed most significantly to better reflect the CO/CO_2 observed in the shock tube experiments. For the abstraction reactions, the updated pre-exponential factors increased consistently by an order of magnitude for all of R3 and R4. The modified mechanism indicates that pre-exponential factors A for the targeted reactions should generally fall between those published in the Yang et al. and Dakshnamurthy et al. models. The optimization resulted in a near-negligible change to the temperature exponents n of the decomposition reaction (R1 and moderate changes (< 30 %) for the other modified reactions

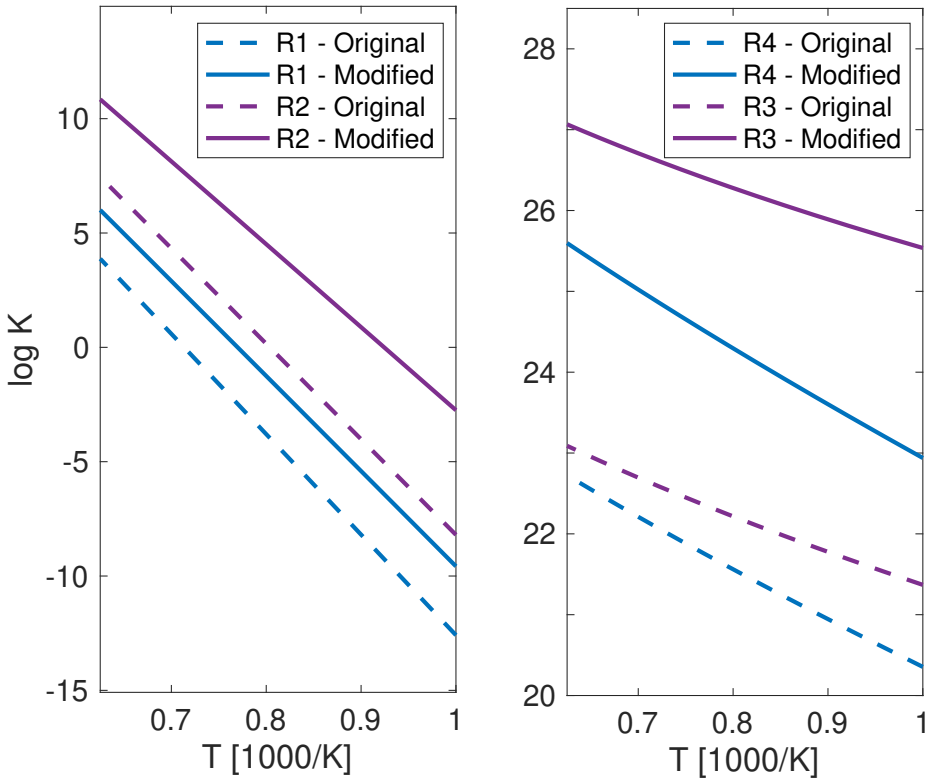

Figure 6.10 Comparison of rates between the Dakshnamurthy mechanism and the modified mechanism for the unimolecular decomposition reactions of MMA (left) and hydrogen abstraction reactions (right).

(R2, R3, R4). The activation energies E for the allylic site hydrogen abstraction reaction was decreased as were both of the decomposition reactions, falling between the values published in the Yang et al. and Dakshnamurthy et al. models for decomposition reactions (R1 and R2) and lower than both existing models for the allylic H-abstraction (R3). Notably, the ordering of the activation energy and overall rate constant magnitudes remained unchanged for the abstraction reactions such as to follow the ordering of the relative C-H bond dissociation energies.

The predictions using the refined mechanism model are compared with the experimental species time-histories and existing mechanism in Fig. 6.5 and Fig. 6.6. The experimental

and simulated mole fraction yields are shown in Fig. 6.7. As discussed in Section 6.3, the modified mechanism overall more closely predicts the experimental data of CO, CO_2, and CH_2O than either the unmodified version of the short MMA mechanism and the original detailed chemical model. However, the mole fraction magnitude agreement with the data worsens at the higher temperatures ($T_5 > 1500$ K), particularly so for CO_2 and CH_2O. Both the detailed Yang et al. and the modified mechanisms predict the plateau level of the CO_2 mole fraction to be around $X = 0.4\%$ whereas we measure this to be around $X = 0.6\%$. For CH_2O, we measure a more dramatic decline in mole fraction at $T_5 = 1555$ K than is captured by our modified model, though agreement is improved for the other four lower temperature tests for which CH_2O was measured. Despite these magnitude discrepancies at select conditions, we observe good agreement in the time-evolution trends for all three measured species across the temperature range. Most notably, the modified mechanism shows significant improvement in capturing the initial highly temperature-dependent formation timescales of the decomposition products relative to both the Yang et al. and Dakshnamurthy et al. across all conditions. As a check on the impact of these changes regarding prior experimental works, flame speed predictions using the updated model were found to generally agree well with the flame speeds reported by Dakshnamurthy et al., with deviation ranging from 0.3–8% over all conditions with an average disagreement of 4%. Comparisons of laminar flame speeds and species profiles can be found in the appendix. The modest differences observed between the models in laminar flame conditions highlights the enhanced sensitivity of the more targeted shock tube pyrolysis studies performed in this work to the early decomposition reactions, which cannot be readily isolated in flame experiments. Overall, these kinetic rate adjustments represent a starting point in the refinement of a detailed mechanism for MMA oxidation. Future shock tube studies with oxidizing mixtures are expected to elucidate contributions of other reactions such as H-abstraction by O and OH.

6.5 Conclusion

In this work, the chemical kinetics of methyl methacrylate (MMA, $C_5H_8O_2$) pyrolysis were examined in a shock tube reactor using infrared laser absorption spectroscopy. Experiments were conducted over a range of temperatures from 1200–1600 K and near atmospheric pressure. Quantitative interpretations of spectra obtained by laser absorption during the decomposition of MMA enabled species time-history measurements of carbon monoxide (CO), carbon dioxide (CO_2), and formaldehyde (CH_2O). The data were subsequently compared to existing models for MMA combustion, revealing significant disagreements. Guided by sensitivity analyses and genetic algorithm based optimization, we propose modified Arrhenius rate parameters for the two unimolecular decomposition reactions and key H abstractions that initiate MMA pyrolysis. Updating these rates within the short MMA mechanism of Dakshnamurthy et al. led to significantly improved agreement with speciation measurements. Some discrepant behavior still exists at higher temperatures that future experimental studies in different environments may reconcile. The data-driven insights and reaction mechanism improvements from this work are expected to help advance PMMA combustion models for hybrid rocket propulsion systems and fire science studies.

CHAPTER 7

Polytetrafluorethylene (PTFE) burn characteristics in a convective oxidizer cross-flow

7.1 Introduction

Fire-resistant polymers are used extensively in modern structures to reduce flammability and the probability of fire-related loss or death. However, gas-phase emissions from these materials are often more toxic than those from conventional fuels. Specifically, halogenated polymers are considered fire resistant due to their chemical stability at high temperatures and the release of halides or halogen acids which can interfere with gas-phase combustion and limit heat release [34]. Unfortunately, hydrogen halides are acutely toxic and incomplete combustion leads to elevated emissions of carbon monoxide and unburned hydrocarbons including aromatics.

Figure 7.1 shows a typical fire growth curve for a compartment experiencing flashover including growth, developed, and decay phases. Towards the tail end of the cooling/decay phases is when firefighter "overhaul operations" occur. The conditions during overhaul are often identified qualitatively by the firefighting personnel and quantitatively by fuel mass loss rate (as a proxy for heat release rate), local temperature, and gas species concentrations, where applicable. Once a fire is decaying, as during overhaul operations, there is often the perception that toxicant exposure risks are minimal however, in reality, emissions from asphyxiants, irritants, and carcinogens can be very high depending on the materials fueling the fire. These toxicants significantly increase the health and safety risk associated with

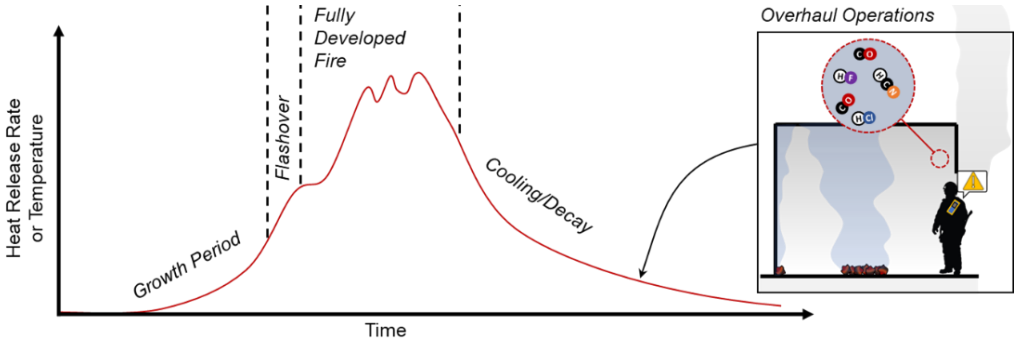

Figure 7.1 Fire growth/decay stages of compartment fire experiments with firefighter operations.

smoke inhalation for first responders and civilians in close proximity to structural fires. While these challenges are well known, the detailed physics (kinetics, transport) associated with toxicant formation are insufficiently understood for many halogenated polymers, precluding accurate model prediction of fire toxicity and inhibiting risk quantification.

Polytetrafluoroethylene (PTFE), or Teflon, is a common fire-resistant fluoropolymer used extensively in construction and industrial applications due to its chemical inertness and high-temperature stability. The stability of PTFE may be attributed to the carbon-fluorine bond associated with the monomer tetrafluoroethylene (C_2F_4). The bond dissociation energy of the C–F single bond is higher than any other carbon-halogen as well as carbon-hydrogen bonds. As such, the pyrolysis of PTFE requires higher temperatures than most other synthetic or natural polymers and the material does not easily burn. However, upon thermal decomposition of PTFE in a fire environment, fluorine and fluorocarbon radicals will form and participate in combustion. Fluorine has the highest electronegativity of any element, and thus strongly attracts shared electrons, more so than oxygen. In the presence of H_2O, which is common to any ambient or fire environment, fluorinated radicals will react to form hydrogen fluoride (HF). HF is an acutely toxic gas with a lethal human exposure limit of approximately 50 ppm for a 30 minute period [153]. Here we aim to examine the incipient formation of HF (as well as CO) and associated burn characteristics of PTFE at fire con-

ditions. HF also readily dissolves in liquid water to form hydrofluoric acid which can cause pulmonary edema and cardiac failure through dermal fluoride uptake.

Recent research conducted at the Air Force Civil Engineer Center found that thermal decomposition of HFC fire extinguishing agents rapidly produce high concentrations of hydrogen fluoride gas, in some cases reaching the IDLH level within 45s of deployment [154]. The study also references a tragic instance in 2012 in which a U.S. military vehicle was hit by a grenade which activated its automatic fire suppression system containing HFCs, leading to HF gas production. Three personnel suffered from acute respiratory failure from HF poisoning within a short time frame that resulted in death.

A number of previous theoretical and experimental studies have examined fluorocarbon combustion to advance chemical models towards predictive capability of toxicant formation. The foundational shock tube studies by Modica and LaGraff introduced a simple two-step mechanism to capture high-temperature C_2F_4 pyrolysis and oxidation, respectively, determining formation rates of CO and F atoms [155]:

$$C_2F_4 \longrightarrow 2CF_2 \tag{R1}$$

$$CF_2 + O_2 \longrightarrow CO + 2F + O \tag{R2}$$

Subsequent studies have built more detailed reaction mechanisms that account for additional steps and pathways for pyrolysis, oxidation, and hydrogen interactions, with the latter required to predict HF. Modeling hydrofluorocarbon chemistry has required more sophisticated theoretical approaches to determine the many potential reaction pathways. Burgess et al used a combination of empirical data and ab initio calculations to produce a comprehensive mechanism of C1 and C2 fluorinated hydrocarbon chemistry [156], which has been tested and modified in other works [157, 158, 159]. Recent efforts towards understanding high-temperature hydrofluorocarbon chemistry have included shock tube studies to interrogate additional pyrolysis pathways [160, 161] and refined calculations of thermochemical properties [162, 163]. To ultimately predict toxic emissions in a realistic fire environment, addi-

tional physics including heat transfer mechanisms and fluid dynamics must be considered, and coupled with the chemistry. State-of-the-art computational studies have recently shown promise to couple such detailed chemistry with multi-dimensional solid-fuel combustion models [164, 165, 166]. Complementary and computationally tractable experiments are needed with quantitative in situ measurements of species, temperature, and other spatially-evolving parameters to constrain and anchor such models.

In this work, we present a solid-fuel combustion experiment for fire-resistant polymers subject to forced convective cross-flow to assess burn characteristics and toxicant formation from PTFE using laser absorption diagnostics for in situ species and temperature measurements near the fuel surface. The paper first describes the axi-symmetric solid-fuel experimental configuration and optical diagnostic integration, which involves an oxygen-enriched pre-burner flame using polymethyl methacrylate (PMMA) to create well-defined high-temperature boundary conditions to which the PTFE is exposed. The laser absorption tomography methods are then detailed, highlighting the advantage of the axi-symmetric geometry to reconstruct quantitative two-dimensional images of thermochemical flow structure near the material surface. A novel dataset of quantitative hydrogen fluoride and carbon monoxide species profiles as well as temperature is presented. The results are discussed with an accompanying first-order analysis using available thermochemical models that describe high-temperature chemical reaction pathways for fluorocarbon oxidation in a fire-like environment.

7.2 Methods

7.2.1 Solid Fuel Burner

The solid-fuel combustion experiment was adapted from our prior work [6] and is shown in Fig. 7.2. The experiment involves forced convection of a gaseous oxidizer across a cylindrical solid fuel grain. The cylindrical grain geometry provides 2D axi-symmetry (r,z) of the

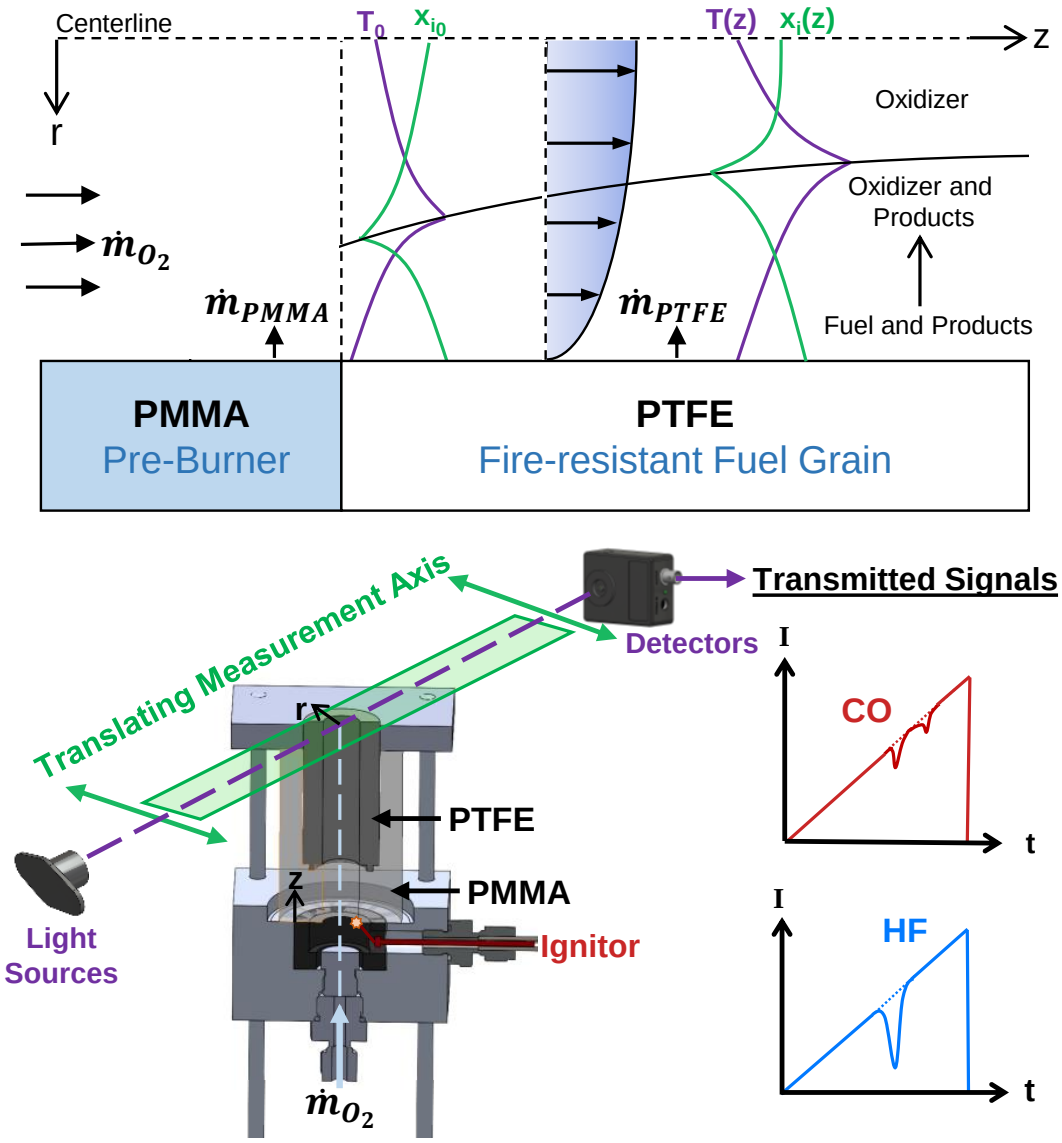

Figure 7.2 Composite solid fuel combustion experiment with forced oxidizer convection and two-dimensional laser absorption tomography setup.

gas-solid interface, enabling quantitative tomographic reconstruction of line-of-sight optical measurements from a single view angle (discussed further below) while avoiding the edge effects of planar slab burners. The cylindrical axi-symmetry also provides a relatively simple geometry for detailed computational modeling [164]. The test rig is designed to accommodate fuel grains of varying composition and length, the latter of which enables two-dimensional measurements based on exit plane measurements at different axial distances (z). Due to the high-temperature stability and fire resistance of PTFE, a composite fuel grain assembly was used in place of a homogeneous fuel cylinder. Notably, PTFE combustion proved difficult to initiate even in a pure oxygen environment at ambient temperature. As such, a 25.4 mm (1 in.) long polymethyl methacrylate (PMMA) fuel grain was used as a pilot burner to expose PTFE to both sustained high temperatures that initiate pyrolysis as well as hydrocarbon combustion product gases typically present in fires. PTFE fuel grains from 12.7-127mm (0.5-5 in.) in length were examined, each mated to the top surface of the PMMA pilot fuel grain. The boundary condition (temperature, species) created by the pre-burner was characterized (shown later) and held constant across experiments. Importantly, the PMMA pre-burner combustion facilitates HF formation by supplying hydrogen (via water vapor) to the oxygen-enriched core flow with which the fluorocarbons can react, as would be the case in a fire environment. The test rig, and all associated experimental components, were contained within a high-flow (1150 cfm) laboratory fume hood to exhaust combustion products.

The composite fuel grain, including both the PTFE and PMMA components, had an inner diameter of 12.7 mm (0.5 in.). All tests were performed with a consistent oxidizer mass flow rate of $\dot{m}_{ox} = 1.5$ g/s using a single central injection port previously characterized [71]. Ignition was controlled remotely with an electrically-initiated pyrotechnic charge directed into a precombustion chamber directly beneath the bottom surface of PMMA [6]. The mass of the heterogeneous fuel grain was measured before and after each test to estimate a test time-integrated mass loss, equivalence ratio and regression rate. A graphite gasket ($\sim$3 mm thick) was moulded to the top of the PTFE component to mitigate top surface

pyrolysis. Burn durations for tests, including start up time and the quasi steady-state measurement period, were approximately 14 seconds. At the end of the test time, nitrogen gas was immediately flushed through the oxygen line to extinguish the flame and purge the plumbing.

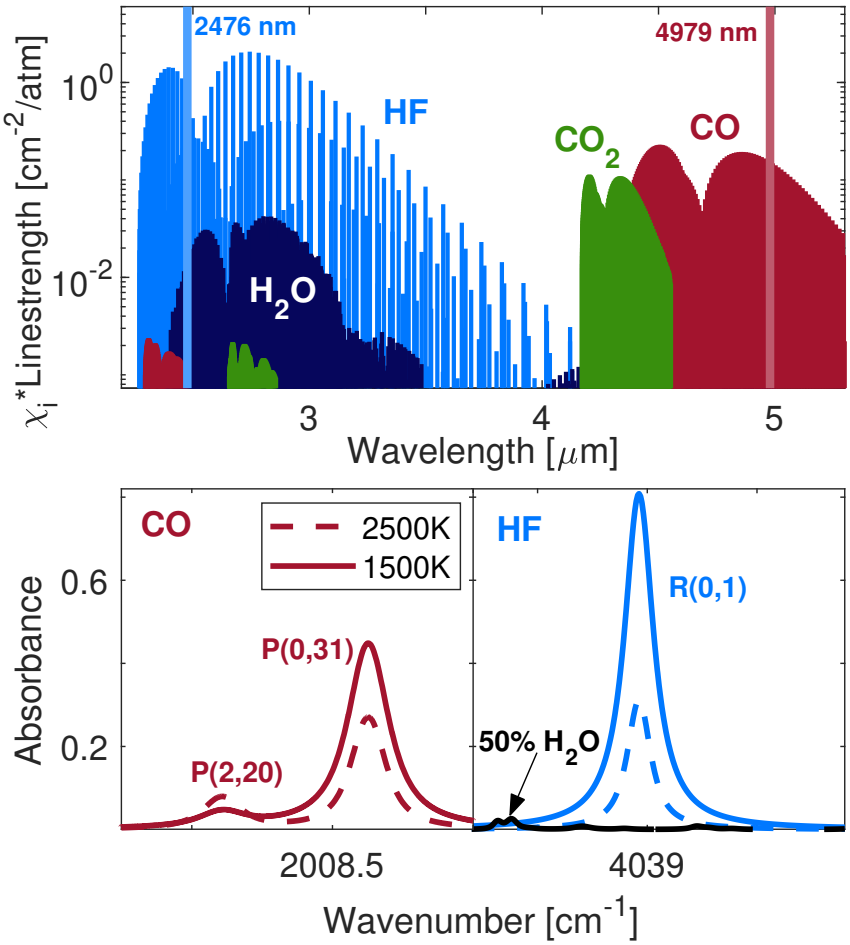

Figure 7.3 *Top.* Absorption line strengths of HF, CO, and other relevant combustion species simulated at 2500 K [7]. *Bottom.* Simulated target transitions of CO and HF ($X = 15\%$) with exaggerated water interference.

7.2.2 Laser Absorption Spectroscopy

In situ species and temperature measurements in the near-surface reaction layer were performed using infrared laser absorption spectroscopy (LAS). LAS relates the attenuation of light through a gas medium to thermophysical properties of the absorbing molecules. Species-specific absorption spectra can be obtained by tuning lasers in spectral frequency or wavelength across individual lines associated with quantum energy transitions of the species of interest. In this study, we probe the mid-infrared fundamental vibrational bands of HF and CO in order to quantitatively recover species mole fraction and temperature in the reacting flow. The targeted wavelengths or frequencies are highlighted in Fig. 7.3. Specifically, we probe the hydrogen fluoride spectra in the R-branch of the fundamental band near 2475 nm. The R(1) rovibrational line at 4038.965 cm^{-2}, simulated in Fig. 7.3, was selected due to its high strength and lack of spectral interference from other atmospheric and combustion gases. It should be noted that non-optical ex situ detection and quantification of HF is particularly difficult due to its propensity to irreversibly interact with solid surfaces associated with sensors and sampling [167]. For carbon monoxide, we probe the P(0,31) and P(2,20) transitions near 2008.5 cm^{-1} as also shown in Fig. 7.3. This line pair can be measured simultaneously within the typical injection current tuning range of a semi-conductor laser. The CO lines were selected in part due to the large difference in lower state energies, $\Delta E" = 3151$ cm^{-1}, which enhances temperature sensitivity [6]. We note the spectroscopic parameters of all target transitions are compiled in the HITRAN database [7].

The laser spectroscopy optical setup was coupled with the solid fuel combustion test rig as depicted in Fig. 7.2. A distributed feedback (DFB) diode laser (Norcada) with ∼5 mW output centered around 4040 cm^{-1} was utilized to target the hydrogen fluoride line. For carbon monoxide, a DFB quantum cascade laser (Alpes) with ∼75 mW output centered around 2008 cm^{-1} was used. The output beams of both lasers were combined via a CaF_2 beam splitter to make them colinear before being focused across the exit plane of the fuel grain with a beam waste of ∼0.5 mm. On the catch side, a second beam splitter was used

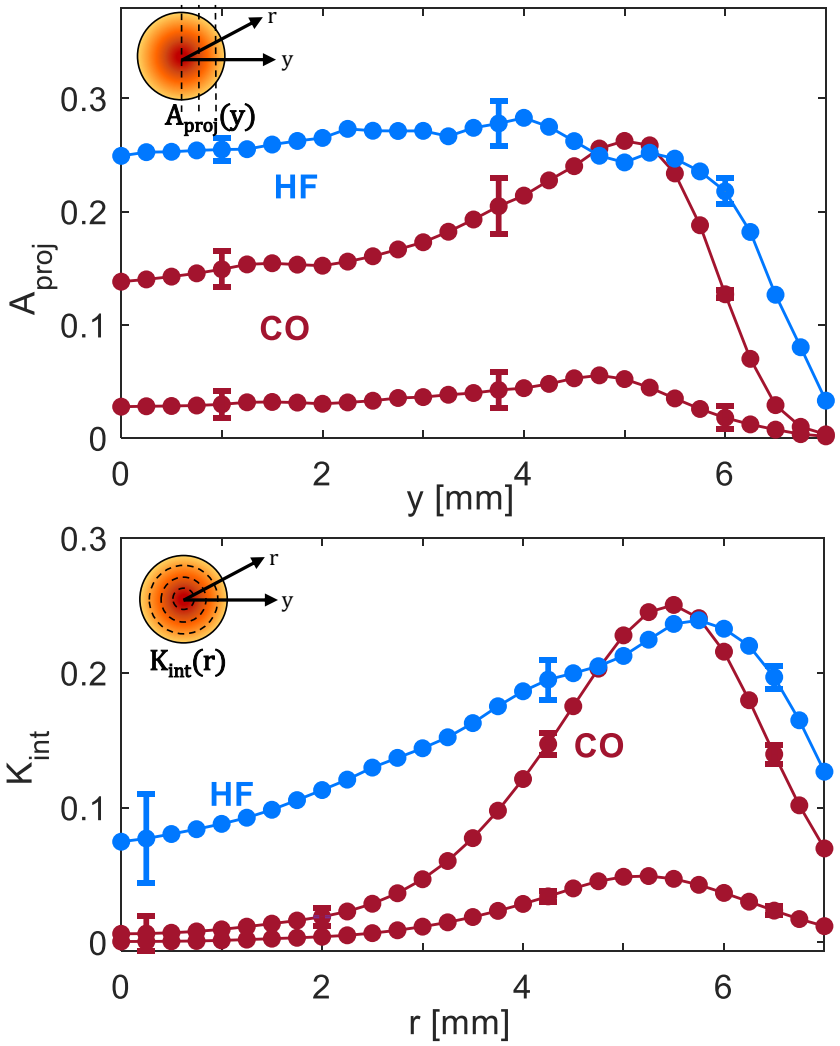

Figure 7.4 *Left.* Projected integrated absorbance area verses distance y from the center of the reacting flow. *Right.* Tomographically-inverted radially-resolved integrated absorption coefficient.

to spatially de-multiplex the colinear beams, producing two perpendicular beams. Narrow bandpass spectral filters were placed along the separate beam paths to isolate each wavelength in front of distinct photodetectors (VIGO PVI-4TE-5 and Thorlabs PDA10D) used for CO and HF measurements. Both lasers were injection-current scanned in intensity and wavelength at a frequency of 2 kHz using a sawtooth waveform, while the transmission signals from the photodetectors were recorded at a 2.5 MHz sample rate. The multi-plexed optical line of sight was translated at 2.5 mm/s across the exhaust plane. The recorded transmission signals were time-averaged (every 200 scans) to yield a measurement radial resolution of half the beam diameter, such that the beam diameter (0.5 mm) effectively determines the radial spatial resolution.

7.2.3 Tomographic Imaging

Attaining the spatial profiles of temperature and species involves a tomographic inversion of the path-integrated line-of-sight laser absorption signals. Each of the three target lines for HF and CO are spectrally-resolved via the laser scans. The intensity signals can be converted to spectral absorbance, $\alpha(\nu)$, and spectrally integrated to yield projected absorbance areas, A_{proj}, for each target line, spatially-resolved across the measurement plane (see figure 7.4, top). These spatially-resolved path-integrated line areas, A_{proj}, can be directly related to the line-of-sight distribution of the integrated spectral absorption coefficient, $K(l)$:

$$\begin{aligned} A_{\mathrm{proj}}(y) = \int_{-\infty}^{\infty} \alpha(\nu)\mathrm{d}\nu &= \int_{0}^{L(y)} K(l)\mathrm{d}l \\ &= \int_{0}^{L(y)} PS_j(T(l))X_i(l)\mathrm{d}l \end{aligned} \tag{7.1}$$

To invert the line-of-sight absorption measurements, we exploit the axisymmetry of the flow-field to employ a Tikhonov-regularized onion peeling deconvolution [52, 6, 71] to convert the projected absorbance areas to line-integrated spectral absorption coefficients, $K(r)$, in the radial dimension (see figure 7.4, bottom). The radially-resolved ratio of the inte-

grated absorption coefficients of the two CO lines is used to obtain temperature, $T(r)$, where the ratio reduces to a linestrength ratio that is only a function of temperature: $R(r) = K_1(r)/K_2(r) = S_1(T(r))/S_2(T(r))$. With the gas temperature distribution known, the radially-resolved mole fraction can be determined from the radially-resolved spectral absorption coefficient of a single line via: $X(r) = K_j(r)/PS_jT(r)$. To produce two-dimensional images of the reaction layer, the radial absorption profiles were acquired at different axial lengths of the PTFE fuel grain, while holding the PMMA pre-burner length and oxidizer flow rate constant.

7.3 Results

Experiments were conducted for PTFE fuel grain lengths of 25.4mm–127mm (1–5 in.) with 25.4 mm (1 in.) interval spacing, with an additional test of a 12.7 mm (0.5 inch) fuel grain to add spatial resolution in a region where a higher gradient was expected near the PMMA boundary condition. The forced convection oxidizer flow rate was held constant at $\dot{m}_{ox} =$ 1.5 g/s. Several tests were conducted at a single fuel grain length to verify experimental repeatability and to assess the quasi-steady state and axisymmetric assumptions over the measurement time.

Global fuel regression behavior was assessed based on post-burn mass loss and geometric measurements of the fuel grain; key results of this analysis are presented in Table. 7.1. The total consumed fuel mass was determined for each of the PMMA pilot burner and the PTFE fuel grain by measuring the masses before and after each hot-fire test. This mass loss is used along with the total burn time to determine the space-time averaged parameters discussed. The space-time averaged regression rate, $\bar{\dot{r}}$, is observed to decrease with fuel grain length due to the declining availability of oxygen from ongoing reactions and formation of oxygenated product species. The averaged mass burn rate of regressing PTFE with fuel grain length are also shown. The rates were corrected for burn time variation by accounting for variation in

mass burn rates measured from the 25.4 mm (1 in.) PMMA pilot burner fuel grain which ranged from 0.22 +/- 0.03 g/s. Over axial length, we observe a diminishing marginal increase in $\dot{m}$, consistent with the declining regression rate. Compared to a study with PMMA as the sole fuel, the rates measured for PTFE regression are over 50% lower [71]. The O/F ratio decreases with fuel grain length as fuel mass is added to the constant oxidizer mass flow, trending from fuel-lean towards fuel-rich conditions. These global burn characteristics, although space-time averaged, provide an important reference for more granular species and temperature measurements.

L_f	$\bar{\dot{r}}$	$\bar{G}$	$\bar{\dot{m}}_{PTFE}$	$O/F\|_{t_b}$
in.	[mm]	[mm/s]	[kg/m^{2}s]	[g/s]
0.5	0.069	0.010	0.17	9.8
1	0.041	0.011	0.23	7.6
2	0.039	0.012	0.35	5.1
3	0.024	0.014	0.44	3.0
4	0.021	0.014	0.55	3.1
5	0.017	0.015	0.58	2.2

Table 7.1 Global fuel regression parameters for PTFE with PMMA/GOx pre-burner and $\dot{m}_{ox} = 1.5$ g/s

7.3.1 PMMA pre-burner boundary condition

The pre-burner boundary condition was measured using the laser absorption tomography method to determine the initial temperature and gas composition to which the PTFE was exposed. Fig. 7.6 shows the measured temperature and CO species as a function of radial position from the core. Given the PMMA mass burn rate, the global equivalence ratio at the boundary was approximately $\phi = 0.28$. Despite this very fuel-lean global condition, a peak temperature ($\sim$2950 K) slightly lower than the stoichiometric value is reached within

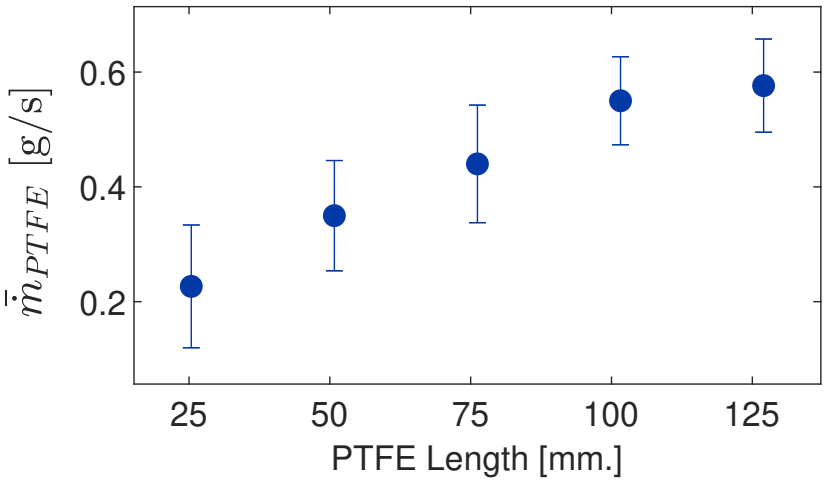

Figure 7.5 PTFE mass burn rate versus PTFE fuel grain length. The mass burn rates are space- and temporally-averaged parameters over the total burn duration.

4 mm of the fuel surface due to the radial distribution of O/F ratio moving from fuel rich at the surface to the core which is primary oxygen. The carbon monoxide mole fraction is measured to peak at nearly 20% within 2 mm of the fuel surface while reducing to nearly zero within 5 mm of the PMMA surface. Overall, based on the global O/F, it is estimated that approximately 60% of the bulk cross-flow remains oxygen.

7.3.2 PTFE reaction layer measurements

Laser absorption tomography results from the aforementioned combustion tests of PTFE with the hot vitiated oxygen cross-flow are shown for select axial distances in Fig. 7.7 and compiled across the full experimental domain in two-dimensional images in Fig. 7.8. Quantitative spatially-resolved temperature and species profiles illustrate the thermochemical evolution in the reaction layer. Select trends are noted here and discussed further in the following section. It is notable that due to the inherently faster fuel regression of PMMA compared to PTFE, the respective port diameters and thus radial domains differ, rendering a slight flow convergence at the interface. Temperature and species uncertainty, as repre-

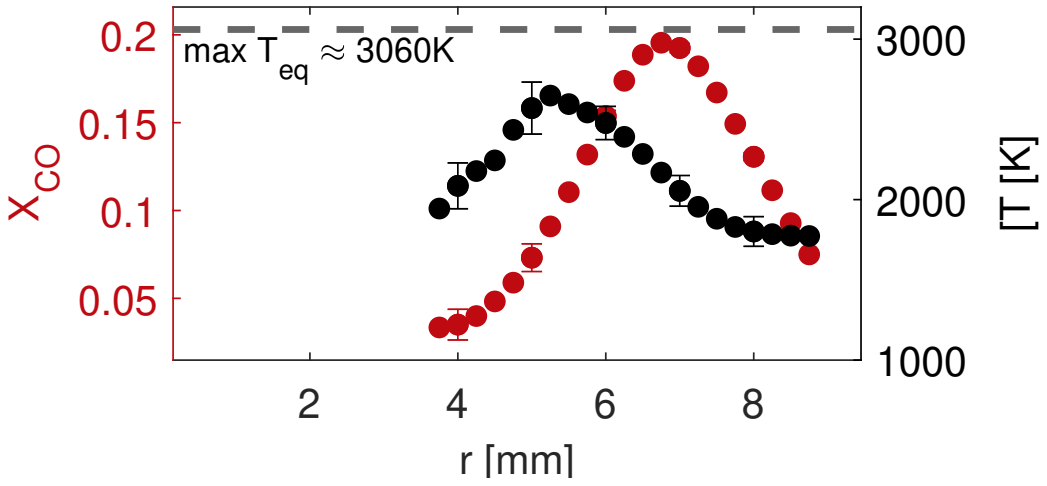

Figure 7.6 CO mole fraction and temperature radial distribution measured from the 25.4 mm long PMMA pilot burner in GOx cross-flow.

sented by error bar magnitudes, reflects variation in axisymmetry across the flow centerline, uncertainty associated to tomographic deconvolution, and uncertainty in spectral parameters from HITRAN [7]. Further details on this uncertainty analysis can be found in previous works from our group [52, 71].

Radial temperature distributions indicate a decrease in peak temperature and broadening with axial distance reflecting radial diffusion and mixing. The radial location of the peak temperature shifts towards the oxygen-enriched core flow with increased axial distance as the O/F ratio decreases. The first measurement downstream of the fuel interface, at 12.7 mm (0.5 in.), most closely resembles the temperature profile measured at the PMMA surface initial condition. For the first few axial distances, there is insufficient concentration of carbon monoxide in the core flow (near $r = 0$) to obtain a reliable temperature measurement, thus the profiles are not fully-resolved. Moving downstream, more CO has been produced and has diffused into the core region such that local temperature can be calculated, albeit with greater uncertainty than in the more fuel and product rich regions near the fuel surface. The axial temperature decrease can also be attributed to increased distance from the PMMA

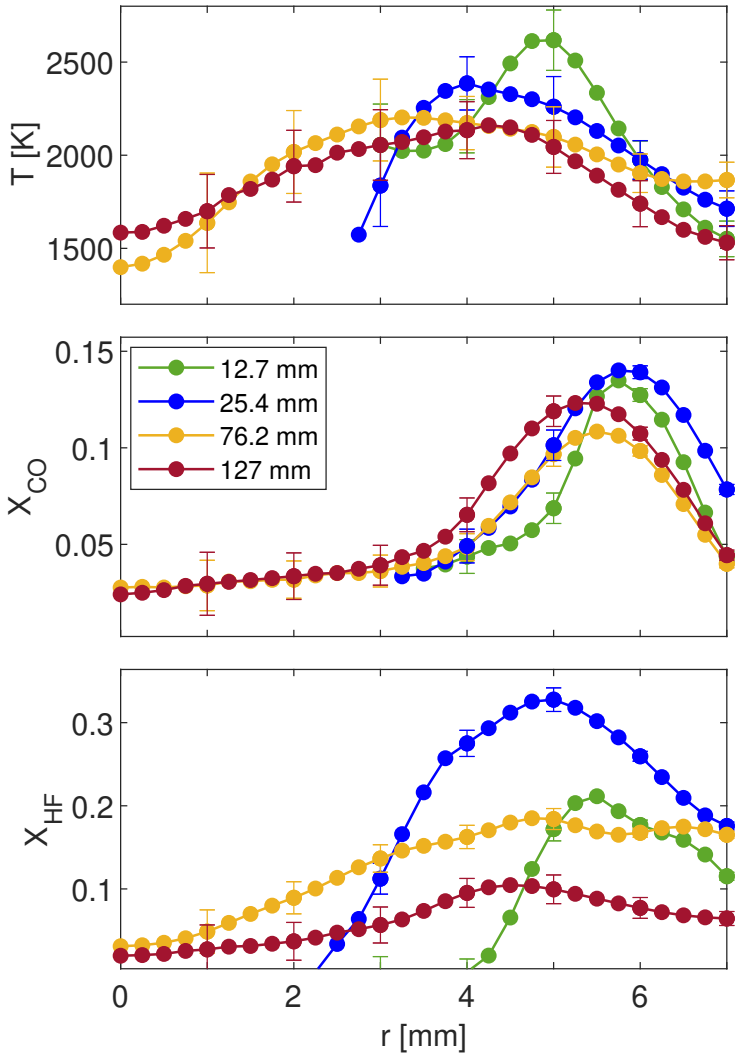

Figure 7.7 Planar species and temperature measurements for PTFE combustion along the radial dimension at different axial planes.

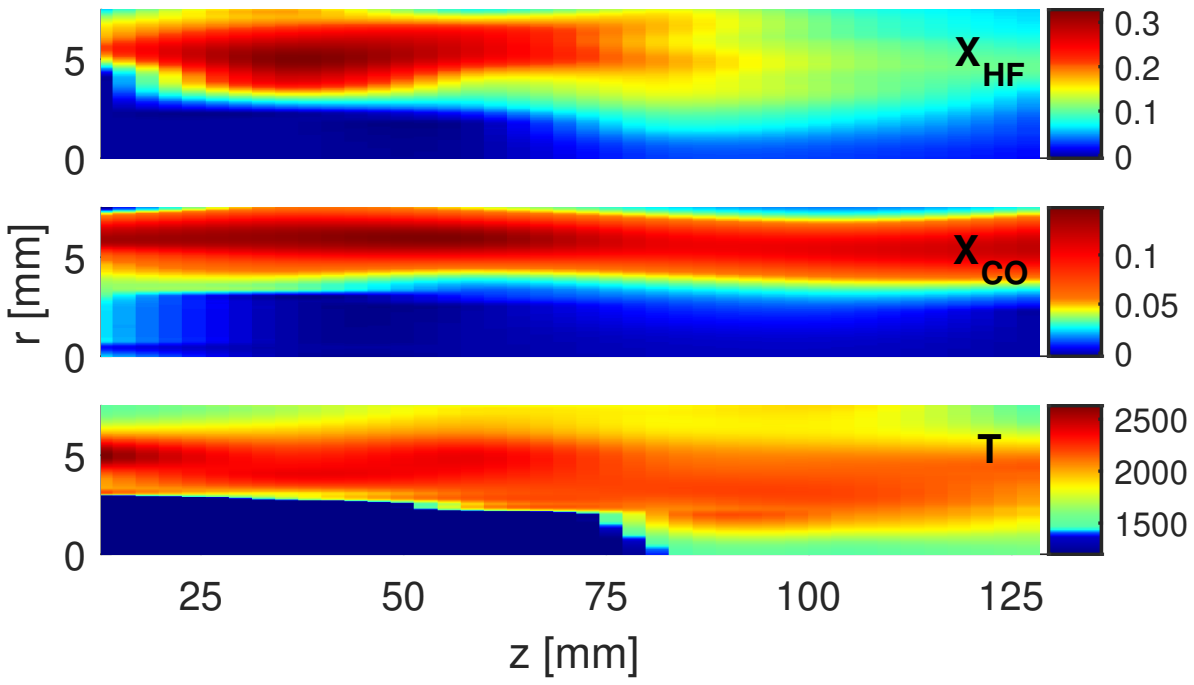

Figure 7.8 Two-dimensional thermochemical structure in the near-surface reaction layer of PTFE in an oxidizer cross-flow

pilot burner, and lower expected heat release of PTFE relative to PMMA.

The species measurements reflect an abundance of toxicant formation in the reaction layer, with HF reaching localized mole fraction values above 30%, and CO mole fraction peaking near 15%. In the bottom plot of Fig. 7.7, we observe a two phase evolution trend in X_{HF}. From the first to second measurement locations beyond the PMMA-PTFE interface where the gas is hottest, spanning 12.7 - 25.4 mm, the peak concentration of HF increases significantly and shifts about 0.5 mm towards the core. Beyond this point, however, we observe a decrease in peak HF concentration coupled with a rapid broadening across the radial domain. The more concentrated peaks seen at shorter lengths appear to spread out from their maxima a few millimeters inward of the fuel grain wall and distribute into the oxidizer core flow, though the concentrations in the core remain relatively low (X<0.05) through-

out the range of fuel lengths tested. Conversely, the high CO concentrations are largely maintained with increasing axial distances, likely reflecting a balance of radial diffusion with increasing CO formation with lower O/F. Throughout the full axial domain, encompassing 127 mm, the peak CO location moves gradually towards the core for a total variation of approximately 1 mm.

7.4 Discussion/Analysis

The measured species and temperature results discussed in the prior section reflect radial and axial variation of O/F as well as chemical reaction kinetics that compete with the transport timescales. To assess the observed trends, a thermochemical equilibrium model and chemical kinetics mechanism were used to simulate relevant conditions. Simulations were performed using 0-D reactors in the Cantera toolbox, with hydrofluorocarbon thermodynamic data and reaction rate parameters from Burgess et al. [158, 159].

7.4.1 Chemical equilibrium analysis

To estimate chemical equilibrium for PTFE combustion with the pilot PMMA burner, a two-step simulation was performed. First a chemical equilibrium simulation of PMMA and oxygen was used to attain product gas composition over a range of O/F reflecting the radial variation of O/F at the PMMA-PTFE boundary. Second, PMMA-O_2 product gas was used to prescribe the vitiated oxidizer initial conditions for PTFE combustion, using the TFE monomer as the primary fuel. The final simulated product composition is presented here in Figure 7.9 as a function of the experimental range of mass burn rates of PTFE, reflecting an increase in axial distance and corresponding reduction in O/F, which is similarly expected in radial variation moving towards the PTFE surface. The subplots show resulting composition for different initial equivalence ratios of MMA/GOx, representative of the radially-varied initial conditions [168]. The final subplot of Figure 7.9 indicates the maximum temperature

(for any O/F) expected at equilibrium based on the ratio of PTFE and PMMA mass consumption rates at different axial distances, where as $\bar{\dot{m}}_{PTFE} \rightarrow 0$, the temperature would be the maximum temperature for pure PMMA. The simulations presented here are intended to provide a reference for the range of species concentration and temperatures measured in the PTFE reaction layer.

Despite the relatively simplicity of the 0-D chemical equilibrium model, many of the observed trends in measured temperature and species are consistent. The maximum magnitude of HF mole fraction is simulated to be approximately 40% across the various initial conditions, just higher than the maximum measured values. Notably, an initial spike in HF, peaking at fuel mass flow rates between 0.1 and 0.2 g/s, is followed by a gradual decay. This trend is reflected in the experimental data wherein the peak HF concentration increases between 12.7 mm and 25.4 mm, followed by a steady decline over the sequential axial positions. The initial rise is HF corresponds with a decline in H_2O, which is presumed the dominant hydrogen-containing species in the vitiated oxidizer exiting the PMMA-O_2 pilot burner. After HF peaks, the subsequent decline corresponds to a rise in atomic fluorine and carbonyl fluoride, COF_2, provided sufficient oxygen is present. The atomic fluorine and COF_2 concentrations decline at more fuel rich conditions, which become dominated by CO and CF_2, along with diluted HF, pronounced in the most oxygen-deficient initial condition. CO is predicted to form in large concentrations at most conditions. In comparison to the experimental measurements, the equilibrium model estimates notably higher peak CO concentrations ($\sim$40%) in the fuel-rich regions by about a factor of 2. Some of the difference can certainly be related to over-simplification of the model, but carbon predicted to form carbon monoxide and other gaseous products may also disproportionately exist in solid carbon char or particles.

The equilibrium temperature shown is the maximum value across the range of radial fuel-lean to fuel-rich equivalence ratios for a given global balance of PTFE and PMMA mass burn rates at each axial position. As $\bar{\dot{m}}_{PTFE} \rightarrow 0$, the maximum equilibrium tempera-

ture approaches that of purely MMA/GOx combustion, approximately 3060K. Downstream, further away from the PMMA fuel grain, the temperature decreases to a plateau of around 2350K which is slightly higher, but within uncertainty, compared to the experimentally measured temperatures downstream. Beyond the first 25.4 mm downstream, corresponding in the model to $\bar{\dot{m}}$ of approximately 0.2, the peak temperature stabilizes. These trends are consistent with experimental data. The formation of HF is exothermic, however, the formation, by way of fluorocarbon decomposition, of the F radical is endothermic. The effects of the trade off in these fluorinated end product species is seen in the temperature trend. As less hydrogen is available for F to abstract to form HF, F radical product concentration increases and the equilibrium temperature decreases. The formation of COF_2 is similarly endothermic, thus its concentration peaks also contribute to local lower temperatures in fuel lean conditions where it is most present.

7.4.2 Reaction kinetics analysis

To better understand the reactions responsible for the observed trends in species and temperature for PTFE combustion, a high-temperature chemical kinetic reaction pathway analysis was performed. Key pathways from PTFE to CO and HF formation at 2500 K are shown in Fig. 7.10. PTFE thermally decomposes at high temperatures ($> 400°C$) primarily into the monomer, tetrafluoroeythylene (TFE), from which numerous reaction pathways exist to form HF and CO as products by way of intermediate fluorocarbons, hydrofluorocarbons (HFCs), and carbon oxofluorides (COFs). As mentioned, the PMMA combustion products serve as the primary source of hydrogen, largely via water molecules, which is required in the formation of HF. The case shown reflects the relative reaction contributions simulated at an early time step of 2.5 μs for equal mass contributions from PTFE and PMMA (the pilot burner fuel) analogous to approximately 25.4 mm downstream of the PMMA/PTFE interface. Here, the PMMA contribution is again represented by the product species resulting from a prior equilibrium simulation of MMA/GOx where $\phi = 1$. While the relative

contributions towards the formation of HF and CO are dependent on the initial fuel-oxidizer mixture and temperature, the case in Figure 7.10 was selected as it is representative of the many major contributing pathways found across initial conditions and reactor progression at combustion temperatures.

Beyond the initial depolymerization, TFE primarily decomposes into two difluoromethylene (CF_2) molecules, although some reacts to form difluoromethylide (CHF_2) and carbonyl fluoride (COF_2). The magnitude of these alternate pathways is directly impacted by the initial concentrations of H_2O and O_2 available as dictated by the preliminary MMA combustion equilibrium. The predominant pathways we observe here towards CO formation involve the oxidation of CF_2 to produce the carbon oxofluorides, CFO and CH:FO, followed by decomposition (see R3 and R4 below); the reaction following the latter species also produces HF.

$$\text{CF:O} \longrightarrow \text{CO} + \text{F} \tag{R3}$$

$$\text{CHF:O} \longrightarrow \text{CO} + \text{HF} \tag{R4}$$

Although the reaction rates (shown in $kmol/m^3s$) resulting in CO are shown to be relatively low compared to the pathways producing HF, this is largely due to the time step as the formation of HF is relatively rapid compared to that of CO.

The fluorocarbons, HFCs, and COFs nearly all have direct reactions that produce HF; however, the favored pathways consistently involve dissociation to produce the fluorine atom from these molecules. Thereafter, the highly reactive fluorine radicals rapidly abstract hydrogen from water and react with the hydrogen molecules and radicals to produce HF, per R5.

$$\text{F} + \text{H}_2\text{O} \longrightarrow \text{OH} + \text{HF} \tag{R5}$$

Numerous works have found, by way of modeling and experimental efforts, hydrogen fluoride to be formed preferably over water as a final endpoint product for hydrogen [157]. This is due to the relatively high electronegativity of fluorine and H-F bond strength, making it a more

stable product of the two. In fact, provided there are sufficient fluorine atoms available, the chemical model predicts that any water present will decompose and the hydrogen atoms will react to form, as follows from the experimental HF trend and was noted in the equilibrium simulation results above.

7.5 Conclusion

In this work, the burn characteristics and toxicant formation of polytetrafluoroethylene (PTFE) combustion were examined using laser absorption tomography. Experiments were conducted in a solid fuel combustion facility with gaseous oxygen cross-flow and a PMMA pilot burner to emulate fire-like conditions. Radially-resolved temperature and species (CO and HF) concentration profiles were obtained by inverting line-of-sight absorption measurements across the fuel grain exit planes. Quantitative, two dimensional thermochemical images were produced by compiling planar results from tests with varied fuel grain lengths. The data were compared to chemical models for fluorocarbon thermal decomposition and combustion, revealing similar trends to the experimental results and highlighting the underlying reaction pathways responsible for some observations. The geometries, operating conditions, and experimental measurements of these experiments are detailed so that the data can serve as validation targets for higher-fidelity models of toxicant formation and destruction in PTFE combustion.

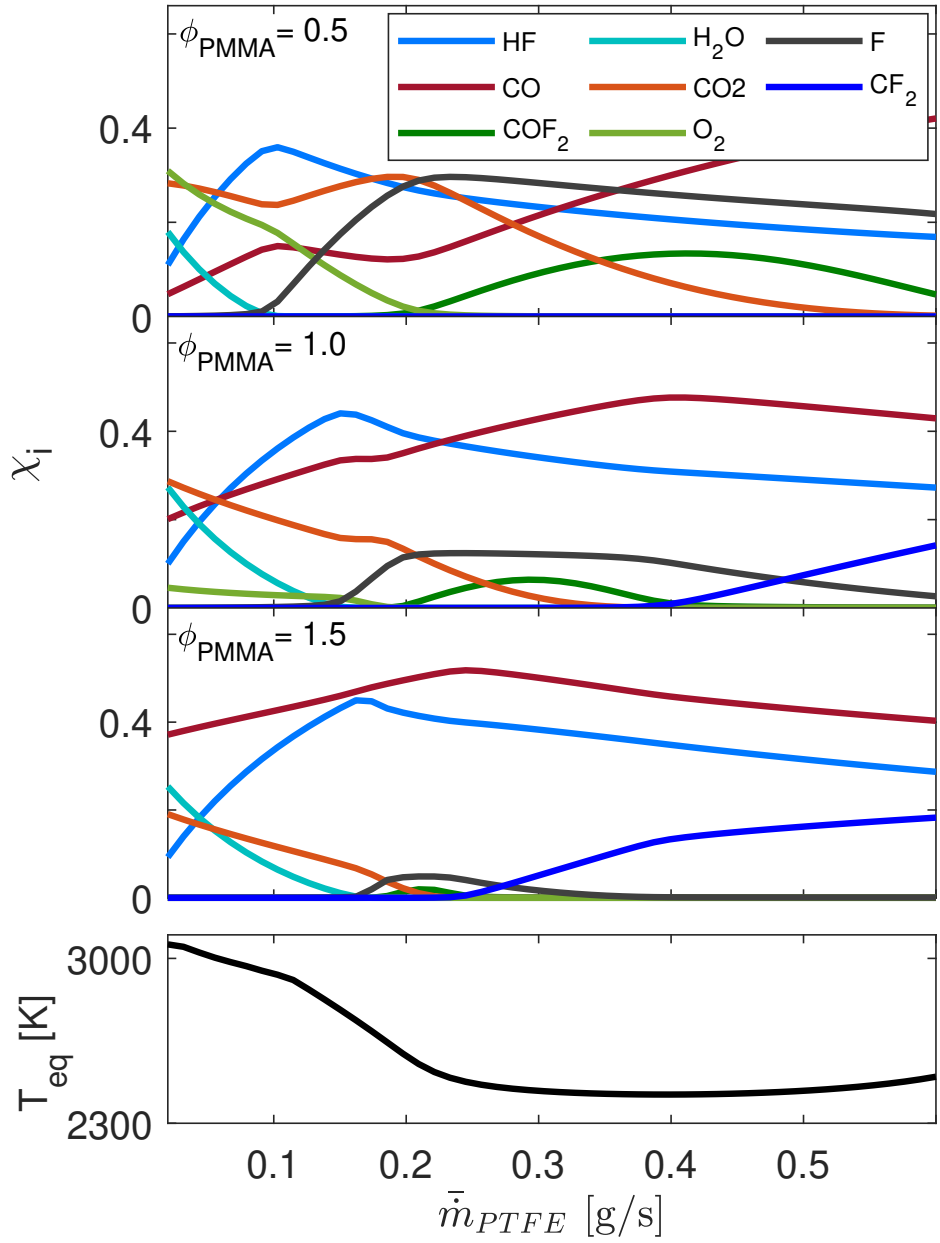

Figure 7.9 Species mole fractions (X_i) and max temperature at chemical equilibrium, T_{eq}, for PTFE combustion over a range of mass flow rates of PTFE, with oxidizer vitiated with MMA/GOx products at equivalence ratios of 0.5 and 1.5.

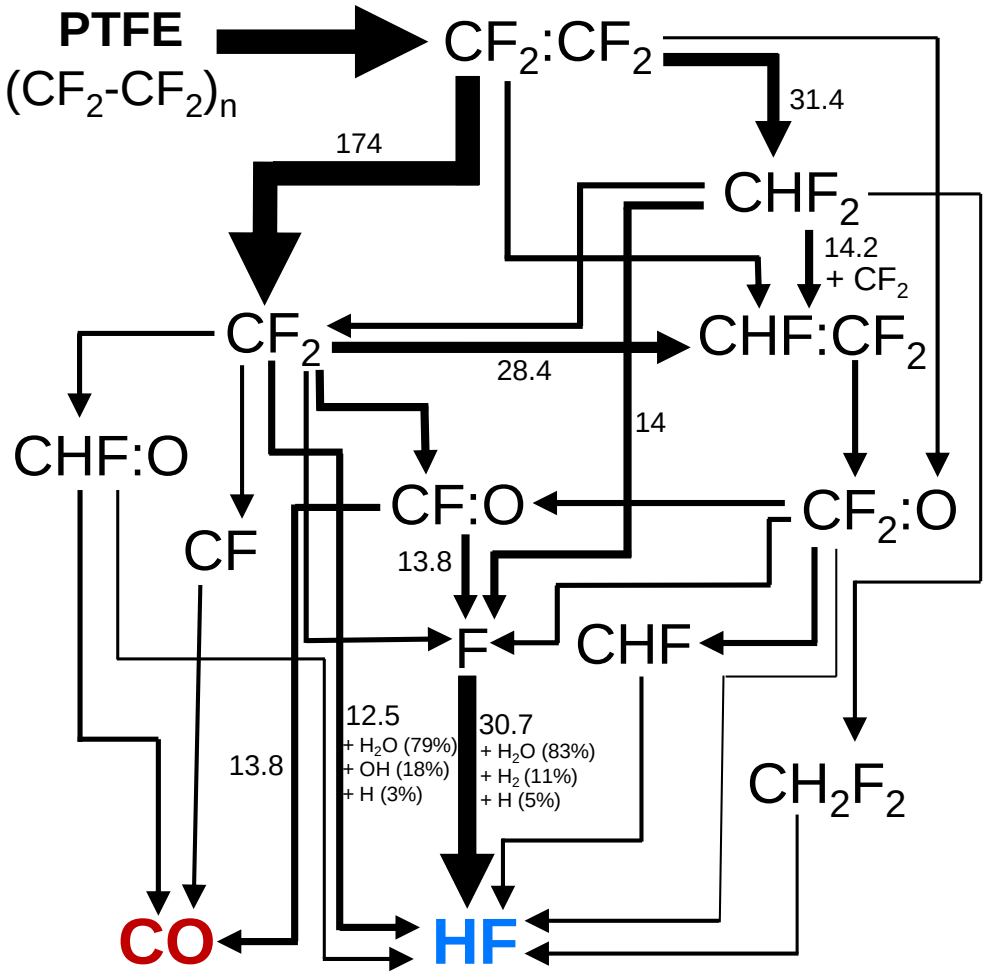

Figure 7.10 Reaction pathway diagram tracking the fluorine atom through PTFE pyrolysis and oxidation with water along pathways that result in hydrogen fluoride (and carbon monoxide) production (T = 2500K)

CHAPTER 8

Conclusions and Future Research

The research detailed in this dissertation covers the experimental methods and tools developed and employed to gain insight into hybrid combustion of solid fuels with gaseous oxidizer cross-flow. An axisymmetric solid fuel burner was used to facilitate 2D spectroscopic measurements of species and temperature in the reacting boundary layer near the fuel surface. This facility was adapted to accommodate varied flow rates, fuel types, and hybrid rocket motor geometries. Combustion intermediate and product species specific to the fuels were measured by pitching coherent laser light across the exit plane of the fuel grains to photodetectors at wavelengths corresponding to species-specific absorption transitions in the infrared. Laser absorption tomographic methods were employed to obtain spatially-resolved images of temperature and mole fraction, enabling uniquely quantitative and granular insight into the combustion physics. The data obtained from these experiments were compared to relevant combustion models. Where large discrepancies existed between models and data, as for (poly)methyl methacrylate, additional studies were performed and the chemical model adapted to more closely reproduce the experimental datasets.

The included studies cover diagnostics and fuels selected for varied applications. Chapters 3 through 6 are focused on assessing PMMA/GOx combustion for hybrid rocket propulsion performance, while Chapter 7 details an extension of the methods used for propulsion analysis to study hybrid combustion of PTFE to improve toxicant predictions and develop useful sensors for fire safety. It is envisioned that the data in this dissertation will continue to be used to anchor and improve reacting flow models relevant to both hybrid rocket propulsion

and fire safety. The sensors, experimental facilities, and analysis procedures can be used in the future to study a wide range of solid fuels and IR-absorbing species across applications.

The solid fuel combustion facility developed for assessing hybrid rocket motors was first applied to quantify effects of axial oxidizer injectors with varied port numbers as detailed in Chapter 3. Two-dimensional spatially-resolved images of carbon monoxide, carbon dioxide, water, and temperature provided one of the first quantitative measurements to compare to and validate the theorized structure of axial injection into a hybrid rocket motor. Significantly enhanced fuel regression and combustion progression was observed for injectors with multiple ports, motivating further investigation into the potential performance improvements that could be gain by novel injector geometries.

Chapter 4 discusses the next phase of hybrid rocket injector study. Aided by ANSYS fluent cold-flow studies, two swirl injectors with varied angles were designed and manufactured. Spatially-resolved thermochemical measurements again highlighted the large effect that the oxidizer injector has on hybrid combustion . Enhancements in the fuel regression and thermochemical progression were observed for a swirl injector with both a canted and swirling angle; however, it was observed that much of the improvement from incipient swirl generation is contained to regions near downstream of the oxidizer injection. Although the aforementioned thermochemical images provided great insight into the combustion progression and the relative injector performance, a direct method was desired to quantify combustion performance and efficiency within the typical rocket analysis parameters. In Chapter 5, a method for calculating spatially-resolved characteristic velocity, c^*, from thermochemical laser absorption data is presented. The local measured product species are compared to equilibrium simulations to infer a local equivalence ratio, from which local mixture molecular weight can be estimated. The measured temperature and the estimated mixture weight can be used to directly calculate the characteristic velocity. This method, compared to classical c^* measurements that rely on global aggregate measurements, more directly reflects the chemical-to-thermal energy conversion and highlights localized performance loss effects.

Chapter 6 delves into the underlying reaction chemistry that contributes to the aforementioned PMMA/GOx combustion performance results. Experiments of dilute methyl methacrylate (the monomer of PMMA) thermal decomposition were conducted with a High Enthalpy Shock Tube (HEST) facility. Time-resolved laser absorption spectroscopy measurements of intermediate and product species were recorded over a range of temperatures around atmospheric pressure. Sensitive reactions with high uncertainty in existing mechanisms were selected and their rates modified via a genetic algorithm optimization procedure anchored to the experimental data. The resulting updated chemical kinetic model can be used to improve reacting flow models and performance predicts for hybrid rocket motors using PMMA as a propellant.

In Chapter 7, similar laser absorption tomographic and experimental methods are utilized to study polytetrafluoroethylene (PTFE), often referred to by the brand name Teflon. Combustion of PTFE with PMMA as a pilot burner is analyzed via measurements of carbon monoxide and the highly hazardous toxicant, hydrogen fluoride. The resulting thermochemical measurements were used to validate kinetic models and provide crucial insight for predicting toxicity of widely used synthetic fluoropolymers.

8.1 Current and future research directions

8.1.1 Hybrid rocket motor designs

Despite the cost, safety, and theoretical performance advantages of hybrid rocket, historically poor performance largely due to low-regression rate fuels has hindered the technological maturity and scale of implementation compared to solid and liquid propellant rockets. However, in recent years, there has been a large renewed interest in hybrid rockets thanks, in part, to development of novel higher regression-rate fuels and numerous research efforts. The solid fuel combustion facility coupled with robust laser absorption tomography diagnostics, as detailed in this dissertation, can help to advance the technological maturity by way of

assessing chemical and physical engine factors that effect performance.

Subsequent studies can provide additional useful data for optimizing motor designs and improving reacting flow models. Namely, experiments can be conducted to test the influence of varied components such as additional oxidizer injectors, fuels, port diameters, and pre-combustion chamber lengths on the combustion performance.

8.1.2 High-pressure hybrid combustion measurements

The measurements included in this dissertation have been conducted at atmospheric pressure; however, a post-combustion chamber with optical access has been manufactured that can enable similar thermochemical measurements at elevated pressures. This chamber has been tested and validated for operation at pressures up to 20 atm, more representative of realistic hybrid rocket operating chamber pressures. Figure 8.1 shows the components of the high pressure chamber and an assembled view of the final assembled test facility. Further details on the high pressure chamber are included in Appendix F.

8.1.3 Laser absorption imaging for hybrid combustion analysis

Despite the successful two-dimensional measurements discussed, there are alternative strategies to obtain the same spatial-resolution that could potentially reduce uncertainty further and extend resolution into the time domain as well. Advances in infra-red camera technology have enabled quantitative measurements of many species with high spatial- and temporal-resolution [53, 94]. The light sources could be pitched across the fuel grain exit planes as in this work, but instead of relying on translating the light-of-sight, a concave lens beam expander could be used to broaden the beam profiles to span the width of the reaction zone. On the catch side, the transmitted light would be focused onto an IR-camera, with the pixel array representative of the measurement spatial domain. Measurements could be recorded at multiple times during the transient hot fire start up and steady burn to provide addi-

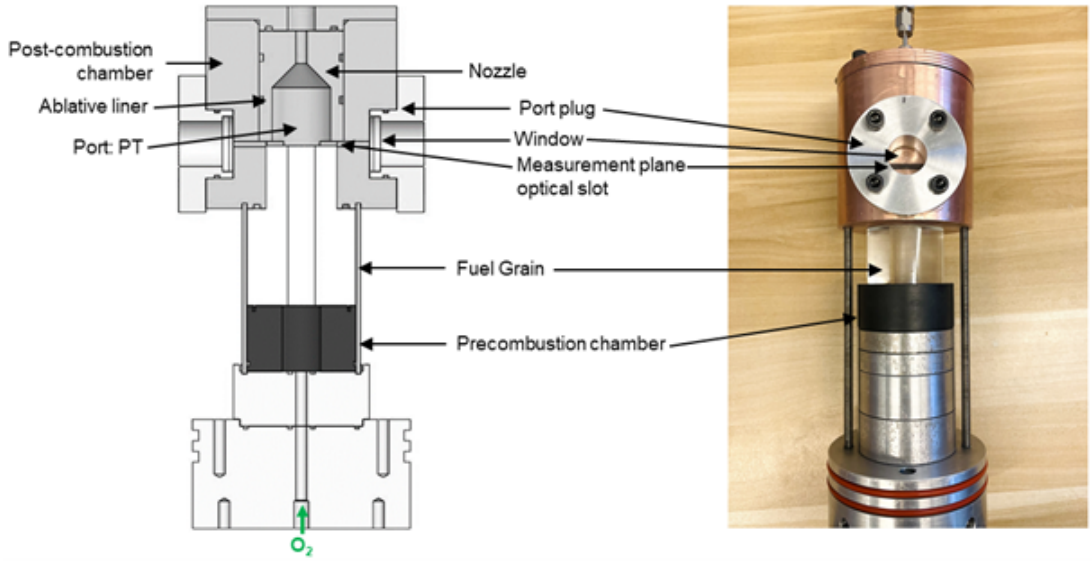

Figure 8.1 *Left:* Diagram of test facility setup for hybrid combustion measurements at elevated chamber pressures with optical access. *Right:* Assembled view of hybrid rocket motor test facility

tional insight into the combustion performance. Expected limitations of this method include the significantly higher equipment cost of an IR-camera and difficulty taking simultaneous multi-species measurements on a single camera.

8.1.4 Fire-resistant fuel characterization

The solid fuel burner experiment used for studying polytetrafluoroethylene (PTFE) with a PMMA pilot burner can be re-configured to obtain similar measurements of toxicant formation resulting from hybrid combustion of other fire-resistant polymers. Those include halogenated, inorganic, organophosphorus, and nitrogen-containing fire-retardent solid polymers.

8.1.5 Lithium-Ion Battery Fires

Lithium ion batteries are increasingly widespread, particularly so in modern electric vehicles. They are selected for their high energy and power densities, long life span, and fast charging capabilities; however, Li-ion batteries contain highly reactive and flammable materials that have led to a number of unfavorable incidents in recent years [169]. Overheating of the batteries can lead to exothermic reactions and thermal runaway with significant heat, fire, and toxic gas emissions. A known resulting toxicant of particular concern is hydrogen fluoride (HF). Some of the HF is known to form via decomposition of electrolytes containing $LiPF_6$, although this has been studied mainly at ambient temperature and under mild heating conditions. There exists a lack of sufficient understanding of HF emissions from Li-Ion batteries at high temperature relevant to electric vehicle fires [170]. Experimental toxicant data in Li-Ion battery combustion and chemical kinetic models at relevant environmental conditions will be essential for predicting hazard levels and mitigating harm due to HF emissions. The sensor developed for measuring HF for fire toxicity applications as well as the kinetic modeling approach discussed in Chapter 7 could be used to provide some of this critically lacking information.

8.1.6 TFE Chemical Kinetics

Despite the adequate agreement in speciation results from the polytetrafluoroethylene (PTFE) combustion experiments and kinetic modelling in Chapter 7, the discrepancy observed, particularly for carbon monoxide, is notable and motivates further work to ensure adequate toxicity predictions from models. Improvements can be made by way of kinetic experimental studies and the subsequent modifying of reaction rate parameters in the chemical kinetic mechanisms. Chapter 6 describes an approach for improving (poly)methyl methacrylate models through shock-heated thermal decomposition experiments of the monomer methyl methacrylate (MMA), the data from which was used to optimize the kinetic mechanism.

Figure 8.2 Tesla Model S e-vehicle in the midst of an uncrolled lithium-ion battery fire [12].

Similarly, modelling of PTFE combustion would benefit greatly from study of its monomer, tetrafluoroethylene (TFE), through shock tube thermal decomposition and/or oxidation with laser absorption spectroscopy diagnostics targeting multuple relevant intermediate and product species, such as CF_2, HF, COF_2, CO, and CO_2. The monomer TFE is gaseous at room temperature and can be procured directly from many typical chemical distributors. Experiments should be run at dilute concentrations of TFE to reduce uncertainty in post-shock temperature and mitigate potential contamination and/or damage to the shock tube facility.

listings

APPENDIX A

Uncertainty analysis

In this paper, we implement a novel absorption spectroscopy method for quantitative measurements of temperature and species mole fractions (CO, CO_2, H_2O) to evaluate the influence of injector design on hybrid rocket combustion performance. Additionally, we provide experimental results for space-time averaged measurements of O/F, regression rate, and oxidizer mass flux. To facilitate comparison to computational models and other works, this Appendix details experimental uncertainties associated with space-time averaged measurements. For uncertainties in temperature and species mole fractions, the reader is referred to a recent work from our research group [88, 53], where similar spectroscopic techniques are applied.

As in that work, unless otherwise noted, we follow a Taylor series method of uncertainty propagation [101], in which the uncertainty of a variable r, Δr, is given by:

$$(\Delta r)^2 = \left(\frac{\partial r}{\partial x_1}\Delta x_1\right)^2 + \left(\frac{\partial r}{\partial x_2}\Delta x_2\right)^2 + \cdots \tag{A.1}$$

where x_i are dependent variables and Δx_i are their associated uncertainties.

A.1 O/F uncertainty

The reported values for space-time averaged O/F were obtained through oxidizer and fuel mass flow rate measurements, $\dot{m}_{ox}$ [kg/s] and $\bar{\dot{m}}_f$ [kg/s], respectively, as shown in Eq. 3.6. In this study, oxidizer mass flow rate was measured and regulated using a choked orifice and was kept constant throughout the hot-fire experiments. With knowledge of the sonic orifice area, A_o [m^2], the discharge coefficient, C_d, and the upstream pressure, P [Pa], and

temperature, T [K], $\dot{m}_{ox}$ can be calculated using the equation for choked flow:

$$\dot{m}_{ox} = \frac{A_{\mathrm{o}} C_{\mathrm{d}} P}{\sqrt{T}} \left[\sqrt{\frac{\gamma}{R}} \left(\frac{\gamma+1}{2} \right)^{\frac{-\gamma-1}{2(\gamma-1)}} \right] \tag{A.2}$$

where γ and R [J/kg·K] are the specific heat ratio and gas constant of the oxidizer, respectively. Space-time averaged fuel mass flow rate was obtained by measuring the total consumed fuel mass, ΔM_f [kg], and the total burn time, t_b [s]:

$$\bar{\dot{m}}_f = \frac{\Delta M_f}{t_b} \tag{A.3}$$

The uncertainty in O/F is then be determined by applying Eq. A.1 to Eqs. 3.6–A.3, which results in:

$$\begin{aligned} \left(\frac{\Delta \mathrm{O/F}}{\mathrm{O/F}} \right)^2 = & \left(\frac{\Delta A_{\mathrm{o}}}{A_{\mathrm{o}}} \right)^2 + \left(\frac{\Delta C_{\mathrm{d}}}{C_{\mathrm{d}}} \right)^2 + \left(\frac{\Delta P}{P} \right)^2 \\ & + \left(\frac{\Delta T}{2T} \right)^2 + \left(\frac{\Delta t_b}{t_b} \right)^2 + \left(\frac{\Delta (\Delta M_f)}{\Delta M_f} \right)^2 \end{aligned} \tag{A.4}$$

Evaluating the experimental uncertainties of all the contributing dependent variables in Eq. A.4 results in a total O/F uncertainty of 4.56%. A visual summary of the individual

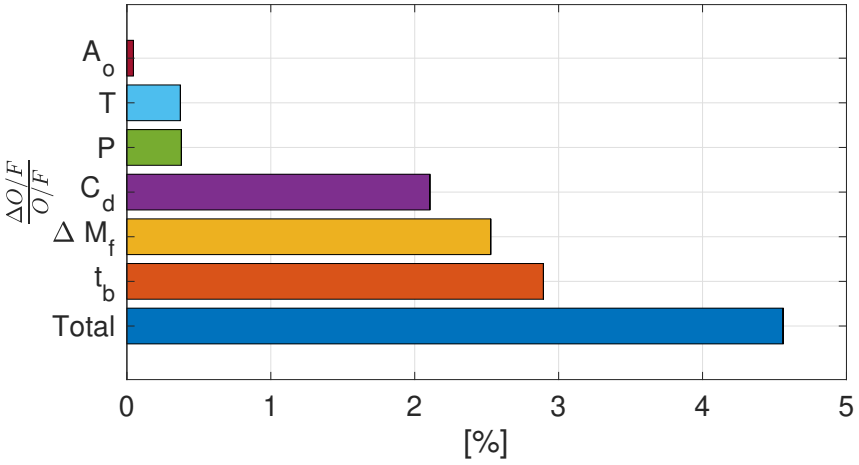

Figure A.1 Representative experimental uncertainties contributing to the overall uncertainty in the reported O/F values in Table 7.1

contributions is shown in Fig. A.1. The three major contributors were found to be the uncertainty in the total burn time, t_b, the total consumed fuel mass, ΔM_f, and the orifice discharge coefficient, C_d, which, respectively, make up 2.90%, 2.53%, and 2.11% of the total uncertainty. The uncertainties in t_b and ΔM_f primarily result from errors inherent to the measurement devices. C_d and ΔC_d were determined through a least-squares linear regression fit of Eq. A.2. The remaining uncertainties in O/F are due to contributions from uncertainties in pressure, P, temperature, T, and orifice area, A_o, which, respectively, make up 0.38%, 0.37%, and 0.05% of the total uncertainty. Pressure and temperature were measured using a pressure transducer (Setra 225G) with an accuracy of ±0.25% of the full scale (100 psia) and a K-type thermocouple with an uncertainty of ±0.75%, respectively. The diameter of the choked orifice was measured using precision plug gauges to within 0.001 in., which was used to determine A_o and ΔA_o.

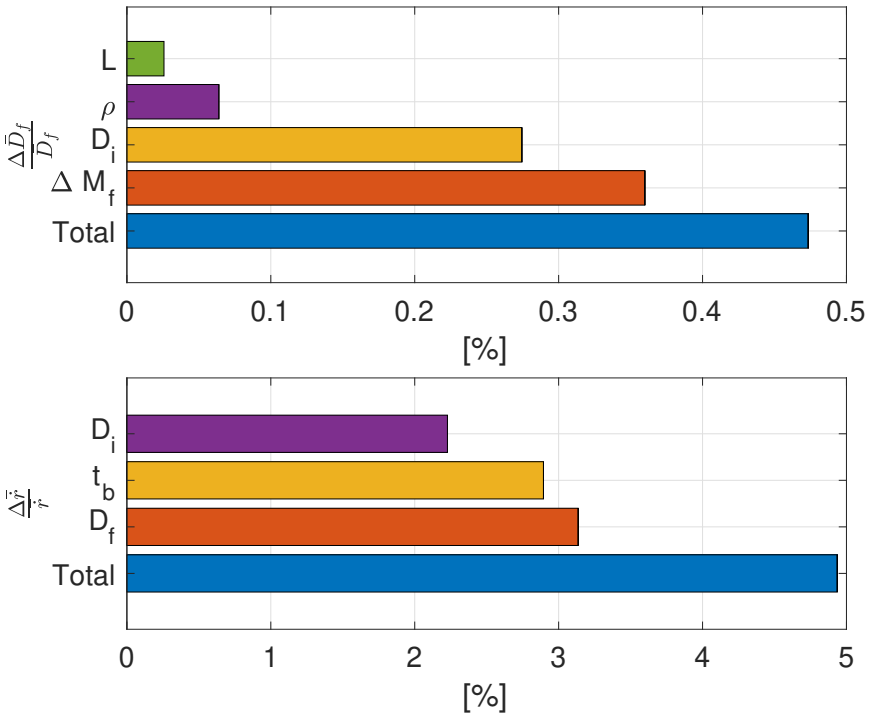

Figure A.2 Representative experimental uncertainties contributing to the overall uncertainty in the reported $\bar{\dot{r}}$ values in Table 7.1

A.2 Regression rate uncertainty

Space-time averaged regression rates, $\bar{\dot{r}}$ [mm/s], are measured using the methods developed by Karabeyoglu et al. [65] as shown in Eq. 4.6. Uncertainties in the reported $\bar{\dot{r}}$ values are found by applying Eq. A.1 to Eq. 4.6, which results in:

$$\left(\frac{\Delta\bar{\dot{r}}}{\bar{\dot{r}}}\right)^2 = \left[\left(\frac{\bar{D}_f}{2t_b\bar{\dot{r}}}\right)\frac{\Delta\bar{D}_f}{\bar{D}_f}\right]^2 + \left[\left(\frac{D_i}{2t_b\bar{\dot{r}}}\right)\frac{\Delta D_i}{D_i}\right]^2 + \left(\frac{\Delta t_b}{t_b}\right)^2 \tag{A.5}$$

As seen in Eq. A.5, the regression rate uncertainty is primarily composed of contributions from the associated errors in the average final port diameter, $\bar{D}_f$, the initial port diameter, D_i, and the total burn time, t_b. The initial port diameter for each fuel grain was measured within 0.05 mm prior to any hot-fire experiments, resulting in an uncertainty of $\Delta D_i/D_i = 0.39\%$ due to the measurement device. Similarly, the measurement device uncertainty in total burn time is $\Delta t_b/t_b = 2.90\%$, as discussed in Sec. A.1. In order to determine the uncertainty contribution of $\bar{D}_f$ in the regression rate, the individual uncertainty contributions of $\bar{D}_f$ must first be evaluated using Eq. 4.8. This results in an expression for $\Delta\bar{D}_f/\bar{D}_f$ given by:

$$\begin{aligned}\left(\frac{\Delta\bar{D}_f}{\bar{D}_f}\right)^2 =& \left(\frac{4\Delta M_f}{2\pi\bar{D}_f^2 L_f\rho_f}\right)^2\left[\left(\frac{\Delta(\Delta M_f)}{\Delta M_f}\right)^2 + \left(\frac{\Delta\rho_f}{\rho_f}\right)^2 + \left(\frac{\Delta L_f}{L_f}\right)^2\right] \\ &+ \left[\left(\frac{D_i}{\bar{D}_f}\right)^2\frac{\Delta D_i}{D_i}\right]^2\end{aligned} \tag{A.6}$$

To minimize the uncertainty in the average final port diameter and, ultimately, in the regression rate, the density of the PMMA stock, ρ_f, was measured prior to manufacturing and the length of each fuel grain was measured post-manufacturing. This results in a density uncertainty of $\Delta\rho_f/\rho_f = 0.42\%$ and a fuel-grain length uncertainty of $\Delta L_f/L_f = 0.16\%$. The overall uncertainty in the average final port diameter is $\Delta\bar{D}_f/\bar{D}_f = 0.47\%$. The uncertainty contributions to $\bar{D}_f$ are then propagated into the measured uncertainty in regression rate through Eq. A.5, resulting in a total $\bar{\dot{r}}$ uncertainty of 4.94%. The contributions to both $\bar{D}_f$ and $\bar{\dot{r}}$ are illustrated in Fig. A.2.

A.3 Oxidizer mass flux uncertainty

Similar to the preceding sections, the uncertainty in the reported space-time averaged oxidizer mass flux, $\bar{G}_{ox}$ [kg/m^{2}s], measurements can be evaluated through Eq. 3.4:

$$\left(\frac{\Delta\bar{G}_{ox}}{\bar{G}_{ox}}\right)^2 = \left(\frac{\Delta\dot{m}_{ox}}{\dot{m}_{ox}}\right)^2 + \left[\left(\frac{2D_i}{D_i+\bar{D}_f}\right)\frac{\Delta D_i}{D_i}\right]^2 + \left[\left(\frac{2\bar{D}_f}{D_i+\bar{D}_f}\right)\frac{\Delta\bar{D}_f}{\bar{D}_f}\right]^2 \tag{A.7}$$

This results in a total oxidizer mass flux uncertainty of $\Delta\bar{G}_{ox}/\bar{G}_{ox} = 2.27\%$ with the primary contributor being the error in oxidizer mass flow rate. $\Delta\dot{m}_{ox}/\dot{m}_{ox}$ was calculated to be 2.17% through Eq. A.2 and $\Delta D_i/Di$ and $\Delta\bar{D}_f/\bar{D}_f$ were 0.39% and 0.47%, respectively, as discussed in the previous sections. The individual contributions resulting in the total oxidizer mass flux uncertainty are summarized in Fig. A.3.

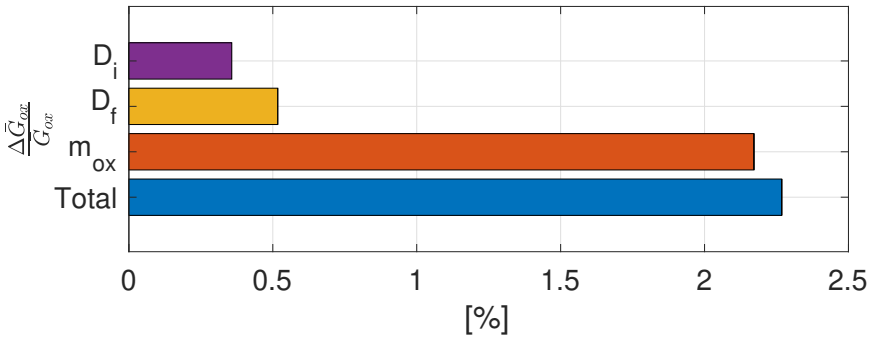

Figure A.3 Representative experimental uncertainties contributing to the overall uncertainty in the reported $\bar{G}_{ox}$ values in Table 7.1

Grid no.	Max. size [m]	SOI 1 min. size [m]	SOI 2 min. size [m]	SOI 3 min. size [m]	Total elements	Total nodes	Max. Axial Velocity [m/s]	Inlet Pressure [Pa]
Single-port injector								
1	6.0×10^{-3}	4.0×10^{-3}	1.0×10^{-3}	–	60,000	25,000	66.2	1.038×10^{5}
2	3.0×10^{-3}	2.3×10^{-3}	9.0×10^{-4}	–	130,000	55,000	55.8	1.021×10^{5}
3	1.5×10^{-3}	1.0×10^{-3}	8.0×10^{-4}	–	270,000	100,000	53.5	1.020×10^{5}
Axial showerhead injector								
1	1×10^{-3}	1×10^{-3}	9×10^{-4}	7.0×10^{-4}	110,000	45,000	106	1.978×10^{5}
2	1×10^{-3}	9×10^{-4}	7.5×10^{-4}	4.0×10^{-4}	225,000	100,000	82.4	1.814×10^{5}
3	1×10^{-3}	8×10^{-4}	4.5×10^{-4}	2.0×10^{-4}	450,000	140,000	80.0	1.772×10^{5}

Table A.1 Details of mesh convergence study for CFD cold-flow analysis

APPENDIX B

JPP supplementary material

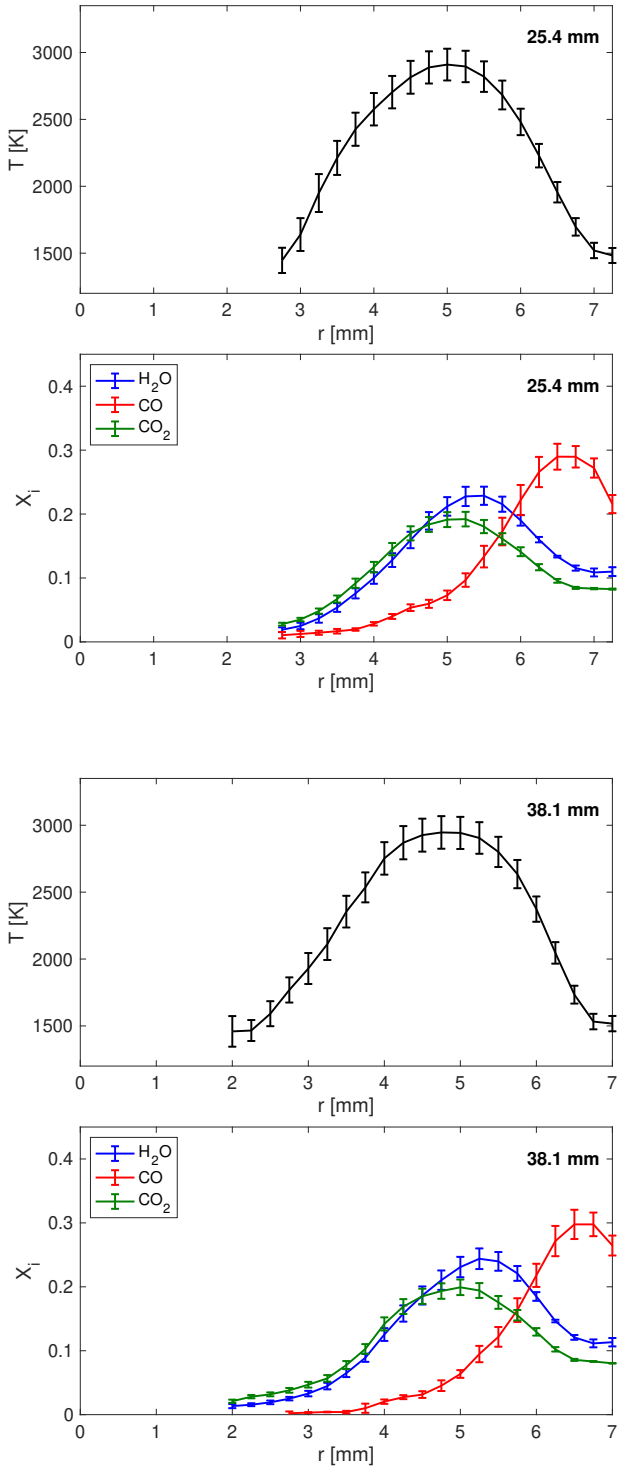

Figure B.1 Planar thermochemistry measurements for PMMA/GOx combustion at 25.4 and 38.1 mm using a single-port injector geometry

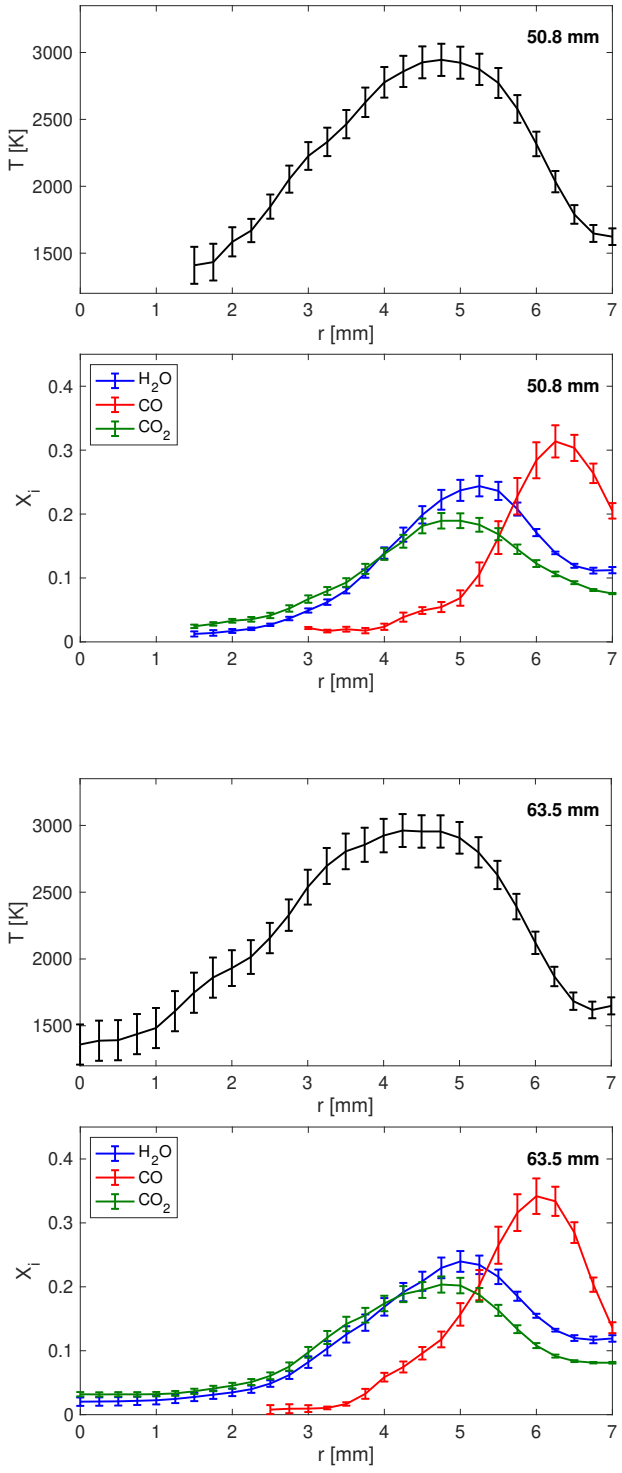

Figure B.2 Planar thermochemistry measurements for PMMA/GOx combustion at 50.8 and 63.5 mm using a single-port injector geometry

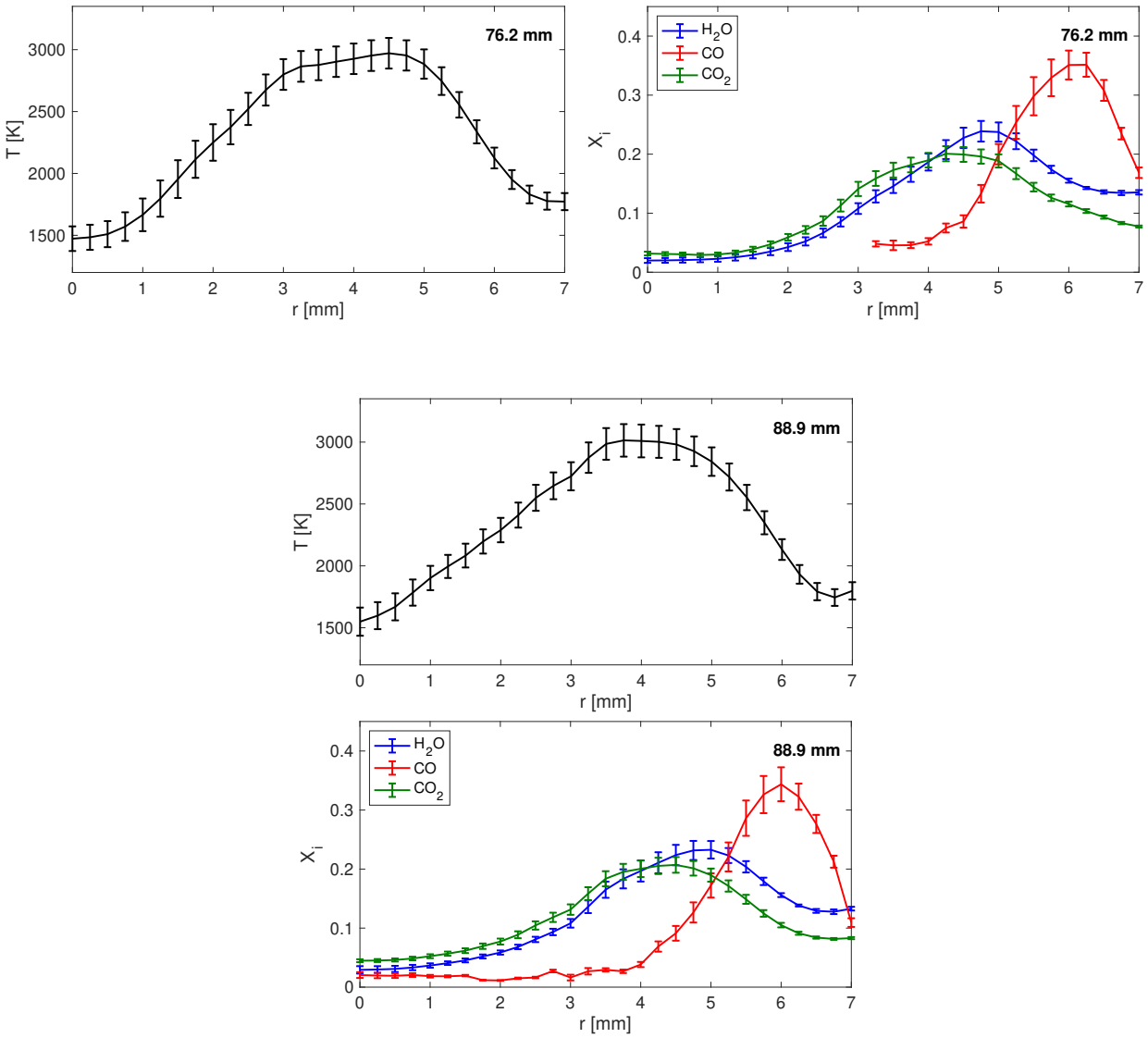

Figure B.3 Planar thermochemistry measurements for PMMA/GOx combustion at 76.2 and 88.9 mm using a single-port injector geometry

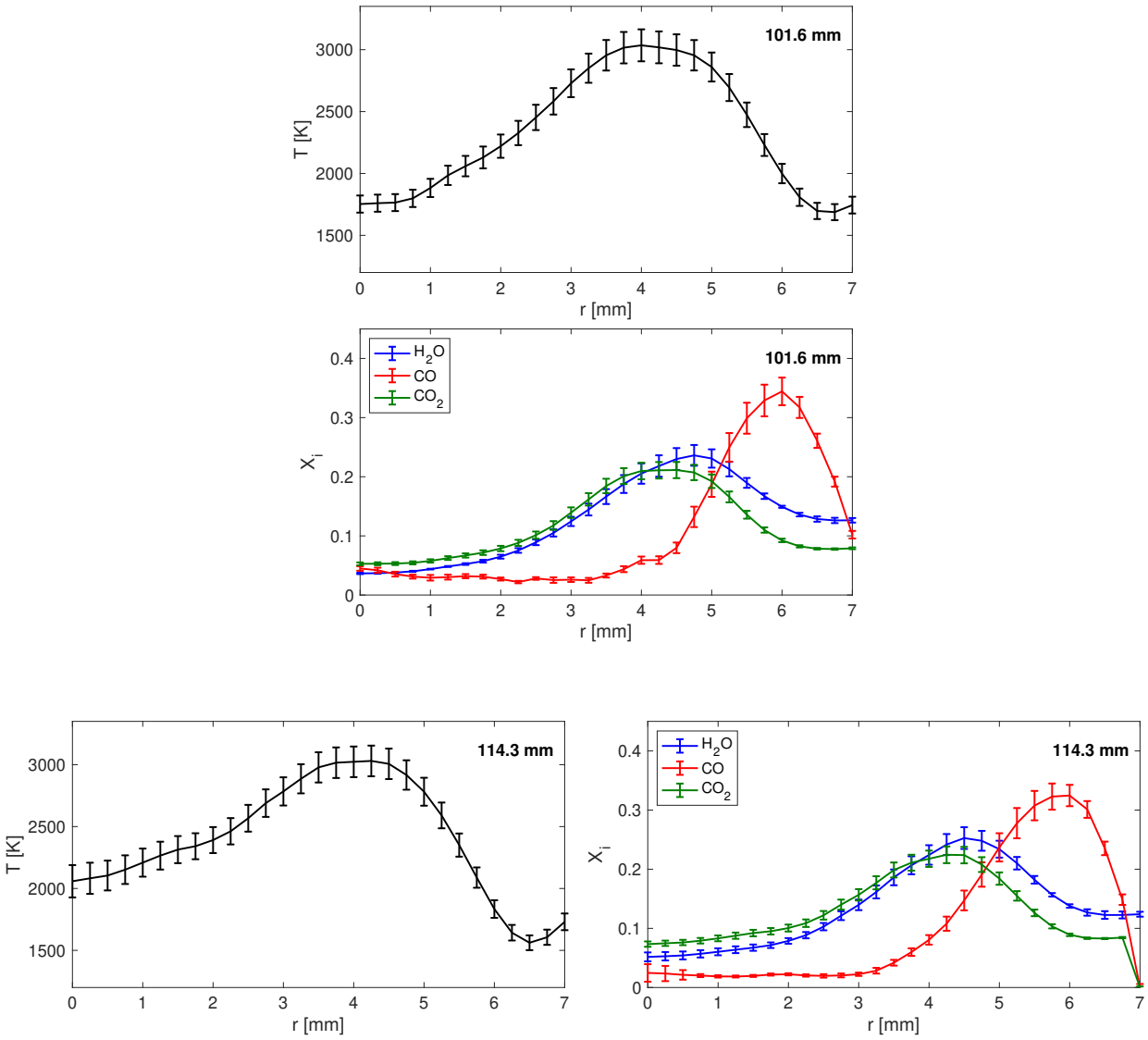

Figure B.4 Planar thermochemistry measurements for PMMA/GOx combustion at 101.6 and 114.3 mm using a single-port injector geometry

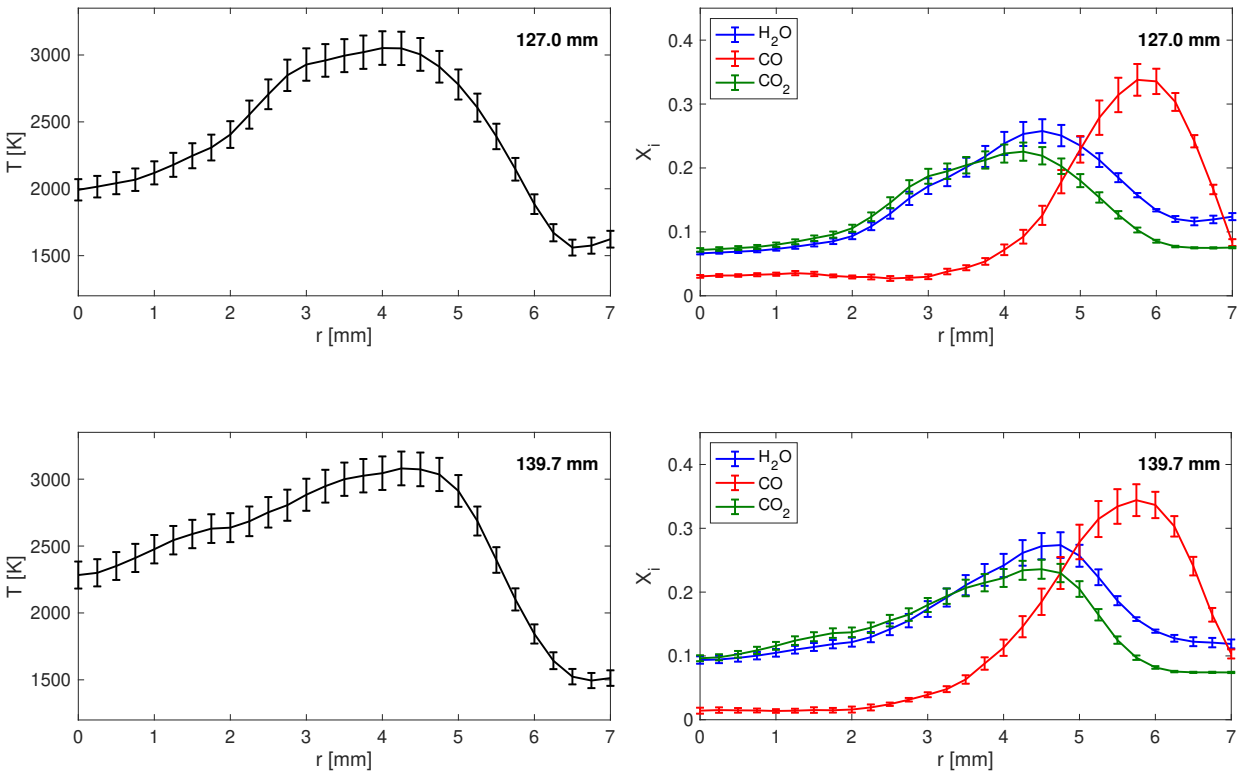

Figure B.5 Planar thermochemistry measurements for PMMA/GOx combustion at 127.0 and 139.7 mm using a single-port injector geometry

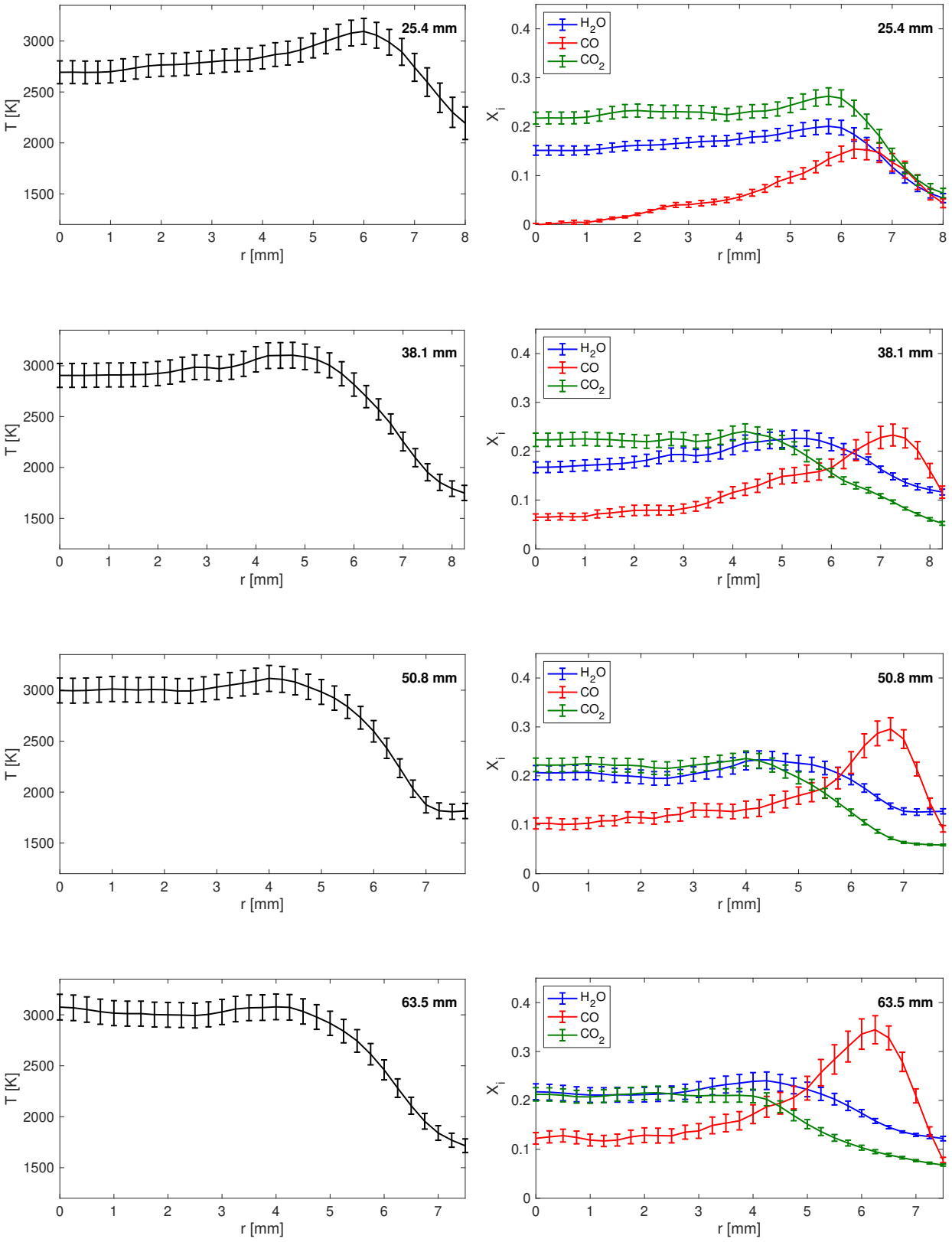

Figure B.6 Planar thermochemistry measurements for PMMA/GOx combustion at 25.4, 38.1, 50.8, and 63.5 mm using an axial showerhead injector geometry

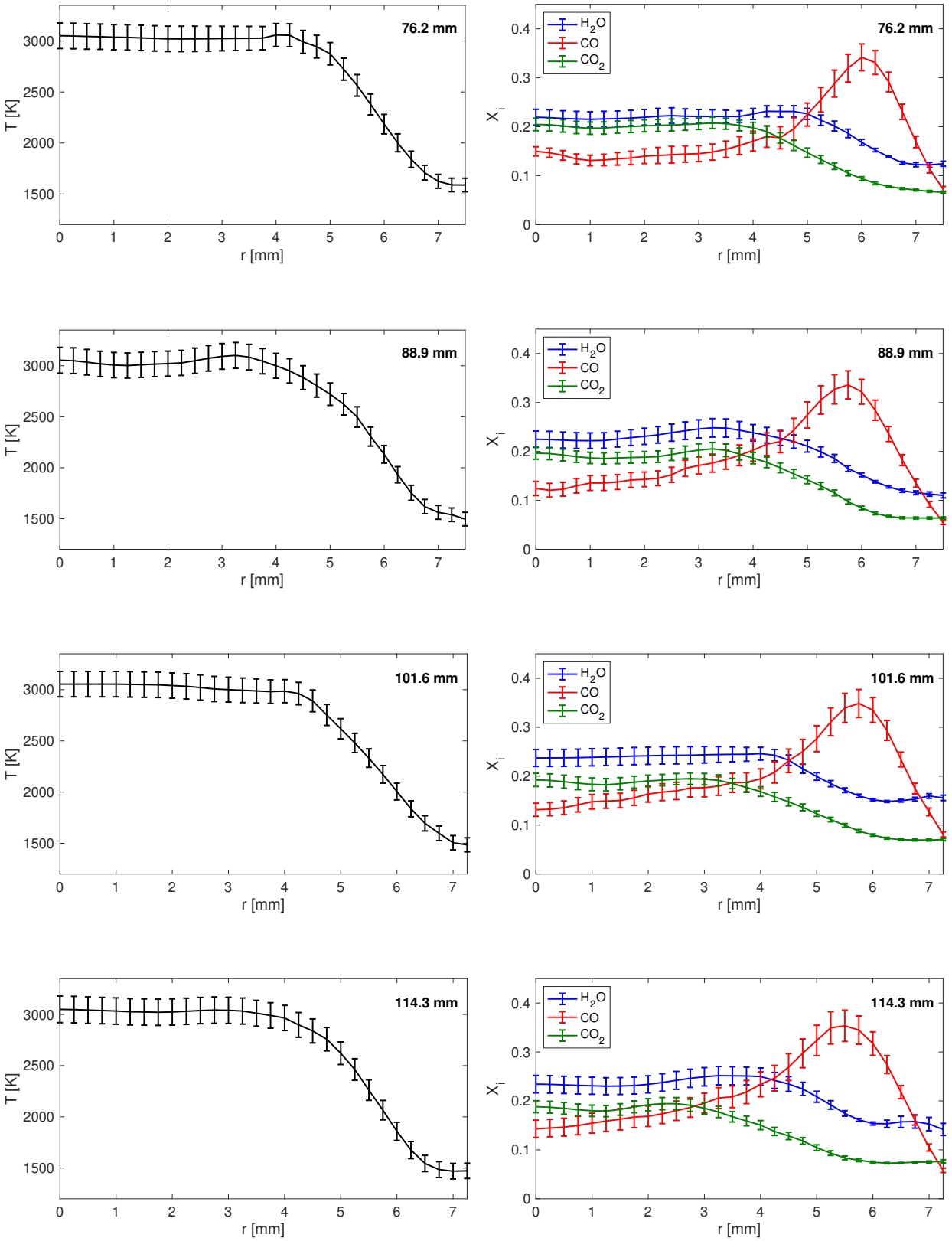

Figure B.7 Planar thermochemistry measurements for PMMA/GOx combustion at 76.2, 88.9, 101.6, and 114.3 mm using an axial showerhead injector geometry

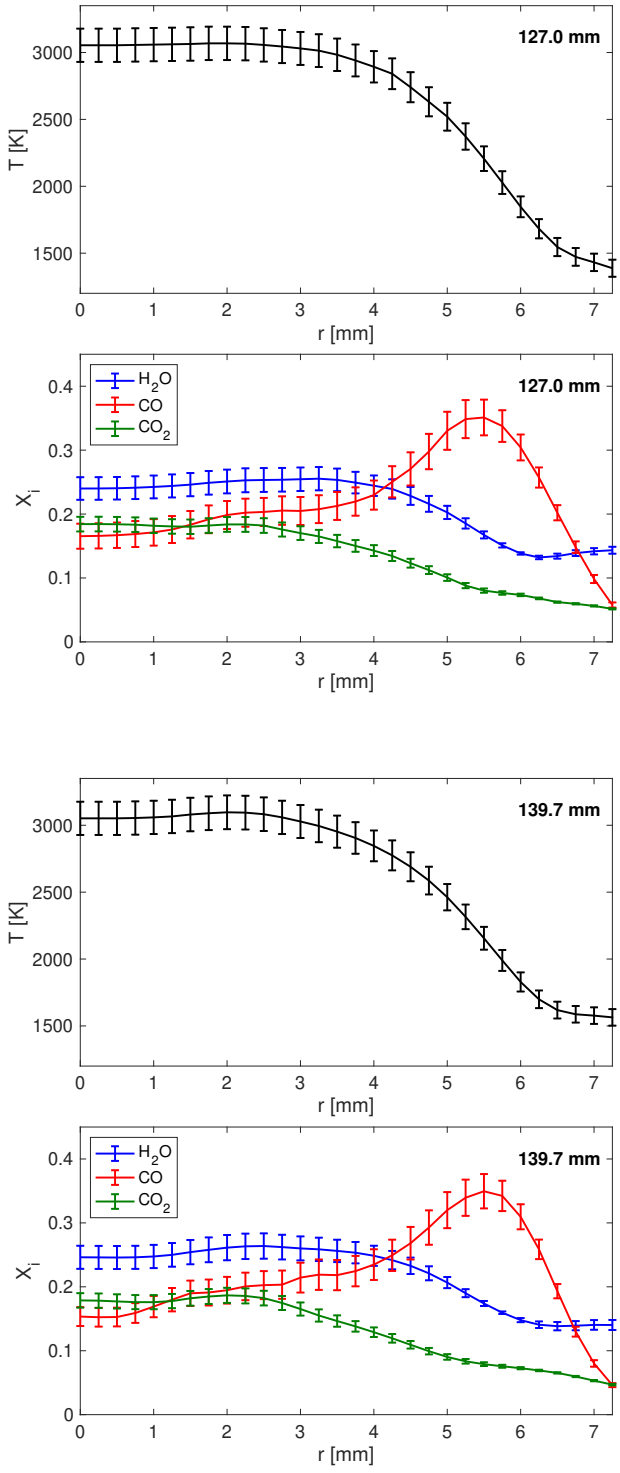

Figure B.8 Planar thermochemistry measurements for PMMA/GOx combustion at 127.0 and 139.7 mm using an axial showerhead injector geometry

APPENDIX C

CFD mesh convergence study

A mesh convergence study was done on the fluid domain of each injector. The minimal acceptable residual value for convergence of simulations was 1×10^{-4}, required for axial, swirl, and tangential velocity directions. A relatively coarse mesh element size was used as the base for each grid, which was then refined using two or three separate spheres of influence (SOI) with varied radii and element size. The spheres' centers were placed at the interface of the injector and pre-combustion chamber. The radii used were 3.5×10^{-2} m and 1.5×10^{-2} m for SOI 1 and SOI 2 for the single-port injector study. For the showerhead injector, the radii for SOI 1, 2, and 3 were 3.5×10^{-2} m, 2×10^{-2} m, and 4×10^{-3}, respectively. The elements within these spheres were refined by decreasing the element sizes such that the total number of elements increased by approximately a factor of 2 for each consecutive mesh study, as is common for such studies.

This was repeated until the resulting maximum axial (y-component) velocity in the core flow on the injector outlet plane converged reasonably. We looked for convergence by quantifying the error in two values of interest as the difference between the result from a given grid and the result from the most refined grid studied. Specifically, we looked to see a 5% or lesser change in velocity between results from a mesh to this fine mesh. Similarly, the inlet pressure was also recorded and looked to for a maximum 5% change. This pressure result can additionally be compared to the pressure upstream of the injector that was measured experimentally with a digital pressure gauge during cold-flow tests conducted in the test rig setup with both injector geometries (shown by the dashed line in Fig. C.1). All values

presented are absolute pressures.

Details on the progression of the grid refining results are shown in Table A.1 and Fig. C.1. Both the second mesh of medium coarseness (grid no. 2) and the most refined mesh (grid no. 3) for the single-port injector showed similar velocity and inlet pressure values. The resulting velocity and pressure of interest errors were 2.3 m/s (a 4.1% difference from the fine grid solution) and 1860 Pa (1.8% error), respectively, between the grid no. 2 and grid no. 3 simulations. Thus, this third grid with 270,000 elements and 100,000 nodes was deemed sufficient and used for the presented CFD results. For the axial showerhead injector, the error between the grid no. 2 and grid no. 3 mesh results for maximum core axial velocity (2.4 m/s or 3.0% error) and inlet pressure (4000 Pa or 2.4% error) were sufficient. Thus, grid no. 3 with 450,000 elements and 140,000 nodes was used for the showerhead analysis. The grid no. 3 pressure results for both injectors deviated from the experimentally measured pressure by less than 0.1%.

For completeness, after the mesh convergence study, the simulations were also conducted with a pressure inlet boundary condition using the experimentally measured upstream pressures to verify that the resulting oxidizer mass flow rate was consistent with the known value of 1.2 g/s.

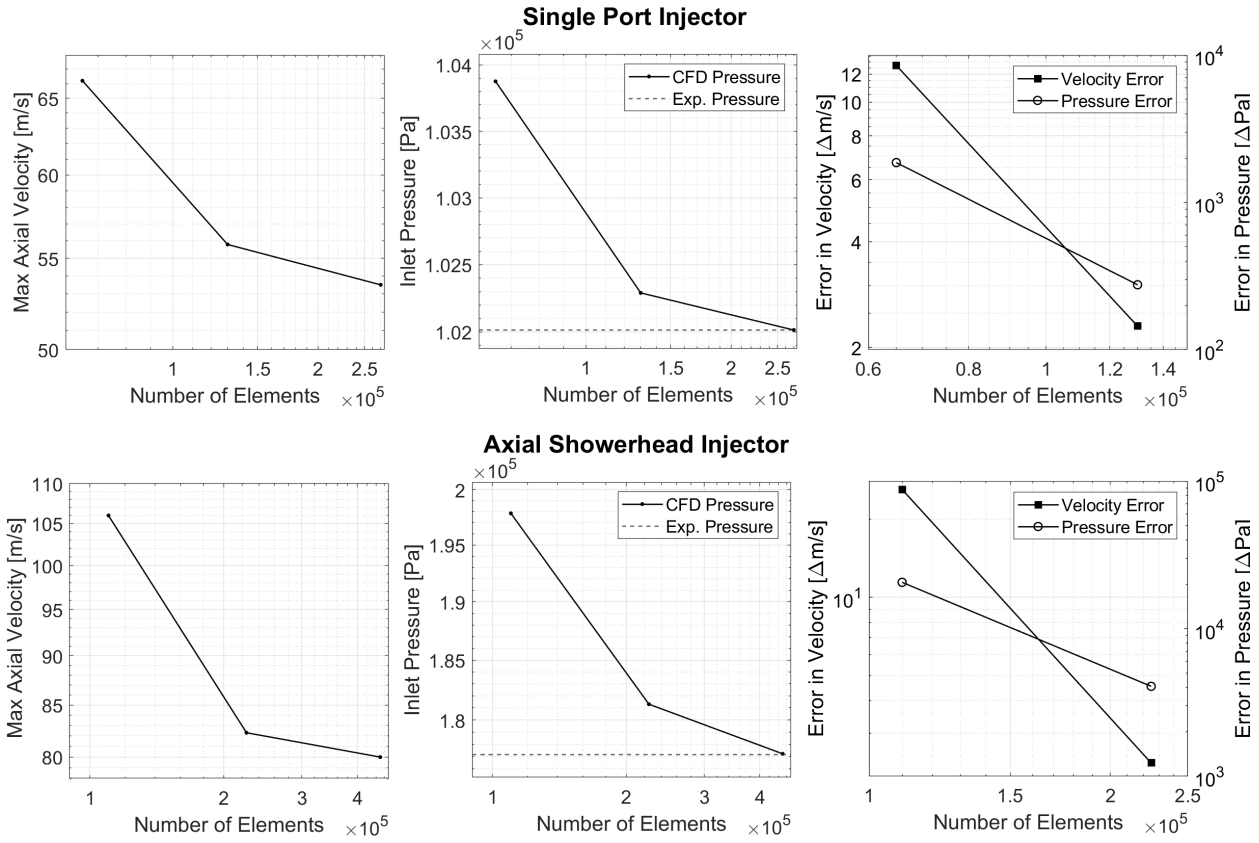

Figure C.1 Plot of maximum axial velocity in the injector outlet plane (*left*) and inlet pressure (*middle*) over a range of mesh coarseness for the single-port and axial showerhead injector simulations. Error in results from each mesh compared to the most fine grid results are shown (*right*)

APPENDIX D

Fuel: Supplementary Material

D.1 Sample spectral data

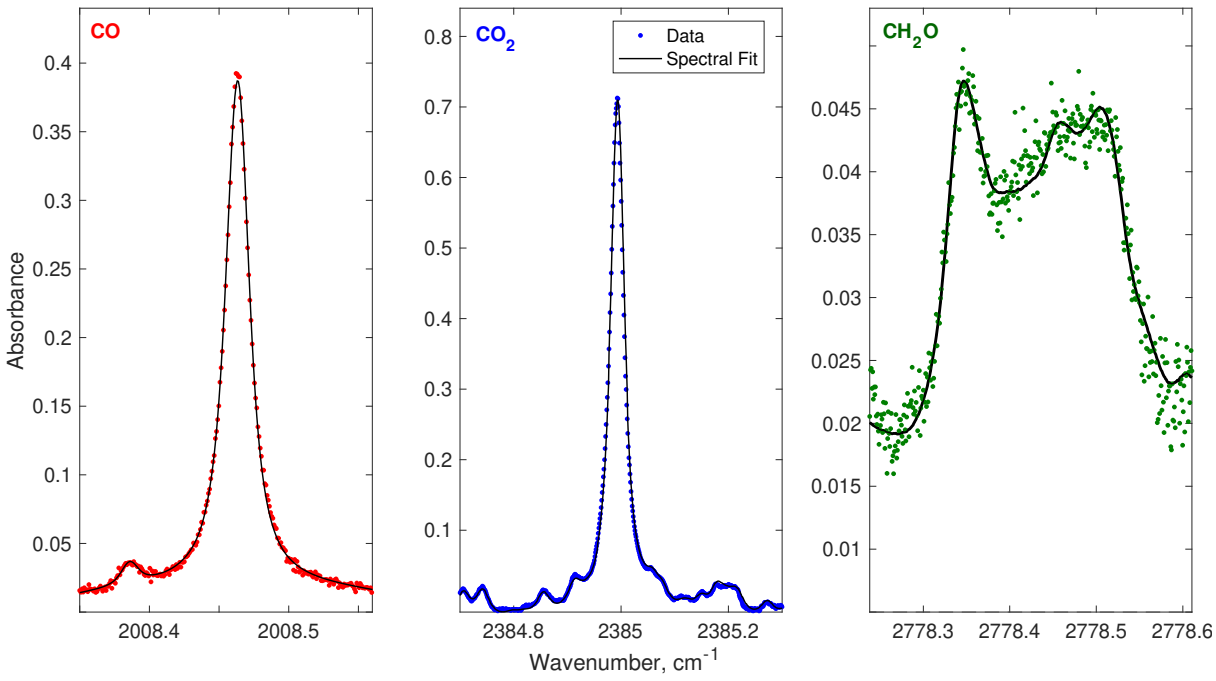

Figure D.1 Spectrally-resolved CO, CO_2, and CH_2O measurements during a representative MMA thermal decomposition experiment.

D.2 Comparison of modified and existing MMA models

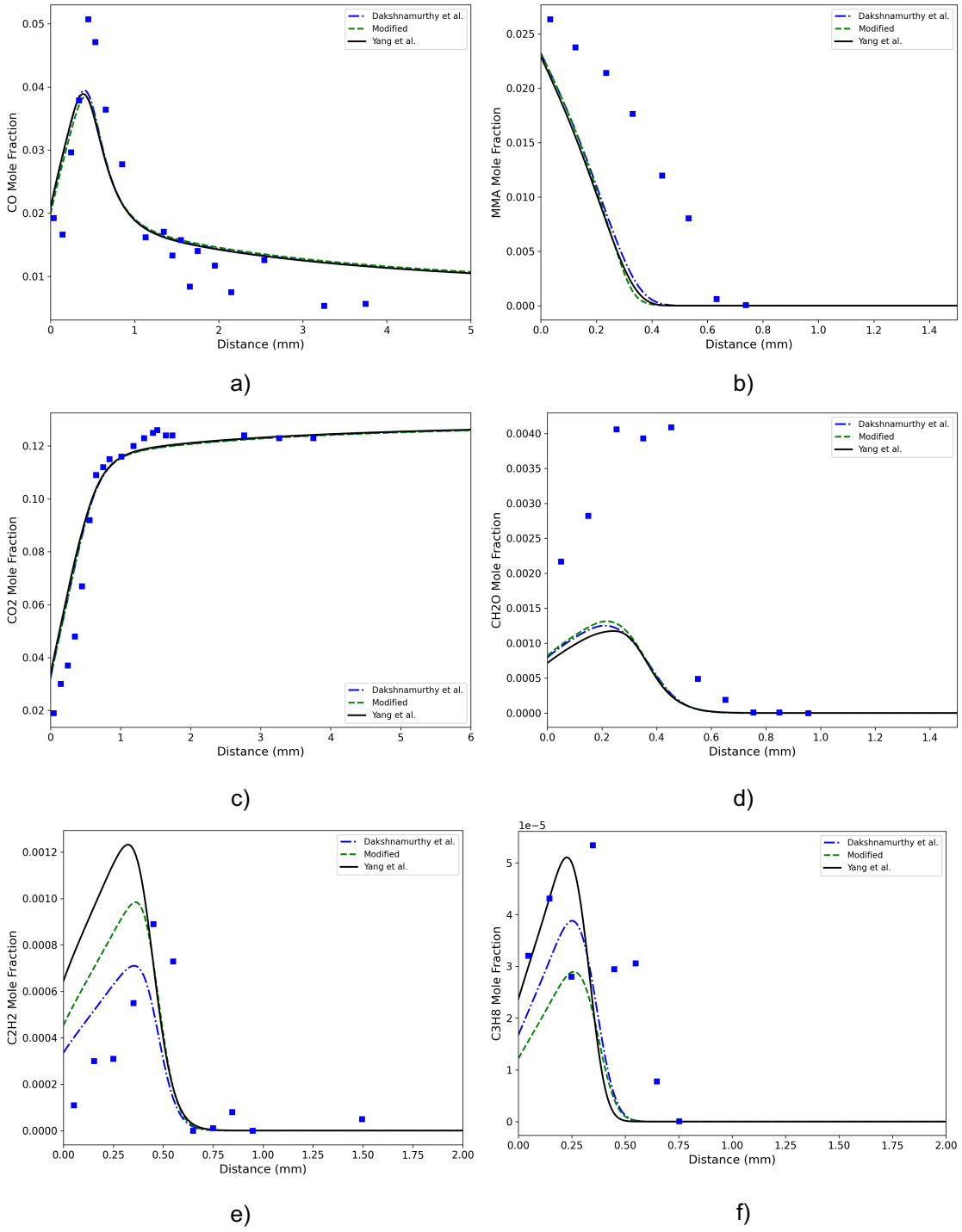

Figure D.2 Comparison of simulated species profiles in a pre-mixed laminar flame at atmospheric pressure for the existing and modified mechanisms. Symbols represent the experimental speciation data from [23].

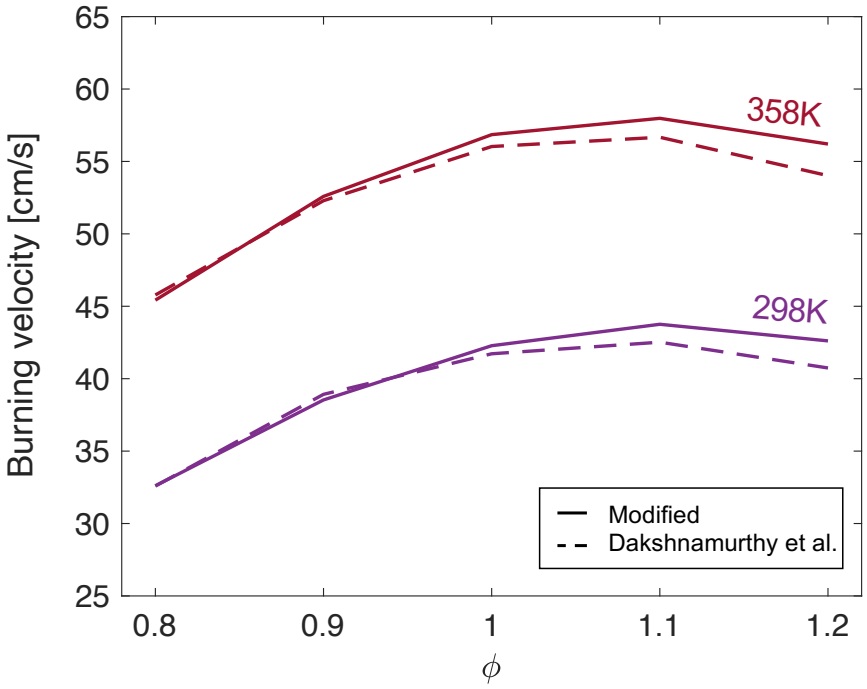

Figure D.3 Laminar flame speeds for MMA/Ar mixture at P = 1 atm. Simulations using existing mechanism and modified mechanism are shown as dashed and solid lines, respectively.

APPENDIX E

MMA Mechanism

This section includes the kinetic model for MMA combustion referenced in Chapter 6. The mechanism, assembled in the *'yaml'* format for intended use with Cantera, includes thermochemical properties and reactions from *Dakshnamurthy et al.* with the updated rate parameters from the optimization procedure discussed [11].

```
units: length: cm, quantity: mol, activation-energy: cal/mol

phases:
- name: gas
  thermo: ideal-gas
  elements: [N, Ar, He, H, O, C]
  species: [N2, AR, HE, H, O2, O, OH, H2, H2O, HO2, H2O2, CO, CO2, HCO,
    C, CH, TXCH2, CH3, CH2O, HCCO, C2H, CH2CO, C2H2, SXCH2, CH3OH, CH2OH,
    CH3O, CH4, CH3O2, C2H3, C2H4, C2H5, HCCOH, CH2CHO, CH3CHO, H2C2, C2H5O,
    NXC3H7, C2H6, C3H8, C3H6, C3H3, PXC3H4, AXC3H4, SXC3H5, NXC4H3, C2H3CHO,
    AXC3H5, C2O, C4H4, CH3OCO, C3H2, C3H2O, C4H2, IXC4H3, TXC3H5, C3H5O,
    C4H, C8H2, C6H2, C4H6, NXC4H5, IXC4H5, A1XC6H6, C4H7, C4H7O, PXC4H8,
    IXC3H7, HOCHO, C4H8X2, CH3CHCO, CH3COCH2, C2H4O2H, C2H3CHOCH2, C4H6O23,
    SXC3H5CHO, C2H3CHCHO, CH3CO, CH3COCH3, IXC3H5CO, CH3CHCHCHO, MP2D, MP2J,
    MP3J, MMETHMJ, MMETHVJ, MMETHAC, MMETHPJ]
  kinetics: gas
  reactions: all
  transport: mixture-averaged
  state:
    T: 300.0
```

```
    P: 1.01325e+05

species:
- name: N2
  composition: N: 2
  thermo:
    model: NASA7
    temperature-ranges: [300.0, 1000.0, 5000.0]
    data:
    - [3.298677, 1.40824e-03, -3.963222e-06, 5.641515e-09, -2.444855e-12,
      -1020.9, 3.950372]
    - [2.92664, 1.487977e-03, -5.684761e-07, 1.009704e-10, -6.753351e-15,
      -922.7977, 5.980528]
  transport:
    model: gas
    geometry: linear
    diameter: 3.621
    well-depth: 97.53
    polarizability: 1.76
    rotational-relaxation: 4.0
  note: '121286'
- name: AR
  composition: Ar: 1
  thermo:
    model: NASA7
    temperature-ranges: [300.0, 1000.0, 5000.0]
    data:
    - [2.5, 0.0, 0.0, 0.0, 0.0, -745.375, 4.366001]
    - [2.5, 0.0, 0.0, 0.0, 0.0, -745.375, 4.366001]
  transport:
    model: gas
    geometry: atom
    diameter: 3.33
```

```
    well-depth: 136.5
  note: '120186'
- name: HE
  composition: He: 1
  thermo:
    model: NASA7
    temperature-ranges: [300.0, 1000.0, 5000.0]
    data:
    - [2.5, 0.0, 0.0, 0.0, 0.0, -745.375, 0.9153488]
    - [2.5, 0.0, 0.0, 0.0, 0.0, -745.375, 0.9153489]
  transport:
    model: gas
    geometry: atom
    diameter: 2.576
    well-depth: 10.2
  note: '120186'
- name: H
  composition: H: 1
  thermo:
    model: NASA7
    temperature-ranges: [300.0, 1000.0, 5000.0]
    data:
    - [2.5, 0.0, 0.0, 0.0, 0.0, 2.547163e+04, -0.4601176]
    - [2.5, 0.0, 0.0, 0.0, 0.0, 2.547163e+04, -0.4601176]
  transport:
    model: gas
    geometry: atom
    diameter: 2.05
    well-depth: 145.0
  note: '120186'
- name: O2
  composition: O: 2
  thermo:
```

```
    model: NASA7
    temperature-ranges: [300.0, 1000.0, 5000.0]
    data:
    - [3.212936, 1.127486e-03, -5.75615e-07, 1.313877e-09, -8.768554e-13,
      -1005.249, 6.034738]
    - [3.697578, 6.135197e-04, -1.258842e-07, 1.775281e-11, -1.136435e-15,
      -1233.93, 3.189166]
  transport:
    model: gas
    geometry: linear
    diameter: 3.458
    well-depth: 107.4
    polarizability: 1.6
    rotational-relaxation: 3.8
  note: '121386'
- name: O
  composition: O: 1
  thermo:
    model: NASA7
    temperature-ranges: [300.0, 1000.0, 5000.0]
    data:
    - [2.946429, -1.638166e-03, 2.421032e-06, -1.602843e-09, 3.890696e-13,
      2.914764e+04, 2.963995]
    - [2.54206, -2.755062e-05, -3.102803e-09, 4.551067e-12, -4.368052e-16,
      2.92308e+04, 4.920308]
  transport:
    model: gas
    geometry: atom
    diameter: 2.75
    well-depth: 80.0
  note: '120186'
- name: OH
  composition: H: 1, O: 1
```

```
  thermo:
    model: NASA7
    temperature-ranges: [200.0, 1000.0, 6000.0]
    data:
    - [4.12530561, -3.22544939e-03, 6.52764691e-06, -5.79853643e-09, 2.06237379e-12,
      3346.30913, -0.69043296]
    - [2.86472886, 1.05650448e-03, -2.59082758e-07, 3.05218674e-11, -1.33195876e-15,
      3683.62875, 5.70164073]
  transport:
    model: gas
    geometry: linear
    diameter: 2.75
    well-depth: 80.0
  note: S9/01
- name: H2
  composition: H: 2
  thermo:
    model: NASA7
    temperature-ranges: [300.0, 1000.0, 5000.0]
    data:
    - [3.298124, 8.249442e-04, -8.143015e-07, -9.475434e-11, 4.134872e-13,
      -1012.521, -3.294094]
    - [2.991423, 7.000644e-04, -5.633829e-08, -9.231578e-12, 1.582752e-15,
      -835.034, -1.35511]
  transport:
    model: gas
    geometry: linear
    diameter: 2.92
    well-depth: 38.0
    polarizability: 0.79
    rotational-relaxation: 280.0
  note: '121286'
- name: H2O
```

```
  composition: H: 2, O: 1
  thermo:
    model: NASA7
    temperature-ranges: [300.0, 1000.0, 5000.0]
    data:
    - [3.386842, 3.474982e-03, -6.354696e-06, 6.968581e-09, -2.506588e-12,
      -3.020811e+04, 2.590233]
    - [2.672146, 3.056293e-03, -8.73026e-07, 1.200996e-10, -6.391618e-15,
      -2.989921e+04, 6.862817]
  transport:
    model: gas
    geometry: nonlinear
    diameter: 2.605
    well-depth: 572.4
    dipole: 1.844
    rotational-relaxation: 4.0
  note: '20387'
- name: HO2
  composition: H: 1, O: 2
  thermo:
    model: NASA7
    temperature-ranges: [200.0, 1000.0, 3500.0]
    data:
    - [4.30179801, -4.74912051e-03, 2.11582891e-05, -2.42763894e-08, 9.29225124e-12,
      294.80804, 3.71666245]
    - [4.0172109, 2.23982013e-03, -6.3365815e-07, 1.1424637e-10, -1.07908535e-14,
      111.856713, 3.78510215]
  transport:
    model: gas
    geometry: nonlinear
    diameter: 3.458
    well-depth: 107.4
    rotational-relaxation: 1.0
```

```
  note: L5/89
- name: H2O2
  composition: H: 2, O: 2
  thermo:
    model: NASA7
    temperature-ranges: [300.0, 1000.0, 5000.0]
    data:
    - [3.388754, 6.569226e-03, -1.485013e-07, -4.625806e-09, 2.471515e-12,
      -1.766315e+04, 6.785363]
    - [4.573167, 4.336136e-03, -1.474689e-06, 2.348904e-10, -1.431654e-14,
      -1.800696e+04, 0.501137]
  transport:
    model: gas
    geometry: nonlinear
    diameter: 3.458
    well-depth: 107.4
    rotational-relaxation: 3.8
  note: '120186'
- name: CO
  composition: C: 1, O: 1
  thermo:
    model: NASA7
    temperature-ranges: [300.0, 1000.0, 5000.0]
    data:
    - [3.262452, 1.511941e-03, -3.881755e-06, 5.581944e-09, -2.474951e-12,
      -1.431054e+04, 4.848897]
    - [3.025078, 1.442689e-03, -5.630828e-07, 1.018581e-10, -6.910952e-15,
      -1.426835e+04, 6.108218]
  transport:
    model: gas
    geometry: linear
    diameter: 3.65
    well-depth: 98.1
```

```
    polarizability: 1.95
    rotational-relaxation: 1.8
  note: '121286'
- name: CO2
  composition: C: 1, O: 2
  thermo:
    model: NASA7
    temperature-ranges: [300.0, 1000.0, 5000.0]
    data:
    - [2.275725, 9.922072e-03, -1.040911e-05, 6.866687e-09, -2.11728e-12,
      -4.837314e+04, 10.18849]
    - [4.453623, 3.140169e-03, -1.278411e-06, 2.393997e-10, -1.669033e-14,
      -4.896696e+04, -0.9553959]
  transport:
    model: gas
    geometry: linear
    diameter: 3.763
    well-depth: 244.0
    polarizability: 2.65
    rotational-relaxation: 2.1
  note: '121286'
- name: HCO
  composition: C: 1, H: 1, O: 1
  thermo:
    model: NASA7
    temperature-ranges: [200.0, 1000.0, 3500.0]
    data:
    - [4.22118584, -3.24392532e-03, 1.37799446e-05, -1.33144093e-08, 4.33768865e-12,
      3839.56496, 3.39437243]
    - [2.77217438, 4.95695526e-03, -2.48445613e-06, 5.89161778e-10, -5.33508711e-14,
      4011.91815, 9.79834492]
  transport:
    model: gas
```

```
    geometry: nonlinear
    diameter: 3.59
    well-depth: 498.0
  note: L12/89
- name: C
  composition: C: 1
  thermo:
    model: NASA7
    temperature-ranges: [200.0, 1000.0, 3500.0]
    data:
    - [2.55423955, -3.21537724e-04, 7.33792245e-07, -7.32234889e-10, 2.66521446e-13,
      8.54438832e+04, 4.53130848]
    - [2.49266888, 4.79889284e-05, -7.2433502e-08, 3.74291029e-11, -4.87277893e-15,
      8.54512953e+04, 4.80150373]
  transport:
    model: gas
    geometry: atom
    diameter: 3.298
    well-depth: 71.4
  note: L11/88
- name: CH
  composition: C: 1, H: 1
  thermo:
    model: NASA7
    temperature-ranges: [200.0, 1000.0, 3500.0]
    data:
    - [3.48981665, 3.23835541e-04, -1.68899065e-06, 3.16217327e-09, -1.40609067e-12,
      7.07972934e+04, 2.08401108]
    - [2.87846473, 9.70913681e-04, 1.44445655e-07, -1.30687849e-10, 1.76079383e-14,
      7.10124364e+04, 5.48497999]
  transport:
    model: gas
    geometry: linear
```

```
    diameter: 2.75
    well-depth: 80.0
  note: TPIS79
- name: TXCH2
  composition: C: 1, H: 2
  thermo:
    model: NASA7
    temperature-ranges: [300.0, 1000.0, 5000.0]
    data:
    - [3.76267867, 9.68872143e-04, 2.79489841e-06, -3.85091153e-09, 1.68741719e-12,
      4.60040401e+04, 1.56253185]
    - [2.87410113, 3.65639292e-03, -1.40894597e-06, 2.60179549e-10, -1.87727567e-14,
      4.6263604e+04, 6.17119324]
  transport:
    model: gas
    geometry: linear
    diameter: 3.8
    well-depth: 144.0
  note: '000000'
- name: CH3
  composition: C: 1, H: 3
  thermo:
    model: NASA7
    temperature-ranges: [200.0, 1000.0, 6000.0]
    data:
    - [3.6571797, 2.1265979e-03, 5.4583883e-06, -6.6181003e-09, 2.4657074e-12,
      1.6422716e+04, 1.6735354]
    - [2.9781206, 5.797852e-03, -1.97558e-06, 3.072979e-10, -1.7917416e-14,
      1.6509513e+04, 4.7224799]
  transport:
    model: gas
    geometry: linear
    diameter: 3.8
```

```
    well-depth: 144.0
  note: METHYLIU0702
- name: CH2O
  composition: C: 1, H: 2, O: 1
  thermo:
    model: NASA7
    temperature-ranges: [200.0, 1000.0, 3500.0]
    data:
    - [4.79372315, -9.90833369e-03, 3.73220008e-05, -3.79285261e-08, 1.31772652e-11,
      -1.43089567e+04, 0.6028129]
    - [1.76069008, 9.20000082e-03, -4.42258813e-06, 1.00641212e-09, -8.8385564e-14,
      -1.39958323e+04, 13.656323]
  transport:
    model: gas
    geometry: nonlinear
    diameter: 3.59
    well-depth: 498.0
    rotational-relaxation: 2.0
  note: L8/88
- name: HCCO
  composition: C: 2, H: 1, O: 1
  thermo:
    model: NASA7
    temperature-ranges: [300.0, 1000.0, 4000.0]
    data:
    - [2.2517214, 0.017655021, -2.3729101e-05, 1.7275759e-08, -5.0664811e-12,
      2.0059449e+04, 12.490417]
    - [5.6282058, 4.0853401e-03, -1.5934547e-06, 2.8626052e-10, -1.9407832e-14,
      1.9327215e+04, -3.9302595]
  transport:
    model: gas
    geometry: nonlinear
    diameter: 2.5
```

```
    well-depth: 150.0
    rotational-relaxation: 1.0
  note: SRIC91
- name: C2H
  composition: C: 2, H: 1
  thermo:
    model: NASA7
    temperature-ranges: [200.0, 1000.0, 3500.0]
    data:
    - [2.88965733, 0.0134099611, -2.84769501e-05, 2.94791045e-08, -1.09331511e-11,
      6.68393932e+04, 6.22296438]
    - [3.16780652, 4.75221902e-03, -1.83787077e-06, 3.04190252e-10, -1.7723277e-14,
      6.7121065e+04, 6.63589475]
  transport:
    model: gas
    geometry: linear
    diameter: 4.1
    well-depth: 209.0
    rotational-relaxation: 2.5
  note: L1/91
- name: CH2CO
  composition: C: 2, H: 2, O: 1
  thermo:
    model: NASA7
    temperature-ranges: [200.0, 1000.0, 3500.0]
    data:
    - [2.1358363, 0.0181188721, -1.73947474e-05, 9.34397568e-09, -2.01457615e-12,
      -7042.91804, 12.215648]
    - [4.51129732, 9.00359745e-03, -4.16939635e-06, 9.23345882e-10, -7.94838201e-14,
      -7551.05311, 0.632247205]
  transport:
    model: gas
    geometry: nonlinear
```

```
    diameter: 3.97
    well-depth: 436.0
    rotational-relaxation: 2.0
  note: L5/90
- name: C2H2
  composition: C: 2, H: 2
  thermo:
    model: NASA7
    temperature-ranges: [200.0, 1000.0, 3500.0]
    data:
    - [0.808681094, 0.0233615629, -3.55171815e-05, 2.80152437e-08, -8.50072974e-12,
      2.64289807e+04, 13.9397051]
    - [4.14756964, 5.96166664e-03, -2.37294852e-06, 4.67412171e-10, -3.61235213e-14,
      2.59359992e+04, -1.23028121]
  transport:
    model: gas
    geometry: linear
    diameter: 4.1
    well-depth: 209.0
    rotational-relaxation: 2.5
  note: L1/91
- name: SXCH2
  composition: C: 1, H: 2
  thermo:
    model: NASA7
    temperature-ranges: [300.0, 1000.0, 5000.0]
    data:
    - [4.19860411, -2.36661419e-03, 8.2329622e-06, -6.68815981e-09, 1.94314737e-12,
      5.04968163e+04, -0.769118967]
    - [2.29203842, 4.65588637e-03, -2.01191947e-06, 4.17906e-10, -3.39716365e-14,
      5.09259997e+04, 8.62650169]
  transport:
    model: gas
```

```
    geometry: linear
    diameter: 3.8
    well-depth: 144.0
  note: '000000'
- name: CH3OH
  composition: C: 1, H: 4, O: 1
  thermo:
    model: NASA7
    temperature-ranges: [200.0, 1000.0, 3500.0]
    data:
    - [5.71539582, -0.0152309129, 6.52441155e-05, -7.10806889e-08, 2.61352698e-11,
      -2.56427656e+04, -1.50409823]
    - [1.78970791, 0.0140938292, -6.36500835e-06, 1.38171085e-09, -1.1706022e-13,
      -2.53748747e+04, 14.5023623]
  transport:
    model: gas
    geometry: nonlinear
    diameter: 3.626
    well-depth: 481.8
    rotational-relaxation: 1.0
  note: L8/88
- name: CH2OH
  composition: C: 1, H: 3, O: 1
  thermo:
    model: NASA7
    temperature-ranges: [200.0, 1000.0, 3500.0]
    data:
    - [3.86388918, 5.59672304e-03, 5.93271791e-06, -1.04532012e-08, 4.36967278e-12,
      -3193.91367, 5.47302243]
    - [3.69266569, 8.64576797e-03, -3.7510112e-06, 7.87234636e-10, -6.48554201e-14,
      -3242.50627, 5.81043215]
  transport:
    model: gas
```

```
    geometry: nonlinear
    diameter: 3.69
    well-depth: 417.0
    dipole: 1.7
    rotational-relaxation: 2.0
  note: GUNL93
- name: CH3O
  composition: C: 1, H: 3, O: 1
  thermo:
    model: NASA7
    temperature-ranges: [300.0, 1000.0, 3000.0]
    data:
    - [2.106204, 7.216595e-03, 5.338472e-06, -7.377636e-09, 2.07561e-12,
      978.6011, 13.152177]
    - [3.770799, 7.871497e-03, -2.656384e-06, 3.944431e-10, -2.112616e-14,
      127.83252, 2.929575]
  transport:
    model: gas
    geometry: nonlinear
    diameter: 3.69
    well-depth: 417.0
    dipole: 1.7
    rotational-relaxation: 2.0
  note: '121686'
- name: CH4
  composition: C: 1, H: 4
  thermo:
    model: NASA7
    temperature-ranges: [200.0, 1000.0, 6000.0]
    data:
    - [5.14911468, -0.0136622009, 4.91453921e-05, -4.84246767e-08, 1.66603441e-11,
      -1.02465983e+04, -4.63848842]
    - [1.65326226, 0.0100263099, -3.31661238e-06, 5.36483138e-10, -3.14696758e-14,
```

```
      -1.00095936e+04, 9.90506283]
  transport:
    model: gas
    geometry: nonlinear
    diameter: 3.746
    well-depth: 141.4
    polarizability: 2.6
    rotational-relaxation: 13.0
  note: g8/99
- name: CH3O2
  composition: C: 1, H: 3, O: 2
  thermo:
    model: NASA7
    temperature-ranges: [200.0, 1000.0, 6000.0]
    data:
    - [4.76597792, -3.51077148e-03, 4.54394152e-05, -5.66763729e-08, 2.21591482e-11,
      -482.401289, 4.76095141]
    - [5.92505819, 9.00194542e-03, -3.24254309e-06, 5.24362718e-10, -3.14263003e-14,
      -1532.58958, -4.93669747]
  transport:
    model: gas
    geometry: nonlinear
    diameter: 3.626
    well-depth: 481.8
    rotational-relaxation: 1.0
  note: PEROXYMETHT04/02
- name: C2H3
  composition: C: 2, H: 3
  thermo:
    model: NASA7
    temperature-ranges: [200.0, 1000.0, 3500.0]
    data:
    - [3.21246645, 1.51479162e-03, 2.59209412e-05, -3.57657847e-08, 1.47150873e-11,
```

```
      3.48598468e+04, 8.51054025]
    - [3.016724, 0.0103302292, -4.68082349e-06, 1.01763288e-09, -8.62607041e-14,
      3.46128739e+04, 7.78732378]
  transport:
    model: gas
    geometry: nonlinear
    diameter: 4.1
    well-depth: 209.0
    rotational-relaxation: 1.0
  note: L2/92
- name: C2H4
  composition: C: 2, H: 4
  thermo:
    model: NASA7
    temperature-ranges: [200.0, 1000.0, 3500.0]
    data:
    - [3.95920148, -7.57052247e-03, 5.70990292e-05, -6.91588753e-08, 2.69884373e-11,
      5089.77593, 4.09733096]
    - [2.03611116, 0.0146454151, -6.71077915e-06, 1.47222923e-09, -1.25706061e-13,
      4939.88614, 10.3053693]
  transport:
    model: gas
    geometry: nonlinear
    diameter: 3.971
    well-depth: 280.8
    rotational-relaxation: 1.5
  note: L1/91
- name: C2H5
  composition: C: 2, H: 5
  thermo:
    model: NASA7
    temperature-ranges: [200.0, 1000.0, 3500.0]
    data:
```

```
    - [4.30646568, -4.18658892e-03, 4.97142807e-05, -5.99126606e-08, 2.30509004e-11,
      1.28416265e+04, 4.70720924]
    - [1.95465642, 0.0173972722, -7.98206668e-06, 1.75217689e-09, -1.49641576e-13,
      1.285752e+04, 13.4624343]
  transport:
    model: gas
    geometry: nonlinear
    diameter: 4.302
    well-depth: 252.3
    rotational-relaxation: 1.5
  note: L12/92
- name: HCCOH
  composition: C: 2, H: 2, O: 1
  thermo:
    model: NASA7
    temperature-ranges: [300.0, 1000.0, 5000.0]
    data:
    - [1.2423733, 0.031072201, -5.0866864e-05, 4.3137131e-08, -1.4014594e-11,
      8031.6143, 13.874319]
    - [5.9238291, 6.79236e-03, -2.5658564e-06, 4.4987841e-10, -2.9940101e-14,
      7264.626, -7.6017742]
  transport:
    model: gas
    geometry: nonlinear
    diameter: 3.97
    well-depth: 436.0
    rotational-relaxation: 2.0
  note: SRI91
- name: CH2CHO
  composition: C: 2, H: 3, O: 1
  thermo:
    model: NASA7
    temperature-ranges: [300.0, 1000.0, 3000.0]
```

```
    data:
    - [1.09685733, 0.0220228796, -1.44583444e-05, 3.00779578e-09, 6.08992877e-13,
      1069.43322, 19.0094813]
    - [2.42606357, 0.0172400021, -9.77132119e-06, 2.66555672e-09, -2.82120078e-13,
      833.10699, 12.6038737]
  transport:
    model: gas
    geometry: nonlinear
    diameter: 3.97
    well-depth: 436.0
    rotational-relaxation: 2.0
  note: G3B3
- name: CH3CHO
  composition: C: 2, H: 4, O: 1
  thermo:
    model: NASA7
    temperature-ranges: [300.0, 1000.0, 3000.0]
    data:
    - [1.40653856, 0.0216984438, -1.47573265e-05, 7.30435478e-09, -2.09119467e-12,
      -2.17973223e+04, 17.7513265]
    - [2.68543112, 0.0176802373, -8.65402739e-06, 2.03680589e-09, -1.87630935e-13,
      -2.21653701e+04, 11.1635653]
  transport:
    model: gas
    geometry: nonlinear
    diameter: 3.97
    well-depth: 436.0
    rotational-relaxation: 2.0
  note: G3B3
- name: H2C2
  composition: C: 2, H: 2
  thermo:
    model: NASA7
```

```
    temperature-ranges: [200.0, 1000.0, 6000.0]
    data:
    - [3.2815483, 6.9764791e-03, -2.3855244e-06, -1.2104432e-09, 9.8189545e-13,
      4.8621794e+04, 5.920391]
    - [4.278034, 4.7562804e-03, -1.6301009e-06, 2.5462806e-10, -1.4886379e-14,
      4.8316688e+04, 0.64023701]
  transport:
    model: gas
    geometry: nonlinear
    diameter: 4.1
    well-depth: 209.0
    rotational-relaxation: 2.5
  note: L12/89
- name: C2H5O
  composition: C: 2, H: 5, O: 1
  thermo:
    model: NASA7
    temperature-ranges: [300.0, 1000.0, 5000.0]
    data:
    - [0.494420708, 0.0271774434, -1.6590901e-05, 5.152042e-09, -6.48496915e-13,
      -3352.52925, 22.8079378]
    - [2.46262349, 0.0209503959, -9.3929175e-06, 1.56440627e-09, 0.0, -3839.32658,
      12.8738847]
  transport:
    model: gas
    geometry: nonlinear
    diameter: 4.41
    well-depth: 470.6
    rotational-relaxation: 1.5
- name: NXC3H7
  composition: C: 3, H: 7
  thermo:
    model: NASA7
```

```
    temperature-ranges: [300.0, 1000.0, 5000.0]
    data:
    - [1.0475473, 0.026007794, 2.3562252e-06, -1.9592317e-08, 9.3680116e-12,
      1.0632637e+04, 21.141876]
    - [7.7040405, 0.01604154, -5.2815967e-06, 7.6254403e-10, -3.9353462e-14,
      8297.9531, -15.487514]
  transport:
    model: gas
    geometry: nonlinear
    diameter: 4.982
    well-depth: 266.8
    rotational-relaxation: 1.0
  note: '000000'
- name: C2H6
  composition: C: 2, H: 6
  thermo:
    model: NASA7
    temperature-ranges: [200.0, 1000.0, 3500.0]
    data:
    - [4.29142492, -5.5015427e-03, 5.99438288e-05, -7.08466285e-08, 2.68685771e-11,
      -1.15222055e+04, 2.66682316]
    - [1.0718815, 0.0216852677, -1.00256067e-05, 2.21412001e-09, -1.9000289e-13,
      -1.14263932e+04, 15.1156107]
  transport:
    model: gas
    geometry: nonlinear
    diameter: 4.302
    well-depth: 252.3
    rotational-relaxation: 1.5
  note: L8/88
- name: C3H8
  composition: C: 3, H: 8
  thermo:
```

```
    model: NASA7
    temperature-ranges: [300.0, 1000.0, 5000.0]
    data:
    - [0.93355381, 0.026424579, 6.1059727e-06, -2.1977499e-08, 9.5149253e-12,
      -1.395852e+04, 19.201691]
    - [7.5341368, 0.018872239, -6.2718491e-06, 9.1475649e-10, -4.7838069e-14,
      -1.6467516e+04, -17.892349]
  transport:
    model: gas
    geometry: nonlinear
    diameter: 4.982
    well-depth: 266.8
    rotational-relaxation: 1.0
  note: L4/85
- name: C3H6
  composition: C: 3, H: 6
  thermo:
    model: NASA7
    temperature-ranges: [300.0, 1000.0, 3000.0]
    data:
    - [-2.2926167e-03, 0.0310261065, -1.67151548e-05, 1.8959417e-09, 1.24957915e-12,
      1134.37406, 23.5719601]
    - [0.471697982, 0.028951307, -1.56601819e-05, 4.11443199e-09, -4.23075141e-13,
      1126.03387, 21.5237289]
  transport:
    model: gas
    geometry: nonlinear
    diameter: 4.982
    well-depth: 266.8
    rotational-relaxation: 1.0
  note: G3B3
- name: C3H3
  composition: C: 3, H: 3
```

```
  thermo:
    model: NASA7
    temperature-ranges: [300.0, 1000.0, 3000.0]
    data:
    - [1.40299238, 0.0301773327, -3.98449373e-05, 2.93534629e-08, -8.70554579e-12,
      3.9310822e+04, 15.1527845]
    - [6.14915291, 9.34063166e-03, -3.75055354e-06, 6.90156316e-10, -4.60824994e-14,
      3.83854848e+04, -7.45345215]
  transport:
    model: gas
    geometry: nonlinear
    diameter: 4.76
    well-depth: 252.0
    rotational-relaxation: 1.0
  note: G3B3
- name: PXC3H4
  composition: C: 3, H: 4
  thermo:
    model: NASA7
    temperature-ranges: [300.0, 1000.0, 5000.0]
    data:
    - [1.46175323, 0.0246026602, -1.90219395e-05, 8.60363422e-09, -1.6672924e-12,
      2.09209793e+04, 14.9262585]
    - [2.81460543, 0.0185524496, -9.55026768e-06, 2.3995137e-09, -2.37485257e-13,
      2.07010771e+04, 8.60604972]
  transport:
    model: gas
    geometry: nonlinear
    diameter: 4.76
    well-depth: 252.0
    rotational-relaxation: 1.0
  note: '000000'
- name: AXC3H4
```

```
  composition: C: 3, H: 4
  thermo:
    model: NASA7
    temperature-ranges: [300.0, 1000.0, 5000.0]
    data:
    - [0.368928265, 0.0289351397, -2.44386408e-05, 1.12547166e-08, -2.03040262e-12,
      2.17585256e+04, 19.5267211]
    - [2.56128757, 0.0195080128, -1.04061366e-05, 2.70165173e-09, -2.75074329e-13,
      2.13894289e+04, 9.20550397]
  transport:
    model: gas
    geometry: nonlinear
    diameter: 4.76
    well-depth: 252.0
    rotational-relaxation: 1.0
  note: '000000'
- name: SXC3H5
  composition: C: 3, H: 5
  thermo:
    model: NASA7
    temperature-ranges: [300.0, 1000.0, 5000.0]
    data:
    - [0.313106581, 0.0318769663, -2.53420013e-05, 1.02999073e-08, -1.35301854e-12,
      3.13767683e+04, 22.3728832]
    - [2.0250936, 0.0235513249, -1.28254556e-05, 3.39579222e-09, -3.51794724e-13,
      3.11812042e+04, 14.6653302]
  transport:
    model: gas
    geometry: nonlinear
    diameter: 4.982
    well-depth: 266.8
    rotational-relaxation: 1.0
  note: '000000'
```

```
- name: NXC4H3
  composition: C: 4, H: 3
  thermo:
    model: NASA7
    temperature-ranges: [300.0, 1000.0, 5000.0]
    data:
    - [-0.0355175031, 0.0430508503, -5.75729147e-05, 4.15883142e-08, -1.20750857e-11,
      6.43506593e+04, 24.3816855]
    - [7.25330164, 0.0119580846, -5.26715675e-06, 1.09981875e-09, -8.84016751e-14,
      6.28977574e+04, -10.5283126]
  transport:
    model: gas
    geometry: nonlinear
    diameter: 5.18
    well-depth: 357.0
    rotational-relaxation: 1.0
  note: '000000'
- name: C2H3CHO
  composition: C: 3, H: 4, O: 1
  thermo:
    model: NASA7
    temperature-ranges: [300.0, 1000.0, 5000.0]
    data:
    - [0.292355162, 0.0354321417, -2.94936324e-05, 1.28100124e-08, -2.26144108e-12,
      -1.16521584e+04, 22.887828]
    - [5.56154592, 0.0179295837, -8.03464758e-06, 1.32295375e-09, 0.0, -1.29035886e+04,
      -3.47372739]
  transport:
    model: gas
    geometry: nonlinear
    diameter: 4.958
    well-depth: 428.8
    dipole: 2.9
```

```
    rotational-relaxation: 1.0
- name: AXC3H5
  composition: C: 3, H: 5
  thermo:
    model: NASA7
    temperature-ranges: [300.0, 1000.0, 5000.0]
    data:
    - [-1.03516444, 0.0375043366, -3.26381242e-05, 1.47662613e-08, -2.43741154e-12,
      1.88792254e+04, 27.1451071]
    - [2.28794927, 0.0236401575, -1.2789145e-05, 3.3683854e-09, -3.47449449e-13,
      1.83033514e+04, 11.4063418]
  transport:
    model: gas
    geometry: nonlinear
    diameter: 4.982
    well-depth: 266.8
    rotational-relaxation: 1.0
  note: '000000'
- name: C2O
  composition: C: 2, O: 1
  thermo:
    model: NASA7
    temperature-ranges: [200.0, 1000.0, 6000.0]
    data:
    - [2.86278214, 0.0119701204, -1.80851222e-05, 1.5277773e-08, -5.20063163e-12,
      3.37501779e+04, 8.89759099]
    - [5.42468378, 1.85393945e-03, -5.17932956e-07, 6.7764623e-11, -3.53315237e-15,
      3.31537194e+04, -3.69608405]
  transport:
    model: gas
    geometry: linear
    diameter: 3.828
    well-depth: 232.4
```

```
    rotational-relaxation: 1.0
  note: g8/00
- name: C4H4
  composition: C: 4, H: 4
  thermo:
    model: NASA7
    temperature-ranges: [300.0, 1000.0, 3000.0]
    data:
    - [-0.231343354, 0.0411814497, -4.47624056e-05, 2.75434157e-08, -7.06376813e-12,
      3.40632704e+04, 24.2662442]
    - [4.9723721, 0.0193139904, -9.81196508e-06, 2.43005054e-09, -2.37099738e-13,
      3.30561454e+04, -0.623055157]
  transport:
    model: gas
    geometry: nonlinear
    diameter: 5.18
    well-depth: 357.0
    rotational-relaxation: 1.0
  note: G3B3
- name: CH3OCO
  composition: C: 2, H: 3, O: 2
  thermo:
    model: NASA7
    temperature-ranges: [300.0, 1000.0, 5000.0]
    data:
    - [2.83313145, 0.0153447505, 1.89583962e-06, -7.70200413e-09, 2.4156441e-12,
      -2.13431832e+04, 13.9524183]
    - [0.0896049645, 0.0264901996, -1.45801232e-05, 2.78768018e-09, 0.0,
      -2.08196859e+04, 27.1039098]
  transport:
    model: gas
    geometry: nonlinear
    diameter: 4.037
```

```
    well-depth: 395.0
    dipole: 1.3
    rotational-relaxation: 1.0
- name: C3H2
  composition: C: 3, H: 2
  thermo:
    model: NASA7
    temperature-ranges: [300.0, 1000.0, 3000.0]
    data:
    - [4.52861333, 0.0177565501, -2.54882946e-05, 2.01674629e-08, -6.28544707e-12,
      6.35410087e+04, 0.809423748]
    - [7.67920588, 3.85560826e-03, -8.23429967e-07, -6.18108592e-11, 2.93114202e-14,
      6.29136323e+04, -14.2211873]
  transport:
    model: gas
    geometry: nonlinear
    diameter: 4.1
    well-depth: 209.0
    rotational-relaxation: 1.0
  note: G3B3
- name: C3H2O
  composition: C: 3, H: 2, O: 1
  thermo:
    model: NASA7
    temperature-ranges: [300.0, 1000.0, 3000.0]
    data:
    - [1.89401982, 0.0266301486, -2.97185216e-05, 1.94290386e-08, -5.43402767e-12,
      1.37271761e+04, 15.5182339]
    - [5.5155171, 0.0120296564, -6.09058988e-06, 1.48866261e-09, -1.42588474e-13,
      1.29567538e+04, -2.05439127]
  transport:
    model: gas
    geometry: nonlinear
```

```
    diameter: 4.76
    well-depth: 252.0
    rotational-relaxation: 1.0
  note: G3B3
- name: C4H2
  composition: C: 4, H: 2
  thermo:
    model: NASA7
    temperature-ranges: [300.0, 1000.0, 3000.0]
    data:
    - [0.173325212, 0.045394903, -7.3012383e-05, 5.95251736e-08, -1.87484716e-11,
      5.42239385e+04, 18.0184355]
    - [9.75839793, 3.78873223e-03, 3.06142015e-07, -6.33655024e-10, 1.12930032e-13,
      5.22698696e+04, -27.9084005]
  transport:
    model: gas
    geometry: linear
    diameter: 5.18
    well-depth: 357.0
    rotational-relaxation: 1.0
  note: G3B3
- name: IXC4H3
  composition: C: 4, H: 3
  thermo:
    model: NASA7
    temperature-ranges: [300.0, 1000.0, 5000.0]
    data:
    - [3.02566263, 0.0304693624, -3.68345185e-05, 2.60035352e-08, -7.62154351e-12,
      5.80551505e+04, 9.87268458]
    - [7.29283596, 0.0121664949, -5.50925306e-06, 1.1929135e-09, -1.00493092e-13,
      5.71961011e+04, -10.5737251]
  transport:
    model: gas
```

```
    geometry: nonlinear
    diameter: 5.18
    well-depth: 357.0
    rotational-relaxation: 1.0
  note: '000000'
- name: TXC3H5
  composition: C: 3, H: 5
  thermo:
    model: NASA7
    temperature-ranges: [300.0, 1000.0, 5000.0]
    data:
    - [0.880980628, 0.0296361924, -2.52725602e-05, 1.43651816e-08, -3.89566621e-12,
      2.92321259e+04, 20.0163594]
    - [3.15893724, 0.0204649335, -1.00947812e-05, 2.41157382e-09, -2.26535162e-13,
      2.87351148e+04, 8.93041515]
  transport:
    model: gas
    geometry: nonlinear
    diameter: 4.982
    well-depth: 266.8
    rotational-relaxation: 1.0
  note: '000000'
- name: C3H5O
  composition: C: 3, H: 5, O: 1
  thermo:
    model: NASA7
    temperature-ranges: [300.0, 1000.0, 5000.0]
    data:
    - [1.19822582, 0.0305579837, -1.80630276e-05, 4.86150033e-09, -4.19854562e-13,
      9582.17784, 21.5566221]
    - [3.39074577, 0.024130162, -1.13650894e-05, 1.97900938e-09, 0.0, 9007.57452,
      10.3459501]
  transport:
```

```
    model: gas
    geometry: nonlinear
    diameter: 4.82
    well-depth: 411.0
    rotational-relaxation: 1.0
- name: C4H
  composition: C: 4, H: 1
  thermo:
    model: NASA7
    temperature-ranges: [300.0, 1000.0, 3000.0]
    data:
    - [3.23559253, 0.0227091533, -3.18443291e-05, 2.44864804e-08, -7.5798644e-12,
      9.3908096e+04, 7.90671244]
    - [7.44964925, 5.23173174e-03, -1.96340383e-06, 3.00667811e-10, -1.16121546e-14,
      9.30052443e+04, -12.4961267]
  transport:
    model: gas
    geometry: nonlinear
    diameter: 5.18
    well-depth: 357.0
    rotational-relaxation: 1.0
  note: G3B3
- name: C8H2
  composition: C: 8, H: 2
  thermo:
    model: NASA7
    temperature-ranges: [200.0, 1000.0, 6000.0]
    data:
    - [-0.326701608, 0.0943328676, -1.72876384e-04, 1.56816538e-07, -5.40488426e-11,
      1.05392079e+05, 22.032212]
    - [16.3586996, 0.0108592595, -3.91654796e-06, 6.34107033e-10, -3.80413156e-14,
      1.02366984e+05, -55.6746562]
  transport:
```

```
    model: gas
    geometry: linear
    diameter: 5.68
    well-depth: 495.3
    dipole: 0.43
    polarizability: 12.3
    rotational-relaxation: 1.0
  note: T11/07
- name: C6H2
  composition: C: 6, H: 2
  thermo:
    model: NASA7
    temperature-ranges: [200.0, 1000.0, 6000.0]
    data:
    - [-0.54109216, 0.074532628, -1.3578252e-04, 1.222663e-07, -4.1825207e-11,
      8.2115132e+04, 21.88271]
    - [12.532801, 8.7766321e-03, -3.1329616e-06, 5.037182e-10, -3.0071921e-14,
      7.9784338e+04, -38.85858]
  transport:
    model: gas
    geometry: linear
    diameter: 5.18
    well-depth: 357.0
    rotational-relaxation: 1.0
  note: T3/92
- name: C4H6
  composition: C: 4, H: 6
  thermo:
    model: NASA7
    temperature-ranges: [300.0, 1000.0, 3000.0]
    data:
    - [4.01336263, 4.4462685e-03, 7.80683019e-05, -1.11674129e-07, 4.60753846e-11,
      1.14807231e+04, 6.77079654]
```

```
    - [-8.99531092, 0.0601715069, -4.20057758e-05, 1.33330056e-08, -1.5742369e-12,
      1.49296107e+04, 71.1866909]
  transport:
    model: gas
    geometry: nonlinear
    diameter: 5.18
    well-depth: 357.0
    rotational-relaxation: 1.0
  note: G3B3
- name: NXC4H5
  composition: C: 4, H: 5
  thermo:
    model: NASA7
    temperature-ranges: [300.0, 1000.0, 5000.0]
    data:
    - [4.87674639, 0.0227534299, -1.17714698e-05, 2.95251455e-09, -2.91456566e-13,
      4.11081097e+04, 2.21507772]
    - [4.87674639, 0.0227534299, -1.17714698e-05, 2.95251455e-09, -2.91456566e-13,
      4.11081097e+04, 2.21507772]
  transport:
    model: gas
    geometry: nonlinear
    diameter: 5.18
    well-depth: 357.0
    rotational-relaxation: 1.0
  note: '000000'
- name: IXC4H5
  composition: C: 4, H: 5
  thermo:
    model: NASA7
    temperature-ranges: [300.0, 1000.0, 5000.0]
    data:
    - [-0.331905498, 0.0440163876, -4.27690246e-05, 2.31284316e-08, -5.17171519e-12,
```

```
      3.67510686e+04, 25.6362838]
    - [4.34643669, 0.024576144, -1.30953685e-05, 3.38848125e-09, -3.43519633e-13,
      3.5870978e+04, 3.29579091]
  transport:
    model: gas
    geometry: nonlinear
    diameter: 5.18
    well-depth: 357.0
    rotational-relaxation: 1.0
  note: '000000'
- name: A1XC6H6
  composition: C: 6, H: 6
  thermo:
    model: NASA7
    temperature-ranges: [300.0, 1000.0, 5000.0]
    data:
    - [-5.51558393, 0.0645453225, -4.41402928e-05, 7.47712161e-09, 3.10282254e-12,
      9110.31457, 46.5332293]
    - [-0.206240612, 0.046412244, -2.77653536e-05, 7.88910537e-09, -8.60365259e-13,
      8098.83905, 20.6566629]
  transport:
    model: gas
    geometry: nonlinear
    diameter: 5.29
    well-depth: 464.8
    polarizability: 10.32
    rotational-relaxation: 1.0
  note: '000000'
- name: C4H7
  composition: C: 4, H: 7
  thermo:
    model: NASA7
    temperature-ranges: [200.0, 1000.0, 6000.0]
```

```
    data:
    - [5.07355313, 5.27619329e-03, 6.23441322e-05, -8.54203458e-08, 3.45890031e-11,
      2.24615054e+04, 5.60318035]
    - [8.49073768, 0.0191056974, -6.74370664e-06, 1.07343267e-09, -6.36251837e-14,
      2.04659294e+04, -17.4555814]
  transport:
    model: gas
    geometry: nonlinear
    diameter: 4.65
    well-depth: 355.0
    rotational-relaxation: 1.0
  note: 3butene-1ylT05/04
- name: C4H7O
  composition: C: 4, H: 7, O: 1
  thermo:
    model: NASA7
    temperature-ranges: [300.0, 1000.0, 5000.0]
    data:
    - [-1.60619192, 0.0558562682, -4.35595767e-05, 1.70589279e-08, -2.6563518e-12,
      4850.90326, 34.7112559]
    - [6.21920403, 0.031037311, -1.47414983e-05, 2.57805897e-09, 0.0, 2917.90666,
      -4.77187791]
  transport:
    model: gas
    geometry: nonlinear
    diameter: 5.2
    well-depth: 496.0
    rotational-relaxation: 1.0
- name: PXC4H8
  composition: C: 4, H: 8
  thermo:
    model: NASA7
    temperature-ranges: [200.0, 1000.0, 6000.0]
```

```
    data:
    - [3.14396651, -5.04251513e-03, 1.20644999e-04, -1.5841e-07, 6.38394284e-11,
      1919.48331, 10.6617564]
    - [8.06072102, 0.023210476, -8.36819112e-06, 1.35405859e-09, -8.11852286e-14,
      -1276.26185, -24.3229092]
  transport:
    model: gas
    geometry: nonlinear
    diameter: 6.0
    well-depth: 546.2
    dipole: 0.13
    polarizability: 15.0
    rotational-relaxation: 1.0
  note: '000000'
- name: IXC3H7
  composition: C: 3, H: 7
  thermo:
    model: NASA7
    temperature-ranges: [300.0, 1000.0, 5000.0]
    data:
    - [1.7133, 0.02542616, 1.580808e-06, -1.821286e-08, 8.82771e-12, 7535.809,
      12.97901]
    - [8.063369, 0.01574488, -5.182392e-06, 7.477245e-10, -3.854422e-14,
      5313.871, -21.92647]
  transport:
    model: gas
    geometry: nonlinear
    diameter: 4.81
    well-depth: 303.4
    rotational-relaxation: 1.0
  note: '000000'
- name: HOCHO
  composition: C: 1, H: 2, O: 2
```

```
  thermo:
    model: NASA7
    temperature-ranges: [300.0, 1000.0, 5000.0]
    data:
    - [1.28069021, 0.0152887758, -5.64150476e-06, -1.22968799e-09, 8.14273233e-13,
      -4.64347524e+04, 18.3142081]
    - [1.24573687, 0.0167242062, -9.22177878e-06, 1.7643822e-09, 0.0, -4.65097525e+04,
      18.1159087]
  transport:
    model: gas
    geometry: nonlinear
    diameter: 3.97
    well-depth: 436.0
    rotational-relaxation: 2.0
- name: C4H8X2
  composition: C: 4, H: 8
  thermo:
    model: NASA7
    temperature-ranges: [300.0, 1000.0, 5000.0]
    data:
    - [-0.831372089, 0.0452580978, -2.93658559e-05, 1.00220436e-08, -1.4319168e-12,
      -1578.75035, 29.5084236]
    - [3.04470367, 0.0327451765, -1.45363237e-05, 2.39744017e-09, 0.0, -2521.77534,
      10.0151514]
  transport:
    model: gas
    geometry: nonlinear
    diameter: 5.088
    well-depth: 345.7
    dipole: 0.3
    rotational-relaxation: 1.0
  note: '000000'
- name: CH3CHCO
```

```
  composition: C: 3, H: 4, O: 1
  thermo:
    model: NASA7
    temperature-ranges: [300.0, 1000.0, 5000.0]
    data:
    - [1.48380119, 0.0322203013, -2.70250033e-05, 1.20499164e-08, -2.18365931e-12,
      -1.1527654e+04, 17.1552068]
    - [6.45951145, 0.0156117, -6.5512722e-06, 1.02541702e-09, 0.0, -1.27042477e+04,
      -7.715128]
  transport:
    model: gas
    geometry: nonlinear
    diameter: 4.12
    well-depth: 443.2
    rotational-relaxation: 1.0
- name: CH3COCH2
  composition: C: 3, H: 5, O: 1
  thermo:
    model: NASA7
    temperature-ranges: [300.0, 1000.0, 5000.0]
    data:
    - [1.22337251, 0.0324546742, -2.13542518e-05, 6.96777735e-09, -8.99160299e-13,
      -6594.19324, 20.5537233]
    - [4.1274301, 0.0233730564, -1.10040288e-05, 1.89595418e-09, 0.0, -7319.39257,
      5.86552803]
  transport:
    model: gas
    geometry: nonlinear
    diameter: 4.86
    well-depth: 435.5
    rotational-relaxation: 1.0
- name: C2H4O2H
  composition: C: 2, H: 5, O: 2
```

```
  thermo:
    model: NASA7
    temperature-ranges: [300.0, 1000.0, 5000.0]
    data:
    - [3.40977031, 0.0265939711, -1.57408161e-05, 4.41132564e-09, -4.49209001e-13,
      2058.74655, 13.5264941]
    - [5.13616373, 0.02132812, -9.9390851e-06, 1.69984335e-09, 0.0, 1619.39714,
      4.75750168]
  transport:
    model: gas
    geometry: nonlinear
    diameter: 4.41
    well-depth: 470.6
    rotational-relaxation: 1.5
- name: C2H3CHOCH2
  composition: C: 4, H: 6, O: 1
  thermo:
    model: NASA7
    temperature-ranges: [300.0, 1000.0, 5000.0]
    data:
    - [0.79798544, 0.034403432, -1.2459851e-05, -5.1806279e-18, 1.9935954e-21,
      -648.92754, 21.889698]
    - [-4.7209336, 0.039141378, -6.5287265e-06, -7.682095e-09, 2.5147331e-12,
      1753.52252, 51.719042]
  transport:
    model: gas
    geometry: nonlinear
    diameter: 5.413
    well-depth: 454.0
    dipole: 3.3
    rotational-relaxation: 1.0
- name: C4H6O23
  composition: C: 4, H: 6, O: 1
```

```
  thermo:
    model: NASA7
    temperature-ranges: [300.0, 1000.0, 5000.0]
    data:
    - [2.67053463, 4.9258642e-03, 8.86967406e-05, -1.26219194e-07, 5.23991321e-11,
      -1.02787872e+04, 14.5722395]
    - [8.60658242, 0.0208310051, -8.42229481e-06, 1.5671764e-09, -1.09391202e-13,
      -1.32392815e+04, -23.246475]
  transport:
    model: gas
    geometry: nonlinear
    diameter: 4.984
    well-depth: 350.4
    rotational-relaxation: 1.0
- name: SXC3H5CHO
  composition: C: 4, H: 6, O: 1
  thermo:
    model: NASA7
    temperature-ranges: [300.0, 1000.0, 5000.0]
    data:
    - [0.627183793, 0.0466780254, -3.74430631e-05, 1.58330542e-08, -2.73952155e-12,
      -1.57203117e+04, 21.6034294]
    - [7.19597854, 0.0249956291, -1.10451332e-05, 1.8092043e-09, 0.0, -1.72891601e+04,
      -11.2990296]
  transport:
    model: gas
    geometry: nonlinear
    diameter: 5.352
    well-depth: 436.4
    rotational-relaxation: 1.0
  note: '000000'
- name: C2H3CHCHO
  composition: C: 4, H: 5, O: 1
```

```
  thermo:
    model: NASA7
    temperature-ranges: [300.0, 1000.0, 5000.0]
    data:
    - [0.144549897, 0.0440495223, -3.63262463e-05, 1.57451928e-08, -2.78406786e-12,
      1234.3152, 29.1294645]
    - [6.57071278, 0.0226589441, -1.00395106e-05, 1.63880462e-09, 0.0, -289.020319,
      -3.00757327]
  transport:
    model: gas
    geometry: nonlinear
    diameter: 5.009
    well-depth: 464.2
    dipole: 2.6
    rotational-relaxation: 1.0
- name: CH3CO
  composition: C: 2, H: 3, O: 1
  thermo:
    model: NASA7
    temperature-ranges: [300.0, 1000.0, 5000.0]
    data:
    - [2.5288415, 0.0137152173, -4.28607476e-06, -7.71684278e-10, 4.8383638e-13,
      -3025.46532, 14.0340315]
    - [2.01002485, 0.0158541129, -7.49125231e-06, 1.29725074e-09, 0.0, -2928.17041,
      16.5128972]
  transport:
    model: gas
    geometry: nonlinear
    diameter: 3.97
    well-depth: 436.0
    rotational-relaxation: 2.0
- name: CH3COCH3
  composition: C: 3, H: 6, O: 1
```

```
  thermo:
    model: NASA7
    temperature-ranges: [200.0, 1000.0, 6000.0]
    data:
    - [5.5563892, -2.83863547e-03, 7.05722951e-05, -8.78130984e-08, 3.40290951e-11,
      -2.78325393e+04, 2.31960221]
    - [7.29796974, 0.0175656913, -6.31678065e-06, 1.02025553e-09, -6.10903592e-14,
      -2.95368927e+04, -12.7591704]
  transport:
    model: gas
    geometry: nonlinear
    diameter: 4.86
    well-depth: 435.5
  note: acetoneATcTA
- name: IXC3H5CO
  composition: C: 4, H: 5, O: 1
  thermo:
    model: NASA7
    temperature-ranges: [300.0, 1000.0, 5000.0]
    data:
    - [1.85097069, 0.0418855846, -3.62553731e-05, 1.65690659e-08, -3.05850846e-12,
      170.381441, 15.3014433]
    - [8.63232766, 0.0191159224, -8.00161116e-06, 1.24510072e-09, 0.0, -1424.77548,
      -18.5563686]
  transport:
    model: gas
    geometry: nonlinear
    diameter: 5.352
    well-depth: 436.4
    rotational-relaxation: 1.0
  note: '000000'
- name: CH3CHCHCHO
  composition: C: 4, H: 6, O: 1
```

```
  thermo:
    model: NASA7
    temperature-ranges: [300.0, 1000.0, 5000.0]
    data:
    - [-1.5557766, 0.040964063, -1.6986881e-05, -6.0092814e-18, 2.3136853e-21,
      -1.4139492e+04, 37.470758]
    - [19.879454, -0.020913055, 4.45360508e-05, -2.6037487e-08, 4.8683612e-12,
      -1.95278768e+04, -68.720032]
  transport:
    model: gas
    geometry: nonlinear
    diameter: 5.009
    well-depth: 464.2
    dipole: 2.6
    rotational-relaxation: 1.0
  note: '000000'
- name: MP2D
  composition: C: 4, H: 6, O: 2
  thermo:
    model: NASA7
    temperature-ranges: [300.0, 1000.0, 5000.0]
    data:
    - [2.05265608, 0.04426545, -2.98476063e-05, 1.02829815e-08, -1.46723207e-12,
      -3.94315114e+04, 19.2244429]
    - [5.87894841, 0.0318268733, -1.49820978e-05, 2.56252532e-09, 0.0, -4.03570172e+04,
      5.85170825e-03]
  transport:
    model: gas
    geometry: nonlinear
    diameter: 5.664
    well-depth: 523.2
    dipole: 1.7
    rotational-relaxation: 1.0
```

```
  note: '000000'
- name: MP2J
  composition: C: 4, H: 7, O: 2
  thermo:
    model: NASA7
    temperature-ranges: [300.0, 1000.0, 5000.0]
    data:
    - [3.01226869, 0.0452562271, -2.87009424e-05, 9.04524035e-09, -1.16253018e-12,
      -3.32370243e+04, 13.0032094]
    - [6.05545008, 0.035360873, -1.68772482e-05, 2.91118868e-09, 0.0, -3.39727532e+04,
      -2.28078456]
  transport:
    model: gas
    geometry: nonlinear
    diameter: 5.664
    well-depth: 523.2
    dipole: 1.7
    rotational-relaxation: 1.0
  note: '000000'
- name: MP3J
  composition: C: 4, H: 7, O: 2
  thermo:
    model: NASA7
    temperature-ranges: [300.0, 1000.0, 5000.0]
    data:
    - [4.0657748, 0.0388324925, -2.0804875e-05, 5.06251249e-09, -4.21741752e-13,
      -2.98351498e+04, 10.380341]
    - [5.25654053, 0.0349900668, -1.6270579e-05, 2.75813474e-09, 0.0, -3.01243886e+04,
      4.39279096]
  transport:
    model: gas
    geometry: nonlinear
    diameter: 5.664
```

```
    well-depth: 523.2
    dipole: 1.7
    rotational-relaxation: 1.0
  note: '000000'
- name: MMETHMJ
  composition: C: 5, H: 7, O: 2
  thermo:
    model: NASA7
    temperature-ranges: [300.0, 1000.0, 5000.0]
    data:
    - [3.31845142, 0.0503804264, -3.44292678e-05, 1.21616702e-08, -1.79043255e-12,
      -1.89667805e+04, 16.5319599]
    - [7.88808413, 0.035463841, -1.65145625e-05, 2.8034851e-09, 0.0, -2.00682292e+04,
      -6.40292488]
  transport:
    model: gas
    geometry: nonlinear
    diameter: 5.664
    well-depth: 523.2
    dipole: 1.7
    rotational-relaxation: 1.0
  note: '000000'
- name: MMETHVJ
  composition: C: 5, H: 7, O: 2
  thermo:
    model: NASA7
    temperature-ranges: [300.0, 1000.0, 5000.0]
    data:
    - [3.51643548, 0.0512966154, -3.66135902e-05, 1.37143487e-08, -2.1524754e-12,
      -1.39670905e+04, 14.1932082]
    - [8.71528211, 0.0341402007, -1.57448253e-05, 2.65067646e-09, 0.0, -1.52085618e+04,
      -11.8473479]
  transport:
```

```
    model: gas
    geometry: nonlinear
    diameter: 5.664
    well-depth: 523.2
    dipole: 1.7
    rotational-relaxation: 1.0
  note: '000000'
- name: MMETHAC
  composition: C: 5, H: 8, O: 2
  thermo:
    model: NASA7
    temperature-ranges: [300.0, 1000.0, 5000.0]
    data:
    - [2.35246332, 0.0556934032, -3.81321664e-05, 1.36196767e-08, -2.03920463e-12,
      -4.35452573e+04, 18.8827111]
    - [7.44668994, 0.0389920812, -1.79729976e-05, 3.02839868e-09, 0.0, -4.47685673e+04,
      -6.66459726]
  transport:
    model: gas
    geometry: nonlinear
    diameter: 5.664
    well-depth: 523.2
    dipole: 1.7
    rotational-relaxation: 1.0
  note: '000000'
- name: MMETHPJ
  composition: C: 5, H: 7, O: 2
  thermo:
    model: NASA7
    temperature-ranges: [300.0, 1000.0, 5000.0]
    data:
    - [3.31845142, 0.0503804264, -3.44292678e-05, 1.21616702e-08, -1.79043255e-12,
      -1.89667805e+04, 16.5319599]
```

```
    - [7.88808413, 0.035463841, -1.65145625e-05, 2.8034851e-09, 0.0, -2.00682292e+04,
      -6.40292488]
  transport:
    model: gas
    geometry: nonlinear
    diameter: 5.664
    well-depth: 523.2
    dipole: 1.7
    rotational-relaxation: 1.0
  note: '000000'

reactions:
- equation: H + O2 <=> O + OH  # Reaction 1
  rate-constant: A: 1.04e+14, b: 0.0, Ea: 1.528609e+04
- equation: O + H2 <=> H + OH  # Reaction 2
  rate-constant: A: 3.818e+12, b: 0.0, Ea: 7947.9
  duplicate: true
- equation: O + H2 <=> H + OH  # Reaction 3
  rate-constant: A: 8.792e+14, b: 0.0, Ea: 1.916993e+04
  duplicate: true
- equation: H2 + OH <=> H2O + H  # Reaction 4
  rate-constant: A: 2.16e+08, b: 1.51, Ea: 3429.97
- equation: 2 OH <=> O + H2O  # Reaction 5
  rate-constant: A: 3.34e+04, b: 2.42, Ea: -1929.97
- equation: H2 + M <=> 2 H + M  # Reaction 6
  type: three-body
  rate-constant: A: 4.577e+19, b: -1.4, Ea: 1.0438002e+05
  efficiencies: AR: 0.0, CO: 1.9, CO2: 3.8, H2: 2.5, H2O: 12.0, HE: 0.0
- equation: H2 + AR <=> 2 H + AR  # Reaction 7
  rate-constant: A: 5.84e+18, b: -1.1, Ea: 1.0438002e+05
- equation: H2 + HE <=> 2 H + HE  # Reaction 8
  rate-constant: A: 5.84e+18, b: -1.1, Ea: 1.0438002e+05
- equation: 2 O + M <=> O2 + M  # Reaction 9
```

```
  type: three-body
  rate-constant: A: 6.165e+15, b: -0.5, Ea: 0.0
  efficiencies: AR: 0.0, CO: 1.9, CO2: 3.8, H2: 2.5, H2O: 12.0, HE: 0.0
- equation: 2 O + AR <=> O2 + AR  # Reaction 10
  rate-constant: A: 1.886e+13, b: 0.0, Ea: -1788.0
- equation: 2 O + HE <=> O2 + HE  # Reaction 11
  rate-constant: A: 1.886e+13, b: 0.0, Ea: -1788.0
- equation: O + H + M <=> OH + M  # Reaction 12
  type: three-body
  rate-constant: A: 4.714e+18, b: -1.0, Ea: 0.0
  efficiencies: AR: 0.75, CO: 1.9, CO2: 3.8, H2: 2.5, H2O: 12.0, HE: 0.75
- equation: H2O + M <=> H + OH + M  # Reaction 13
  type: three-body
  rate-constant: A: 6.064e+27, b: -3.322, Ea: 1.2078991e+05
  efficiencies: CO: 1.9, CO2: 3.8, H2: 3.0, H2O: 0.0, HE: 1.1, N2: 2.0,
    O2: 1.5
- equation: 2 H2O <=> H + OH + H2O  # Reaction 14
  rate-constant: A: 1.006e+26, b: -2.44, Ea: 1.2017997e+05
- equation: H + O2 (+ M) <=> HO2 (+ M)  # Reaction 15
  type: falloff
  low-P-rate-constant: A: 9.042e+19, b: -1.5, Ea: 492.11
  high-P-rate-constant: A: 4.651e+12, b: 0.44, Ea: 0.0
  Troe: A: 0.5, T3: 0.0, T1: 1.0e+30
  efficiencies: CO: 2.7, CO2: 5.4, H2: 3.0, H2O: 21.0, HE: 1.2, N2: 1.5,
    O2: 1.1
- equation: HO2 + H <=> H2 + O2  # Reaction 16
  rate-constant: A: 2.75e+06, b: 2.09, Ea: -1451.0
- equation: HO2 + H <=> 2 OH  # Reaction 17
  rate-constant: A: 7.079e+13, b: 0.0, Ea: 294.93
- equation: HO2 + O <=> O2 + OH  # Reaction 18
  rate-constant: A: 2.85e+10, b: 1.0, Ea: -723.95
- equation: HO2 + OH <=> H2O + O2  # Reaction 19
  rate-constant: A: 2.89e+13, b: 0.0, Ea: -496.89
```

```
- equation: 2 HO2 <=> H2O2 + O2  # Reaction 20
  rate-constant: A: 4.2e+14, b: 0.0, Ea: 1.198207e+04
  duplicate: true
- equation: 2 HO2 <=> H2O2 + O2  # Reaction 21
  rate-constant: A: 1.3e+11, b: 0.0, Ea: -1629.3
  duplicate: true
- equation: H2O2 (+ M) <=> 2 OH (+ M)  # Reaction 22
  type: falloff
  low-P-rate-constant: A: 2.49e+24, b: -2.3, Ea: 4.875e+04
  high-P-rate-constant: A: 2.0e+12, b: 0.9, Ea: 4.874904e+04
  Troe: A: 0.43, T3: 0.0, T1: 1.0e+30
  efficiencies: CO: 2.8, CO2: 1.6, H2: 3.7, H2O: 7.5, H2O2: 7.7, HE: 0.65,
    N2: 1.5, O2: 1.2
- equation: H2O2 + H <=> H2O + OH  # Reaction 23
  rate-constant: A: 2.41e+13, b: 0.0, Ea: 3969.89
- equation: H2O2 + H <=> HO2 + H2  # Reaction 24
  rate-constant: A: 4.82e+13, b: 0.0, Ea: 7950.05
- equation: H2O2 + O <=> OH + HO2  # Reaction 25
  rate-constant: A: 9.55e+06, b: 2.0, Ea: 3969.89
- equation: H2O2 + OH <=> HO2 + H2O  # Reaction 26
  rate-constant: A: 1.74e+12, b: 0.0, Ea: 318.12
  duplicate: true
- equation: H2O2 + OH <=> HO2 + H2O  # Reaction 27
  rate-constant: A: 7.59e+13, b: 0.0, Ea: 7270.08
  duplicate: true
- equation: CO + O (+ M) <=> CO2 (+ M)  # Reaction 28
  type: falloff
  low-P-rate-constant: A: 1.55e+24, b: -2.79, Ea: 4192.16
  high-P-rate-constant: A: 1.8e+10, b: 0.0, Ea: 2385.28
  Troe: A: 1.0, T3: 1.0, T1: 1.0e+07, T2: 1.0e+07
  efficiencies: AR: 0.7, CO: 1.75, CO2: 3.6, H2: 2.0, H2O: 12.0
- equation: CO + OH <=> CO2 + H  # Reaction 29
  rate-constant: A: 7.046e+04, b: 2.053, Ea: -355.64
```

```
  duplicate: true
- equation: CO + OH <=> CO2 + H  # Reaction 30
  rate-constant: A: 5.757e+12, b: -0.664, Ea: 331.74
  duplicate: true
- equation: CO + O2 <=> CO2 + O  # Reaction 31
  rate-constant: A: 1.05e+12, b: 0.0, Ea: 4.770005e+04
- equation: CO + HO2 <=> CO2 + OH  # Reaction 32
  rate-constant: A: 1.57e+05, b: 2.18, Ea: 1.794264e+04
- equation: HCO + H <=> CO + H2  # Reaction 33
  rate-constant: A: 1.2e+14, b: 0.0, Ea: 0.0
- equation: HCO + O <=> CO + OH  # Reaction 34
  rate-constant: A: 3.0e+13, b: 0.0, Ea: 0.0
- equation: HCO + O <=> CO2 + H  # Reaction 35
  rate-constant: A: 3.0e+13, b: 0.0, Ea: 0.0
- equation: HCO + OH <=> CO + H2O  # Reaction 36
  rate-constant: A: 3.02e+13, b: 0.0, Ea: 0.0
- equation: HCO + M <=> CO + H + M  # Reaction 37
  type: three-body
  rate-constant: A: 4.748e+11, b: 0.659, Ea: 1.48738e+04
  efficiencies: CO: 1.75, CO2: 3.6, H2: 2.0, H2O: 0.0
- equation: HCO + O2 <=> CO + HO2  # Reaction 38
  rate-constant: A: 7.58e+12, b: 0.0, Ea: 409.89
- equation: C + OH <=> CO + H  # Reaction 39
  rate-constant: A: 5.0e+13, b: 0.0, Ea: 0.0
- equation: C + O2 <=> CO + O  # Reaction 40
  rate-constant: A: 5.8e+13, b: 0.0, Ea: 576.0
- equation: CH + H <=> C + H2  # Reaction 41
  rate-constant: A: 1.65e+14, b: 0.0, Ea: 0.0
- equation: CH + O <=> CO + H  # Reaction 42
  rate-constant: A: 5.7e+13, b: 0.0, Ea: 0.0
- equation: CH + OH <=> HCO + H  # Reaction 43
  rate-constant: A: 3.0e+13, b: 0.0, Ea: 0.0
- equation: CH + H2 <=> TXCH2 + H  # Reaction 44
```

```
  rate-constant: A: 1.08e+14, b: 0.0, Ea: 3109.46
- equation: CH + H2 (+ M) <=> CH3 (+ M)  # Reaction 45
  type: falloff
  low-P-rate-constant: A: 4.82e+25, b: -2.8, Ea: 590.34
  high-P-rate-constant: A: 1.97e+12, b: 0.43, Ea: -370.46
  Troe: A: 0.578, T3: 122.0, T1: 2535.0, T2: 9365.0
  efficiencies: AR: 0.7, C2H6: 3.0, CH4: 2.0, CO: 1.75, CO2: 3.6, H2: 2.0,
    H2O: 12.0
- equation: CH + H2O <=> CH2O + H  # Reaction 46
  rate-constant: A: 5.71e+12, b: 0.0, Ea: -755.26
- equation: CH + O2 <=> HCO + O  # Reaction 47
  rate-constant: A: 6.71e+13, b: 0.0, Ea: 0.0
- equation: CH + CO (+ M) <=> HCCO (+ M)  # Reaction 48
  type: falloff
  low-P-rate-constant: A: 2.69e+28, b: -3.74, Ea: 1935.95
  high-P-rate-constant: A: 5.0e+13, b: 0.0, Ea: 0.0
  Troe: A: 0.5757, T3: 237.0, T1: 1652.0, T2: 5069.0
  efficiencies: AR: 0.7, C2H6: 3.0, CH4: 2.0, CO: 1.75, CO2: 3.6, H2: 2.0,
    H2O: 12.0
- equation: CH + CO2 <=> HCO + CO  # Reaction 49
  rate-constant: A: 1.9e+14, b: 0.0, Ea: 1.579111e+04
- equation: CO + H2 (+ M) <=> CH2O (+ M)  # Reaction 50
  type: falloff
  low-P-rate-constant: A: 5.07e+27, b: -3.42, Ea: 8.43499e+04
  high-P-rate-constant: A: 4.3e+07, b: 1.5, Ea: 7.960086e+04
  Troe: A: 0.932, T3: 197.0, T1: 1540.0, T2: 1.03e+04
  efficiencies: AR: 0.7, C2H6: 3.0, CH4: 2.0, CO: 1.75, CO2: 3.6, H2: 2.0,
    H2O: 12.0
- equation: HCO + H (+ M) <=> CH2O (+ M)  # Reaction 51
  type: falloff
  low-P-rate-constant: A: 2.47e+24, b: -2.57, Ea: 425.43
  high-P-rate-constant: A: 1.09e+12, b: 0.48, Ea: -260.52
  Troe: A: 0.7824, T3: 271.0, T1: 2755.0, T2: 6570.0
```

```
  efficiencies: AR: 0.7, C2H6: 3.0, CH4: 2.0, CO: 1.75, CO2: 3.6, H2: 2.0,
    H2O: 12.0
- equation: TXCH2 + H (+ M) <=> CH3 (+ M)  # Reaction 52
  type: falloff
  low-P-rate-constant: A: 1.04e+26, b: -2.76, Ea: 1598.95
  high-P-rate-constant: A: 6.0e+14, b: 0.0, Ea: 0.0
  Troe: A: 0.562, T3: 91.0, T1: 5836.0, T2: 8552.0
  efficiencies: AR: 0.7, C2H6: 3.0, CH4: 2.0, CO: 1.75, CO2: 3.6, H2: 2.0,
    H2O: 12.0
- equation: TXCH2 + O <=> HCO + H  # Reaction 53
  rate-constant: A: 8.0e+13, b: 0.0, Ea: 0.0
- equation: TXCH2 + OH <=> CH2O + H  # Reaction 54
  rate-constant: A: 2.0e+13, b: 0.0, Ea: 0.0
- equation: TXCH2 + OH <=> CH + H2O  # Reaction 55
  rate-constant: A: 1.13e+07, b: 2.0, Ea: 2999.52
- equation: TXCH2 + H2 <=> H + CH3  # Reaction 56
  rate-constant: A: 5.0e+05, b: 2.0, Ea: 7229.92
- equation: TXCH2 + O2 => CO2 + 2 H  # Reaction 57
  rate-constant: A: 5.8e+12, b: 0.0, Ea: 1500.96
- equation: TXCH2 + O2 <=> CH2O + O  # Reaction 58
  rate-constant: A: 2.4e+12, b: 0.0, Ea: 1500.96
- equation: TXCH2 + O2 => OH + H + CO  # Reaction 59
  rate-constant: A: 5.0e+12, b: 0.0, Ea: 1500.96
- equation: TXCH2 + HO2 <=> CH2O + OH  # Reaction 60
  rate-constant: A: 2.0e+13, b: 0.0, Ea: 0.0
- equation: TXCH2 + C <=> C2H + H  # Reaction 61
  rate-constant: A: 5.0e+13, b: 0.0, Ea: 0.0
- equation: TXCH2 + CO (+ M) <=> CH2CO (+ M)  # Reaction 62
  type: falloff
  low-P-rate-constant: A: 2.69e+33, b: -5.11, Ea: 7096.08
  high-P-rate-constant: A: 8.1e+11, b: 0.5, Ea: 4510.04
  Troe: A: 0.5907, T3: 275.0, T1: 1226.0, T2: 5185.0
  efficiencies: AR: 0.7, C2H6: 3.0, CH4: 2.0, CO: 1.75, CO2: 3.6, H2: 2.0,
```

```
    H2O: 12.0
- equation: TXCH2 + CH <=> C2H2 + H  # Reaction 63
  rate-constant: A: 4.0e+13, b: 0.0, Ea: 0.0
- equation: 2 TXCH2 <=> C2H2 + H2  # Reaction 64
  rate-constant: A: 1.6e+15, b: 0.0, Ea: 1.194312e+04
- equation: 2 TXCH2 => C2H2 + 2 H  # Reaction 65
  rate-constant: A: 2.0e+14, b: 0.0, Ea: 1.098948e+04
- equation: SXCH2 + N2 <=> TXCH2 + N2  # Reaction 66
  rate-constant: A: 1.5e+13, b: 0.0, Ea: 599.9
- equation: SXCH2 + AR <=> TXCH2 + AR  # Reaction 67
  rate-constant: A: 9.0e+12, b: 0.0, Ea: 599.9
- equation: SXCH2 + H <=> CH + H2  # Reaction 68
  rate-constant: A: 3.0e+13, b: 0.0, Ea: 0.0
- equation: SXCH2 + O <=> CO + H2  # Reaction 69
  rate-constant: A: 1.5e+13, b: 0.0, Ea: 0.0
- equation: SXCH2 + O <=> HCO + H  # Reaction 70
  rate-constant: A: 1.5e+13, b: 0.0, Ea: 0.0
- equation: SXCH2 + OH <=> CH2O + H  # Reaction 71
  rate-constant: A: 3.0e+13, b: 0.0, Ea: 0.0
- equation: SXCH2 + H2 <=> CH3 + H  # Reaction 72
  rate-constant: A: 7.0e+13, b: 0.0, Ea: 0.0
- equation: SXCH2 + O2 <=> H + OH + CO  # Reaction 73
  rate-constant: A: 2.8e+13, b: 0.0, Ea: 0.0
- equation: SXCH2 + O2 <=> CO + H2O  # Reaction 74
  rate-constant: A: 1.2e+13, b: 0.0, Ea: 0.0
- equation: SXCH2 + H2O (+ M) <=> CH3OH (+ M)  # Reaction 75
  type: falloff
  low-P-rate-constant: A: 1.88e+38, b: -6.36, Ea: 5040.63
  high-P-rate-constant: A: 4.82e+17, b: -1.16, Ea: 1144.84
  Troe: A: 0.6027, T3: 208.0, T1: 3922.0, T2: 1.018e+04
  efficiencies: AR: 0.7, C2H6: 3.0, CH4: 2.0, CO: 1.75, CO2: 3.6, H2: 2.0,
    H2O: 12.0
- equation: SXCH2 + H2O <=> TXCH2 + H2O  # Reaction 76
```

```
  rate-constant: A: 3.0e+13, b: 0.0, Ea: 0.0
- equation: SXCH2 + H2O => H2 + CH2O  # Reaction 77
  rate-constant: A: 6.82e+10, b: 0.25, Ea: -934.51
- equation: SXCH2 + CO <=> TXCH2 + CO  # Reaction 78
  rate-constant: A: 9.0e+12, b: 0.0, Ea: 0.0
- equation: SXCH2 + CO2 <=> TXCH2 + CO2  # Reaction 79
  rate-constant: A: 7.0e+12, b: 0.0, Ea: 0.0
- equation: SXCH2 + CO2 <=> CH2O + CO  # Reaction 80
  rate-constant: A: 1.4e+13, b: 0.0, Ea: 0.0
- equation: CH2O + H (+ M) <=> CH2OH (+ M)  # Reaction 81
  type: falloff
  low-P-rate-constant: A: 1.27e+32, b: -4.82, Ea: 6529.64
  high-P-rate-constant: A: 5.4e+11, b: 0.45, Ea: 3599.43
  Troe: A: 0.7187, T3: 103.0, T1: 1291.0, T2: 4160.0
  efficiencies: AR: 0.7, C2H6: 3.0, CH4: 2.0, CO: 1.75, CO2: 3.6, H2: 2.0,
    H2O: 12.0
- equation: CH2O + H (+ M) <=> CH3O (+ M)  # Reaction 82
  type: falloff
  low-P-rate-constant: A: 2.2e+30, b: -4.8, Ea: 5559.27
  high-P-rate-constant: A: 5.4e+11, b: 0.45, Ea: 2600.38
  Troe: A: 0.758, T3: 94.0, T1: 1555.0, T2: 4200.0
  efficiencies: AR: 0.7, C2H6: 3.0, CH4: 2.0, CO: 1.75, CO2: 3.6, H2: 2.0,
    H2O: 12.0
- equation: CH2O + H <=> HCO + H2  # Reaction 83
  rate-constant: A: 5.74e+07, b: 1.9, Ea: 2741.4
- equation: CH2O + O <=> HCO + OH  # Reaction 84
  rate-constant: A: 3.9e+13, b: 0.0, Ea: 3539.67
- equation: CH2O + OH <=> HCO + H2O  # Reaction 85
  rate-constant: A: 3.43e+09, b: 1.18, Ea: -446.94
- equation: CH2O + O2 <=> HCO + HO2  # Reaction 86
  rate-constant: A: 1.0e+14, b: 0.0, Ea: 4.0e+04
- equation: CH2O + HO2 <=> HCO + H2O2  # Reaction 87
  rate-constant: A: 5.6e+06, b: 2.0, Ea: 1.200048e+04
```

```
- equation: CH2O + CH <=> CH2CO + H  # Reaction 88
  rate-constant: A: 9.46e+13, b: 0.0, Ea: -516.25
- equation: CH3 + H (+ M) <=> CH4 (+ M)  # Reaction 89
  type: falloff
  low-P-rate-constant: A: 3.47e+38, b: -6.3, Ea: 5074.09
  high-P-rate-constant: A: 6.92e+13, b: 0.18, Ea: 0.0
  Troe: A: 0.783, T3: 74.0, T1: 2941.0, T2: 6964.0
  efficiencies: AR: 0.7, C2H6: 3.0, CH4: 3.0, CO: 1.5, CO2: 2.0, H2: 2.0,
    H2O: 6.0
- equation: CH3 + O <=> CH2O + H  # Reaction 90
  rate-constant: A: 5.06e+13, b: 0.0, Ea: 0.0
- equation: CH3 + O => H + H2 + CO  # Reaction 91
  rate-constant: A: 3.37e+13, b: 0.0, Ea: 0.0
- equation: CH3 + OH (+ M) <=> CH3OH (+ M)  # Reaction 92
  type: falloff
  low-P-rate-constant: A: 4.0e+36, b: -5.92, Ea: 3140.54
  high-P-rate-constant: A: 2.79e+18, b: -1.43, Ea: 1331.26
  Troe: A: 0.412, T3: 195.0, T1: 5900.0, T2: 6394.0
  efficiencies: AR: 0.7, C2H6: 3.0, CH4: 2.0, CO: 1.75, CO2: 3.6, H2: 2.0,
    H2O: 12.0
- equation: CH3 + OH <=> TXCH2 + H2O  # Reaction 93
  rate-constant: A: 5.6e+07, b: 1.6, Ea: 5420.65
- equation: CH3 + OH => H2 + CH2O  # Reaction 94
  rate-constant: A: 8.0e+09, b: 0.0, Ea: -1754.3
- equation: CH3 + OH <=> SXCH2 + H2O  # Reaction 95
  rate-constant: A: 6.44e+17, b: -1.34, Ea: 1417.3
- equation: CH3 + O2 <=> CH3O + O  # Reaction 96
  rate-constant: A: 1.38e+13, b: 0.0, Ea: 3.052103e+04
- equation: CH3 + O2 <=> CH2O + OH  # Reaction 97
  rate-constant: A: 5.87e+11, b: 0.0, Ea: 1.384082e+04
- equation: CH3 + O2 (+ M) <=> CH3O2 (+ M)  # Reaction 98
  type: falloff
  low-P-rate-constant: A: 3.82e+31, b: -4.89, Ea: 3432.12
```

```
  high-P-rate-constant: A: 1.01e+08, b: 1.63, Ea: 0.0
  Troe: A: 0.045, T3: 880.1, T1: 2.5e+09, T2: 1.786e+09
- equation: CH3O2 + CH3 <=> 2 CH3O  # Reaction 99
  rate-constant: A: 1.0e+13, b: 0.0, Ea: -1199.81
- equation: 2 CH3O2 => 2 CH3O + O2  # Reaction 100
  rate-constant: A: 1.4e+16, b: -1.61, Ea: 1859.46
- equation: CH3O2 + HO2 => CH3O + OH + O2  # Reaction 101
  rate-constant: A: 2.47e+11, b: 0.0, Ea: -1570.27
- equation: CH3O2 + CH2O => CH3O + OH + HCO  # Reaction 102
  rate-constant: A: 1.99e+12, b: 0.0, Ea: 1.167065e+04
- equation: CH3 + HO2 <=> CH3O + OH  # Reaction 103
  rate-constant: A: 1.0e+13, b: 0.0, Ea: 0.0
- equation: CH3 + HO2 <=> CH4 + O2  # Reaction 104
  rate-constant: A: 3.61e+12, b: 0.0, Ea: 0.0
- equation: CH3 + H2O2 <=> CH4 + HO2  # Reaction 105
  rate-constant: A: 2.45e+04, b: 2.47, Ea: 5179.25
- equation: CH3 + C <=> C2H2 + H  # Reaction 106
  rate-constant: A: 5.0e+13, b: 0.0, Ea: 0.0
- equation: CH3 + CH <=> C2H3 + H  # Reaction 107
  rate-constant: A: 3.0e+13, b: 0.0, Ea: 0.0
- equation: CH3 + HCO <=> CH4 + CO  # Reaction 108
  rate-constant: A: 2.65e+13, b: 0.0, Ea: 0.0
- equation: CH3 + CH2O <=> CH4 + HCO  # Reaction 109
  rate-constant: A: 3320.0, b: 2.81, Ea: 5860.42
- equation: CH3 + TXCH2 <=> C2H4 + H  # Reaction 110
  rate-constant: A: 1.0e+14, b: 0.0, Ea: 0.0
- equation: CH3 + SXCH2 <=> C2H4 + H  # Reaction 111
  rate-constant: A: 1.2e+13, b: 0.0, Ea: -571.22
- equation: 2 CH3 <=> C2H5 + H  # Reaction 112
  rate-constant: A: 6.84e+12, b: 0.1, Ea: 1.05999e+04
- equation: CH3O + H (+ M) <=> CH3OH (+ M)  # Reaction 113
  type: falloff
  low-P-rate-constant: A: 4.66e+41, b: -7.44, Ea: 1.407983e+04
```

```
  high-P-rate-constant: A: 2.43e+12, b: 0.52, Ea: 50.19
  Troe: A: 0.7, T3: 100.0, T1: 9.0e+04, T2: 1.0e+04
  efficiencies: AR: 0.7, C2H6: 3.0, CH4: 2.0, CO: 1.75, CO2: 3.6, H2: 2.0,
    H2O: 12.0
- equation: CH3O + H <=> CH2OH + H  # Reaction 114
  rate-constant: A: 4.15e+07, b: 1.63, Ea: 1924.0
- equation: CH3O + H <=> CH2O + H2  # Reaction 115
  rate-constant: A: 2.0e+13, b: 0.0, Ea: 0.0
- equation: CH3O + H <=> CH3 + OH  # Reaction 116
  rate-constant: A: 1.5e+12, b: 0.5, Ea: -109.94
- equation: CH3O + H <=> SXCH2 + H2O  # Reaction 117
  rate-constant: A: 2.62e+14, b: -0.23, Ea: 1070.75
- equation: CH3O + O <=> CH2O + OH  # Reaction 118
  rate-constant: A: 1.0e+13, b: 0.0, Ea: 0.0
- equation: CH3O + OH <=> CH2O + H2O  # Reaction 119
  rate-constant: A: 5.0e+12, b: 0.0, Ea: 0.0
- equation: CH3O + O2 <=> CH2O + HO2  # Reaction 120
  rate-constant: A: 4.28e-13, b: 7.6, Ea: -3530.11
- equation: CH2OH + H (+ M) <=> CH3OH (+ M)  # Reaction 121
  type: falloff
  low-P-rate-constant: A: 4.36e+31, b: -4.65, Ea: 5081.26
  high-P-rate-constant: A: 1.06e+12, b: 0.5, Ea: 86.04
  Troe: A: 0.6, T3: 100.0, T1: 9000.0, T2: 1.0e+04
  efficiencies: AR: 0.7, C2H6: 3.0, CH4: 2.0, CO: 1.75, CO2: 3.6, H2: 2.0,
    H2O: 12.0
- equation: CH2OH + H <=> CH2O + H2  # Reaction 122
  rate-constant: A: 2.0e+13, b: 0.0, Ea: 0.0
- equation: CH2OH + H <=> CH3 + OH  # Reaction 123
  rate-constant: A: 1.65e+11, b: 0.65, Ea: -284.42
- equation: CH2OH + H <=> SXCH2 + H2O  # Reaction 124
  rate-constant: A: 3.28e+13, b: -0.09, Ea: 609.46
- equation: CH2OH + O <=> CH2O + OH  # Reaction 125
  rate-constant: A: 1.0e+13, b: 0.0, Ea: 0.0
```

```
- equation: CH2OH + OH <=> CH2O + H2O  # Reaction 126
  rate-constant: A: 5.0e+12, b: 0.0, Ea: 0.0
- equation: CH2OH + O2 <=> CH2O + HO2  # Reaction 127
  rate-constant: A: 1.8e+13, b: 0.0, Ea: 901.05
- equation: CH4 + H <=> CH3 + H2  # Reaction 128
  rate-constant: A: 6.6e+08, b: 1.62, Ea: 1.08413e+04
- equation: CH4 + O <=> CH3 + OH  # Reaction 129
  rate-constant: A: 1.02e+09, b: 1.5, Ea: 8599.43
- equation: CH4 + OH <=> CH3 + H2O  # Reaction 130
  rate-constant: A: 1.0e+08, b: 1.6, Ea: 3119.02
- equation: CH4 + CH <=> C2H4 + H  # Reaction 131
  rate-constant: A: 6.0e+13, b: 0.0, Ea: 0.0
- equation: CH4 + TXCH2 <=> 2 CH3  # Reaction 132
  rate-constant: A: 2.46e+06, b: 2.0, Ea: 8269.6
- equation: CH4 + SXCH2 <=> 2 CH3  # Reaction 133
  rate-constant: A: 1.6e+13, b: 0.0, Ea: -571.22
- equation: CH3OH + H <=> CH2OH + H2  # Reaction 134
  rate-constant: A: 1.7e+07, b: 2.1, Ea: 4870.94
- equation: CH3OH + H <=> CH3O + H2  # Reaction 135
  rate-constant: A: 4.2e+06, b: 2.1, Ea: 4870.94
- equation: CH3OH + O <=> CH2OH + OH  # Reaction 136
  rate-constant: A: 3.88e+05, b: 2.5, Ea: 3099.9
- equation: CH3OH + O <=> CH3O + OH  # Reaction 137
  rate-constant: A: 1.3e+05, b: 2.5, Ea: 5000.0
- equation: CH3OH + OH <=> CH2OH + H2O  # Reaction 138
  rate-constant: A: 1.44e+06, b: 2.0, Ea: -841.3
- equation: CH3OH + OH <=> CH3O + H2O  # Reaction 139
  rate-constant: A: 6.3e+06, b: 2.0, Ea: 1500.96
- equation: CH3OH + CH3 <=> CH2OH + CH4  # Reaction 140
  rate-constant: A: 3.0e+07, b: 1.5, Ea: 9940.25
- equation: CH3OH + CH3 <=> CH3O + CH4  # Reaction 141
  rate-constant: A: 1.0e+07, b: 1.5, Ea: 9940.25
- equation: C2H + H (+ M) <=> C2H2 (+ M)  # Reaction 142
```

```
  type: falloff
  low-P-rate-constant: A: 2.6e+33, b: -4.8, Ea: 1900.1
  high-P-rate-constant: A: 1.0e+17, b: -1.0, Ea: 0.0
  Troe: A: 0.6464, T3: 132.0, T1: 1315.0, T2: 5566.0
  efficiencies: AR: 0.7, C2H6: 3.0, CH4: 2.0, CO: 1.75, CO2: 3.6, H2: 2.0,
    H2O: 12.0
- equation: C2H + O <=> CH + CO  # Reaction 143
  rate-constant: A: 5.0e+13, b: 0.0, Ea: 0.0
- equation: C2H + OH <=> H + HCCO  # Reaction 144
  rate-constant: A: 2.0e+13, b: 0.0, Ea: 0.0
- equation: C2H + O2 <=> HCO + CO  # Reaction 145
  rate-constant: A: 1.0e+13, b: 0.0, Ea: -755.26
- equation: C2H + H2 <=> C2H2 + H  # Reaction 146
  rate-constant: A: 3.31e+06, b: 2.26, Ea: 901.05
- equation: HCCO + H <=> SXCH2 + CO  # Reaction 147
  rate-constant: A: 1.0e+14, b: 0.0, Ea: 0.0
- equation: HCCO + O <=> H + 2 CO  # Reaction 148
  rate-constant: A: 1.0e+14, b: 0.0, Ea: 0.0
- equation: HCCO + O2 <=> OH + 2 CO  # Reaction 149
  rate-constant: A: 4.2e+10, b: 0.0, Ea: 853.25
- equation: HCCO + CH <=> C2H2 + CO  # Reaction 150
  rate-constant: A: 5.0e+13, b: 0.0, Ea: 0.0
- equation: HCCO + TXCH2 <=> C2H3 + CO  # Reaction 151
  rate-constant: A: 3.0e+13, b: 0.0, Ea: 0.0
- equation: 2 HCCO <=> C2H2 + 2 CO  # Reaction 152
  rate-constant: A: 1.0e+13, b: 0.0, Ea: 0.0
- equation: C2H2 + H (+ M) <=> C2H3 (+ M)  # Reaction 153
  type: falloff
  low-P-rate-constant: A: 6.34e+31, b: -4.66, Ea: 3781.07
  high-P-rate-constant: A: 1.71e+10, b: 1.27, Ea: 2707.93
  Troe: A: 0.2122, T3: 1.0, T1: -1.0212e+04
  efficiencies: AR: 0.7, C2H6: 3.0, CH4: 2.0, CO: 1.75, CO2: 3.6, H2: 2.0,
    H2O: 12.0
```

```
- equation: C2H2 + O <=> HCCO + H  # Reaction 154
  rate-constant: A: 8.1e+06, b: 2.0, Ea: 1900.1
- equation: C2H2 + O <=> TXCH2 + CO  # Reaction 155
  rate-constant: A: 1.25e+07, b: 2.0, Ea: 1900.1
- equation: C2H + OH <=> C2H2 + O  # Reaction 156
  rate-constant: A: 1.81e+13, b: 0.0, Ea: 0.0
- equation: C2H2 + OH <=> C2H + H2O  # Reaction 157
  rate-constant: A: 2.63e+06, b: 2.14, Ea: 1.706023e+04
- equation: C2H2 + OH <=> HCCOH + H  # Reaction 158
  rate-constant: A: 2.41e+06, b: 2.0, Ea: 1.271272e+04
- equation: C2H2 + OH <=> CH2CO + H  # Reaction 159
  rate-constant: A: 7.53e+06, b: 1.55, Ea: 2105.64
- equation: C2H2 + OH <=> CH3 + CO  # Reaction 160
  rate-constant: A: 1.28e+09, b: 0.73, Ea: 2578.87
- equation: CH2CO + H <=> HCCO + H2  # Reaction 161
  rate-constant: A: 5.0e+13, b: 0.0, Ea: 7999.52
- equation: CH2CO + H <=> CH3 + CO  # Reaction 162
  rate-constant: A: 1.5e+09, b: 1.38, Ea: 614.24
- equation: CH2CO + O <=> HCCO + OH  # Reaction 163
  rate-constant: A: 1.0e+13, b: 0.0, Ea: 7999.52
- equation: CH2CO + O <=> TXCH2 + CO2  # Reaction 164
  rate-constant: A: 1.75e+12, b: 0.0, Ea: 1350.38
- equation: CH2CO + OH <=> HCCO + H2O  # Reaction 165
  rate-constant: A: 7.5e+12, b: 0.0, Ea: 2000.48
- equation: HCCOH + H <=> CH2CO + H  # Reaction 166
  rate-constant: A: 1.0e+13, b: 0.0, Ea: 0.0
- equation: C2H3 + H (+ M) <=> C2H4 (+ M)  # Reaction 167
  type: falloff
  low-P-rate-constant: A: 1.4e+30, b: -3.86, Ea: 3319.79
  high-P-rate-constant: A: 6.08e+12, b: 0.27, Ea: 279.64
  Troe: A: 0.782, T3: 207.5, T1: 2663.0, T2: 6095.0
  efficiencies: AR: 0.7, C2H6: 3.0, CH4: 2.0, CO: 1.75, CO2: 3.6, H2: 2.0,
    H2O: 12.0
```

```
- equation: C2H3 + H <=> C2H2 + H2  # Reaction 168
  rate-constant: A: 3.0e+13, b: 0.0, Ea: 0.0
- equation: C2H3 + O <=> CH2CHO  # Reaction 169
  rate-constant: A: 1.03e+13, b: 0.21, Ea: -427.82
- equation: C2H3 + OH <=> C2H2 + H2O  # Reaction 170
  rate-constant: A: 5.0e+12, b: 0.0, Ea: 0.0
- equation: C2H3 + O2 <=> C2H2 + HO2  # Reaction 171
  rate-constant: A: 1.34e+06, b: 1.61, Ea: -384.8
- equation: C2H3 + O2 <=> CH2CHO + O  # Reaction 172
  rate-constant: A: 3.03e+11, b: 0.29, Ea: 11.95
- equation: C2H3 + O2 <=> HCO + CH2O  # Reaction 173
  rate-constant: A: 4.58e+16, b: -1.39, Ea: 1015.77
- equation: CH2CHO <=> CH2CO + H  # Reaction 174
  rate-constant: A: 1.32e+34, b: -6.57, Ea: 4.945746e+04
- equation: CH2CHO <=> CH3 + CO  # Reaction 175
  rate-constant: A: 6.51e+34, b: -6.87, Ea: 4.719407e+04
- equation: CH2CHO + O <=> CH2O + HCO  # Reaction 176
  rate-constant: A: 3.17e+13, b: 0.03, Ea: -394.36
- equation: CH2CHO + O2 => OH + CO + CH2O  # Reaction 177
  rate-constant: A: 1.81e+10, b: 0.0, Ea: 0.0
- equation: CH2CHO + O2 => OH + 2 HCO  # Reaction 178
  rate-constant: A: 2.35e+10, b: 0.0, Ea: 0.0
- equation: CH2CHO + H <=> CH3 + HCO  # Reaction 179
  rate-constant: A: 2.2e+13, b: 0.0, Ea: 0.0
- equation: CH2CHO + H <=> CH2CO + H2  # Reaction 180
  rate-constant: A: 1.1e+13, b: 0.0, Ea: 0.0
- equation: CH2CHO + OH <=> H2O + CH2CO  # Reaction 181
  rate-constant: A: 1.2e+13, b: 0.0, Ea: 0.0
- equation: CH2CHO + OH <=> HCO + CH2OH  # Reaction 182
  rate-constant: A: 3.01e+13, b: 0.0, Ea: 0.0
- equation: CH3 + HCO <=> CH3CHO  # Reaction 183
  rate-constant: A: 5.0e+13, b: 0.0, Ea: 0.0
- equation: CH3CHO + O <=> CH2CHO + OH  # Reaction 184
```

```
  rate-constant: A: 2.92e+12, b: 0.0, Ea: 1809.27
- equation: CH3CHO + H <=> CH2CHO + H2  # Reaction 185
  rate-constant: A: 2.05e+09, b: 1.16, Ea: 2404.4
- equation: CH3CHO + H => CH3 + CO + H2  # Reaction 186
  rate-constant: A: 2.05e+09, b: 1.16, Ea: 2404.4
- equation: CH3CHO + O => CH3 + CO + OH  # Reaction 187
  rate-constant: A: 2.92e+12, b: 0.0, Ea: 1809.27
- equation: CH3CHO + O2 => CH3 + CO + HO2  # Reaction 188
  rate-constant: A: 3.01e+13, b: 0.0, Ea: 3.914914e+04
- equation: CH3CHO + OH => CH3 + CO + H2O  # Reaction 189
  rate-constant: A: 2.34e+10, b: 0.73, Ea: -1113.77
- equation: CH3CHO + HO2 => CH3 + CO + H2O2  # Reaction 190
  rate-constant: A: 3.01e+12, b: 0.0, Ea: 1.1924e+04
- equation: CH3CHO + CH3 => CH3 + CO + CH4  # Reaction 191
  rate-constant: A: 2.72e+06, b: 1.77, Ea: 5920.17
- equation: C2H4 (+ M) <=> H2C2 + H2 (+ M)  # Reaction 192
  type: falloff
  low-P-rate-constant: A: 7.0e+50, b: -9.31, Ea: 9.989962e+04
  high-P-rate-constant: A: 8.0e+12, b: 0.44, Ea: 8.880019e+04
  Troe: A: 0.735, T3: 180.0, T1: 1035.0, T2: 5417.0
  efficiencies: AR: 0.7, C2H6: 3.0, CH4: 2.0, CO: 1.75, CO2: 3.6, H2: 2.0,
    H2O: 6.0
- equation: C2H4 + H (+ M) <=> C2H5 (+ M)  # Reaction 193
  type: falloff
  low-P-rate-constant: A: 2.03e+39, b: -6.64, Ea: 5769.6
  high-P-rate-constant: A: 1.37e+09, b: 1.46, Ea: 1355.16
  Troe: A: -0.569, T3: 299.0, T1: -9147.0, T2: 152.4
  efficiencies: AR: 0.7, C2H6: 3.0, CH4: 2.0, CO: 1.75, CO2: 3.6, H2: 2.0,
    H2O: 12.0
- equation: C2H4 + H <=> C2H3 + H2  # Reaction 194
  rate-constant: A: 1.27e+05, b: 2.75, Ea: 1.164914e+04
- equation: C2H4 + O <=> CH2CHO + H  # Reaction 195
  rate-constant: A: 7.66e+09, b: 0.88, Ea: 1140.06
```

```
- equation: C2H4 + O <=> TXCH2 + CH2O  # Reaction 196
  rate-constant: A: 7.15e+04, b: 2.47, Ea: 929.73
- equation: C2H4 + O <=> CH3 + HCO  # Reaction 197
  rate-constant: A: 3.89e+08, b: 1.36, Ea: 886.71
- equation: C2H4 + OH <=> C2H3 + H2O  # Reaction 198
  rate-constant: A: 0.131, b: 4.2, Ea: -860.42
- equation: C2H4 + OH <=> C2H5O  # Reaction 199
  rate-constant: A: 3.75e+36, b: -7.8, Ea: 7060.23
- equation: C2H4 + CH3 <=> C2H3 + CH4  # Reaction 200
  rate-constant: A: 2.27e+05, b: 2.0, Ea: 9199.33
- equation: C2H4 + CH3 (+ M) <=> NXC3H7 (+ M)  # Reaction 201
  type: falloff
  low-P-rate-constant: A: 3.0e+63, b: -14.6, Ea: 1.816922e+04
  high-P-rate-constant: A: 2.55e+06, b: 1.6, Ea: 5700.29
  Troe: A: 0.1894, T3: 277.0, T1: 8748.0, T2: 7891.0
  efficiencies: AR: 0.7, C2H6: 3.0, CH4: 2.0, CO: 1.75, CO2: 3.6, H2: 2.0,
    H2O: 12.0
- equation: C2H5 + H (+ M) <=> C2H6 (+ M)  # Reaction 202
  type: falloff
  low-P-rate-constant: A: 1.99e+41, b: -7.08, Ea: 6684.99
  high-P-rate-constant: A: 5.21e+17, b: -0.99, Ea: 1579.83
  Troe: A: 0.8422, T3: 125.0, T1: 2219.0, T2: 6882.0
  efficiencies: AR: 0.7, C2H6: 3.0, CH4: 2.0, CO: 1.75, CO2: 3.6, H2: 2.0,
    H2O: 12.0
- equation: C2H5 + H <=> C2H4 + H2  # Reaction 203
  rate-constant: A: 2.0e+12, b: 0.0, Ea: 0.0
- equation: C2H5 + CH3 <=> C2H4 + CH4  # Reaction 204
  rate-constant: A: 1.18e+04, b: 2.45, Ea: 2920.65
- equation: C2H5 + O <=> C2H5O  # Reaction 205
  rate-constant: A: 3.17e+13, b: 0.03, Ea: -394.36
- equation: C2H5O <=> CH3 + CH2O  # Reaction 206
  rate-constant: A: 1.32e+20, b: -2.02, Ea: 2.075048e+04
- equation: C2H5O <=> CH3CHO + H  # Reaction 207
```

```
  rate-constant: A: 5.45e+15, b: -0.69, Ea: 2.222992e+04
- equation: C2H5O + O2 <=> CH3CHO + HO2  # Reaction 208
  rate-constant: A: 2.29e+10, b: 0.0, Ea: 874.76
- equation: C2H5 + O2 <=> C2H4 + HO2  # Reaction 209
  rate-constant: A: 1.92e+07, b: 1.02, Ea: -2033.94
- equation: C3H8 (+ M) <=> C2H5 + CH3 (+ M)  # Reaction 210
  type: falloff
  low-P-rate-constant: A: 5.64e+74, b: -15.74, Ea: 9.871893e+04
  high-P-rate-constant: A: 1.29e+37, b: -5.84, Ea: 9.738767e+04
  Troe: A: 0.31, T3: 50.0, T1: 3000.0, T2: 9000.0
  efficiencies: AR: 0.7, C2H6: 3.0, CH4: 2.0, CO: 1.75, CO2: 3.6, H2: 2.0,
    H2O: 12.0
- equation: C2H6 (+ M) <=> 2 CH3 (+ M)  # Reaction 211
  type: falloff
  low-P-rate-constant: A: 3.72e+65, b: -13.14, Ea: 1.0157983e+05
  high-P-rate-constant: A: 1.88e+50, b: -9.72, Ea: 1.0734226e+05
  Troe: A: 0.39, T3: 100.0, T1: 1900.0, T2: 6000.0
  efficiencies: AR: 0.7, C2H6: 3.0, CH4: 2.0, CO: 1.75, CO2: 3.6, H2: 2.0,
    H2O: 12.0
- equation: C2H6 + H <=> C2H5 + H2  # Reaction 212
  rate-constant: A: 1.7e+05, b: 2.7, Ea: 5740.92
- equation: C2H6 + O <=> C2H5 + OH  # Reaction 213
  rate-constant: A: 31.7, b: 3.8, Ea: 3130.98
- equation: C2H6 + OH <=> C2H5 + H2O  # Reaction 214
  rate-constant: A: 1.61e+06, b: 2.22, Ea: 740.92
- equation: C2H6 + SXCH2 <=> C2H5 + CH3  # Reaction 215
  rate-constant: A: 4.0e+13, b: 0.0, Ea: -549.71
- equation: C2H6 + CH3 <=> C2H5 + CH4  # Reaction 216
  rate-constant: A: 8.43e+14, b: 0.0, Ea: 2.225621e+04
- equation: NXC3H7 + O <=> C2H5 + CH2O  # Reaction 217
  rate-constant: A: 3.17e+13, b: 0.03, Ea: -394.36
- equation: NXC3H7 + H (+ M) <=> C3H8 (+ M)  # Reaction 218
  type: falloff
```

```
  low-P-rate-constant: A: 4.42e+61, b: -13.55, Ea: 1.135755e+04
  high-P-rate-constant: A: 3.61e+13, b: 0.0, Ea: 0.0
  Troe: A: 0.315, T3: 369.0, T1: 3285.0, T2: 6667.0
  efficiencies: AR: 0.7, C2H6: 3.0, CH4: 2.0, CO: 1.75, CO2: 3.6, H2: 2.0,
    H2O: 12.0
- equation: NXC3H7 + OH <=> C3H6 + H2O  # Reaction 219
  rate-constant: A: 2.41e+13, b: 0.0, Ea: 0.0
- equation: NXC3H7 + CH3 <=> C3H6 + CH4  # Reaction 220
  rate-constant: A: 3.31e+12, b: 0.0, Ea: -769.6
- equation: C3H6 + H (+ M) <=> NXC3H7 (+ M)  # Reaction 221
  type: falloff
  low-P-rate-constant: A: 6.26e+38, b: -6.66, Ea: 7000.48
  high-P-rate-constant: A: 3.06e+14, b: -0.37, Ea: 4032.03
  Troe: A: 1.0, T3: 1000.0, T1: 1310.0, T2: 4.8097e+04
  efficiencies: AR: 0.7, C2H6: 3.0, CH4: 2.0, CO: 1.75, CO2: 3.6, H2: 2.0,
    H2O: 12.0
- equation: NXC3H7 + O2 <=> C3H6 + HO2  # Reaction 222
  rate-constant: A: 3.7e+16, b: -1.63, Ea: 3417.78
- equation: C3H8 + H <=> NXC3H7 + H2  # Reaction 223
  rate-constant: A: 0.058, b: 4.71, Ea: 6211.76
- equation: C3H8 + O <=> NXC3H7 + OH  # Reaction 224
  rate-constant: A: 2.35, b: 4.09, Ea: 2545.41
- equation: C3H8 + OH <=> NXC3H7 + H2O  # Reaction 225
  rate-constant: A: 5.36e+06, b: 2.01, Ea: 365.68
- equation: C3H8 + CH3 <=> NXC3H7 + CH4  # Reaction 226
  rate-constant: A: 0.903, b: 3.65, Ea: 7153.44
- equation: C3H8 + HO2 <=> NXC3H7 + H2O2  # Reaction 227
  rate-constant: A: 9640.0, b: 2.6, Ea: 1.391013e+04
- equation: C2H2 + M <=> H2C2 + M  # Reaction 228
  type: three-body
  rate-constant: A: 2.45e+15, b: -0.64, Ea: 4.969885e+04
  efficiencies: AR: 0.7, C2H6: 3.0, CH4: 2.0, CO: 1.75, CO2: 3.6, H2: 2.0,
    H2O: 6.0
```

```
- equation: H2C2 + O2 <=> TXCH2 + CO2  # Reaction 229
  rate-constant: A: 3.3e+12, b: 0.0, Ea: 0.0
- equation: H2C2 + O2 <=> 2 HCO  # Reaction 230
  rate-constant: A: 1.0e+13, b: 0.0, Ea: 0.0
- equation: C2H2 + SXCH2 <=> C3H3 + H  # Reaction 231
  rate-constant: A: 1.9e+14, b: 0.0, Ea: 0.0
- equation: C2H2 + CH3 <=> PXC3H4 + H  # Reaction 232
  rate-constant: A: 2.56e+09, b: 1.1, Ea: 1.364388e+04
- equation: AXC3H4 + H <=> C2H2 + CH3  # Reaction 233
  rate-constant: A: 8.95e+13, b: -0.02, Ea: 1.125e+04
- equation: C2H2 + CH3 <=> SXC3H5  # Reaction 234
  rate-constant: A: 7.45e+43, b: -10.13, Ea: 1.852294e+04
- equation: C2H2 + C2H <=> NXC4H3  # Reaction 235
  rate-constant: A: 7.8e+13, b: 0.0, Ea: 0.0
- equation: C2H2 + HCCO <=> C3H3 + CO  # Reaction 236
  rate-constant: A: 1.0e+11, b: 0.0, Ea: 2999.52
- equation: C2H3 + H2O2 <=> C2H4 + HO2  # Reaction 237
  rate-constant: A: 1.21e+10, b: 0.0, Ea: -595.12
- equation: C2H3 + HCO <=> C2H4 + CO  # Reaction 238
  rate-constant: A: 9.0e+13, b: 0.0, Ea: 0.0
- equation: C2H3 + HCO <=> C2H3CHO  # Reaction 239
  rate-constant: A: 1.8e+13, b: 0.0, Ea: 0.0
- equation: C2H3 + CH3 <=> C2H2 + CH4  # Reaction 240
  rate-constant: A: 9.03e+12, b: 0.0, Ea: -764.82
- equation: C3H6 <=> C2H3 + CH3  # Reaction 241
  rate-constant: A: 4.04e+42, b: -7.67, Ea: 1.1183078e+05
- equation: C2H3 + CH3 <=> AXC3H5 + H  # Reaction 242
  rate-constant: A: 1.93e+18, b: -1.25, Ea: 7669.69
- equation: AXC3H5 + H <=> C3H6  # Reaction 243
  rate-constant: A: 5.93e+54, b: -11.76, Ea: 2.354924e+04
- equation: C2H + CH3 <=> C3H3 + H  # Reaction 244
  rate-constant: A: 2.41e+13, b: 0.0, Ea: 0.0
- equation: C2O + H <=> CH + CO  # Reaction 245
```

```
  rate-constant: A: 5.0e+13, b: 0.0, Ea: 0.0
- equation: C2O + O <=> 2 CO  # Reaction 246
  rate-constant: A: 5.0e+13, b: 0.0, Ea: 0.0
- equation: C2O + OH <=> H + 2 CO  # Reaction 247
  rate-constant: A: 2.0e+13, b: 0.0, Ea: 0.0
- equation: C2O + O2 <=> O + 2 CO  # Reaction 248
  rate-constant: A: 2.0e+13, b: 0.0, Ea: 0.0
- equation: HCCO + CH3 <=> C2H4 + CO  # Reaction 249
  rate-constant: A: 5.0e+13, b: 0.0, Ea: 0.0
- equation: HCCO + OH <=> C2O + H2O  # Reaction 250
  rate-constant: A: 3.0e+13, b: 0.0, Ea: 0.0
- equation: HCCO + OH <=> 2 HCO  # Reaction 251
  rate-constant: A: 1.0e+13, b: 0.0, Ea: 0.0
- equation: CH2CO + OH <=> CH2OH + CO  # Reaction 252
  rate-constant: A: 5.0e+12, b: 0.0, Ea: 0.0
- equation: CH2CO + TXCH2 <=> C2H4 + CO  # Reaction 253
  rate-constant: A: 1.0e+12, b: 0.0, Ea: 0.0
- equation: CH2CO + TXCH2 <=> HCCO + CH3  # Reaction 254
  rate-constant: A: 3.6e+13, b: 0.0, Ea: 1.099904e+04
- equation: CH2CO + CH3 <=> C2H5 + CO  # Reaction 255
  rate-constant: A: 9.0e+10, b: 0.0, Ea: 0.0
- equation: CH2CO + CH3 <=> HCCO + CH4  # Reaction 256
  rate-constant: A: 7.5e+12, b: 0.0, Ea: 1.299952e+04
- equation: CH2CHO + CH3 <=> C2H5 + HCO  # Reaction 257
  rate-constant: A: 4.9e+14, b: -0.5, Ea: 0.0
- equation: C2H4 + C2H <=> C4H4 + H  # Reaction 258
  rate-constant: A: 1.2e+13, b: 0.0, Ea: 0.0
- equation: C2H4 + O2 <=> C2H3 + HO2  # Reaction 259
  rate-constant: A: 4.22e+13, b: 0.0, Ea: 6.210086e+04
- equation: C2H4 + O2 => CH3 + CO2 + H  # Reaction 260
  rate-constant: A: 4.9e+12, b: 0.42, Ea: 7.580067e+04
- equation: CH3OCO => CH3 + CO2  # Reaction 261
  rate-constant: A: 3.59e+14, b: -0.172, Ea: 1.601004e+04
```

```
- equation: CH3 + CO2 => CH3OCO  # Reaction 262
  rate-constant: A: 4.76e+07, b: 1.54, Ea: 3.470005e+04
- equation: CH3OCO => CH3O + CO  # Reaction 263
  rate-constant: A: 1.431e+15, b: -0.041, Ea: 2.377008e+04
- equation: CH3O + CO => CH3OCO  # Reaction 264
  rate-constant: A: 1.55e+06, b: 2.02, Ea: 5729.92
- equation: C2H5 + HCO <=> C2H6 + CO  # Reaction 265
  rate-constant: A: 1.2e+14, b: 0.0, Ea: 0.0
- equation: C2H5 + HO2 <=> C2H6 + O2  # Reaction 266
  rate-constant: A: 3.0e+11, b: 0.0, Ea: 0.0
- equation: C2H5 + HO2 <=> C2H4 + H2O2  # Reaction 267
  rate-constant: A: 3.0e+11, b: 0.0, Ea: 0.0
- equation: C2H5 + HO2 <=> C2H5O + OH  # Reaction 268
  rate-constant: A: 3.1e+13, b: 0.0, Ea: 0.0
- equation: C2H6 + HO2 <=> C2H5 + H2O2  # Reaction 269
  rate-constant: A: 261.0, b: 3.37, Ea: 1.5913e+04
- equation: C3H2 + O <=> C3H2O  # Reaction 270
  rate-constant: A: 1.36e+14, b: 0.0, Ea: 0.0
- equation: C3H2 + OH <=> C2H2 + HCO  # Reaction 271
  rate-constant: A: 1.0e+13, b: 0.0, Ea: 0.0
- equation: C3H2 + O2 <=> HCCO + CO + H  # Reaction 272
  rate-constant: A: 1.25e+11, b: 0.0, Ea: 999.04
- equation: C3H2 + CH <=> C4H2 + H  # Reaction 273
  rate-constant: A: 5.0e+13, b: 0.0, Ea: 0.0
- equation: C3H2 + TXCH2 <=> NXC4H3 + H  # Reaction 274
  rate-constant: A: 5.0e+13, b: 0.0, Ea: 0.0
- equation: C3H2 + CH3 <=> C4H4 + H  # Reaction 275
  rate-constant: A: 5.0e+12, b: 0.0, Ea: 0.0
- equation: C3H2 + HCCO <=> NXC4H3 + CO  # Reaction 276
  rate-constant: A: 1.0e+13, b: 0.0, Ea: 0.0
- equation: C2H + HCO <=> C3H2O  # Reaction 277
  rate-constant: A: 5.0e+13, b: 0.0, Ea: 0.0
- equation: C3H2O + H <=> C2H2 + HCO  # Reaction 278
```

```
  rate-constant: A: 3.46e+12, b: 0.44, Ea: 5463.67
- equation: C3H2O + H => C2H + CO + H2  # Reaction 279
  rate-constant: A: 2.05e+09, b: 1.16, Ea: 2404.4
- equation: C3H2O + O => C2H + CO + OH  # Reaction 280
  rate-constant: A: 2.92e+12, b: 0.0, Ea: 1809.27
- equation: C3H2O + O2 => C2H + CO + HO2  # Reaction 281
  rate-constant: A: 3.01e+13, b: 0.0, Ea: 3.914914e+04
- equation: C3H2O + OH => C2H + CO + H2O  # Reaction 282
  rate-constant: A: 2.34e+10, b: 0.73, Ea: -1113.77
- equation: C3H2O + HO2 => C2H + CO + H2O2  # Reaction 283
  rate-constant: A: 3.01e+12, b: 0.0, Ea: 1.1924e+04
- equation: C3H2O + CH3 => C2H + CO + CH4  # Reaction 284
  rate-constant: A: 2.72e+06, b: 1.77, Ea: 5920.17
- equation: C3H2 + H (+ M) <=> C3H3 (+ M)  # Reaction 285
  type: falloff
  low-P-rate-constant: A: 2.8e+30, b: -3.86, Ea: 3319.79
  high-P-rate-constant: A: 1.02e+13, b: 0.27, Ea: 279.64
  Troe: A: 0.782, T3: 207.5, T1: 2663.0, T2: 6095.0
  efficiencies: AR: 0.7, C2H6: 3.0, CH4: 2.0, CO: 1.75, CO2: 3.6, H2: 2.0,
    H2O: 12.0
- equation: C3H3 + H <=> C3H2 + H2  # Reaction 286
  rate-constant: A: 1.1e+10, b: 1.13, Ea: 1.392925e+04
- equation: C3H3 + H <=> PXC3H4  # Reaction 287
  rate-constant: A: 7.94e+29, b: -5.06, Ea: 4861.38
- equation: C3H3 + H <=> AXC3H4  # Reaction 288
  rate-constant: A: 3.16e+29, b: -5.0, Ea: 4710.8
- equation: C3H3 + OH <=> C2H3CHO  # Reaction 289
  rate-constant: A: 7.53e+06, b: 1.55, Ea: 2105.64
- equation: C3H3 + OH <=> C2H4 + CO  # Reaction 290
  rate-constant: A: 1.28e+09, b: 0.73, Ea: 2578.87
- equation: C3H3 + OH <=> C3H2 + H2O  # Reaction 291
  rate-constant: A: 1.13e+05, b: 2.28, Ea: 2466.54
- equation: C3H3 + OH <=> CH2O + C2H2  # Reaction 292
```

```
  rate-constant: A: 1.88e+36, b: -7.8, Ea: 7060.23
- equation: C3H3 + O => CH2O + C2H  # Reaction 293
  rate-constant: A: 2.0e+13, b: 0.0, Ea: 0.0
- equation: C3H3 + O <=> C3H2O + H  # Reaction 294
  rate-constant: A: 1.38e+14, b: 0.0, Ea: 0.0
- equation: C3H3 + O2 <=> CH2CO + HCO  # Reaction 295
  rate-constant: A: 1.7e+05, b: 1.7, Ea: 1500.96
- equation: C3H3 + HO2 <=> OH + CO + C2H3  # Reaction 296
  rate-constant: A: 8.0e+11, b: 0.0, Ea: 0.0
- equation: C3H3 + HO2 <=> AXC3H4 + O2  # Reaction 297
  rate-constant: A: 3.0e+11, b: 0.0, Ea: 0.0
- equation: C3H3 + HO2 <=> PXC3H4 + O2  # Reaction 298
  rate-constant: A: 3.0e+11, b: 0.0, Ea: 0.0
- equation: PXC3H4 + O2 <=> CH3 + HCO + CO  # Reaction 299
  rate-constant: A: 4.0e+14, b: 0.0, Ea: 4.192878e+04
- equation: C3H3 + HCO <=> AXC3H4 + CO  # Reaction 300
  rate-constant: A: 2.5e+13, b: 0.0, Ea: 0.0
- equation: C3H3 + HCO <=> PXC3H4 + CO  # Reaction 301
  rate-constant: A: 2.5e+13, b: 0.0, Ea: 0.0
- equation: C3H3 + CH <=> IXC4H3 + H  # Reaction 302
  rate-constant: A: 5.0e+13, b: 0.0, Ea: 0.0
- equation: C3H3 + TXCH2 <=> C4H4 + H  # Reaction 303
  rate-constant: A: 5.0e+13, b: 0.0, Ea: 0.0
- equation: AXC3H4 <=> PXC3H4  # Reaction 304
  rate-constant: A: 7.76e+39, b: -7.8, Ea: 7.844646e+04
- equation: AXC3H4 + H <=> PXC3H4 + H  # Reaction 305
  rate-constant: A: 2.47e+15, b: -0.33, Ea: 6436.42
- equation: AXC3H4 + H <=> AXC3H5  # Reaction 306
  rate-constant: A: 2.01e+49, b: -10.77, Ea: 1.962237e+04
- equation: AXC3H4 + H <=> TXC3H5  # Reaction 307
  rate-constant: A: 6.7e+42, b: -12.46, Ea: 1.635994e+04
- equation: PXC3H4 + H <=> TXC3H5  # Reaction 308
  rate-constant: A: 8.83e+52, b: -12.36, Ea: 1.644598e+04
```

```
- equation: PXC3H4 + H <=> SXC3H5  # Reaction 309
  rate-constant: A: 1.53e+49, b: -11.97, Ea: 1.414436e+04
- equation: PXC3H4 + H <=> C3H3 + H2  # Reaction 310
  rate-constant: A: 8.5e+04, b: 2.7, Ea: 5740.92
- equation: PXC3H4 + O <=> C3H3 + OH  # Reaction 311
  rate-constant: A: 4.49e+07, b: 1.92, Ea: 5690.73
- equation: PXC3H4 + OH <=> C3H3 + H2O  # Reaction 312
  rate-constant: A: 783.0, b: 3.01, Ea: -1139.82
- equation: PXC3H4 + CH3 <=> C3H3 + CH4  # Reaction 313
  rate-constant: A: 4.22e+14, b: 0.0, Ea: 2.225621e+04
- equation: PXC3H4 + HO2 <=> C3H3 + H2O2  # Reaction 314
  rate-constant: A: 130.0, b: 3.37, Ea: 1.5913e+04
- equation: AXC3H4 + H <=> C3H3 + H2  # Reaction 315
  rate-constant: A: 1.33e+06, b: 2.53, Ea: 1.223948e+04
- equation: AXC3H4 + OH <=> C3H3 + H2O  # Reaction 316
  rate-constant: A: 512.0, b: 3.05, Ea: -2295.89
- equation: AXC3H4 + CH3 <=> C3H3 + CH4  # Reaction 317
  rate-constant: A: 2.27e+05, b: 2.0, Ea: 9199.33
- equation: AXC3H4 + HO2 <=> C3H3 + H2O2  # Reaction 318
  rate-constant: A: 9.76e+10, b: 0.12, Ea: 2.336998e+04
- equation: AXC3H4 + O <=> CH2CO + TXCH2  # Reaction 319
  rate-constant: A: 9.63e+06, b: 2.05, Ea: 179.25
- equation: PXC3H4 + O <=> HCCO + CH3  # Reaction 320
  rate-constant: A: 4.05e+06, b: 2.0, Ea: 1900.1
- equation: PXC3H4 + O <=> C2H4 + CO  # Reaction 321
  rate-constant: A: 6.25e+06, b: 2.0, Ea: 1900.1
- equation: AXC3H4 + C2H <=> C2H2 + C3H3  # Reaction 322
  rate-constant: A: 1.0e+13, b: 0.0, Ea: 0.0
- equation: PXC3H4 + C2H <=> C2H2 + C3H3  # Reaction 323
  rate-constant: A: 1.0e+13, b: 0.0, Ea: 0.0
- equation: PXC3H4 + OH <=> HCCOH + CH3  # Reaction 324
  rate-constant: A: 2.41e+06, b: 2.0, Ea: 1.271272e+04
- equation: PXC3H4 + OH <=> CH2CO + CH3  # Reaction 325
```

```
  rate-constant: A: 7.53e+06, b: 1.55, Ea: 2105.64
- equation: PXC3H4 + OH <=> C2H5 + CO  # Reaction 326
  rate-constant: A: 1.28e+09, b: 0.73, Ea: 2578.87
- equation: C2H3CHO + H => C2H3 + CO + H2  # Reaction 327
  rate-constant: A: 4.09e+09, b: 1.16, Ea: 2404.4
- equation: C2H3CHO + O => C2H3 + CO + OH  # Reaction 328
  rate-constant: A: 5.84e+12, b: 0.0, Ea: 1809.27
- equation: C2H3CHO + OH => C2H3 + CO + H2O  # Reaction 329
  rate-constant: A: 2.89e+08, b: 1.35, Ea: -1572.66
- equation: C2H3CHO + HO2 => C2H3 + CO + H2O2  # Reaction 330
  rate-constant: A: 4.09e+04, b: 2.5, Ea: 1.020315e+04
- equation: C2H3CHO + CH3 => C2H3 + CO + CH4  # Reaction 331
  rate-constant: A: 3.49e-08, b: 6.21, Ea: 1630.02
- equation: AXC3H5 <=> TXC3H5  # Reaction 332
  rate-constant: A: 7.06e+56, b: -14.08, Ea: 7.586759e+04
- equation: AXC3H5 <=> SXC3H5  # Reaction 333
  rate-constant: A: 5.0e+51, b: -13.02, Ea: 7.330067e+04
- equation: TXC3H5 <=> SXC3H5  # Reaction 334
  rate-constant: A: 1.5e+48, b: -12.71, Ea: 5.390057e+04
- equation: AXC3H5 + H <=> AXC3H4 + H2  # Reaction 335
  rate-constant: A: 9560.0, b: 2.8, Ea: 3291.11
- equation: AXC3H5 + OH <=> AXC3H4 + H2O  # Reaction 336
  rate-constant: A: 6.03e+12, b: 0.0, Ea: 0.0
- equation: AXC3H5 + CH3 <=> AXC3H4 + CH4  # Reaction 337
  rate-constant: A: 4.86e+11, b: -0.32, Ea: -131.45
- equation: AXC3H5 + C2H3 <=> AXC3H4 + C2H4  # Reaction 338
  rate-constant: A: 2.41e+12, b: 0.0, Ea: 0.0
- equation: AXC3H5 + C2H5 <=> AXC3H4 + C2H6  # Reaction 339
  rate-constant: A: 9.64e+11, b: 0.0, Ea: -131.45
- equation: 2 AXC3H5 <=> AXC3H4 + C3H6  # Reaction 340
  rate-constant: A: 1.0e+12, b: 0.0, Ea: 0.0
- equation: AXC3H5 + O2 <=> AXC3H4 + HO2  # Reaction 341
  rate-constant: A: 2.06e+04, b: 2.19, Ea: 1.759082e+04
```

```
- equation: AXC3H5 + O2 <=> C2H3CHO + OH  # Reaction 342
  rate-constant: A: 3.36e+05, b: 1.81, Ea: 1.918977e+04
- equation: AXC3H5 + O2 => C2H2 + CH2O + OH  # Reaction 343
  rate-constant: A: 9.71e+20, b: -2.7, Ea: 2.498088e+04
- equation: AXC3H5 + O2 <=> CH2CHO + CH2O  # Reaction 344
  rate-constant: A: 3.08e+09, b: 0.37, Ea: 1.690966e+04
- equation: AXC3H4 + HO2 => CH2CO + TXCH2 + OH  # Reaction 345
  rate-constant: A: 4.0e+12, b: 0.0, Ea: 1.9e+04
- equation: AXC3H5 + O <=> C3H5O  # Reaction 346
  rate-constant: A: 3.17e+13, b: 0.03, Ea: -394.36
- equation: AXC3H5 + OH <=> C2H3CHO + H2  # Reaction 347
  rate-constant: A: 4.2e+32, b: -5.16, Ea: 3.012667e+04
- equation: AXC3H5 + HCO <=> C3H6 + CO  # Reaction 348
  rate-constant: A: 6.0e+13, b: 0.0, Ea: 0.0
- equation: AXC3H5 + HO2 <=> C3H6 + O2  # Reaction 349
  rate-constant: A: 2.66e+12, b: 0.0, Ea: 0.0
- equation: AXC3H5 + HO2 <=> C3H5O + OH  # Reaction 350
  rate-constant: A: 1.06e+16, b: -0.94, Ea: 2523.9
- equation: AXC3H5 + CH3O2 <=> C3H5O + CH3O  # Reaction 351
  rate-constant: A: 7.0e+12, b: 0.0, Ea: -999.04
- equation: TXC3H5 + H <=> PXC3H4 + H2  # Reaction 352
  rate-constant: A: 3.34e+12, b: 0.0, Ea: 0.0
- equation: TXC3H5 + O <=> CH3 + CH2CO  # Reaction 353
  rate-constant: A: 6.0e+13, b: 0.0, Ea: 0.0
- equation: TXC3H5 + OH => CH3 + CH2CO + H  # Reaction 354
  rate-constant: A: 5.0e+12, b: 0.0, Ea: 0.0
- equation: TXC3H5 + HO2 <=> CH3 + CH2CO + OH  # Reaction 355
  rate-constant: A: 2.0e+13, b: 0.0, Ea: 0.0
- equation: TXC3H5 + HCO <=> C3H6 + CO  # Reaction 356
  rate-constant: A: 9.0e+13, b: 0.0, Ea: 0.0
- equation: TXC3H5 + CH3 <=> PXC3H4 + CH4  # Reaction 357
  rate-constant: A: 1.0e+11, b: 0.0, Ea: 0.0
- equation: SXC3H5 + H <=> PXC3H4 + H2  # Reaction 358
```

```
  rate-constant: A: 3.34e+12, b: 0.0, Ea: 0.0
- equation: SXC3H5 + O <=> C2H4 + HCO  # Reaction 359
  rate-constant: A: 6.0e+13, b: 0.0, Ea: 0.0
- equation: SXC3H5 + OH => C2H4 + HCO + H  # Reaction 360
  rate-constant: A: 5.0e+12, b: 0.0, Ea: 0.0
- equation: SXC3H5 + HO2 <=> C2H4 + HCO + OH  # Reaction 361
  rate-constant: A: 2.0e+13, b: 0.0, Ea: 0.0
- equation: SXC3H5 + HCO <=> C3H6 + CO  # Reaction 362
  rate-constant: A: 9.0e+13, b: 0.0, Ea: 0.0
- equation: SXC3H5 + CH3 <=> PXC3H4 + CH4  # Reaction 363
  rate-constant: A: 1.0e+11, b: 0.0, Ea: 0.0
- equation: TXC3H5 + O2 <=> PXC3H4 + HO2  # Reaction 364
  rate-constant: A: 1.34e+06, b: 1.61, Ea: -384.8
- equation: SXC3H5 + O2 <=> PXC3H4 + HO2  # Reaction 365
  rate-constant: A: 6.7e+05, b: 1.61, Ea: -384.8
- equation: TXC3H5 + O2 => CH2CO + CH3 + O  # Reaction 366
  rate-constant: A: 3.03e+11, b: 0.29, Ea: 11.95
- equation: SXC3H5 + O2 => C2H3CHO + H + O  # Reaction 367
  rate-constant: A: 3.03e+11, b: 0.29, Ea: 11.95
- equation: TXC3H5 + O2 => CH3 + CO + CH2O  # Reaction 368
  rate-constant: A: 4.58e+16, b: -1.39, Ea: 1015.77
- equation: SXC3H5 + O2 <=> CH3CHO + HCO  # Reaction 369
  rate-constant: A: 4.58e+16, b: -1.39, Ea: 1015.77
- equation: TXC3H5 + O2 <=> AXC3H4 + HO2  # Reaction 370
  rate-constant: A: 1.92e+07, b: 1.02, Ea: -2033.94
- equation: C3H5O + O2 => C2H3CHO + HO2  # Reaction 371
  rate-constant: A: 1.0e+12, b: 0.0, Ea: 5999.04
- equation: C3H5O <=> C2H3CHO + H  # Reaction 372
  rate-constant: A: 1.0e+14, b: 0.0, Ea: 2.909895e+04
- equation: C3H5O => C2H3 + CH2O  # Reaction 373
  rate-constant: A: 2.03e+12, b: 0.09, Ea: 2.356119e+04
- equation: C3H6 + H <=> C2H4 + CH3  # Reaction 374
  rate-constant: A: 8.0e+21, b: -2.39, Ea: 1.118069e+04
```

```
- equation: C3H6 + O <=> CH2CHO + CH3  # Reaction 375
  rate-constant: A: 1.2e+08, b: 1.6, Ea: 327.44
- equation: C3H6 + O <=> C2H5 + HCO  # Reaction 376
  rate-constant: A: 3.5e+07, b: 1.6, Ea: -972.75
- equation: C3H6 + H <=> AXC3H5 + H2  # Reaction 377
  rate-constant: A: 6.6e+05, b: 2.54, Ea: 6756.69
- equation: C3H6 + O <=> AXC3H5 + OH  # Reaction 378
  rate-constant: A: 9.65e+04, b: 2.68, Ea: 3716.54
- equation: C3H6 + OH <=> AXC3H5 + H2O  # Reaction 379
  rate-constant: A: 2.0e+08, b: 1.46, Ea: 537.76
- equation: C3H6 + HO2 <=> AXC3H5 + H2O2  # Reaction 380
  rate-constant: A: 9600.0, b: 2.6, Ea: 1.391013e+04
- equation: C3H6 + CH3 <=> AXC3H5 + CH4  # Reaction 381
  rate-constant: A: 0.452, b: 3.65, Ea: 7153.44
- equation: C3H6 + H <=> TXC3H5 + H2  # Reaction 382
  rate-constant: A: 4.0e+05, b: 2.5, Ea: 9789.67
- equation: C3H6 + O <=> TXC3H5 + OH  # Reaction 383
  rate-constant: A: 6.0e+10, b: 0.7, Ea: 7629.06
- equation: C3H6 + OH <=> TXC3H5 + H2O  # Reaction 384
  rate-constant: A: 1.1e+06, b: 2.0, Ea: 1450.76
- equation: C3H6 + CH3 <=> TXC3H5 + CH4  # Reaction 385
  rate-constant: A: 0.84, b: 3.5, Ea: 1.166109e+04
- equation: C3H6 + H <=> SXC3H5 + H2  # Reaction 386
  rate-constant: A: 6.65e+05, b: 2.53, Ea: 1.223948e+04
- equation: C3H6 + O <=> SXC3H5 + OH  # Reaction 387
  rate-constant: A: 1.21e+11, b: 0.7, Ea: 8960.33
- equation: C3H6 + OH <=> SXC3H5 + H2O  # Reaction 388
  rate-constant: A: 0.0655, b: 4.2, Ea: -860.42
- equation: C3H6 + CH3 <=> SXC3H5 + CH4  # Reaction 389
  rate-constant: A: 1.14e+05, b: 2.0, Ea: 9199.33
- equation: C4H + O2 <=> C2H + 2 CO  # Reaction 390
  rate-constant: A: 1.0e+13, b: 0.0, Ea: -755.26
- equation: C4H + H <=> C4H2  # Reaction 391
```

```
  rate-constant: A: 6.0e+13, b: 0.0, Ea: 0.0
- equation: C4H2 + H <=> C4H + H2  # Reaction 392
  rate-constant: A: 3.2e+09, b: 1.8, Ea: 3.010755e+04
- equation: C4H2 + H2 <=> C4H4  # Reaction 393
  rate-constant: A: 4.0e+14, b: 0.0, Ea: 5.390057e+04
- equation: 2 C4H2 => C8H2 + 2 H  # Reaction 394
  rate-constant: A: 1.51e+14, b: 0.0, Ea: 5.599904e+04
- equation: 2 C4H2 <=> C8H2 + H2  # Reaction 395
  rate-constant: A: 1.51e+13, b: 0.0, Ea: 4.270076e+04
- equation: C4H2 + O2 <=> 2 HCCO  # Reaction 396
  rate-constant: A: 9.56e+12, b: 0.0, Ea: 3.109943e+04
- equation: C4H2 + O <=> C3H2 + CO  # Reaction 397
  rate-constant: A: 2.06e+07, b: 2.0, Ea: 1900.1
- equation: C4H2 + H (+ M) <=> IXC4H3 (+ M)  # Reaction 398
  type: falloff
  low-P-rate-constant: A: 2.3e+45, b: -8.1, Ea: 2507.17
  high-P-rate-constant: A: 4.31e+10, b: 1.16, Ea: 1751.91
  Troe: A: 0.0748, T3: 1.0, T1: -4216.0
  efficiencies: AR: 0.7, C2H6: 3.0, CH4: 2.0, CO: 1.75, CO2: 3.6, H2: 2.0,
    H2O: 12.0
- equation: C4H2 + H <=> NXC4H3  # Reaction 399
  rate-constant: A: 1.37e+39, b: -7.87, Ea: 1.544216e+04
- equation: C4H2 + OH <=> C4H + H2O  # Reaction 400
  rate-constant: A: 9.15e+09, b: 1.03, Ea: 2.174713e+04
- equation: C4H2 + OH <=> C3H3 + CO  # Reaction 401
  rate-constant: A: 3.3e+12, b: -0.25, Ea: 2375.72
- equation: NXC4H3 <=> IXC4H3  # Reaction 402
  rate-constant: A: 4.1e+43, b: -9.5, Ea: 5.299952e+04
- equation: NXC4H3 + H <=> IXC4H3 + H  # Reaction 403
  rate-constant: A: 2.5e+20, b: -1.67, Ea: 1.080067e+04
- equation: NXC4H3 + H <=> C4H4  # Reaction 404
  rate-constant: A: 2.0e+47, b: -10.26, Ea: 1.306883e+04
- equation: IXC4H3 + H <=> C4H4  # Reaction 405
```

```
  rate-constant: A: 3.4e+43, b: -9.01, Ea: 1.211998e+04
- equation: NXC4H3 + H <=> 2 C2H2  # Reaction 406
  rate-constant: A: 6.3e+25, b: -3.34, Ea: 1.000956e+04
- equation: IXC4H3 + H <=> 2 C2H2  # Reaction 407
  rate-constant: A: 2.8e+23, b: -2.55, Ea: 1.077916e+04
- equation: NXC4H3 + H <=> C4H2 + H2  # Reaction 408
  rate-constant: A: 1.5e+13, b: 0.0, Ea: 0.0
- equation: IXC4H3 + H <=> C4H2 + H2  # Reaction 409
  rate-constant: A: 3.0e+13, b: 0.0, Ea: 0.0
- equation: NXC4H3 + OH <=> C4H2 + H2O  # Reaction 410
  rate-constant: A: 2.5e+12, b: 0.0, Ea: 0.0
- equation: IXC4H3 + OH <=> C4H2 + H2O  # Reaction 411
  rate-constant: A: 5.0e+12, b: 0.0, Ea: 0.0
- equation: NXC4H3 + O2 <=> C4H2 + HO2  # Reaction 412
  rate-constant: A: 6.7e+05, b: 1.61, Ea: -384.8
- equation: IXC4H3 + O2 <=> C4H2 + HO2  # Reaction 413
  rate-constant: A: 1.34e+06, b: 1.61, Ea: -384.8
- equation: IXC4H3 + O <=> CH2CO + C2H  # Reaction 414
  rate-constant: A: 2.0e+13, b: 0.0, Ea: 0.0
- equation: IXC4H3 + O2 <=> HCCO + CH2CO  # Reaction 415
  rate-constant: A: 1.63e+11, b: 0.0, Ea: -1799.71
- equation: IXC4H3 + O2 <=> HCO + C2H2 + CO  # Reaction 416
  rate-constant: A: 1.7e+05, b: 1.7, Ea: 1500.96
- equation: C4H4 + H <=> NXC4H3 + H2  # Reaction 417
  rate-constant: A: 1.27e+05, b: 2.75, Ea: 1.164914e+04
- equation: C4H4 + H <=> IXC4H3 + H2  # Reaction 418
  rate-constant: A: 6.35e+04, b: 2.75, Ea: 1.164914e+04
- equation: C4H4 + OH <=> NXC4H3 + H2O  # Reaction 419
  rate-constant: A: 0.0655, b: 4.2, Ea: -860.42
- equation: C4H4 + OH <=> IXC4H3 + H2O  # Reaction 420
  rate-constant: A: 0.0328, b: 4.2, Ea: -860.42
- equation: C4H4 + CH3 <=> NXC4H3 + CH4  # Reaction 421
  rate-constant: A: 1.14e+05, b: 2.0, Ea: 9199.33
```

```
- equation: C4H4 + CH3 <=> IXC4H3 + CH4  # Reaction 422
  rate-constant: A: 5.68e+04, b: 2.0, Ea: 9199.33
- equation: C4H4 + O <=> AXC3H4 + CO  # Reaction 423
  rate-constant: A: 6.25e+06, b: 2.0, Ea: 1900.1
- equation: C4H4 + O <=> C3H2 + CH2O  # Reaction 424
  rate-constant: A: 3.58e+04, b: 2.47, Ea: 929.73
- equation: C4H4 + O <=> C3H3 + HCO  # Reaction 425
  rate-constant: A: 1.95e+08, b: 1.36, Ea: 886.71
- equation: C4H2 + C2H <=> C6H2 + H  # Reaction 426
  rate-constant: A: 7.8e+13, b: 0.0, Ea: 0.0
- equation: C2H2 + C4H <=> C6H2 + H  # Reaction 427
  rate-constant: A: 7.8e+13, b: 0.0, Ea: 0.0
- equation: C6H2 + C2H <=> C8H2 + H  # Reaction 428
  rate-constant: A: 7.8e+13, b: 0.0, Ea: 0.0
- equation: C4H2 + C4H <=> C8H2 + H  # Reaction 429
  rate-constant: A: 7.8e+13, b: 0.0, Ea: 0.0
- equation: H2C2 + C2H4 <=> C4H6  # Reaction 430
  rate-constant: A: 1.0e+12, b: 0.0, Ea: 0.0
- equation: H2C2 + C2H2 <=> C4H4  # Reaction 431
  rate-constant: A: 1.9e+14, b: 0.0, Ea: 0.0
- equation: C2H3 + C2H2 <=> NXC4H5  # Reaction 432
  rate-constant: A: 1.32e+12, b: 0.16, Ea: 8312.62
- equation: 2 C2H3 <=> C4H6  # Reaction 433
  rate-constant: A: 8.43e+13, b: 0.0, Ea: 0.0
- equation: 2 C2H3 <=> IXC4H5 + H  # Reaction 434
  rate-constant: A: 1.2e+22, b: -2.44, Ea: 1.36544e+04
- equation: 2 C2H3 <=> NXC4H5 + H  # Reaction 435
  rate-constant: A: 2.4e+20, b: -2.04, Ea: 1.536329e+04
- equation: 2 C2H3 <=> C2H2 + C2H4  # Reaction 436
  rate-constant: A: 9.6e+11, b: 0.0, Ea: 0.0
- equation: C3H3 + CH3 (+ M) <=> C4H6 (+ M)  # Reaction 437
  type: falloff
  low-P-rate-constant: A: 2.6e+57, b: -11.94, Ea: 9772.94
```

```
  high-P-rate-constant: A: 1.5e+12, b: 0.0, Ea: 0.0
  Troe: A: 0.175, T3: 1340.6, T1: 6.0e+04, T2: 9769.8
  efficiencies: AR: 0.7, C2H6: 3.0, CH4: 2.0, CO: 1.75, CO2: 3.6, H2: 2.0,
    H2O: 12.0
- equation: C3H6 + C2H3 <=> C4H6 + CH3  # Reaction 438
  rate-constant: A: 7.23e+11, b: 0.0, Ea: 5000.0
- equation: C4H6 <=> IXC4H5 + H  # Reaction 439
  rate-constant: A: 5.7e+36, b: -6.27, Ea: 1.1235421e+05
- equation: C4H6 <=> NXC4H5 + H  # Reaction 440
  rate-constant: A: 5.3e+44, b: -8.62, Ea: 1.2360899e+05
- equation: C4H6 <=> C4H4 + H2  # Reaction 441
  rate-constant: A: 2.5e+15, b: 0.0, Ea: 9.469885e+04
- equation: PXC3H4 + CH3 <=> C4H6 + H  # Reaction 442
  rate-constant: A: 8.94e+07, b: 1.14, Ea: 1.23805e+04
- equation: AXC3H4 + CH3 <=> C4H6 + H  # Reaction 443
  rate-constant: A: 2.83e+08, b: 1.06, Ea: 1.116157e+04
- equation: C4H6 + H <=> NXC4H5 + H2  # Reaction 444
  rate-constant: A: 1.33e+06, b: 2.53, Ea: 1.223948e+04
- equation: C4H6 + H <=> IXC4H5 + H2  # Reaction 445
  rate-constant: A: 6.65e+05, b: 2.53, Ea: 9239.96
- equation: NXC4H5 + OH <=> C4H6 + O  # Reaction 446
  rate-constant: A: 2.2e+11, b: 0.0, Ea: 0.0
- equation: C4H6 + O <=> IXC4H5 + OH  # Reaction 447
  rate-constant: A: 7.5e+06, b: 1.9, Ea: 3740.44
- equation: C4H6 + OH <=> NXC4H5 + H2O  # Reaction 448
  rate-constant: A: 6.2e+06, b: 2.0, Ea: 3429.73
- equation: C4H6 + OH <=> IXC4H5 + H2O  # Reaction 449
  rate-constant: A: 3.1e+06, b: 2.0, Ea: 430.21
- equation: C4H6 + CH3 <=> NXC4H5 + CH4  # Reaction 450
  rate-constant: A: 2.0e+14, b: 0.0, Ea: 2.283461e+04
- equation: C4H6 + CH3 <=> IXC4H5 + CH4  # Reaction 451
  rate-constant: A: 1.0e+14, b: 0.0, Ea: 1.979924e+04
- equation: C4H6 + C2H3 <=> NXC4H5 + C2H4  # Reaction 452
```

```
  rate-constant: A: 5.0e+13, b: 0.0, Ea: 2.283461e+04
- equation: C4H6 + C2H3 <=> IXC4H5 + C2H4  # Reaction 453
  rate-constant: A: 2.5e+13, b: 0.0, Ea: 1.979924e+04
- equation: C4H6 + O => AXC3H5 + CO + H  # Reaction 454
  rate-constant: A: 7.66e+09, b: 0.88, Ea: 1140.06
- equation: C4H6 + O <=> PXC3H4 + CH2O  # Reaction 455
  rate-constant: A: 7.15e+04, b: 2.47, Ea: 929.73
- equation: C4H6 + O <=> AXC3H5 + HCO  # Reaction 456
  rate-constant: A: 3.89e+08, b: 1.36, Ea: 886.71
- equation: C4H6 + OH <=> AXC3H5 + CH2O  # Reaction 457
  rate-constant: A: 3.75e+36, b: -7.8, Ea: 7060.23
- equation: C4H4 + H <=> NXC4H5  # Reaction 458
  rate-constant: A: 1.3e+51, b: -11.92, Ea: 1.650096e+04
- equation: C4H4 + H <=> IXC4H5  # Reaction 459
  rate-constant: A: 4.9e+51, b: -11.92, Ea: 1.770076e+04
- equation: NXC4H5 <=> IXC4H5  # Reaction 460
  rate-constant: A: 1.5e+67, b: -16.89, Ea: 5.910612e+04
- equation: NXC4H5 + H <=> IXC4H5 + H  # Reaction 461
  rate-constant: A: 3.1e+26, b: -3.35, Ea: 1.742352e+04
- equation: NXC4H5 + H <=> C4H4 + H2  # Reaction 462
  rate-constant: A: 1.5e+13, b: 0.0, Ea: 0.0
- equation: NXC4H5 + OH <=> C4H4 + H2O  # Reaction 463
  rate-constant: A: 2.0e+12, b: 0.0, Ea: 0.0
- equation: NXC4H5 + HCO <=> C4H6 + CO  # Reaction 464
  rate-constant: A: 5.0e+12, b: 0.0, Ea: 0.0
- equation: NXC4H5 + H2O2 <=> C4H6 + HO2  # Reaction 465
  rate-constant: A: 1.21e+10, b: 0.0, Ea: -595.12
- equation: NXC4H5 + HO2 <=> C4H6 + O2  # Reaction 466
  rate-constant: A: 6.0e+11, b: 0.0, Ea: 0.0
- equation: NXC4H5 + O <=> AXC3H5 + CO  # Reaction 467
  rate-constant: A: 1.03e+13, b: 0.21, Ea: -427.82
- equation: NXC4H5 + O2 <=> C4H4 + HO2  # Reaction 468
  rate-constant: A: 1.34e+06, b: 1.61, Ea: -384.8
```

```
- equation: NXC4H5 + O2 => AXC3H5 + CO + O  # Reaction 469
  rate-constant: A: 3.03e+11, b: 0.29, Ea: 11.95
- equation: NXC4H5 + O2 <=> HCO + C2H3CHO  # Reaction 470
  rate-constant: A: 4.58e+16, b: -1.39, Ea: 1015.77
- equation: IXC4H5 + H <=> C4H4 + H2  # Reaction 471
  rate-constant: A: 3.0e+13, b: 0.0, Ea: 0.0
- equation: IXC4H5 + H <=> C3H3 + CH3  # Reaction 472
  rate-constant: A: 2.0e+13, b: 0.0, Ea: 2000.48
- equation: IXC4H5 + OH <=> C4H4 + H2O  # Reaction 473
  rate-constant: A: 4.0e+12, b: 0.0, Ea: 0.0
- equation: IXC4H5 + HCO <=> C4H6 + CO  # Reaction 474
  rate-constant: A: 5.0e+12, b: 0.0, Ea: 0.0
- equation: IXC4H5 + HO2 <=> C4H6 + O2  # Reaction 475
  rate-constant: A: 6.0e+11, b: 0.0, Ea: 0.0
- equation: IXC4H5 + H2O2 <=> C4H6 + HO2  # Reaction 476
  rate-constant: A: 1.21e+10, b: 0.0, Ea: -595.12
- equation: IXC4H5 + O2 <=> CH2CO + CH2CHO  # Reaction 477
  rate-constant: A: 2.16e+10, b: 0.0, Ea: 2500.0
- equation: IXC4H5 + O <=> C3H3 + CH2O  # Reaction 478
  rate-constant: A: 3.17e+13, b: 0.03, Ea: -394.36
- equation: NXC4H5 + C2H3 <=> A1XC6H6 + H2  # Reaction 479
  rate-constant: A: 1.84e-13, b: 7.07, Ea: -3611.38
- equation: C4H6 + O => C2H4 + CH2CO  # Reaction 480
  rate-constant: A: 1.0e+12, b: 0.0, Ea: 0.0
- equation: C4H6 + OH => C2H5 + CH2CO  # Reaction 481
  rate-constant: A: 1.0e+12, b: 0.0, Ea: 0.0
- equation: C4H6 + OH => C2H3 + CH3CHO  # Reaction 482
  rate-constant: A: 1.0e+12, b: 0.0, Ea: 0.0
- equation: C4H7 <=> C4H6 + H  # Reaction 483
  rate-constant: A: 5.01e+31, b: -5.9, Ea: 3.878824e+04
- equation: C2H4 + C2H3 <=> C4H7  # Reaction 484
  rate-constant: A: 1.88e+06, b: 1.84, Ea: 3059.27
- equation: C4H7 + H => C4H6 + H2  # Reaction 485
```

```
  rate-constant: A: 3.16e+13, b: 0.0, Ea: 0.0
- equation: C4H7 + O2 => C4H6 + HO2  # Reaction 486
  rate-constant: A: 1.0e+09, b: 0.0, Ea: 0.0
- equation: C4H7 + CH3 => C4H6 + CH4  # Reaction 487
  rate-constant: A: 8.0e+12, b: 0.0, Ea: 0.0
- equation: C4H7 + C2H5 => C4H6 + C2H6  # Reaction 488
  rate-constant: A: 3.98e+12, b: 0.0, Ea: 0.0
- equation: C4H7 + AXC3H5 => C4H6 + C3H6  # Reaction 489
  rate-constant: A: 6.31e+12, b: 0.0, Ea: 0.0
- equation: C4H7 + HO2 => C4H7O + OH  # Reaction 490
  rate-constant: A: 7.0e+12, b: 0.0, Ea: -999.04
- equation: C4H7 + CH3O2 => C4H7O + CH3O  # Reaction 491
  rate-constant: A: 7.0e+12, b: 0.0, Ea: -999.04
- equation: C4H7O => CH3CHO + C2H3  # Reaction 492
  rate-constant: A: 7.94e+14, b: 0.0, Ea: 1.900096e+04
- equation: C4H7O => C2H3CHO + CH3  # Reaction 493
  rate-constant: A: 7.94e+14, b: 0.0, Ea: 1.900096e+04
- equation: PXC4H8 => AXC3H5 + CH3  # Reaction 494
  rate-constant: A: 5.0e+15, b: 0.0, Ea: 7.099904e+04
- equation: PXC4H8 + H => C4H7 + H2  # Reaction 495
  rate-constant: A: 5.0e+13, b: 0.0, Ea: 3900.57
- equation: PXC4H8 + OH => C4H7 + H2O  # Reaction 496
  rate-constant: A: 2.25e+13, b: 0.0, Ea: 2217.97
- equation: PXC4H8 + O2 => C4H7 + HO2  # Reaction 497
  rate-constant: A: 2.7e+13, b: 0.0, Ea: 3.320029e+04
- equation: PXC4H8 + HO2 => C4H7 + H2O2  # Reaction 498
  rate-constant: A: 1.4e+12, b: 0.0, Ea: 1.489962e+04
- equation: PXC4H8 + CH3 => C4H7 + CH4  # Reaction 499
  rate-constant: A: 1.0e+11, b: 0.0, Ea: 7299.24
- equation: C4H7 + H => PXC4H8  # Reaction 500
  rate-constant: A: 5.0e+13, b: 0.0, Ea: 0.0
- equation: C4H7 + HO2 => PXC4H8 + O2  # Reaction 501
  rate-constant: A: 3.0e+11, b: 0.0, Ea: 0.0
```

```
- equation: PXC4H8 + O => CH3CHO + C2H4  # Reaction 502
  rate-constant: A: 1.3e+13, b: 0.0, Ea: 850.86
- equation: PXC4H8 + O => C2H5 + CH3 + CO  # Reaction 503
  rate-constant: A: 1.3e+13, b: 0.0, Ea: 850.86
- equation: PXC4H8 + O => C3H6 + CH2O  # Reaction 504
  rate-constant: A: 7.23e+05, b: 2.34, Ea: -1049.24
- equation: PXC4H8 + O => C2H5 + HCO + TXCH2  # Reaction 505
  rate-constant: A: 1.3e+13, b: 0.0, Ea: 850.86
- equation: PXC4H8 + OH => NXC3H7 + CH2O  # Reaction 506
  rate-constant: A: 1.0e+12, b: 0.0, Ea: 0.0
- equation: PXC4H8 + OH => C2H6 + CH3 + CO  # Reaction 507
  rate-constant: A: 5.0e+11, b: 0.0, Ea: 0.0
- equation: PXC4H8 + OH => C2H5 + CH3 + HCO  # Reaction 508
  rate-constant: A: 1.0e+12, b: 0.0, Ea: 0.0
- equation: PXC4H8 + OH => C2H5 + CH3CHO  # Reaction 509
  rate-constant: A: 1.0e+12, b: 0.0, Ea: 0.0
- equation: IXC3H7 => C2H4 + CH3  # Reaction 510
  rate-constant: A: 9.77e-09, b: 5.36, Ea: 1.702916e+04
- equation: IXC3H7 => C3H6 + H  # Reaction 511
  rate-constant: A: 9.88e+18, b: -1.59, Ea: 4.034895e+04
- equation: C3H6 + H => IXC3H7  # Reaction 512
  rate-constant: A: 1.73e+13, b: 0.03, Ea: 1797.32
- equation: C2H4 + CH3 => IXC3H7  # Reaction 513
  rate-constant: A: 4.1e+11, b: 0.0, Ea: 7203.63
- equation: IXC3H7 + O2 => C3H6 + HO2  # Reaction 514
  rate-constant: A: 7.65e+11, b: -0.06, Ea: 5145.79
- equation: HCO + OH => HOCHO  # Reaction 515
  rate-constant: A: 1.0e+14, b: 0.0, Ea: 0.0
- equation: HOCHO => CO + H2O  # Reaction 516
  rate-constant: A: 2.45e+12, b: 0.0, Ea: 6.046989e+04
- equation: HOCHO + OH => H2O + CO + OH  # Reaction 517
  rate-constant: A: 1.85e+07, b: 1.51, Ea: -962.0
- equation: HOCHO + OH => H2O + CO2 + H  # Reaction 518
```

```
  rate-constant: A: 2.62e+06, b: 2.06, Ea: 916.11
- equation: HOCHO + H => H2 + CO2 + H  # Reaction 519
  rate-constant: A: 4.24e+06, b: 2.1, Ea: 4868.07
- equation: HOCHO + H => H2 + CO + OH  # Reaction 520
  rate-constant: A: 6.03e+13, b: -0.35, Ea: 2988.05
- equation: HOCHO => HCO + OH  # Reaction 521
  rate-constant: A: 3.471e+22, b: -1.542, Ea: 1.1070005e+05
- equation: HOCHO + CH3 => CH4 + CO + OH  # Reaction 522
  rate-constant: A: 3.9e-07, b: 5.8, Ea: 2200.05
- equation: HOCHO + O => CO + 2 OH  # Reaction 523
  rate-constant: A: 1.77e+18, b: -1.9, Ea: 2974.9
- equation: CH3O2 + H => CH3O + OH  # Reaction 524
  rate-constant: A: 9.6e+13, b: 0.0, Ea: 0.0
- equation: CH3O2 + O => CH3O + O2  # Reaction 525
  rate-constant: A: 3.6e+13, b: 0.0, Ea: 0.0
- equation: C2H5 + C2H3 => 2 C2H4  # Reaction 526
  rate-constant: A: 6.859e+11, b: 0.11, Ea: -4299.95
- equation: C2H3 + C2H5 => PXC4H8  # Reaction 527
  rate-constant: A: 9.0e+12, b: 0.0, Ea: 0.0
- equation: CH3O2 + C2H5 => CH3O + C2H5O  # Reaction 528
  rate-constant: A: 8.0e+12, b: 0.0, Ea: -1000.0
- equation: C2H5 + O2 => CH3CHO + OH  # Reaction 529
  rate-constant: A: 826.5, b: 2.41, Ea: 5284.89
- equation: AXC3H4 + O => C2H2 + CH2O  # Reaction 530
  rate-constant: A: 3.0e-03, b: 4.61, Ea: -4243.07
- equation: AXC3H5 + C2H5 => C2H4 + C3H6  # Reaction 531
  rate-constant: A: 4.0e+11, b: 0.0, Ea: 0.0
- equation: H + C4H7 => C4H8X2  # Reaction 532
  rate-constant: A: 5.0e+13, b: 0.0, Ea: 0.0
- equation: C4H7 + HO2 => C4H8X2 + O2  # Reaction 533
  rate-constant: A: 1.35e+13, b: -0.18, Ea: -924.0
- equation: C4H8X2 + H <=> C4H7 + H2  # Reaction 534
  rate-constant: A: 3.46e+05, b: 2.5, Ea: 2492.11
```

```
- equation: C4H8X2 + OH => C4H7 + H2O  # Reaction 535
  rate-constant: A: 6.24e+06, b: 2.0, Ea: -298.04
- equation: C3H6 + O => CH3CHCO + 2 H  # Reaction 536
  rate-constant: A: 2.5e+07, b: 1.76, Ea: 76.0
- equation: CH3CHCO + O => CH3CHO + CO  # Reaction 537
  rate-constant: A: 3.2e+12, b: 0.0, Ea: -436.9
- equation: CH3CHCO + H => C2H5 + CO  # Reaction 538
  rate-constant: A: 4.4e+12, b: 0.0, Ea: 1458.89
- equation: CH3CHCO + OH => C2H5 + CO2  # Reaction 539
  rate-constant: A: 1.73e+12, b: 0.0, Ea: -1010.04
- equation: CH3COCH2 => CH2CO + CH3  # Reaction 540
  rate-constant: A: 1.0e+14, b: 0.0, Ea: 3.1e+04
- equation: CH2CO + CH3 => CH3COCH2  # Reaction 541
  rate-constant: A: 1.0e+11, b: 0.0, Ea: 6000.0
- equation: 2 CH3O => CH3OH + CH2O  # Reaction 542
  rate-constant: A: 6.03e+13, b: 0.0, Ea: 0.0
- equation: CH3OH + HO2 => CH2OH + H2O2  # Reaction 543
  rate-constant: A: 3.98e+13, b: 0.0, Ea: 1.94001e+04
- equation: C2H2 + HCO => C2H3 + CO  # Reaction 544
  rate-constant: A: 1.0e+07, b: 2.0, Ea: 6000.0
- equation: C2H3 + HO2 => CH2CHO + OH  # Reaction 545
  rate-constant: A: 1.0e+13, b: 0.0, Ea: 0.0
- equation: C2H4 + O => C2H3 + OH  # Reaction 546
  rate-constant: A: 2.42e+11, b: 0.7, Ea: 8960.33
- equation: C2H5 + O2 => C2H4O2H  # Reaction 547
  rate-constant: A: 2.42e+35, b: -8.03, Ea: 8311.9
- equation: CH3CHO + OH => CH3 + HOCHO  # Reaction 548
  rate-constant: A: 3.0e+15, b: -1.08, Ea: 0.0
- equation: C2H4O2H => C2H4 + HO2  # Reaction 549
  rate-constant: A: 9.29e+30, b: -6.1, Ea: 1.992997e+04
- equation: C4H6 + HO2 <=> C2H3CHOCH2 + OH  # Reaction 550
  rate-constant: A: 4.8e+12, b: 0.0, Ea: 1.4e+04
- equation: C2H3CHOCH2 <=> C4H6O23  # Reaction 551
```

```
  rate-constant: A: 2.0e+14, b: 0.0, Ea: 5.05999e+04
- equation: C4H6O23 => C2H4 + CH2CO  # Reaction 552
  rate-constant: A: 5.75e+15, b: 0.0, Ea: 6.929995e+04
- equation: C4H6O23 => SXC3H5CHO  # Reaction 553
  rate-constant: A: 1.95e+13, b: 0.0, Ea: 4.94001e+04
- equation: SXC3H5CHO => H + C2H3CHCHO  # Reaction 554
  rate-constant: A: 1.114e+18, b: -0.382, Ea: 8.639269e+04
- equation: SXC3H5CHO + H => C2H3CHCHO + H2  # Reaction 555
  rate-constant: A: 1.7e+05, b: 2.5, Ea: 2489.96
- equation: SXC3H5CHO => C3H6 + CO  # Reaction 556
  rate-constant: A: 3.9e+14, b: 0.0, Ea: 6.9e+04
- equation: IXC4H5 + HO2 => C2H3 + CH2CO + OH  # Reaction 557
  rate-constant: A: 6.6e+12, b: 0.0, Ea: 0.0
- equation: C4H8X2 + OH => C2H5 + CH3CHO  # Reaction 558
  rate-constant: A: 2.6e+13, b: 0.0, Ea: 0.0
- equation: CH3CO + CH3 => CH2CO + CH4  # Reaction 559
  rate-constant: A: 5.0e+13, b: 0.0, Ea: 0.0
- equation: CH3CO (+ M) <=> CH3 + CO (+ M)  # Reaction 560
  type: falloff
  low-P-rate-constant: A: 1.2e+15, b: 0.0, Ea: 1.252008e+04
  high-P-rate-constant: A: 3.0e+12, b: 0.0, Ea: 1.671989e+04
  Troe: A: 1.0, T3: 1.0, T1: 1.0e+07, T2: 1.0e+07
- equation: C2H3CHO + CH3O2 => C2H3 + CO + CH3O + OH  # Reaction 561
  rate-constant: A: 3.01e+12, b: 0.0, Ea: 1.191993e+04
- equation: C2H3CHO + O2 => C2H3 + CO + HO2  # Reaction 562
  rate-constant: A: 1.005e+13, b: 0.0, Ea: 4.070005e+04
- equation: HO2 + CH3COCH2 => O2 + CH3COCH3  # Reaction 563
  rate-constant: A: 5.978e+10, b: 0.309, Ea: 1544.93
- equation: CH3COCH3 + CH3 => CH3COCH2 + CH4  # Reaction 564
  rate-constant: A: 3.96e+11, b: 0.0, Ea: 9783.94
- equation: CH3COCH3 => CH3CO + CH3  # Reaction 565
  rate-constant: A: 1.31e+42, b: -7.657, Ea: 9.466061e+04
- equation: CH3COCH3 + O => CH3COCH2 + OH  # Reaction 566
```

```
  rate-constant: A: 5.13e+11, b: 0.211, Ea: 4890.06
- equation: CH3COCH3 + OH => CH3COCH2 + H2O  # Reaction 567
  rate-constant: A: 1.25e+05, b: 2.483, Ea: 445.03
- equation: CH3COCH3 + HO2 => CH3COCH2 + H2O2  # Reaction 568
  rate-constant: A: 1.7e+13, b: 0.0, Ea: 2.046009e+04
- equation: CH3COCH3 + H => CH3COCH2 + H2  # Reaction 569
  rate-constant: A: 9.8e+05, b: 2.43, Ea: 5159.89
- equation: C2H3CHCHO <=> AXC3H5 + CO  # Reaction 570
  rate-constant: A: 1.0e+14, b: 0.0, Ea: 2.5e+04
- equation: IXC3H5CO <=> TXC3H5 + CO  # Reaction 571
  rate-constant: A: 1.278e+20, b: -1.89, Ea: 3.446009e+04
- equation: CH3CHCHCHO + CH3 => C2H3CHCHO + CH4  # Reaction 572
  rate-constant: A: 2.1, b: 3.5, Ea: 5674.95
- equation: CH3CHCHCHO + H => C2H3CHCHO + H2  # Reaction 573
  rate-constant: A: 1.7e+05, b: 2.5, Ea: 2489.96
- equation: CH3CHCHCHO + H => C3H6 + HCO  # Reaction 574
  rate-constant: A: 4.0e+21, b: -2.39, Ea: 1.117997e+04
- equation: CH3CHCHCHO => C3H6 + CO  # Reaction 575
  rate-constant: A: 3.9e+14, b: 0.0, Ea: 6.9e+04
- equation: CH3CHCHCHO + H <=> CH3 + C2H3CHO  # Reaction 576
  rate-constant: A: 4.0e+21, b: -2.39, Ea: 1.117997e+04
- equation: MP2D + H => C2H3 + CO + CH2O + H2  # Reaction 577
  rate-constant: A: 9.4e+04, b: 2.75, Ea: 6280.11
- equation: MP2D + HO2 => C2H3 + CO + CH2O + H2O2  # Reaction 578
  rate-constant: A: 4.04e+04, b: 2.5, Ea: 1.669001e+04
- equation: H + MP2D <=> MP2J  # Reaction 579
  rate-constant: A: 1.0e+13, b: 0.0, Ea: 2900.1
- equation: MP2D + OH => C2H3 + CO + CH2O + H2O  # Reaction 580
  rate-constant: A: 5.25e+09, b: 0.97, Ea: 1590.11
- equation: MP2D + O => C2H3 + CO + CH2O + OH  # Reaction 581
  rate-constant: A: 9.65e+04, b: 2.68, Ea: 3716.06
- equation: MP2D <=> C2H3 + CO + CH3O  # Reaction 582
  rate-constant: A: 1.0e+16, b: 0.0, Ea: 7.1e+04
```

```
- equation: H + MP2D <=> MP3J  # Reaction 583
  rate-constant: A: 1.0e+13, b: 0.0, Ea: 2900.1
- equation: MP3J => CH3OCO + C2H4  # Reaction 584
  rate-constant: A: 3.03e+13, b: 0.27, Ea: 3.488934e+04
- equation: MP2J => MP3J  # Reaction 585
  rate-constant: A: 5.478e+08, b: 1.62, Ea: 3.876004e+04
- equation: MMETHMJ => CH2O + IXC3H5CO  # Reaction 586
  rate-constant: A: 1.23e+13, b: 0.375, Ea: 3.671367e+04
- equation: MMETHVJ => PXC3H4 + CH3OCO  # Reaction 587
  rate-constant: A: 2.5e+13, b: 0.0, Ea: 4.99522e+04
- equation: C2H6 + MMETHVJ => C2H5 + MMETHAC  # Reaction 588
  rate-constant: A: 4.567e+11, b: -0.02, Ea: -401.53
- equation: HO2 + MMETHVJ => O2 + MMETHAC  # Reaction 589
  rate-constant: A: 9.524e+09, b: 0.14, Ea: -1827.2
- equation: HO2 + MMETHPJ => O2 + MMETHAC  # Reaction 590
  rate-constant: A: 3.301e+10, b: 0.278, Ea: -110.9
- equation: C2H6 + MMETHPJ => C2H5 + MMETHAC  # Reaction 591
  rate-constant: A: 0.3339, b: 3.768, Ea: 9065.97
- equation: MMETHPJ => AXC3H4 + CH3OCO  # Reaction 592
  rate-constant: A: 1.0e+13, b: 0.0, Ea: 5.1e+04
- equation: MMETHAC + CH3O2 => MMETHVJ + CH3O + OH  # Reaction 593
  rate-constant: A: 3.0e+09, b: 0.0, Ea: 9929.97
- equation: MMETHAC + O => MMETHMJ + OH  # Reaction 594
  rate-constant: A: 9.65e+04, b: 2.6, Ea: 3746.18
- equation: MMETHAC + H <=> MMETHMJ + H2  # Reaction 595
  rate-constant: A: 1.554e+08, b: 2.21, Ea: 8570.5
- equation: MMETHAC + CH3 <=> MMETHVJ + CH4  # Reaction 596
  rate-constant: A: 0.84, b: 3.5, Ea: 1.165989e+04
- equation: MMETHAC + HO2 <=> MMETHPJ + H2O2  # Reaction 597
  rate-constant: A: 2.379e+04, b: 2.55, Ea: 1.648996e+04
- equation: MMETHAC + O2 <=> MMETHMJ + HO2  # Reaction 598
  rate-constant: A: 3.0e+13, b: 0.0, Ea: 5.228991e+04
- equation: MMETHAC + CH3O => MMETHPJ + CH3OH  # Reaction 599
```

```
  rate-constant: A: 2.169e+11, b: 0.0, Ea: 6457.93
- equation: MMETHAC + CH3O2 => MMETHMJ + CH3O + OH  # Reaction 600
  rate-constant: A: 2.379e+04, b: 2.55, Ea: 1.648996e+04
- equation: MMETHAC + C2H5 <=> MMETHMJ + C2H6  # Reaction 601
  rate-constant: A: 0.452, b: 3.65, Ea: 9141.01
- equation: MMETHAC + HO2 <=> MMETHMJ + H2O2  # Reaction 602
  rate-constant: A: 2.379e+04, b: 2.55, Ea: 1.648996e+04
- equation: MMETHAC + H <=> MMETHPJ + H2  # Reaction 603
  rate-constant: A: 2.06e+06, b: 2.69, Ea: 1394.85
- equation: MMETHAC + CH3 <=> MMETHMJ + CH4  # Reaction 604
  rate-constant: A: 1.0e+12, b: 0.0, Ea: 7299.24
- equation: MMETHAC + H <=> MMETHVJ + H2  # Reaction 605
  rate-constant: A: 2.37e+07, b: 2.02, Ea: 1.182309e+04
- equation: MMETHAC + CH3O2 => MMETHPJ + CH3O + OH  # Reaction 606
  rate-constant: A: 2.379e+04, b: 2.55, Ea: 1.648996e+04
- equation: MMETHAC + OH <=> MMETHPJ + H2O  # Reaction 607
  rate-constant: A: 6.98e+06, b: 1.77, Ea: 136.59
- equation: MMETHAC + OH <=> MMETHVJ + H2O  # Reaction 608
  rate-constant: A: 4.524, b: 3.59, Ea: -368.07
- equation: MMETHAC + O => CH3COCH2 + CH3OCO  # Reaction 609
  rate-constant: A: 5.01e+07, b: 1.76, Ea: 75.76
- equation: MMETHAC + OH => CH3COCH3 + CH3OCO  # Reaction 610
  rate-constant: A: 1.37e+12, b: 0.0, Ea: -1039.67
- equation: MMETHAC + O => MMETHPJ + OH  # Reaction 611
  rate-constant: A: 1.75e+11, b: 0.7, Ea: 5884.32
- equation: MMETHAC + HO2 <=> MMETHVJ + H2O2  # Reaction 612
  rate-constant: A: 3.0e+09, b: 0.0, Ea: 9929.97
- equation: MMETHAC + C2H3 <=> MMETHMJ + C2H4  # Reaction 613
  rate-constant: A: 301.5, b: 3.3, Ea: 1.05e+04
- equation: MMETHAC <=> IXC3H5CO + CH3O  # Reaction 614
  rate-constant: A: 4.3586e+15, b: -0.4947, Ea: 8.3788e+04
- equation: MMETHAC <=> TXC3H5 + CH3OCO  # Reaction 615
  rate-constant: A: 7.26e+15, b: -0.370, Ea: 7.2952e+04
```

```
- equation: MMETHAC + C2H3 <=> MMETHPJ + C2H4  # Reaction 616
  rate-constant: A: 301.5, b: 3.3, Ea: 1.05e+04
- equation: MMETHAC + O => MMETHVJ + OH  # Reaction 617
  rate-constant: A: 6.03e+10, b: 0.7, Ea: 7631.93
- equation: MMETHAC + OH <=> MMETHMJ + H2O  # Reaction 618
  rate-constant: A: 6.11e-03, b: 4.28, Ea: -3420.89
- equation: MMETHAC + CH3O => MMETHMJ + CH3OH  # Reaction 619
  rate-constant: A: 2.169e+11, b: 0.0, Ea: 6457.93
- equation: MMETHAC + CH3 <=> MMETHPJ + CH4  # Reaction 620
  rate-constant: A: 0.453, b: 3.65, Ea: 7153.92
- equation: MMETHAC + OH => MP2J + CH2O  # Reaction 621
  rate-constant: A: 1.37e+12, b: 0.0, Ea: -1027.72
```

APPENDIX F

High pressure hybrid combustion rig

A post-combustion chamber with optical access was designed extend the pressure capability of the developed method for spatially-resolving the thermochemical structure of hybrid PMMA combustion. In-chamber measurements at elevated pressures of (5-20 bar) will result in a novel data-set at conditions relevant to hybrid rockets that can demonstrate the pressure-dependance of the flow field and be compared to computational modelling results.

A CAD rendering of the high pressure test rig components is provided in Chapter 8; Figures F.2 and F.1 show the full assembly including the new high pressure post-combustion chamber with optical access during preliminary hot fire tests. In Fig. F.1, the slot (seen illuminated by the internal fire) provides the laser beam's range of line-of-sight domain used to obtain radially-resolved results via tomographic reconstruction.

Figure F.1 Hybrid rocket motor post-combustion chamber.

Figure F.2 High pressure hybrid rocket test rig during a hot fire test with $P_c = 10bar$.

REFERENCES

[1] J. Chen and X. Gao, "Review on the Fundamentals of Polymer Combustion and Flammability Characteristics for Hybrid Propulsion," *Journal of Polymer and Biopolymer Physics Chemistry*, vol. 2, no. 4, pp. 78–83, 2014.

[2] C. Carmicino, A. Russo Sorge, and A. R. Sorge, "Influence of a Conical Axial Injector on Hybrid Rocket Performance," *Journal of Propulsion and Power*, vol. 22, pp. 984–995, Sept. 2006.

[3] F. S. Mechentel and B. J. Cantwell, "Experimental Findings on Pre- and Post-combustion Chamber Effects in a Laboratory-scale Motor," in *AIAA Propulsion and Energy 2019 Forum*, no. August, AIAA 2019-4336, Aug. 2019.

[4] E. T. Jens, A. C. Karp, J. Rabinovitch, and B. Nakazono, "Hybrid Propulsion System Enabling Orbit Insertion Delta-Vs within a 12 U Spacecraft," in *2019 IEEE Aerospace Conference*, vol. 2019-March, pp. 1–3, IEEE, Mar. 2019.

[5] Y. Huang, L. Hu, Y. Ma, N. Zhu, Y. Chen, J. Wahlqvist, M. Mcnamee, and P. van Hees, "Experimental study of flame spread over thermally-thin inclined fuel surface and controlling heat transfer mechanism under concurrent wind," *International Journal of Thermal Sciences*, vol. 165, p. 106936, July 2021.

[6] F. A. Bendana, I. C. Sanders, J. J. Castillo, C. G. Hagström, D. I. Pineda, and R. M. Spearrin, "In-situ thermochemical analysis of hybrid rocket fuel oxidation via laser absorption tomography of $$\text {CO}$$, $$\text {CO}_{2}$$, and $$\text {H}_{2}\text {O}$$," *Experiments in Fluids*, vol. 61, p. 190, Aug. 2020.

[7] I. Gordon, L. Rothman, R. Hargreaves, R. Hashemi, E. Karlovets, F. Skinner, E. Conway, C. Hill, R. Kochanov, Y. Tan, P. Wcisło, A. Finenko, K. Nelson, P. Bernath, M. Birk, V. Boudon, A. Campargue, K. Chance, A. Coustenis, B. Drouin, J. Flaud, R. Gamache, J. Hodges, D. Jacquemart, E. Mlawer, A. Nikitin, V. Perevalov, M. Rotger, J. Tennyson, G. Toon, H. Tran, V. Tyuterev, E. Adkins, A. Baker, A. Barbe, E. Canè, A. Császár, A. Dudaryonok, O. Egorov, A. Fleisher, H. Fleurbaey, A. Foltynowicz, T. Furtenbacher, J. Harrison, J. Hartmann, V. Horneman, X. Huang, T. Karman, J. Karns, S. Kassi, I. Kleiner, V. Kofman, F. Kwabia–Tchana, N. Lavrentieva, T. Lee, D. Long, A. Lukashevskaya, O. Lyulin, V.Yu. Makhnev, W. Matt, S. Massie, M. Melosso, S. Mikhailenko, D. Mondelain, H. Müller, O. Naumenko, A. Perrin, O. Polyansky, E. Raddaoui, P. Raston, Z. Reed, M. Rey, C. Richard, R. Tóbiás, I. Sadiek, D. Schwenke, E. Starikova, K. Sung, F. Tamassia, S. Tashkun, J. Vander Auwera, I. Vasilenko, A. Vigasin, G. Villanueva, B. Vispoel, G. Wagner, A. Yachmenev, and S. Yurchenko, "The HITRAN2020 molecular spectroscopic database," *Journal of Quantitative Spectroscopy and Radiative Transfer*, vol. 277, p. 107949, 2022.

[8] L. Rothman, I. Gordon, R. Barber, H. Dothe, R. Gamache, A. Goldman, V. Perevalov, S. Tashkun, and J. Tennyson, "HITEMP, the High-Temperature Molecular Spectroscopic Database," *Journal of Quantitative Spectroscopy and Radiative Transfer*, vol. 111, pp. 2139–2150, Oct. 2010.

[9] A. R. Al-Derzi, J. Tennyson, S. N. Yurchenko, M. Melosso, N. Jiang, C. Puzzarini, L. Dore, T. Furtenbacher, R. Tóbiás, and A. G. Császár, "An improved rovibrational linelist of formaldehyde, H212C16O," *Journal of Quantitative Spectroscopy and Radiative Transfer*, vol. 266, p. 107563, May 2021.

[10] B. Yang, C. Westbrook, T. Cool, N. Hansen, and K. Kohse-Höinghaus, "Photoionization mass spectrometry and modeling study of premixed flames of three unsaturated C5H8O2 esters," *Proceedings of the Combustion Institute*, vol. 34, pp. 443–451, Jan. 2013.

[11] S. Dakshnamurthy, D. A. Knyazkov, A. M. Dmitriev, O. P. Korobeinichev, E. J. Nilsson, A. A. Konnov, and K. Narayanaswamy, "Experimental Study and a Short Kinetic Model for High-Temperature Oxidation of Methyl Methacrylate," *Combustion Science and Technology*, vol. 191, pp. 1789–1814, Oct. 2019.

[12] "Tesla reduced to ashes after catching fire on Pennsylvania highway." https://www.fox13news.com/news/tesla-reduced-to-ashes-after-catching-fire-on-pennsylvania-highway, Nov. 2022.

[13] M. J. Chiaverini, K. K. Kuo, A. Peretz, and G. C. Harting, "Regression-Rate and Heat-Transfer Correlations for Hybrid Rocket Combustion," *Journal of Propulsion and Power*, vol. 17, no. 1, pp. 99–110, 2001.

[14] G. Leccese, D. Bianchi, F. Nasuti, K. J. Stober, P. Narsai, and B. J. Cantwell, "Experimental and numerical methods for radiative wall heat flux predictions in paraffin–based hybrid rocket engines," *Acta Astronautica*, vol. 158, pp. 304–312, May 2019.

[15] K. Budzinski, S. S. Aphale, E. K. Ismael, G. Surina, and P. E. DesJardin, "Radiation heat transfer in ablating boundary layer combustion theory used for hybrid rocket motor analysis," *Combustion and Flame*, vol. 217, pp. 248–261, July 2020.

[16] G. Marxman and M. Gilbert, "Turbulent Boundary Layer Combustion in the Hybrid Rocket," *Symposium (International) on Combustion*, vol. 9, pp. 371–383, Jan. 1963.

[17] G. A. Marxman, "Boundary-layer Combustion in Propulsion," *Symposium (International) on Combustion*, vol. 11, pp. 269–289, Jan. 1967.

[18] G. Zilliac and M. A. Karabeyoglu, "Hybrid Rocket Fuel Regression Rate Data and Modeling," in *42nd AIAA/ASME/SAE/ASEE Joint Propulsion Conference and Exhibit*, no. July, (Reston, Virginia), pp. 1–21, American Institute of Aeronautics and Astronautics, July 2006.

[19] E. T. Jens, B. J. Cantwell, and G. S. Hubbard, "Hybrid Rocket Propulsion Systems for Outer Planet Exploration Missions," *Acta Astronautica*, vol. 128, pp. 119–130, Nov. 2016.

[20] A. Karabeyoglu, G. Zilliac, B. J. Cantwell, S. DeZilwa, and P. Castellucci, "Scale-Up Tests of High Regression Rate Paraffin-Based Hybrid Rocket Fuels," *Journal of Propulsion and Power*, vol. 20, pp. 1037–1045, Nov. 2004.

[21] M. J. Chiaverini and K. K. Kuo, *Fundamentals of Hybrid Rocket Combustion and Propulsion*. American Institute of Aeronautics and Astronautics, 2007.

[22] S. P. Burke and T. E. W. Schumann, "Diffusion Flames," *Industrial & Engineering Chemistry*, vol. 20, pp. 998–1004, Oct. 1928.

[23] R. W. Bilger, "The Structure of Diffusion Flames," *Combustion Science and Technology*, vol. 13, pp. 155–170, July 1976.

[24] D. E. Keyes and M. D. Smooke, "Flame sheet starting estimates for counterflow diffusion flame problems," *Journal of Computational Physics*, vol. 73, pp. 267–288, Dec. 1987.

[25] A. Linan, "On the Structure of Laminar Diffusion Flames.," tech. rep.

[26] A. Okninski, "On use of hybrid rocket propulsion for suborbital vehicles," *Acta Astronautica*, vol. 145, pp. 1–10, Apr. 2018.

[27] J. Jones and R. Frederick, "Visualization of Recirculation Zones in Hybrid Rocket Motors," in *32nd Joint Propulsion Conference and Exhibit*, no. July, 96-2842, July 1996.

[28] G. Schulte, R. Pein, and A. Hoegl, "Temperature and Concentration Measurements in a Solid Fuel Ramjet Combustion Chamber," *Journal of Propulsion and Power*, vol. 3, no. 2, pp. 114–120, 1987.

[29] F. S. Mechentel, B. R. Hord, and B. J. Cantwell, "Optically Resolved Fuel Regression of a Clear PMMA Hybrid Rocket Motor," in *AIAA Propulsion and Energy 2019 Forum*, vol. Article in, (Reston, Virginia), pp. 1–10, American Institute of Aeronautics and Astronautics, Aug. 2019.

[30] C. P. Kumar and A. Kumar, "Effect of swirl on the regression rate in hybrid rocket motors," *Aerospace Science and Technology*, vol. 29, pp. 92–99, Aug. 2013.

[31] S. R. Gomes, L. Rocco Junior, and J. A. F. F. Rocco, "Swirl Injection Effects on Hybrid Rocket Motors," *Journal of Aerospace Technology and Management*, vol. 7, pp. 418–424, Nov. 2015.

[32] C. Carmicino and A. R. Sorge, "Role of Injection in Hybrid Rockets Regression Rate Behaviour," *Journal of Propulsion and Power*, vol. 21, pp. 606–612, July 2005.

[33] A. Karabeyoglu, "Challenges in the Development of Large-scale Hybrid Rockets," *International Journal of Energetic Materials and Chemical Propulsion*, vol. 16, no. 3, pp. 243–261, 2017.

[34] P. Kiliaris and C. D. Papaspyrides, "Polymers on Fire," in *Polymer Green Flame Retardants* (C. D. Papaspyrides and P. Kiliaris, eds.), pp. 1–43, Amsterdam: Elsevier, Jan. 2014.

[35] V. Babrauskas and R. D. Peacock, "Heat release rate: The single most important variable in fire hazard," *Fire Safety Journal*, vol. 18, pp. 255–272, Jan. 1992.

[36] S. Ebnesajjad, "18 - Properties of Tetrafluoroethylene Homopolymers," in *Fluoroplastics (Second Edition)* (S. Ebnesajjad, ed.), vol. 1, pp. 396–440, Oxford: William Andrew Publishing, Jan. 2015.

[37] M. Lewin and E. D. Weil, "2 - Mechanisms and modes of action in flame retardancy of polymers," in *Fire Retardant Materials* (A. R. Horrocks and D. Price, eds.), pp. 31–68, Woodhead Publishing, Jan. 2001.

[38] A. Chandler, E. Jens, B. Cantwell, and G. S. Hubbard, "Visualization of the Liquid Layer Combustion of Paraffin Fuel for Hybrid Rocket Applications," in *48th AIAA/ASME/SAE/ASEE Joint Propulsion Conference & Exhibit*, no. August, (Reston, Virigina), American Institute of Aeronautics and Astronautics, July 2012.

[39] E. T. Jens, A. A. Chandler, B. Cantwell, G. S. Hubbard, and F. Mechentel, "Combustion Visualization of Paraffin-Based Hybrid Rocket Fuel at Elevated Pressures," in *50th AIAA/ASME/SAE/ASEE Joint Propulsion Conference*, (Reston, Virginia), American Institute of Aeronautics and Astronautics, July 2014.

[40] R. GELAIN, A.E. DE MORAIS BERTOLDI, F. ANGELONI, and P. HENDRICK, "Design and Commissioning of the MOUETTE Hybrid Rocket Slab Burner," p. 16 pages, 2022.

[41] Y. Wada, Y. Kawabata, R. Kato, N. Kato, and K. Hori, "OBSERVATION OF COMBUSTION BEHAVIOR OF LOW MELTING TEMPERATURE FUEL FOR A HYBRID ROCKET USING DOUBLE SLAB MOTOR," *International Journal of Energetic Materials and Chemical Propulsion*, vol. 15, no. 5, 2016.

[42] G. Young, G. Risha, A. G. Miller, R. A. Glass, J. Terrence L. Connell, and R. A. Yetter, "COMBUSTION OF ALANE-BASED SOLID FUELS," *International Journal of Energetic Materials and Chemical Propulsion*, vol. 9, no. 3, 2010.

[43] G. Young, S. Hromisin, S. Loeffler, and T. L. Connell, "Effect of Oxidizer Type on Solid Fuel Combustion," *Journal of Propulsion and Power*, vol. 36, pp. 248–255, Mar. 2020.

[44] H. Pace and L. Massa, "Combustion of PMMA in Solid Fuel Scramjet Cavities," in *AIAA AVIATION 2022 Forum*, (Chicago, IL & Virtual), American Institute of Aeronautics and Astronautics, June 2022.

[45] H. T. Loh and A. C. Fernandez-Pello, "A study of the controlling mechanisms of flow assisted flame spread," *Symposium (International) on Combustion*, vol. 20, pp. 1575–1582, Jan. 1985.

[46] Y. H. C CHAO and A. C. FERNANDEZ-PELLO, "Concurrent Horizontal Flame Spread: The Combined Effect of Oxidizer Flow Velocity, Turbulence and Oxygen Concentration," *Combustion Science and Technology*, vol. 110–111, pp. 19–51, Dec. 1995.

[47] R. Hanson, R. Spearrin, and C. Goldenstein, *Spectroscopy and Optical Diagnostics for Gases*. Springer International Publishing, 2016.

[48] W. Cai and C. F. Kaminski, "Tomographic Absorption Spectroscopy for the study of Gas Dynamics and Reactive Flows," *Progress in Energy and Combustion Science*, vol. 59, pp. 1–31, Mar. 2017.

[49] A. Guha and I. M. Schoegl, "Tomographic Imaging of Flames: Assessment of Reconstruction Error Based on Simulated Results," *Journal of Propulsion and Power*, vol. 30, pp. 350–359, Mar. 2014.

[50] M. Deutsch and I. Beniaminy, "Inversion of Abel's Integral Equation for Experimental Data," *Journal of Applied Physics*, vol. 54, pp. 137–143, Jan. 1983.

[51] I. Gordon, L. Rothman, C. Hill, R. Kochanov, Y. Tan, P. Bernath, M. Birk, V. Boudon, A. Campargue, K. Chance, B. Drouin, J.-M. Flaud, R. Gamache, J. Hodges, D. Jacquemart, V. Perevalov, A. Perrin, K. Shine, M.-A. Smith, J. Tennyson, G. Toon, H. Tran, V. Tyuterev, A. Barbe, A. Császár, V. Devi, T. Furtenbacher, J. Harrison, J.-M. Hartmann, A. Jolly, T. Johnson, T. Karman, I. Kleiner, A. Kyuberis, J. Loos, O. Lyulin, S. Massie, S. Mikhailenko, N. Moazzen-Ahmadi, H. Müller, O. Naumenko, A. Nikitin, O. Polyansky, M. Rey, M. Rotger, S. Sharpe, K. Sung, E. Starikova, S. Tashkun, J. V. Auwera, G. Wagner, J. Wilzewski, P. Wcisło, S. Yu, E. Zak, *et al.*, "The HITRAN2016 molecular spectroscopic database," *Journal of Quantitative Spectroscopy and Radiative Transfer*, vol. 203, pp. 3–69, Dec. 2017.

[52] C. Wei, D. I. Pineda, L. Paxton, F. N. Egolfopoulos, and R. M. Spearrin, "Mid-infrared laser absorption tomography for quantitative 2D thermochemistry measurements in premixed jet flames," *Applied Physics B*, vol. 124, p. 123, June 2018.

[53] C. Wei, D. I. Pineda, C. S. Goldenstein, and R. M. Spearrin, "Tomographic laser absorption imaging of combustion species and temperature in the mid-wave infrared," *Optics Express*, vol. 26, p. 20944, Aug. 2018.

[54] K. J. Daun, K. A. Thomson, F. Liu, and G. J. Smallwood, "Deconvolution of axisymmetric flame properties using Tikhonov regularization," *Applied Optics*, vol. 45, p. 4638, July 2006.

[55] C. J. Dasch, "One-dimensional tomography: A comparison of Abel, onion-peeling, and filtered backprojection methods," *Applied Optics*, vol. 31, p. 1146, Mar. 1992.

[56] P. C. Hansen, *The L-Curve and Its Use in the Numerical Treatment of Inverse Problems*, vol. 4. WIT Press, 2000.

[57] D. D. Cox and P. C. Hansen, "Rank-Deficient and Discrete III-Posed Problems: Numerical Aspects of Linear Inversion," *Journal of the American Statistical Association*, vol. 94, p. 1388, Dec. 1999.

[58] D. G. Goodwin, H. K. Moffat, and R. L. Speth, "Cantera: An object-oriented software toolkit for chemical kinetics, thermodynamics, and transport processes," 2018.

[59] S. Gordon, B. J. McBride, S. Gordon, and B. J. McBride, *Computer Program for Calculation of Complex Chemical Equilibrium Compositions and Applications*. No. January, NASA, 1996.

[60] R. M. Spearrin, C. S. Goldenstein, J. B. Jeffries, and R. K. Hanson, "Quantum cascade laser absorption sensor for carbon monoxide in high-pressure gases using wavelength modulation spectroscopy," *Applied Optics*, vol. 53, p. 1938, Mar. 2014.

[61] R. M. Spearrin, W. Ren, J. B. Jeffries, and R. K. Hanson, "Multi-band infrared CO2 absorption sensor for sensitive temperature and species measurements in high-temperature gases," *Applied Physics B*, vol. 116, pp. 855–865, Sept. 2014.

[62] K.-P. Cheong, L. Ma, Z. Wang, and W. Ren, "Influence of Line Pair Selection on Flame Tomography Using Infrared Absorption Spectroscopy," *Applied Spectroscopy*, vol. 73, pp. 529–539, May 2019.

[63] F. A. Bendana, J. J. Castillo, C. G. Hagström, and R. M. Spearrin, "Thermochemical Structure of a Hybrid Rocket Reaction Layer based on Laser Absorption Tomography," in *AIAA Propulsion and Energy 2019 Forum*, pp. AIAA 2019–4337, American Institute of Aeronautics and Astronautics, Aug. 2019.

[64] D. I. Pineda, J. L. Urban, and R. Mitchell Spearrin, "Interband cascade laser absorption of hydrogen chloride for high-temperature thermochemical analysis of fire-resistant polymer reactivity," *Applied Optics*, vol. 59, p. 2141, Mar. 2020.

[65] M. A. Karabeyoglu, B. J. Cantwell, and G. Zilliac, "Development of Scalable Space-Time Averaged Regression Rate Expressions for Hybrid Rockets," *Journal of Propulsion and Power*, vol. 23, pp. 737–747, July 2007.

[66] C. M. Rhie, "Pressure-based Navier-Stokes Solver using the Multigrid Method," *AIAA Journal*, vol. 27, pp. 1017–1018, Aug. 1989.

[67] I. S. Kavvadias, E. M. Papoutsis-Kiachagias, G. Dimitrakopoulos, and K. C. Giannakoglou, "The Continuous Adjoint Approach to the k-ω SST Turbulence Model with Applications in Shape Optimization," *Engineering Optimization*, vol. 47, no. 11, pp. 1523–1542, 2015.

[68] F. R. Menter, "A Comparison of Some Recent Eddy-Viscosity Turbulence Models," *Journal of Fluids Engineering*, vol. 118, pp. 514–519, Sept. 1996.

[69] F. R. Menter, "Two-equation Eddy-Viscosity Turbulence Models for Engineering Applications," *AIAA Journal*, vol. 32, pp. 1598–1605, Aug. 1994.

[70] I. C. Sanders, F. A. Bendana, C. Hagstrom, and R. M. Spearrin, "Assessing Oxidizer Injector Design via Thermochemical Imaging of PMMA Combustion in a Hybrid Rocket Motor Geometry," in *AIAA Propulsion and Energy 2020 Forum*, American Institute of Aeronautics and Astronautics, Aug. 2020.

[71] I. C. Sanders, F. A. Bendana, C. G. Hagström, and R. Mitchell Spearrin, "Injector Effects on Hybrid Polymethylmethacrylate Combustion Assessed by Thermochemical Tomography," *Journal of Propulsion and Power*, vol. 37, pp. 928–943, Nov. 2021.

[72] X. Liu, G. Zhang, Y. Huang, Y. Wang, and F. Qi, "Two-dimensional temperature and carbon dioxide concentration profiles in atmospheric laminar diffusion flames measured by mid-infrared direct absorption spectroscopy at 4.2 Mm," *Applied Physics B*, vol. 124, p. 61, Apr. 2018.

[73] R. J. Tancin, R. M. Spearrin, and C. S. Goldenstein, "2D mid-infrared laser-absorption imaging for tomographic reconstruction of temperature and carbon monoxide in laminar flames," *Optics Express*, vol. 27, p. 14184, May 2019.

[74] N. Syred and J. M. Beer, "Combustion in Swirling Flows: A Review," *Journal of Physics: Conference Series*, vol. 891, no. 1, pp. 143–201, 2017.

[75] J. Asakawa, K. Nishii, Y. Nakagawa, H. Koizumi, and K. Komurasaki, "Direct measurement of 1-mN-class thrust and 100-s-class specific impulse for a CubeSat propulsion system," *Review of Scientific Instruments*, vol. 91, no. 3, 2020.

[76] J.-Y. Lestrade, J. Anthoine, O. Verberne, A. J. Boiron, G. Khimeche, and C. Figus, "Experimental Demonstration of the Vacuum Specific Impulse of a Hybrid Rocket Engine," *Journal of Spacecraft and Rockets*, vol. 54, pp. 101–108, Jan. 2017.

[77] M. Bouziane, A. Bertoldi, P. Milova, P. Hendrick, and M. Lefebvre, "Performance comparison of oxidizer injectors in a 1-kN paraffin-fueled hybrid rocket motor," *Aerospace Science and Technology*, vol. 89, pp. 392–406, June 2019.

[78] X. Sun, H. Tian, N. Yu, and G. Cai, "Regression rate and combustion performance investigation of aluminum metallized HTPB/98HP hybrid rocket motor with numerical simulation," *Aerospace Science and Technology*, vol. 42, pp. 287–296, Apr. 2015.

[79] K. Sakaki, H. Kakudo, S. Nakaya, M. Tsue, R. Kanai, K. Suzuki, T. Inagawa, and T. Hiraiwa, "Performance Evaluation of Rocket Engine Combustors using Ethanol/Liquid Oxygen Pintle Injector," in *52nd AIAA/SAE/ASEE Joint Propulsion Conference*, pp. 1–16, American Institute of Aeronautics and Astronautics, July 2016.

[80] L. K. Werling, M. Hassler, F. Lauck, H. K. Ciezki, and S. Schlechtriem, "Experimental Performance Analysis (c* & c* Efficiency) of a Premixed Green Propellant consisting of N 2 O and C 2 H 4," in *53rd AIAA/SAE/ASEE Joint Propulsion Conference*, no. July, American Institute of Aeronautics and Astronautics, July 2017.

[81] F. Barato, E. Toson, and D. Pavarin, "Variations and Control of Thrust and Mixture Ratio in Hybrid Rocket Motors," *Advances in Astronautics Science and Technology*, Apr. 2021.

[82] N. Bellomo, F. Barato, M. Faenza, M. Lazzarin, A. Bettella, and D. Pavarin, "Numerical and experimental investigation of unidirectional vortex injection in hybrid rocket engines," *Journal of Propulsion and Power*, vol. 29, no. 5, pp. 1097–1113, 2013.

[83] L. H. Ma, L. Y. Lau, W. Ren, L. Hao, M. Lok, Y. Lau, and W. Ren, "Non-uniform temperature and species concentration measurements in a laminar flame using multiband infrared absorption spectroscopy," *Applied Physics B*, vol. 123, p. 83, Mar. 2017.

[84] S. van der Kley, J. Emmert, A. Schmidt, A. Dreizler, and S. Wagner, "Tomographic spectrometer for the temporally-resolved 2D reconstruction of gas phase parameters within a generic SCR test rig," *Proceedings of the Combustion Institute*, vol. 38, no. 1, pp. 1703–1710, 2021.

[85] R. Sur, K. Sun, J. B. Jeffries, J. G. Socha, and R. K. Hanson, "Scanned-wavelength-modulation-spectroscopy sensor for CO, CO2, CH4 and H2O in a high-pressure engineering-scale transport-reactor coal gasifier," *Fuel*, vol. 150, pp. 102–111, June 2015.

[86] A. W. Caswell, T. Kraetschmer, K. Rein, S. T. Sanders, S. Roy, D. T. Shouse, and J. R. Gord, "Application of time-division-multiplexed lasers for measurements of gas temperature and CH4 and H2O concentrations at 30 kHz in a high-pressure combustor," *Applied Optics*, vol. 49, p. 4963, Sept. 2010.

[87] A. P. Nair, D. D. Lee, D. I. Pineda, J. Kriesel, W. A. Hargus, J. W. Bennewitz, B. Bigler, S. A. Danczyk, and R. M. Spearrin, "Methane-Oxygen Rotating Detonation Exhaust Thermodynamics with Variable Mixing, Equivalence Ratio, and Mass Flux," *Aerospace Science and Technology*, vol. 113, p. 106683, 2021.

[88] A. Nair, D. Lee, D. Pineda, J. Kriesel, W. Hargus, J. Bennewitz, S. Danczyk, and R. Spearrin, "MHz laser absorption spectroscopy via diplexed RF modulation for pressure, temperature, and species in rotating detonation rocket flows," *Applied Physics B*, vol. 126, p. 138, Aug. 2020.

[89] S. J. Cassady, W. Y. Peng, C. L. Strand, D. F. Dausen, J. R. Codoni, C. M. Brophy, and R. K. Hanson, "Time-resolved, single-ended laser absorption thermometry and H2O, CO2, and CO speciation in a H2/C2H4-fueled rotating detonation engine," *Proceedings of the Combustion Institute*, vol. 21, Oct. 2020.

[90] I. A. Schultz, C. S. Goldenstein, R. Mitchell Spearrin, J. B. Jeffries, R. K. Hanson, R. D. Rockwell, and C. P. Goyne, "Multispecies Midinfrared Absorption Measurements in a Hydrocarbon-Fueled Scramjet Combustor," *Journal of Propulsion and Power*, vol. 30, pp. 1595–1604, Nov. 2014.

[91] R. Spearrin, C. Goldenstein, I. Schultz, J. Jeffries, and R. Hanson, "Simultaneous sensing of temperature, CO, and CO2 in a scramjet combustor using quantum cascade laser absorption spectroscopy," *Applied Physics B: Lasers and Optics*, vol. 117, pp. 689–698, Nov. 2014.

[92] C. S. Goldenstein, I. A. Schultz, R. M. Spearrin, J. B. Jeffries, and R. K. Hanson, "Scanned-wavelength-modulation spectroscopy near 2.5 Mm for H2O and temperature in a hydrocarbon-fueled scramjet combustor," *Applied Physics B*, vol. 116, pp. 717–727, Sept. 2014.

[93] D. D. Lee, F. A. Bendana, A. P. Nair, R. M. Spearrin, S. A. Danczyk, and W. A. Hargus, "Laser absorption of carbon dioxide at the vibrational bandhead near 4.2μm in high-pressure rocket combustion environments," in *AIAA Scitech 2020 Forum*, no. January, American Institute of Aeronautics and Astronautics, Jan. 2020.

[94] C. Wei, K. K. Schwarm, D. I. Pineda, and R. M. Spearrin, "Deep neural network inversion for 3D laser absorption imaging of methane in reacting flows," *Optics Letters*, vol. 45, p. 2447, Apr. 2020.

[95] C. Goldenstein, R. Spearrin, J. Jeffries, and R. Hanson, "Infrared laser-absorption sensing for combustion gases," *Progress in Energy and Combustion Science*, vol. 60, pp. 132–176, May 2017.

[96] C. Liu and L. Xu, "Laser absorption spectroscopy for combustion diagnosis in reactive flows: A review," *Applied Spectroscopy Reviews*, vol. 54, no. 1, pp. 1–44, 2019.

[97] C. Wei, K. Schwarm, D. Pineda, and R. Spearrin, "Volumetric laser absorption imaging of temperature, CO and CO2 in laminar flames using 3D masked Tikhonov regularization," *Combustion and Flame*, vol. 224, pp. 239–247, Feb. 2021.

[98] A. Burcat and B. Ruscic, "Third Millennium Ideal Gas and Condensed Phase Thermochemical Database for Combustion with Updates from Active Thermochemical Tables," Tech. Rep. ANL-05/20, Argonne National Laboratory, 2005.

[99] F. A. Bendana, D. D. Lee, S. A. Schumaker, S. A. Danczyk, and R. M. Spearrin, "Cross-band infrared laser absorption of carbon monoxide for thermometry and species sensing in high-pressure rocket flows," *Applied Physics B*, vol. 125, p. 204, Nov. 2019.

[100] D. D. Lee, F. A. Bendana, S. A. Schumaker, and R. M. Spearrin, "Wavelength modulation spectroscopy near 5 Mm for carbon monoxide sensing in a high-pressure kerosene-fueled liquid rocket combustor," *Applied Physics B*, vol. 124, p. 77, May 2018.

[101] H. W. Coleman and W. G. Steele, *Experimentation, Validation, and Uncertainty Analysis for Engineers*. Hoboken, NJ, USA: John Wiley & Sons, Inc., 2009.

[102] L. S. Rothman, I. E. Gordon, Y. Babikov, A. Barbe, D. Chris Benner, P. F. Bernath, M. Birk, L. Bizzocchi, V. Boudon, L. R. Brown, A. Campargue, K. Chance, E. A. Cohen, L. H. Coudert, V. M. Devi, B. J. Drouin, A. Fayt, J.-M. Flaud, R. R. Gamache, J. J. Harrison, J.-M. Hartmann, C. Hill, J. T. Hodges, D. Jacquemart, A. Jolly, J. Lamouroux, R. J. Le Roy, G. Li, D. A. Long, O. M. Lyulin, C. J. Mackie, S. T. Massie, S. Mikhailenko, H. S. P. Müller, O. V. Naumenko, A. V. Nikitin, J. Orphal, V. Perevalov, A. Perrin, E. R. Polovtseva, C. Richard, M. A. H. Smith, E. Starikova, K. Sung, S. Tashkun, J. Tennyson, G. C. Toon, Vl.G. Tyuterev, and G. Wagner, "The HITRAN2012 molecular spectroscopic database," *Journal of Quantitative Spectroscopy and Radiative Transfer*, vol. 130, pp. 4–50, Nov. 2013.

[103] A. Nair, D. Lee, D. Pineda, R. Spearrin, J. Krisel, W. Hargus, J. Bennewitz, and S. Danczyk, "MHz Mid-infrared Laser Absorption of CO and CO 2 for Pressure, Temperature, and Species in Rotating Detonation Rocket Flows," in *AIAA Propulsion and Energy 2020 Forum*, American Institute of Aeronautics and Astronautics, Aug. 2020.

[104] K. Seshadri and F. A. Williams, "Structure and extinction of counterflow diffusion flames above condensed fuels: Comparison between poly(methyl methacrylate) and its liquid monomer, both burning in nitrogen–air mixtures," *Journal of Polymer Science: Polymer Chemistry Edition*, vol. 16, pp. 1755–1778, July 1978.

[105] A. C. Fernandez-Pello and T. Hirano, "Controlling mechanisms of flame spread," *Combustion Science and Technology*, vol. 32, no. 1-4, pp. 1–31, 1983.

[106] W. R. Zeng, S. F. Li, and W. K. Chow, "Review on chemical reactions of burning poly(methyl methacrylate) PMMA," *Journal of Fire Sciences*, vol. 20, no. 5, pp. 401–433, 2002.

[107] S. Kim, J. Lee, H. Moon, J. Kim, H. Sung, and O. C. Kwon, "Regression Characteristics of the Cylindrical Multiport Grain in Hybrid Rockets," *Journal of Propulsion and Power*, vol. 29, pp. 573–581, May 2013.

[108] A. Bhargava, P. Van Hees, and B. Andersson, "Pyrolysis modeling of PVC and PMMA using a distributed reactivity model," *Polymer Degradation and Stability*, vol. 129, pp. 199–211, 2016.

[109] A. Fraters and A. Cervone, "Experimental Characterization of Combustion Instabilities in High-Mass-Flux Hybrid Rocket Engines," *Journal of Propulsion and Power*, vol. 32, pp. 958–966, July 2016.

[110] P. A. Korting, H. F. Schöyer, and Y. M. Timnat, "Advanced hybrid rocket motor experiments," *Acta Astronautica*, vol. 15, pp. 97–104, Feb. 1987.

[111] M. Thomsen, L. Carmignani, A. Rodriguez, C. Scudiere, C. Liveretou, C. Fernandez-Pello, M. Gollner, S. Olson, and P. Ferkul, "Downward Flame Spread Rate Over PMMA Rods Under External Radiant Heating," *Fire Technology*, vol. 58, no. 4, pp. 2229–2250, 2022.

[112] C. Xiong, H. Fan, X. Huang, and C. Fernandez-Pello, "Evaluation of burning rate in microgravity based on the fuel regression, flame area, and spread rate," *Combustion and Flame*, vol. 237, 2022.

[113] J. Rabinovitch, E. T. Jens, A. C. Karp, B. Nakazono, A. Conte, and D. A. Vaughan, "Characterization of PolyMethylMethAcrylate as a Fuel for Hybrid Rocket Motors," in *2018 Joint Propulsion Conference*, (Reston, Virginia), pp. 1–21, American Institute of Aeronautics and Astronautics, July 2018.

[114] A. Ben-Yakar, B. Natan, and A. Gany, "Investigation of a Solid Fuel Scramjet Combustor," *Journal of Propulsion and Power*, vol. 14, pp. 447–455, July 1998.

[115] C. K. Westbrook, W. J. Pitz, and H. J. Curran, "Chemical kinetic modeling study of the effects of oxygenated hydrocarbons on soot emissions from diesel engines," *Journal of Physical Chemistry A*, vol. 110, no. 21, pp. 6912–6922, 2006.

[116] A. Farooq, D. Davidson, R. Hanson, and C. Westbrook, "A comparative study of the chemical kinetics of methyl and ethyl propanoate," *Fuel*, vol. 134, pp. 26–38, Oct. 2014.

[117] H. Wang and M. A. Oehlschlaeger, "Shock tube ignition delay time measurements for methyl propanoate and methyl acrylate: Influence of saturation on small methyl ester high-temperature reactivity," *International Journal of Chemical Kinetics*, vol. 52, pp. 712–722, Oct. 2020.

[118] C. K. Westbrook, W. J. Pitz, P. R. Westmoreland, F. L. Dryer, M. Chaos, P. Osswald, K. Kohse-Höinghaus, T. A. Cool, J. Wang, B. Yang, N. Hansen, and T. Kasper, "A detailed chemical kinetic reaction mechanism for oxidation of four small alkyl esters in laminar premixed flames," *Proceedings of the Combustion Institute*, vol. 32 I, no. 1, pp. 221–228, 2009.

[119] W. Ren, R. M. Spearrin, D. F. Davidson, and R. K. Hanson, "Experimental and Modeling Study of the Thermal Decomposition of C3–C5 Ethyl Esters Behind Reflected Shock Waves," *The Journal of Physical Chemistry A*, vol. 118, pp. 1785–1798, Mar. 2014.

[120] B. Yang, C. K. Westbrook, T. A. Cool, N. Hansen, and K. Kohse-Höinghaus, "Fuel-specific influences on the composition of reaction intermediates in premixed flames of three C5H10O2 ester isomers," *Physical Chemistry Chemical Physics*, vol. 13, no. 15, pp. 6901–6913, 2011.

[121] T. Wang, S. Li, Z. Lin, D. Han, and X. Han, "Experimental study of laminar lean premixed methylmethacrylate/oxygen/argon flame at low pressure," *Journal of Physical Chemistry A*, vol. 112, no. 6, pp. 1219–1227, 2008.

[122] Z. Lin, T. Wang, D. Han, X. Han, S. Li, Y. Li, and Z. Tian, "Study of combustion intermediates in fuel-rich methyl methacrylate flame with tunable synchrotron vacuum ultraviolet photoionization mass spectrometry," *Rapid Communications in Mass Spectrometry*, vol. 23, pp. 85–92, Jan. 2009.

[123] D. A. Knyazkov, T. A. Bolshova, V. M. Shvartsberg, A. A. Chernov, and O. P. Korobeinichev, "Inhibition of premixed flames of methyl methacrylate by trimethylphosphate," *Proceedings of the Combustion Institute*, vol. 38, no. 3, pp. 4625–4633, 2021.

[124] T. A. Bolshova, A. A. Chernov, and A. G. Shmakov, "Reduced Chemical Kinetic Mechanism for the Oxidation of Methyl Methacrylate in Flames at Atmospheric Pressure," *Combustion, Explosion and Shock Waves*, vol. 57, no. 2, pp. 159–170, 2021.

[125] C. K. Law, *Combustion Physics*. New York: Cambridge University Press, 2006.

[126] R. Hanson and D. Davidson, "Recent advances in laser absorption and shock tube methods for studies of combustion chemistry," *Progress in Energy and Combustion Science*, vol. 44, pp. 103–114, Oct. 2014.

[127] D. Bongartz and A. F. Ghoniem, "Chemical kinetics mechanism for oxy-fuel combustion of mixtures of hydrogen sulfide and methane," *Combustion and Flame*, vol. 162, pp. 544–553, Mar. 2015.

[128] N. Sikalo, O. Hasemann, C. Schulz, A. Kempf, and I. Wlokas, "A genetic algorithm-based method for the automatic reduction of reaction mechanisms," *International Journal of Chemical Kinetics*, vol. 46, pp. 41–59, Jan. 2014.

[129] B. Niu, M. Jia, G. Xu, Y. Chang, and M. Xie, "Efficient Approach for the Optimization of Skeletal Chemical Mechanisms with Multiobjective Genetic Algorithm," *Energy and Fuels*, vol. 32, pp. 7086–7102, June 2018.

[130] S. H. Won, B. Windom, B. Jiang, and Y. Ju, "The role of low temperature fuel chemistry on turbulent flame propagation," *Combustion and Flame*, vol. 161, no. 2, pp. 475–483, 2014.

[131] F. A. Williams, "A review of flame extinction," *Fire Safety Journal*, vol. 3, no. 3, pp. 163–175, 1981.

[132] F. A. Bendana, D. D. Lee, C. Wei, D. I. Pineda, and R. M. Spearrin, "Line mixing and broadening in the v(1→3) first overtone bandhead of carbon monoxide at high temperatures and high pressures," *Journal of Quantitative Spectroscopy and Radiative Transfer*, vol. 239, p. 106636, Dec. 2019.

[133] D. I. Pineda, F. A. Bendana, K. K. Schwarm, and R. M. Spearrin, "Multi-isotopologue laser absorption spectroscopy of carbon monoxide for high-temperature chemical kinetic studies of fuel mixtures," *Combustion and Flame*, vol. 207, pp. 379–390, Sept. 2019.

[134] M. F. Campbell, K. G. Owen, D. F. Davidson, and R. K. Hanson, "Dependence of Calculated Postshock Thermodynamic Variables on Vibrational Equilibrium and Input Uncertainty," *Journal of Thermophysics and Heat Transfer*, vol. 31, pp. 586–608, July 2017.

[135] N. M. Kuenning, I. C. Sanders, N. Q. Minesi, D. I. Pineda, and R. M. Spearrin, "High-temperature absorption cross-sections of formaldehyde near 3.6 Mm," *Journal of Spectroscopy and Radiative Transfer (in preparation).*

[136] A. S. Pine, "Doppler-limited spectra of the CH stretching fundamentals of formaldehyde," *Journal of Molecular Spectroscopy*, vol. 70, no. 2, pp. 167–178, 1978.

[137] A. McLean, C. Mitchell, and D. Swanston, "Implementation of an efficient analytical approximation to the Voigt function for photoemission lineshape analysis," *Journal of Electron Spectroscopy and Related Phenomena*, vol. 69, pp. 125–132, Sept. 1994.

[138] E. M. Fisher, W. J. Pitz, H. J. Curran, and C. K. Westbrook, "Detailed chemical kinetic mechanisms for combustion of oxygenated fuels," *Proceedings of the Combustion Institute*, vol. 28, no. 2, pp. 1579–1586, 2000.

[139] M. Akbar Ali and A. Violi, "Reaction pathways for the thermal decomposition of methyl butanoate," *Journal of Organic Chemistry*, vol. 78, pp. 5898–5908, June 2013.

[140] J. Mendes, C. W. Zhou, and H. J. Curran, "Theoretical study of the rate constants for the hydrogen atom abstraction reactions of esters with ȯH radicals," *Journal of Physical Chemistry A*, vol. 118, no. 27, pp. 4889–4899, 2014.

[141] Y. L. Wang, D. J. Lee, C. K. Westbrook, F. N. Egolfopoulos, and T. T. Tsotsis, "Oxidation of small alkyl esters in flames," *Combustion and Flame*, vol. 161, pp. 810–817, Mar. 2014.

[142] Q. D. Wang and W. Zhang, "Influence of the double bond on the hydrogen abstraction reactions of methyl esters with hydrogen radical: An ab initio and chemical kinetic study," *RSC Advances*, vol. 5, no. 84, pp. 68314–68325, 2015.

[143] L. Zhang, Q. Chen, and P. Zhang, "A theoretical kinetics study of the reactions of methylbutanoate with hydrogen and hydroxyl radicals," *Proceedings of the Combustion Institute*, vol. 35, no. 1, pp. 481–489, 2015.

[144] L. K. Huynh and A. Violi, "Thermal decomposition of methyl butanoate: Ab initio study of a biodiesel fuel surrogate," *Journal of Organic Chemistry*, vol. 73, no. 1, pp. 94–101, 2008.

[145] F. Khaled, B. R. Giri, and A. Farooq, "A high-temperature shock tube kinetic study for the branching ratios of isobutene + OH reaction," *Proceedings of the Combustion Institute*, vol. 36, no. 1, pp. 265–272, 2017.

[146] Y. Fenard, G. Dayma, F. Halter, F. Foucher, Z. Serinyel, and P. Dagaut, "Experimental and modeling study of the oxidation of 1-butene and cis -2-butene in a jet-stirred reactor and a combustion vessel," *Energy and Fuels*, vol. 29, no. 2, pp. 1107–1118, 2015.

[147] S. Gaïl, S. M. Sarathy, M. J. Thomson, P. Diévart, and P. Dagaut, "Experimental and chemical kinetic modeling study of small methyl esters oxidation: Methyl (E)-2-butenoate and methyl butanoate," *Combustion and Flame*, vol. 155, no. 4, pp. 635–650, 2008.

[148] K. Yasunaga, Y. Kuraguchi, R. Ikeuchi, H. Masaoka, O. Takahashi, T. Koike, and Y. Hidaka, "Shock tube and modeling study of isobutene pyrolysis and oxidation," *Proceedings of the Combustion Institute*, vol. 32 I, no. 1, pp. 453–460, 2009.

[149] E. T. Es-Sebbar, F. Khaled, A. Elwardany, and A. Farooq, "Rate Coefficients of the Reaction of OH with Allene and Propyne at High Temperatures," *Journal of Physical Chemistry A*, vol. 120, no. 41, pp. 7998–8005, 2016.

[150] K. Narayanaswamy, H. Pitsch, and P. Pepiot, "A component library framework for deriving kinetic mechanisms for multi-component fuel surrogates: Application for jet fuel surrogates," *Combustion and Flame*, vol. 165, pp. 288–309, 2016.

[151] D. I. Pineda, F. A. Bendana, and R. M. Spearrin, "Competitive oxidation of methane and C2 hydrocarbons discerned by isotopic labeling and laser absorption spectroscopy of CO isotopologues in shock-heated mixtures," *Combustion and Flame*, vol. 224, pp. 54–65, Feb. 2021.

[152] S. J. Blanksby and G. B. Ellison, "Bond dissociation energies of organic molecules," *Accounts of Chemical Research*, vol. 36, pp. 255–263, Apr. 2003.

[153] N. R. C. U. S. o. A. E. G. Levels, "Hydrogen Fluoride:Acute Exposure Guideline Levels," in *Acute Exposure Guideline Levels for Selected Airborne Chemicals: Volume 4*, National Academies Press (US), 2004.

[154] D. Zierold and M. Chauviere, "Hydrogen Fluoride Inhalation Injury Because of a Fire Suppression System," *Military Medicine*, vol. 177, pp. 108–112, Jan. 2012.

[155] A. P. Modica and J. E. LaGraff, "Decomposition and Oxidation of C2F4 Behind Shock Waves," *The Journal of Chemical Physics*, vol. 43, pp. 3383–3392, May 2004.

[156] D. R. Burgess, M. R. Zachariah, W. Tsang, and P. R. Westmoreland, "Thermochemical and chemical kinetic data for fluorinated hydrocarbons," *Progress in Energy and Combustion Science*, vol. 21, pp. 453–529, Jan. 1995.

[157] G. T. Linteris and G. W. Gmurczyk, "Prediction of HF Formation During Suppression,"

[158] D. R. Burgess Jr., V. I. Babushok, G. T. Linteris, and J. A. Manion, "A Chemical Kinetic Mechanism for 2-Bromo-3,3,3-trifluoropropene (2-BTP) Flame Inhibition," *International Journal of Chemical Kinetics*, vol. 47, no. 9, pp. 533–563, 2015.

[159] D. R. Burgess Jr., V. I. Babushok, and J. A. Manion, "A chemical kinetic mechanism for combustion and flame propagation of CH2F2/O2/N2 mixtures," *International Journal of Chemical Kinetics*, vol. 54, no. 3, pp. 154–187, 2022.

[160] C. J. Cobos, A. E. Croce, K. Luther, and J. Troe, "Shock Wave Study of the Thermal Decomposition of CF3 and CF2 Radicals," *The Journal of Physical Chemistry A*, vol. 114, pp. 4755–4761, Apr. 2010.

[161] C. J. Cobos, K. Hintzer, L. Sölter, E. Tellbach, A. Thaler, and J. Troe, "High-Temperature Fluorocarbon Chemistry Revisited," *The Journal of Physical Chemistry A*, vol. 125, pp. 5626–5632, July 2021.

[162] D. S. J. Farina, S. K. Sirumalla, E. J. Mazeau, and R. H. West, "Extensive High-Accuracy Thermochemistry and Group Additivity Values for Halocarbon Combustion Modeling," *Industrial & Engineering Chemistry Research*, vol. 60, pp. 15492–15501, Nov. 2021.

[163] S. Sharma, K. Abeywardane, and C. F. Goldsmith, "Theory-Based Mechanism for Fluoromethane Combustion I: Thermochemistry and Abstraction Reactions," *The Journal of Physical Chemistry A*, vol. 127, pp. 1499–1511, Feb. 2023.

[164] C. Dhandapani, G. Blanquart, A. C. Karp, E. T. Jens, and J. Rabinovitch, "Combustion studies of MMA/GOx for a hybrid rocket motor," *Combustion and Flame*, vol. 256, p. 112994, Oct. 2023.

[165] A. Kacem, M. Mense, Y. Pizzo, G. Boyer, S. Suard, P. Boulet, G. Parent, and B. Porterie, "A fully coupled fluid/solid model for open air combustion of horizontally-oriented PMMA samples," *Combustion and Flame*, vol. 170, pp. 135–147, Aug. 2016.

[166] A. Rampazzo and F. Barato, "Modeling and CFD Simulation of Regression Rate in Hybrid Rocket Motors," *Fire*, vol. 6, p. 100, Mar. 2023.

[167] R. Krebs, J. Owens, and H. Luckarift, "Formation and detection of hydrogen fluoride gas during fire fighting scenarios," *Fire Safety Journal*, vol. 127, p. 103489, Jan. 2022.

[168] F. A. Bendana, I. C. Sanders, N. G. Stacy, and R. M. Spearrin, "Localized characteristic velocity (c_*) for rocket combustion analysis based on gas temperature and composition via laser absorption spectroscopy," *Measurement Science and Technology*, vol. 32, p. 125203, Dec. 2021.

[169] D. Sturk, L. Hoffmann, and A. Tidblad, "Fire Tests on E-vehicle Battery Cells and Packs," *Traffic Injury Prevention*, vol. 16, pp. S159–S164, Jan. 2015.

[170] F. Larsson, P. Andersson, P. Blomqvist, A. Lorén, and B.-E. Mellander, "Characteristics of lithium-ion batteries during fire tests," *Journal of Power Sources*, vol. 271, pp. 414–420, Dec. 2014.